



McGuire, Jake (2020) *Relaxation phenomena of dithiolene type radical ligands for quantum computation*. PhD thesis.

<http://theses.gla.ac.uk/81829/>

Copyright and moral rights for this work are retained by the author

A copy can be downloaded for personal non-commercial research or study, without prior permission or charge

This work cannot be reproduced or quoted extensively from without first obtaining permission in writing from the author

The content must not be changed in any way or sold commercially in any format or medium without the formal permission of the author

When referring to this work, full bibliographic details including the author, title, awarding institution and date of the thesis must be given

Enlighten: Theses

<https://theses.gla.ac.uk/>
research-enlighten@glasgow.ac.uk



UNIVERSITY
of
GLASGOW

**Relaxation Phenomena of Dithiolene Type
Radical Ligands for Quantum Computation**

Jake McGuire

Submitted in fulfilment of the requirements of the Degree of Doctor of Philosophy

October 2020

School of Chemistry
College of Science and Engineering
University of Glasgow

Authors Declaration

The work contained within this thesis, submitted for the degree of Doctor of Philosophy, is the result of my own original work, except where explicit reference is made to the contribution of others, and has not been submitted for a degree at the University of Glasgow or any other institution.

Printed Name: Jake McGuire

Signature:

Abstract

The intrinsic redox activity of the dithiolene ligand is used here as the novel spin host in a prototype molecular electron spin qubit where the traditional roles of the metal and ligand components in coordination complexes are inverted. A series of paramagnetic bis(dithiolene) complexes with group 10 metals – nickel, palladium, platinum – provides a backdrop to investigate the spin dynamics of the organic ligand radical using pulsed EPR spectroscopy. The temperature dependence of the phase memory time (T_M) is shown to be dependent on the identity of the diamagnetic metal ion, with the short times recorded for platinum a consequence of a diminishing spin-lattice (T_1) relaxation time driven by spin-orbit coupling. The utility of the radical ligand spin center is confirmed when it delivers one of the longest phase memory times ever recorded for a molecular two-qubit prototype.

A bis(dithiolene)gold complex is presented as a model for an organic molecular electron spin qubit attached to a metallic surface that acts as a conduit to electrically address the qubit. A two-membered electron transfer series is developed of the formula $[\text{Au}^{\text{III}}(\text{adt})_2]^{1-/0}$, where adt is a redox-active dithiolene ligand that is sequentially oxidized as the series is traversed while the central metal ion remains Au^{III} and steadfastly square planar. One-electron oxidation of diamagnetic $[\text{Au}^{\text{III}}(\text{adt})_2]^{1-}$ produces an $S = 1/2$ charge-neutral complex, $[\text{Au}^{\text{III}}(\text{adt})(\text{adt}^{\cdot})]$ which is spectroscopically and theoretically characterized with a near negligible Au contribution to the ground state. A phase memory time (T_M) of 21 μs is recorded in 4:1 CS_2/CCl_4 at 10 K, which is the longest ever reported for a coordination complex possessing a third-row transition metal ion. With increasing temperature, T_M is dramatically decreased becoming unmeasurable above 80 K as a consequence of the diminishing spin-lattice (T_1) relaxation time fuelled by spin-orbit coupling. These relaxation times are 1–2 orders of magnitude shorter for the solid dilution of in isoelectronic $[\text{Ni}(\text{adt})_2]$ because this material is a molecular semiconductor. Although the conducting properties of this material provide efficient pathways to dissipate the energy through the lattice, it can also be used to electrically address the paramagnetic dopant by tapping into the mild reduction potential to switch magnetism “on” and “off” in the gold complex without compromising the integrity of its structure. These results serve to highlight the need to consider the composition of not just the qubit, but all components of these spintronic assemblies.

Addition of Lewis acidic rare earth ions to the bis(dithiooxalato)nickel complex ion generated new charge-neutral heterometallic species where the rare earth M(III) ions ($M = \text{Y}, \text{Nd}, \text{Sm}, \text{Eu}, \text{Gd}, \text{Tb}, \text{Dy}, \text{Ho}, \text{Er}, \text{Tm}, \text{Yb}, \text{Lu}$) occupy the O, O' pocket of both ligands. Together with stabilising hydrotris(pyrazolyl)borate co-ligands on the rare earth ion, chemical reduction of the bridging bis(dithiooxalato)nickel unit led to the first molecular and electronic structure characterisation of the elusive dithiooxalato radical ligand, $(\text{dto})^{3\cdot-}$ for the Y^{III} and Gd^{III}

analogues. The central metal was varied down group 10 with lutetium to form a series with which to further investigate the environment of the radical spin.

Acknowledgements

First and foremost, I would like to thank my excellent supervisor Dr. Stephen Sproules. His tutelage in the chemical arts, keen eye for detail, and patience to develop my relentless and mostly abysmal ideas into something tangible without doubt have been the greatest contributing factors towards any achievements I've made over the course of my PhD and likely will be long into whatever I do next. Stephen has, by his own admission, an 'elephantine memory' and it is always interesting to listen along on his diatribes. If you are not inclined to learn about chemistry prick up your ears and you may learn about the bloodline of British monarchs, Fabergé eggs, or the cast members of neighbours.

I thank Dr. Haralampos Moiras for being a relaxed second supervisor but far more importantly an immaculate crystallographer. Harry has the ability to pick a diffractable crystal out of mud. It's his party trick, yes, he does bring the diffractometer. Harry's underling Dr. James McAllister is thanked for producing a bucket of potassium dithiooxalate ligand for me and for his consolidation of my obscure unit conversions knowledge.

I thank Dr. Emma Richards for allowing us the use of her pulsed EPR spectrometers at the University of Cardiff. I have never met Emma; and I never will.

A big thanks to Prof. James P. Donahue at the University of Tulane in New Orleans. I had the privilege of spending a summer under his supervision where I was introduced to the sun. I thank Jim for introducing me to Abita amber, creole hotdogs, drink driving and the trials of fathering forty children. Another notable mention is Anthony Obanda for his excellent synthetic knowledge, can-do attitude and useful discussions.

I would like to thank Dr. Joy Farnaby for allowing me to use her functioning glovebox and her group as sounding boards and delegates. I've learned far more about rare-earths and beer from working with Joy than I ever had intended to starting my PhD. Individually I would like to thank the members of her group; Dr. James Hickson- for keeping me sane in the before times; Sam Horsewill- for giving me EPR samples to analyse that were genuinely observable paramagnetic compounds and not just reaction mixtures; and Bradley Wilson- for his assistance in the initial preparation of the trimetallics in Chapter 4.

I have learned many lessons from the various and short-lived members of the Sproules group. The longest standing, my predecessor, Dr. Cailean Macleod. Cailean expertly illustrated that bruker plastiglass behaves mostly like plastic upon prolonged heating in an oven. His repeated studies into this effect form the cornerstone of modern plastiglass thermal resistance theory. I once watched Cailean spill concentrated sulphuric acid on his jeans, to rectify this he began rubbing solid sodium bicarbonate onto them till he had rubbed a 6 inch diameter hole in them just above the knee.

The following fallen soldiers are commended for their contribution to the cause;

George Healing for simulating an emergency and giving me practice dialling 4444, Nicole Miller for continuing the investigations on how plastic behaves in an oven, Megan Le Déaut for her synthesis of the many rare-earth trimetallics encountered in this thesis with only two days of supervision and excellent record keeping, Tony Bissoonauth for his investigation on how many days he could survive only eating apples and his general outlook and presence, Big Mike and Adam Mackenzie for introducing me to the trials of project students, Ludovica Credendino for committing to the endeavour, and other Megan for whatever it was that she did.

I wish them all the best and hope that one day they find the courage to ask a question or contribute to the discussion in a group meeting.

Lastly, I would like to thank my amazing wife Divia whom I have just met but whose support I cannot do without.

Abbreviations

15c5bd	15-crown-5-1,2-benzenedithiolate
18c6bd	18-crown-6-1,2-benzenedithiolate
A	nuclear hyperfine splitting parameter
Å	Angstrom
Ar	aryl group
acac	acetylacetonate
adt	dianisylidithiolate
B	magnetic field
ba	bromanilate
bds	benzene-1,2-diselenolate
bd	benzene-1,2-dithiolate
'Big N'	1,1,1-trimethyl- <i>N</i> -(trimethylsilyl)-silanamine
bipy	2,2'-bipyridine
bpdppb	1-butylphenylphosphino-2-diphenylphosphinobenzene
BS	broken symmetry
Bz	benzyl
bzac	benzoylacetonate
cat	catecholate
CCDC	Cambridge crystallographic data centre
CCl ₄	carbon tetrachloride
CDCl ₃	chloroform- <i>d</i>
CH ₂ Cl ₂	dichloromethane
Cl ₃ CCN	trichloroacetonitrile
CN	cyanide
CNOT	controlled NOT
Cp	η ⁵ -cyclopentadienyl

Cp'	η^5 -1-(trimethylsilyl)-2,4-cyclopentadien-1-yl
cr	croconatate
CS ₂	carbon disulphide
CT	charge transfer
CV	cyclic voltammetry
Cw EPR	continuous wave electron paramagnetic resonance
d	days
<i>D</i>	axial magnetic dipole-dipole interaction
dbddto	2,5-dithioxobenz[1,2- <i>d'</i> :3,4- <i>d</i>]bis[1,3]dithiolene-7,8-dithiolate
dbm	dibenzoylmethane
dcpe	bis(dicyclohexylphosphino)ethane
dddt	5,6-dihydro-1,4-dithiin-2,3-dithiolate
ddpd	<i>N,N'</i> -dimethyl- <i>N,N'</i> -dipyridine-2-yl-pyridine-2,6-diamine
DFT	density functional theory
dip	3-(diphenylphosphoryl)-methylbenzene-1,2-dithiolate
dm-dddt	5,6-dimethyl-5,6-dihydro-1,4-dithiin-2,3-dithiolate
dmed	dimethoxyesterdithiolate
DMF	<i>N,N</i> -dimethylformamide
dmid	2-oxo-1,3-dithiole-4,5-dithiolate
dmit	1,3-dithiole-2-thione-4,5-dithiolate
dmobdt	4,5-dimethoxybenzenedithiolate
DMSO	dimethylsulfoxide
dmt	1,2-dithiole-3-thione-4,5-dithiolate
DPNO	diphenyl nitroxide
DPFNO	bis(2,4,6-trifluoro) nitroxide
dpmppb	1,2-bis(methylphenylphosphino)benzene
dppa-e	1,2-bis(diphenylphosphino)ethylamine

dppac	bis(diphenylphosphino)acetylene
dppb	1,2-bis(diphenylphosphino)benzene
dppe	1,2-bis(diphenylphosphino)ethane
dppee	1,2-bis(diphenylphosphino)ethene
dppm	1,2-bis(diphenylphosphino)methane
dppp	1,2-bis(diphenylphosphino)propane
dtbbdt	3,5-di-tert-butylbenzodithiolate ligand
dtbpdtd	1,2-di(4-tert-butylphenyl)ethylene-1,2-dithiolate
dtbsq	3,5-di-tert-butylsemiquinonato
dto	dithiooxalate
<i>E</i>	transversal magnetic dipole-dipole interaction
edt	ethane-1,2-dithiolate
EFG	electric field gradient
ENDOR	electron nuclear double resonance
Epp	peak potential separation
EPR	electron paramagnetic resonance
ESE	electron spin echo
ESEEM	electron spin echo envelope modulation
ESI-MS	electrospray ionisation mass spectroscopy
Et	ethyl
Et-thiazdt	ethylthiazoledithiolate
fa	fluoranilate
Fc	ferrocene/ferrocenyl
Fod	(3 <i>Z</i>)-6,6,7,7,8,8,8-heptafluoro-2,2-dimethyl-5-oxo-3-octen-3-olate
<i>g</i>	<i>g</i> -factor
GLA	glutaconic acid
GoF	goodness of fit

h	hours
hbdt	hexathiobenzene
hfac	hexafluoroacetylacetone
HFEP	high field electron paramagnetic resonance
HMPL	1,3,4,6,7,9-hexamethoxy-1 <i>H</i> -Phenalen-1-yl
HOMO	highest occupied molecular orbital
<i>I</i>	nuclear spin quantum number
<i>i</i> Pr	<i>iso</i> -propyl
IR	infrared
iso	isotropic
IVCT	intervalence charge transfer
<i>J</i>	dipolar interspin coupling
LCAO	linear combination of atomic orbitals
LF	ligand field
LMCT	ligand-to-metal charge transfer
LUMO	lowest unoccupied molecular orbital
m	medium
<i>m</i>	meta
M	bulk magnetisation vector
Me	methyl
mapimp	(<i>E</i>)-2-((3-methylamino)propylimino)methyl)phenol
Me ₂ bipy	dimethylbipyridine
MeCN	acetonitrile
Me-thiazdt	methylthiazoledithiolate
mnt	maleonitrile-1,2-dithiolate
MO	molecular orbital
mppb	1,2-bis(dimethylphosphino)benzene

napdo	2,3-naphthalenediolatate
nbopdt	di(4-nbutoxyphenyl) dithiolate
ⁿ Bu	<i>n</i> -butyl
NIR	near-infrared
NMR	nuclear magnetic resonance
ⁿ Pr	<i>n</i> -propyl
py	pyridine
o	ortho
opyrca	6-(3-oxo-3-(2-hydroxyphenyl)propionyl)pyridine-2-carboxylic acid
ox	oxalate
<i>p</i>	para
Pc	phthalocyanine
pdtd	diphenyldithiolate
Ph	phenyl
pipdt	1,4-dimethyl-piperazine-3,2-dithione
POM	polyoxometalate
ppm	parts per million
PrCN	propylcyanide
prdddt	2-(6,7-dihydro-5H-1,3-dithiolo[4,5-b][1,4]dithiepin-2-ylidene)-1,3-dithiole-4,5-dithiolatate
prddt	2-(1,3-dithian-2-ylidene)-1,3-dithiole-4,5-dithiolatate
prddt	6,7-dihydro-5H-1,4-dithiepin-2,3-dithiolatate
prdt	propane-1,3-dithiolatate
qdt	quinoxalinedithiolate
qim	4,4':2',2":4",4""-quaterimidazole
Qubit	quantum bit
s	strong

S	spin quantum number
SALC	symmetry adapted linear combination
sh	shoulder
SIM	single ion magnet
SMM	single molecule magnet
SOC	spin orbit coupling
SOMO	singly occupied molecular orbital
T	tesla
T_1	spin-lattice relaxation time
$T_{1,f}$	spin-lattice relaxation time fast component
$T_{1,s}$	spin-lattice relaxation time slow component
T_2	spin-spin relaxation time
$T_{2,f}$	spin-spin relaxation time fast component
$T_{2,s}$	spin-spin relaxation time slow component
T_M	phase memory time
$T_{M,f}$	phase memory time fast component
$T_{M,s}$	phase memory time slow component
^t Bu	<i>tert</i> -butyl
tdt	toluene-3,4-dithiolate
TDMQA	3,7,11-tris(1,1-dimethylethyl)-1,13-dimethoxy-5 <i>H</i> -quino[2,3,4- <i>k</i>]acridin-5-yl
tfacac	1,1,1-trifluoroacetylacetone
THF	tetrahydrofurn
tmc	tetramethylaminecyclomer
Tol	tolyl
Tp	tris(pyrazolyl)borate
tpbz	1,2,4,5-tetra(diphenylphosphino)benzene
trensal	2,2',2''-tris(salicylideneimino)triethylamine

tfdt	tetrathiafulvalene dithiolate
tti	1,2,4,5-tetrathiobenzene
TZ2P	valence triple ζ doubly polarized basis set
vs	very strong
XAS	X-ray absorption spectroscopy
Z_{eff}	effective nuclear charge
ZORA	zero order regular approximation
ZFS	zero-field splitting

1.CHAPTER 1: INTRODUCTION	1
1.1.Quantum Computation an Overview	1
1.1.1.Quantum Bits and Pieces	1
1.1.2.The Divencenzo Criteria and their Satisfaction by Electron Paramagnetic Resonance	1
1.2.Monospin Molecular Electron Spin Qubits	7
1.2.1.Organic	8
1.2.2.Inorganic	12
1.2.2.1.Transition Metal Compounds	12
1.2.2.1.1.Group 5	12
1.2.2.1.2.Group 6	18
1.2.2.1.3.Group 7	31
1.2.2.1.4.Group 8	31
1.2.2.1.5.Group 9	32
1.2.2.1.6.Group 10	34
1.2.2.1.7.Group 11	35
1.2.2.2.Rare-earth Metal Compounds	36
1.3.Multispin Molecular Electron Spin Qubits	39
1.3.1.Organic Systems	39
1.3.2.Coordination Systems	41
1.4.Scope of Thesis	45
1.5.References	47
2.CHAPTER 2: GROUP 10 DITHIOLENE RADICAL MAGNETIC RELAXATION	52
2.1.Introduction	52
2.1.1.Innocence and Non-innocence in Coordination Compounds	52
2.1.2.Dithiolene Ligands	52
2.1.2.1.Group 10 Homoleptic Bis Chelates	53
2.1.2.2. Heteroleptic Chelates with Phosphines	58
2.1.3.Scope of Chapter	69
2.2.Synthesis	70
2.3.X-ray Crystallographic Structure	70
2.4.Electronic Structure	72

2.4.1.Electronic Spectra	72
2.4.2.Continuous Wave EPR	74
2.5.Electrochemistry	82
2.6.DFT Calculations	84
2.7.Relaxation Phenomena	89
2.7.1.Spin-Lattice Relaxation	89
2.7.2.Spin-Spin Relaxation	93
2.7.3.Rabi Oscillations	102
2.8.Conclusions	105
2.9.Experimental	106
2.9.1.Synthesis	106
2.9.2.Physical Characterization and Theoretical	106
2.10.References	111
3.CHAPTER 3: GOLD BIS(DITHIOLENE) MAGNETIC RELAXATION	117
3.1.Introduction	117
3.1.1.Electron Transfer Series	117
3.1.2.Neutral Radical Gold Bis(dithiolene)s	118
3.1.2.1.Robin-Day Classification	118
3.3.2.2.Quadrupolar EPR	120
3.1.3.Molecular Semiconductors	120
3.1.4.Scope of Chapter	122
3.2.Synthesis	124
3.3.X-ray Crystallographic Structure	125
3.4.Electronic Structure	126
3.4.1.Electronic Spectra	126
3.4.2.Continuous Wave EPR	126
3.5.DFT Calculations	130
3.6.Pulsed EPR	132
3.6.1.Spin-Lattice relaxation	133
3.6.2.Spin-Spin relaxation	135

3.6.3.Rabi Oscillations	136
3.7.Conclusions	139
3.8.Experimental	140
3.8.1.Synthesis	140
3.8.2.Physical Characterisation and Theoretical	141
3.9.References	145
4.CHAPTER 4: RARE-EARTH GROUP 10 TRIMETALLICS OF DITHIOOXALATE	151
4.1.Introduction	151
4.1.1.The Dithiooxalate Ligand	151
4.1.1.1.Tin Chemistry of the Dithiooxalate Ligand	152
4.1.2.Rare-earth Metal Coordination Chemistry and Scorpionates	153
4.1.3.Multimetallic Mixed Metal Species	155
4.1.4.Scope of Chapter	156
4.2.Synthesis	158
4.3.X-ray Crystallographic Structure	163
4.4.Electronic Structure	167
4.4.1.Electronic Spectra	167
4.4.2.Continuous Wave EPR	168
4.5.Electrochemistry	171
4.6.DFT Calculations	173
4.7.Conclusions	175
4.8.Experimental	176
4.8.1.Synthesis	176
4.8.2.Physical Characterisation and Theoretical	180
4.11.References	186
5.CONCLUSIONS AND FUTUREWORK	191
A.APPENDIX	192

A.1.Calculations	192
A.1.Relaxation data	212

1.Chapter 1: Introduction

1.1.Quantum Computation an Overview

1.1.1.Quantum Bits and Pieces

A quantum computer is a device capable of far exceeding the computing power of a classical computer.¹ Central to its operation is the qubit: a quantum bit. Whereas a classical computer utilises classical bits, which may hold a value of 0 or 1, a qubit makes use of quantum phenomena to hold multiple values of, and between, 0 and 1 in tandem to perform multiple calculations simultaneously. A qubit must therefore be capable of holding distinct quantum states. Promising candidates for qubits are nitrogen-doped vacancies in diamond, quantum dots, phosphorus doped silicon and molecular spin host qubits.²⁻⁵ The latter of which is the focus of this thesis.

The two simplest units of spin accessible to an observer in a molecule are the nuclear and electron spins. Early research into the field of molecular spin host qubits gravitated towards the use of nuclear spins: owed to their long coherence times– the length of time for which a state can be maintained– and the already well-developed nuclear magnetic resonance phase pulse experiments and apparatus required to execute operations and measurements of qubits and qubit gates.⁶⁻⁷ Only in the last five years have electron spin host molecules become viable candidates as qubits. This lag in progression when compared to their nuclear counterparts attributed to their much shorter coherence times (several orders of magnitude shorter) as well as a smaller pool of available techniques to assess qubits and manipulate quantum operations. However, developments by many research groups in extending these coherence times, and engineering molecules so as to circumvent difficulties arising from the limited techniques available (both only possible due to the richer synthetic chemistry at hand when designing electron spin host molecules and the advancements made in electron paramagnetic resonance spectroscopy technologies) has resulted in electron spin host molecules becoming viable contenders in the qubit field.⁸

1.1.2.The Divencenzo Criteria and their Satisfaction by Electron Paramagnetic Resonance

As previously noted the advantages offered by quantum computation stems from the qubits utilisation of quantum phenomena. Classical bits hold states of 0 or 1, designated “on” or “off”- a nomenclature derived from their classical counterparts being transistors either allowing or disallowing the flow of electricity through circuit paths. Quantum bits exist as superpositions of 0 and 1 described by the wavefunction, $|\varphi\rangle = \alpha |0\rangle + \beta |1\rangle$. As a spin host qubit this condition is realised from any two level spin system, the simplest being $S = 1/2$ where the states 0 and 1 are the spin up and spin down states. For an electron spin this correlates to the $m_s = -1/2$ and $m_s = +1/2$ states. These superposition states can be visualised as positions on the surface of the Bloch sphere (Figure 1.1.).⁹

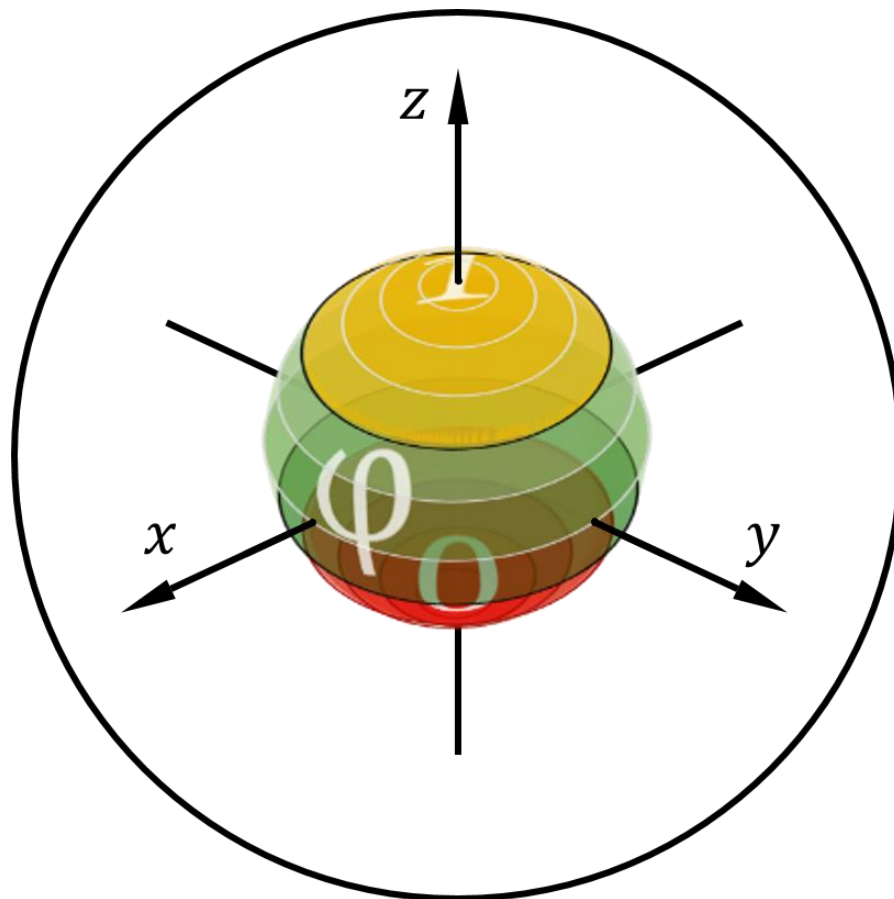


Figure 1.1. The Bloch sphere.

The requirements for a quantum computer to operate are more complicated than simply possessing distinct states. Indeed, for any realisation of a qubit there exists a set of criteria, proposed by DiVincenzo, which must be fulfilled for operation to be possible.¹⁰ Consisting of seven criteria, only the five pertaining to quantum computation are summarised below,

1. a scalable physical system with well characterised qubits
2. the ability to initialise the state of the qubits to a simple fiducial state
3. long coherence times, much longer than the gate operation time
4. a “universal” set of quantum gates
5. a qubit-specific measurement capacity

The other two pertaining to quantum communication are not discussed here.

The former part of the first criterion states that a quantum computer must be composed of enough qubits to function and that more qubits may be added to increase the size and therefore power of computations. For molecular qubits this means increasing the number of molecules present. However, complications arise when the concentration of spins increases as there are more relaxation pathways available. This will be discussed in further detail when addressing the third criterion. The latter part of the first criterion pertains to the

states available to the qubit. For a successful qubit these states must be well defined, states in between are allowed to exist but the fiducial states must be distinct. The simplest case of this is a molecular spin host qubit with $S = 1/2$ in a magnetic field; this is already the spin of the electron and so this condition is satisfied (Figure 1.2.)

The second criterion pertains to the initialisation of one of these states i.e. the system can be turned on to one of the two fiducial states. This is achieved for electrons by cooling of the qubit in a magnetic field: splitting the Zeeman levels and populating the $m_s = -1/2$ ground state. In multiple electron systems the energy gap between the ground and excited state must be large enough to prevent spin admixing and the loss of information, and in the case of single molecule magnets and high spin transition metal ions (not discussed here) requires cooling to much lower temperatures to access the $S = 1/2$ ground state.

The subject matter of the third criterion, the coherence time, has been by far the most researched quantum phenomenon with regard to qubits and is still the primary focus to this day. The coherence time is the length of time a quantum state can exist for, before interactions with the environment destroy it. The nomenclature 'coherence time' is used interchangeably with its inverse: 'decoherence time'. The state is coherent over its coherence lifetime, or— from initialisation— proceeds to decohere over its decoherence lifetime. Both of these lifetimes are the same. Most early efforts at qubit design is devoted to lengthening the coherence time to in turn maximise the computing time available. For spin host molecules the interactions that destroy it are with particles and waves that can interfere with its angular momentum. These primarily consists of phonons, then spins, and to lesser extent orbitals themselves. The phonons can be dealt with by cooling of the system. However, the spin interaction is intractable as interaction between the spins is the design feature fundamental for the operation of the machine, impeding the scalability of both solution and solid-state systems. The coherence time is correlated with how strongly or weakly a spin couples to its environment. Nuclear spins benefit from their weak coupling between each other and so take appreciable time to decohere. Conversely, electron spins exhibit strong coupling between neighbouring electron and nuclear spins and so relax much faster. This is not necessarily a problem. The third criterion states that the coherence time need only be longer than the gating times (gates being operations on qubits i.e. a unitary spin flip) so as to implement calculations. The gating time correlates to the strength of the interaction between the spins, therefore electron spins enjoy much faster gating times than their nuclear brethren. Long gating times threaten the greatest advantage of the quantum computer, its superior speed. However, shortening the gating times- whilst theoretically enabling faster computations- puts strains on the apparatus required to carry out these operations. Gating times for electron spins can be between 10 and 20 ns depending on the method of implementation but the systems are limited by the current technology.

These gate operations are imperative to the operation of a computer, classical or quantum. A computer circuit works by the operation of gates with different functionalities, such as NOT, AND or OR, on each other. By arranging these simple gates in more complex circuit arrays it is possible to construct single logic gates that can execute the action of any gate. These so called universal gates are desired above other simpler iterations for their versatility. Some quantum equivalents of universal gates are the CNOT, $i\sqrt{\text{SWAP}}$ and Toffoli gates that have already been shown to be possible using molecular spin host qubits, satisfying the fourth criterion.¹¹⁻¹² A few of these gates have been used to implement quantum algorithms such as Shors algorithm for factorising large numbers, utilising phase pulse technology for action of the gate.

The final criterion relevant to quantum computation, the qubit-specific measurement capacity, states that the qubits must be able to be written to, and read from. That is; both the input and output must be fiducial states and the quantum computer can never truly be isolated from the environment.

Addressing the first criterion with regards to molecular spin host qubits is delightfully simple as NMR, EPR, electronic, and mass spectroscopies along with X-ray diffraction are easily employed to elucidate structure and characterise the qubit. For electron spin qubits continuous wave EPR is the starting point for more in-depth study. In a magnetic field an $S = 1/2$ electron spin orientates parallel ($m_s = -1/2$) or anti parallel ($m_s = +1/2$) in the field. This is the Zeeman effect. As the magnetic field increases the splitting, the frequency ω , increases. Application of orthogonal microwave radiation at this frequency gives rise to a detectable signal of the electrons. This signal is the difference in population between the two states described by Boltzmann's thermal equilibrium. The population difference gives rise to a bulk magnetisation vector aligned along the magnetic field, this is designated the z-axis. The spectra from cw EPR give information about the environment of the electron spin catalogued as the spin Hamiltonian parameters g , A , D , E , and J . The g value, or g -factor, is a dimensionless quantity that characterises the magnetic moment and gyroscopic ratio of a particle, or atom. The factor for a free electron is one of the most precisely characterised constants with $g_e = 2.0023$. Depending on the orbital environment g will be shifted low-field or high-field of the g -factor of a free electron. A is the hyperfine tensor; the interaction of electron spins with nuclear spins. The local field results in a further splitting of the $m_s = \pm 1/2$ states with the nuclear spin I . As EPR is carried out a specific frequency this coupling gives rise to multiple lines dependant on I , splitting binomially as $(2n+1)^k$ where I is the nuclear spin, n is the number of equivalent nuclei, and k is a multiplier by inequivalent nuclei. D and E are zero-field splitting (ZFS) parameters corresponding to axial and rhombic splitting respectively. They describe the fine structure of paramagnets with $S > 1/2$. As degenerate orbitals are populated by single electron spins degeneracy is broken and gives

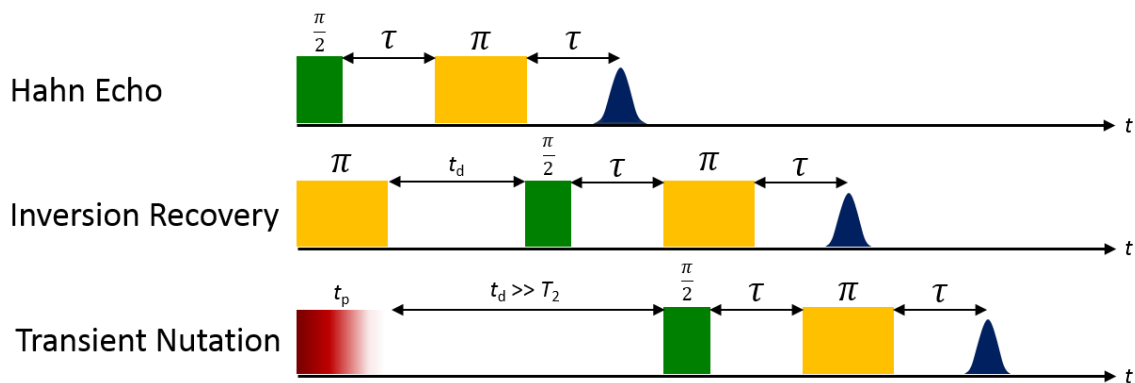


Figure 1.2. Pulse diagrams for the measurement of T_1 , T_2 and Rabi oscillations.

rise to magnetic anisotropy in no applied magnetic field. For qubits a very low ZFS is preferred as a large ZFS enables admixing of states which results in faster relaxation times and complicates the gate operations. However, the greater number of spin states does allow for more transitions within the molecule which if properly manipulated would give rise to more potential qubits within one molecular structure. Possibly the most important spin-hamiltonian parameter for multispin qubits is the exchange coupling tensor J . J describes the total interaction between two electron spins; encompassing direct exchange, super exchange, and double exchange. The exchange interaction strength is dependant on the electron's relative position to each other. If they are close and with favourable orbital arrangement the exchange interaction is incredibly strong, if they are separated by some chemical spacer or have poor orbital alignment the exchange interaction is weak. In favourable circumstances J may be calculated with EPR and can hold positive, negative or 0 values.

After exhausting the capabilities of cw EPR to identify promising electron spin qubit candidates the focus shifts to pulsed EPR techniques to evaluate decoherence phenomena and coherent spin manipulation. Relaxation times, and therefore decoherence times, are measured by pulsed EPR sequences utilising Electron Spin-Echo Envelope Modulation (ESEEM). Decoherence can be described experimentally by the spin-lattice relaxation time T_1 and the spin-spin relaxation time T_2 (T_1 and T_2 also go by the names of longitudinal and transverse relaxation times respectively with T_2 accruing the symbols T_2^*). If T_2 is not directly measurable then the phase memory time T_m is used in its place. This encompasses all processes that contribute toward electron spin decoherence, including T_2 . T_1 describes how the qubit relaxes energetically and T_2 measures the relaxation due to other magnetic components i.e. other qubits or magnetic nuclei. In a magnetic field the electron spins are orientated along the magnetic field vector \mathbf{B}_0 . A bulk magnetisation vector \mathbf{M} is measured along this field (designated the z-axis), the electron spins are also precessing on the z-axis. T_1 is the time it takes for \mathbf{M} to average to thermal equilibrium within a magnetic field. Simultaneously, as all the spins are precessing around the z-axis in the x,y plane but not at

the same rate nor the same direction they will eventually result in an averaging of magnetisation in the x,y plane to zero. The time this takes is T_2 . T_1 is typically far longer than T_2 and so T_2 is used invariably as a measure of decoherence. However, T_2 is limited by T_1 so it is important for a qubit to possess appreciable times in both.

Microwave pulses of specific phases applied to the sample reorientate \mathbf{M} to specific points of a Cartesian coordinate system visualised on a Bloch sphere (Figure 1.2.). The Hahn Echo is a simple two pulse procedure implemented to measure T_2 . Firstly, a $\pi/2$ pulse is applied, shifting \mathbf{M} along the y -axis. A time τ is waited while the spins fan out and dephase in the xy plane. Applying a π pulse then flips these spins across the x -axis. The individual spins precess at the same rate they were previously dephasing at and so come back into phase after time τ and are observed as an echo. By varying τ and measuring the intensity of the echo T_2 can be calculated with the monoexponential:

$$I(2\tau) = I(0)\exp\left[-\frac{2\tau}{T_2}\right]$$

Where 2τ is twice the interpulse delay time, $I(2\tau)$ is the integrated echo intensity for the pulse separation, $I(0)$ the intensity extrapolated to $\tau = 0$ and T_2 the decoherence time.¹³ In cases where the plotted data is not concurrent with the monoexponential the stretched exponential

$$I(2\tau) = I(0)\exp\left[-\left(\frac{2\tau}{T_2}\right)^k\right]$$

is used. A value of k greater than 1 is typically the result of interaction of the electron spins with surrounding protons and is dubbed shallow proton modulation. T_1 is calculated from the inversion recovery experiment. A π pulse is applied and \mathbf{M} flipped from the z -axis to along the $-z$ -axis. A time t_d is waited over which longitudinal relaxation occurs and \mathbf{M} returns to the z -axis. Before this happens a standard Hahn echo is implemented and the same exponential used with t_d to calculate T_1 .

Variable power transient nutation is used to assess whether a matter spin qubit can be coherently manipulated. A tipping pulse, t_p , is applied at the beginning of the experiment to position \mathbf{M} at some position on the Bloch sphere. A time t_d that is much longer than T_2 is waited. This ensures that any magnetisation in the x,y plane is averaged to zero and only magnetisation along the z -axis remains. A $\pi/2$ pulse is then applied. In its simplest form the free induction decay (FID) profile of the spin may be recorded at this point but it is much shorter than T_2 . To achieve a signal with appreciable length a Hahn echo pulse sequence is applied. Key to the transient nutation experiment and qubits is the observation of Rabi oscillations in the detected signal. These oscillations are the result of coherent emission and absorption of microwave radiation and are representative of transitions between the

ground and excited spin states under investigation. A linear dependence of the frequency with the intensity of the Rabi oscillations is indicative of a super position of states and coherent spin manipulation.¹⁴ The Rabi frequency Ω_R is a measure of gating time. For a viable qubit Ω_R is desired to be a factor of 10^4 shorter than the decoherence time T_2 . This factor Q_m (the qubit figure of merit) may be quantified as $2 \Omega_R T_2$.

1.2. Monospin Molecular Electron Spin Qubits

The molecular electron spin host qubits can be separated into two categories; organic and inorganic, each with their own benefits and deficits. A selection of qubits are provided in Figure 1.3. for comparison of coherence times. Organic based electron spin host qubits enjoy luxurious decoherence times when compared with their inorganic counterparts but suffer from the small pool of stable organic radicals available. Unsurprisingly one of the most prominent organic spin qubits is the ubiquitous nitroxide, a staple of introductory EPR spectroscopy for its robustness, spectral simplicity, and low cost. The bulk of organic qubit research performed is on these nitroxides or endohedral fullerene derivatives with a peppering of other stable radicals– and some photogenerated radicals– across the literature (Figure 1.4).¹⁵⁻¹⁸

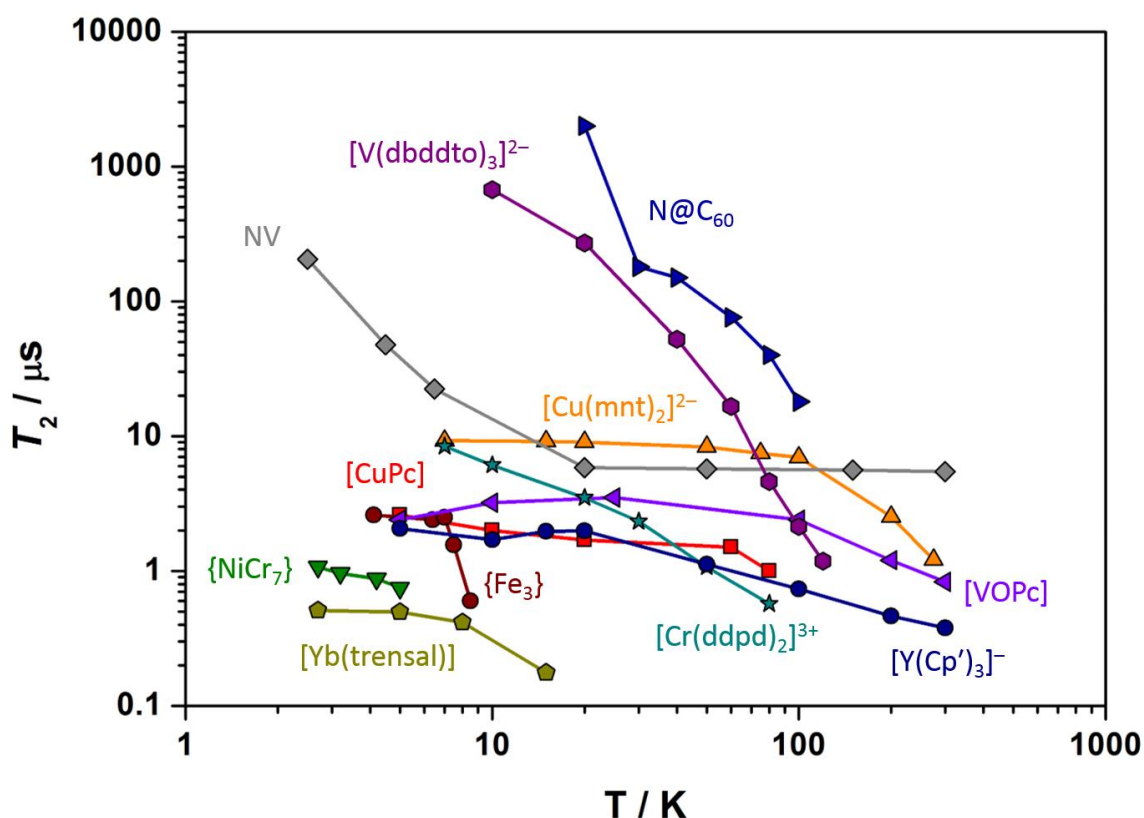


Figure 1.3. Selected qubits and their coherence times T_2 at variable temperatures.

Inorganic qubits benefit from far simpler synthesis and the potential to incorporate many electron spins within a molecular qubit system with relative ease. They also possess a far greater range of customisability than organic qubits given that the metal, geometry, ligand, and- if charged- counter ions, can all be changed to influence the properties of the qubit. By far the most researched inorganic qubits are those of V^{IV} and Cu^{II} owing to their explicit $S = 1/2$ ground state. As is the case for nitroxide radicals these spin systems are very well characterised and stem from the cardinal research into relaxation phenomena of these systems by Eaton and Eaton.¹³ However, there are still a wealth of other qubits and motifs at hand. As investigations into qubit properties can be so varied research has been somewhat sporadic across the periodic table and so qubits are here organised by group for the transition metals and collectively for the rare earths.

1.2.1.Organic

The record for decoherence times of electron spin host qubits over the last decade is 250 μs at 170 K (a remarkably high temperature for such coherence times) and is held by the $N@C_{60}$ endohedral fullerene in 0.01 mM CS_2 .¹⁹ Endohedral fullerenes are C_{60} cages with an atom or molecule trapped inside. The C_{60} cage acts as a diamagnetic host that insulates the contents from the surrounding environment. Should the contents be a paramagnetic

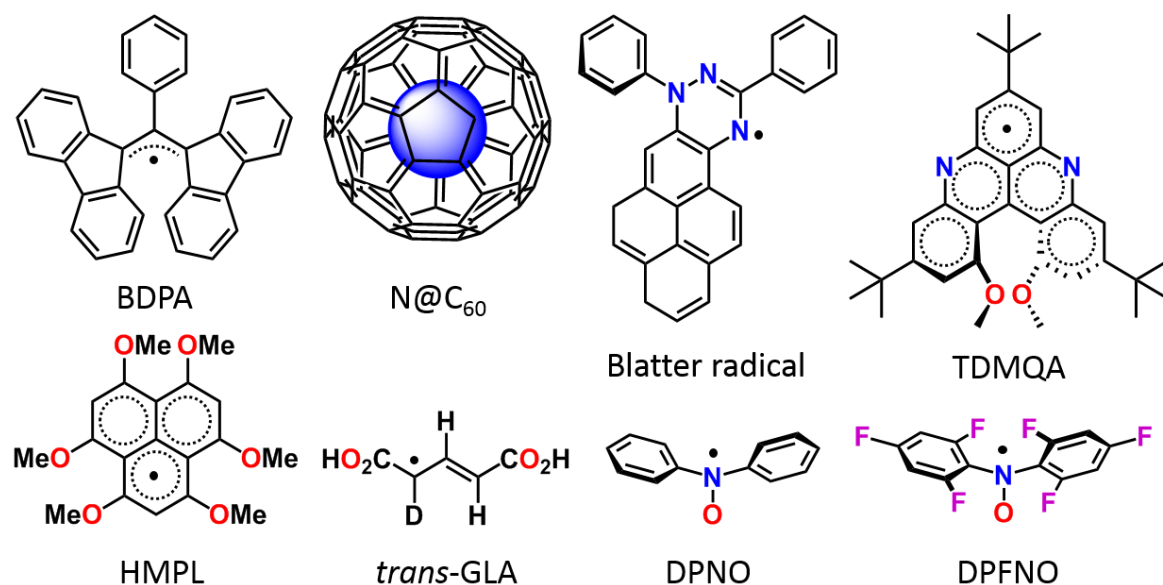


Figure 1.4. Selected organic electron-spin qubits.

entity such as in the cases of $N@C_{60}$ and $P@C_{60}$ then the result is an isolated qubit. For these group 5 elements the resulting endohedral fullerene consists of one trapped group 5 atom with half-filled p orbitals resulting in an isotropic g -factor of 2.0036 and a spin-quartet ground state. The synthesis of an endohedral fullerene is not simple, nor is it cheap, and as a result the scalability of such a system is impeded.

Far simpler— though still synthetically taxing— organic spin qubits are those produced by Takui et al.²⁰⁻²³ These qubits are centred around the archetypal nitroxyl radical. Prized for its chemical versatility the nitroxyl radical is extremely resistant to oxygen and heat and can take part in non-radical reactions without disturbance of the free-valence. A further oddity is that the unpaired electron resides on the nitroxyl bond without the need for stabilisation through conjugated π -systems as is the case with most organic radicals. This highly localized valence gives appreciable coherence times of up to even $\sim 1 \mu\text{s}$ at room temperature and can be subject to chemical manipulation to incorporate into larger architectures. Takui et al have also explored the other stable organic polyaromatic radicals as spin qubits. One such example is phenalenyl— a neutral π -radical fused ring system in which the open shell is stabilised by the highly symmetric D_{3h} 13 π -system.²⁴ By substituting six methoxy groups onto the α -carbons of the phenalenyl radical the Takui group developed a quantum simulator. Spin simulators are useful for studying a large number of equivalent spins in the surrounding molecular frameworks. In this case it was the investigation of the proton of the methoxy group and the quantum coherence measured from the system was indicative of decoherence via rotation of the methoxy groups. Takui and Morita also synthesised and investigated the first helicene-like phenalenyl radical 3,7,11-tris(1,1-dimethylethyl)-1,13-dimethoxy-5*H*-quino[2,3,4-*k*]acridin-5-yl (TDMQA).²⁵ The molecule

consists of a diazaphenalenyl with two methoxy substituted benzene rings fused to the cis α -carbons of the phenalenyl moiety. The methoxy substituents enforce a helical structure through steric interaction and also offer stabilisation to the 21 π system in tandem with the three tert butyl substituents. The advantage of using such a molecule is that the helical π system possesses optical magnetic properties that may enable optical addressability. ENDOR confirms the radical is extensively delocalised across the 21 π electron system by the presence of appreciably high hyperfine coupling constants for each magnetically active nuclei across the π system. The radical has a g value of 2.0032—remarkably close to the free electron g value— and is split by a hyperfine interaction to six conjugated ^1H nuclei in three environments with hyperfine coupling constants of 0.785, 0.166, 0.218 mT; two ^{14}N nuclei at 0.369 mT; and the six ^1H nuclei of the methoxy groups at 0.004 mT. Circular dichroism measurements of the compound showed the two enantiomers to be stable to interconversion having a $t_{1/2}$ of 23 days at 303 K, well above the operating temperature of a potential quantum computer.

Casu et al investigated the pyrene-Blatter radical 7,9-diphenyl-pyreno[1,2-*e*][1,2,4]triazin-8(7*H*)-yl and its interaction with a copper beryllium microplate surface.¹⁷ The radical is a planar structure of a pyrene fused to a 1,2,4-triazine ring with two phenyl groups substituted to the α -carbon of the triazine and a nitrogen. Hyperfine values of $A_{\text{N}1} = 6.94$ G, $A_{\text{N}4} = 4.73$ G, $A_{\text{N}2} = 4.29$ G, $A_{\text{H}6} = 1.55$ G and a g value of 2.00368 illustrate that the radical itself is primarily situated on the triazine moiety. The spin dynamics of the radical were assessed in 1 mM toluene- d_8 with pulsed EPR to extract $T_1 = 116$ ms and $T_2 = 7.2$ μs . While these values are not large the pyrene-Blatter radical is exceptionally stable, a key feature when designing addressable qubits on surfaces as these usually tend to degrade rapidly. HF-EPR and XPS were used in tandem to evaluate the stability and interaction of a 30 Å nomenclatural thick film on the CuBe surface. XPS involves the excitation of core electrons out of the atom. Electrons in higher orbitals of allowed symmetry then transfer to the core orbital emitting radiation which is indicative of environment. For the free pyrene-Blatter radical nitrogen XPS shows three peaks of energy 401.0 eV, 399.3 eV, and 398.3 eV for N1, N2 and N4 respectively where N4 shows the most radical character. In the thick film sample a fourth contribution of 400.2 eV is present in the XPS. This value is attributed to a Cu—N interaction as it is closely related to the energy of photoelectrons emitted by several nitrogen containing organic molecules after coordinating to copper. HF-EPR was performed at various low temperatures on the film. Approaching 5 K it is noted that the resonance for the free radical broadens and shifts to 2.00261 accompanied by the appearance of a broad feature attributed to a possible surface—radical magnetic interaction. The salient point of this study is the impeccable stability of the film being resistant to air, moisture, vacuum, annealing and X-rays.

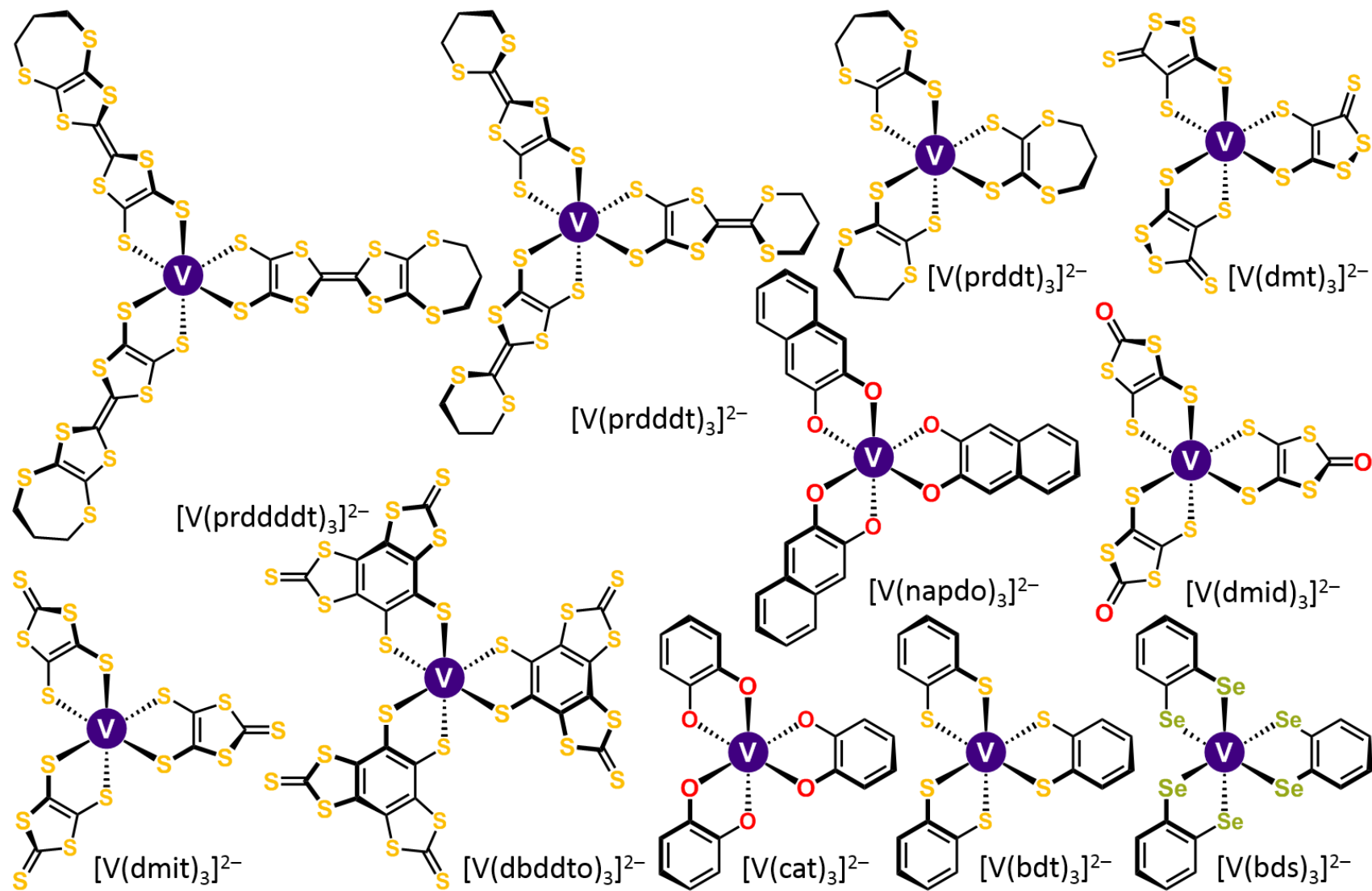


Figure 1.5. All monospin tris(vanadium) electron-spin qubits.

1.2.2. Inorganic

1.2.2.1. Transition Metal Compounds

1.2.2.1.1. Group 5

The only member of group five used in any study on molecular qubits is $V^{IV} [Ar] d^1$. However, it is by far the most studied element of the transition metals for qubits forming two classes to consider: tris-vanadium and bis-vanadyl complexes. Vanadium qubits possess long coherence times from the unpaired electron centred on the metal d_{z^2} orbital of 2a_1 symmetry in a D_3 octahedral environment ligated exclusively by chalcogenide ligands, the most prevalent being dithiolates (Figure 1.5.). Vanadyl complexes exhibit a square pyramidal geometry and a characteristic V—O bond of order 3. The unpaired electron resides in the non-bonding d_{xy} orbital of b_2 symmetry and is typically ligated by chalcogenides with the exception of phthalocyanine and again the most used being dithiolates (Figure 1.8.). As nuclear spin free dithiolates can be synthesised with relative ease in comparison to other ligands this class of compound has seen extensive use in investigations of the interaction with an electron spin qubit and the surrounding spin bath. Nuclear spin free ligands are composed of non-magnetic (^{32}S , ^{16}O , ^{12}C) or very magnetically dilute (^{14}N , ^{15}N , ^{13}C) nuclei and are used to deprive the complex under study of means of spin interactions in the immediate vicinity of the complex. Aside, of course, from the ^{51}V 99.8% abundant $I = 7/2$ nucleus which gives rise to the iconic eight line EPR spectrum of any vanadium species. In this area, none have been more prolific than the Freedman group.

In 2017 two studies were published investigating the spin diffusion barrier of the bis(vanadyl) and tris(vanadium) complexes.²⁶⁻²⁷ The electron spin is a much stronger magnet than a nuclear spin and as such it exerts a stronger magnetic field. Any nuclei within a specified radius of this field will be spin polarized and will not undergo spin flipping readily. Past this barrier other spins can freely flip and this combined oscillation of magnetic spins in the bath flipping provides decoherence pathways for the electron spin. Unusually the nuclear spin diffusion in the bath does not depend on a r^{-3} law and is separated instead by regime. Inside the barrier radius or outside, an exact value for this would be of great advantage as any nuclear spins located within the barrier would have a minimal effect on coherence and so more synthetic freedom in ligand variance could be exploited. Similarly the converse is also useful, at some longer distance the effects of nuclear spins in the bath stop effectively decohering the electron spin giving a maximal decoherence radius. This spin diffusion barrier is highly system specific and given the prevalence of vanadium qubits in the literature a quantitative value was required. Four ligands containing a cyclic propyl moiety at defined distances r ; propane-1,3-dithiolate (prdt) $r = 4.0 \text{ \AA}$, 6,7-dihydro-5H-1,4-dithiepin-2,3-dithiolate (prddt) $r = 6.6 \text{ \AA}$, 2-(1,3-dithian-2-ylidene)-1,3-dithiole-4,5-dithiolate (prddd) $r = 9.3 \text{ \AA}$, and 2-(6,7-dihydro-5H-1,3-dithiolo[4,5-b][1,4]dithiepin-2-ylidene)-1,3-dithiole-4,5-

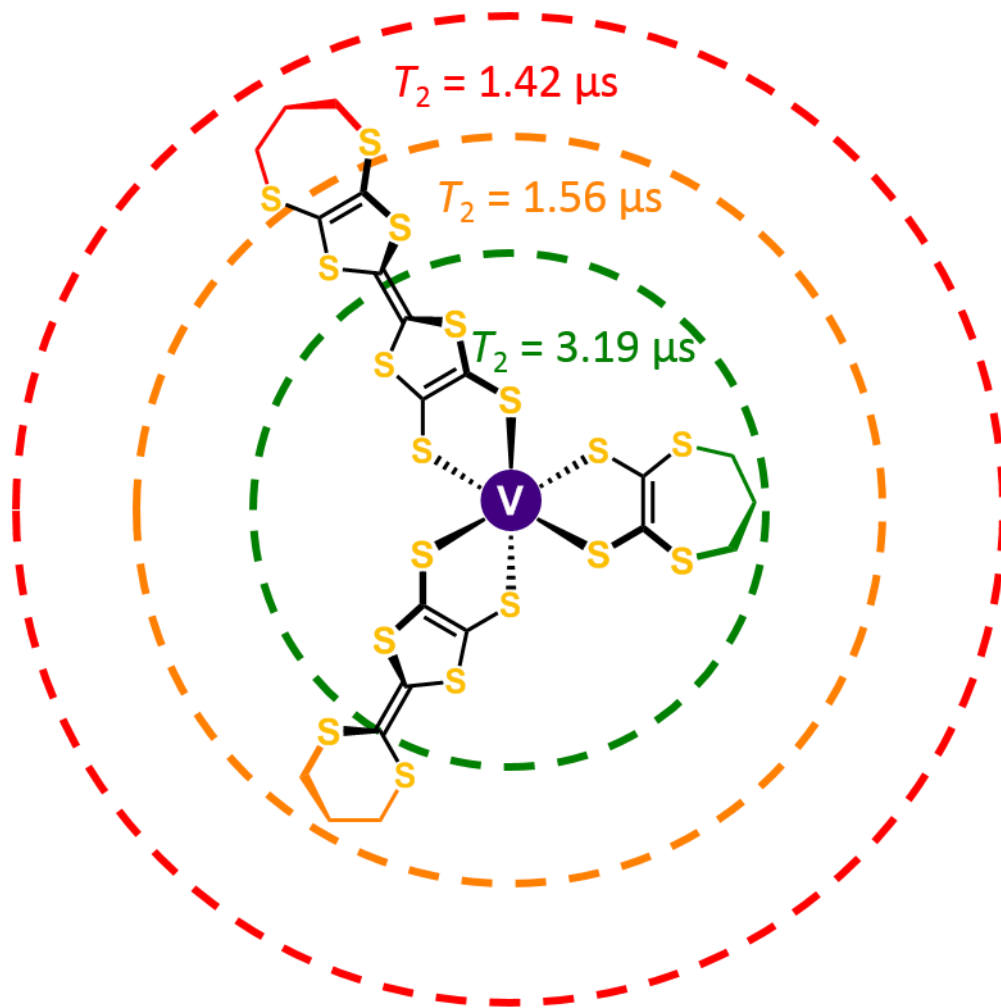


Figure 1.6. Representation of a tris(vanadium) complex with the coherence times of the complex with each length of ligand.

dithiolate (prdddt) $r = 12.6 \text{ \AA}$ were employed as molecular rulers to investigate vanadyl and the latter three used for tris(vanadium). The distal component of the ligands consisted entirely of carbon or sulfur and so are nuclear spin free with r representing the distance between V—H where H is the furthest ^1H nuclei (Figure 1.6.). For the vanadyl series in 0.5 mM 1:1 DMF- d_7 /toluene- d_8 at 10 K the T_2 dropped from 10.11 μs to 6.02 μs within the shortest ligands so the spin diffusion barrier lies between 4.0 and 6.6 \AA . T_2 then begins to plateau with 6.59 μs and 5.95 μs for $[\text{VO}(\text{prdddt})_2]^{2-}$ and $[\text{VO}(\text{prdddt})_2]^{2-}$ respectively. Extrapolation of these values gives a maximal decoherence radius of around 13 \AA .

For the tris(vanadium) complexes T_2 was found to be 8.0 μs , 5.9 μs , and 5.3 μs for $[\text{VO}(\text{prddt})_3]^{2-}$, $[\text{VO}(\text{prdddt})_3]^{2-}$, and $[\text{VO}(\text{prdddt})_3]^{2-}$ in 0.32 mM 45 vol % DMF- d_7 /toluene- d_8 at 10 K respectively. These values mirror the conclusions from the vanadyl study that a diffusion barrier exists within the 4.0 to 6.6 \AA radius but cannot be reliably extrapolated to find a maximal decoherence radius. This was taken further by repeating the measurements in 0.32 mM 45 vol % MeCN- d_3 /toluene- d_8 to extract the values for T_2 as 6.8 μs , 2.8 μs , and 2.5 μs respectively. Moving to a less polar solvent system allowed the assessment of a

secondary contributing factor, the charge to size ratio, from the large decrease in T_2 between $[\text{VO}(\text{prdddt})_3]^{2-}$, and $[\text{VO}(\text{prdddt})_3]^{2-}$, going from 45 vol % DMF- d_7 /toluene- d_8 to 45 vol % MeCN- d_3 /toluene- d_8 . The less polar MeCN- d_3 contains a methyl group which is known to induce decoherence by rotation as shown by the quantum simulations of Takui et al. The stronger the interaction of charge on the surrounding solvent molecules increases the barrier to methyl rotation— provided the complex is negatively charged— and subsequently increases T_2 by eliminating decoherence pathways. As $[\text{VO}(\text{prdddt})_3]^{2-}$, and $[\text{VO}(\text{prdddt})_3]^{2-}$ have much lower charge to size ratios they are much more susceptible to this methyl rotation induced decoherence suggesting that a higher charge is preferable for longer coherence times.

Of course, a more effective way to limit the effects of nuclear spins on T_2 is to eliminate them from the system. This was shown with the Freedman groups *pièce de résistance* $[\text{V}^{\text{IV}}(\text{dbddto})_3]^{2-}$ where $(\text{dbddto})^{2-}$ is 2,5-dithioxobenzo[1,2- d :3,4- d']bis[1,3]dithiolene-7,8-dithiolate.²⁸ Previous studies had employed $[\text{NBu}_4]_2[\text{V}^{\text{IV}}(\text{dbddto})_3]$ with a modest T_2 of 1.5 μs at 5 K.²⁹ Changing counter cation from NBu_4^+ to PPh_4^+ and switching solvent systems from 1 mM butyronitrile to 0.5 mM 1:1 DMF- d_7 /toluene- d_8 increased T_2 by 430%. Further isolation from magnetic nuclei by opting for a fully deuterated counter cation $\text{PPh}_4\text{-}d_{20}^+$ and switching to a dilute 0.01 mM carbon disulfide solution increased T_2 to 675 μs . This is the highest T_2 recorded for any inorganic molecular qubit and even surpasses many solid state qubits. Three other compounds containing nuclear spin free ligands $[\text{V}^{\text{IV}}(\text{dmit})_3]^{2-}$ (1,3-dithiole-2-thione-4,5-dithiolate), $[\text{V}^{\text{IV}}(\text{dmt})_3]^{2-}$ (1,2-dithiole-3-thione-4,5-dithiolate), and $[\text{V}^{\text{IV}}(\text{dmid})_3]^{2-}$ (2-oxo-1,3-dithiole-4,5-dithiolate) were investigated alongside $[\text{V}^{\text{IV}}(\text{dbddto})_3]^{2-}$. Their T_2 values while appreciable at 6.0, 6.1 and 6.3 μs fail to surpass $[\text{V}^{\text{IV}}(\text{dbddto})_3]^{2-}$ although the

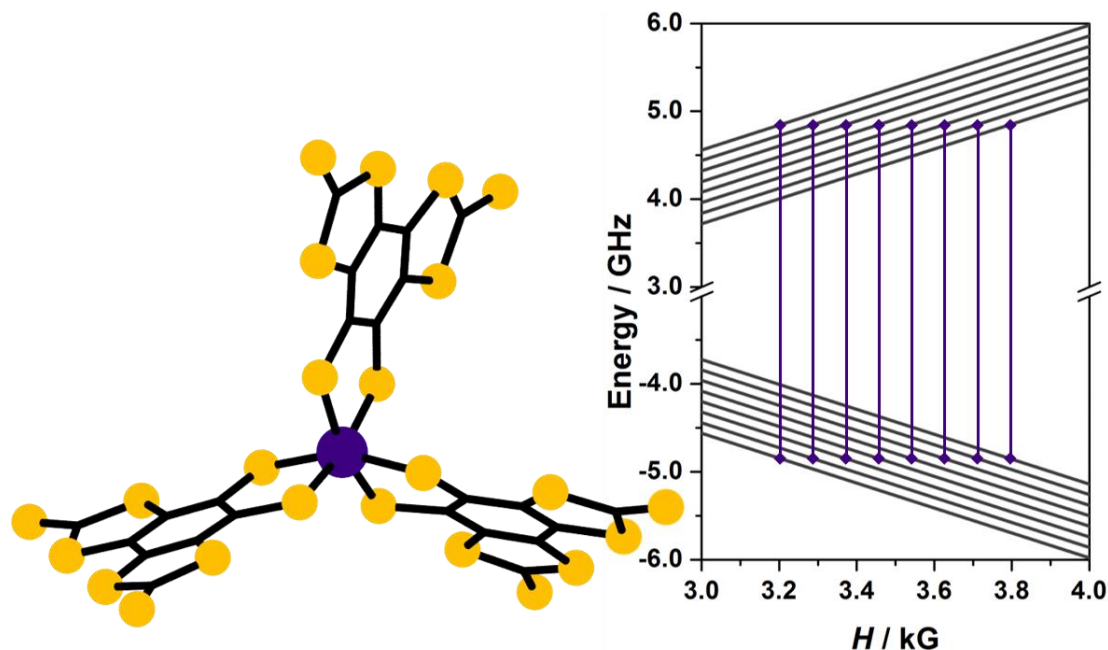


Figure 1.7. Left, the structure of $[\text{V}(\text{dbddto})_3]^{2-}$. Right, the nuclear spin manifold for a ^{51}V $I = 7/2$ complex.

synthesis of each is much simpler, involving the reflux of carbon disulphide with metallic Na/K in DMF to afford $(\text{dmit})^{2-}$ from which the $(\text{dmt})^{2-}$ and $(\text{dmid})^{2-}$ can be readily generated.

The aforementioned $[\text{V}^{\text{IV}}(\text{dbddto})_3]^{2-}$ qubit has also been shown to utilise the $I = 7/2$ nuclear spin of the ^{51}V ion as a platform to access multiple quantum states for a simple $S = 1/2$ paramagnetic centre (Figure 1.7.).²⁹ Whilst such a large hyperfine coupling constant is inimical to the decoherence time— via low excited states mixing with the ground state— the Freedman group used the eight available coherence states to their advantage. Variable power transient nutation experiments allowed for the observation of Rabi frequencies at each hyperfine coupling peak maximum, demonstrating that all eight separate transitions can be potentially utilised for quantum information processing. The spacing incurred between each state in the nuclear spin manifold is substantial enough to prevent mixing of states and allow coherent spin manipulation.

The Freedman group's adventures in vanadium chemistry continued in 2019 this time exploring the effects of metal-ligand covalency utilising the ligands benzene-1,2-dithiolate (bdt).³⁰ The tris complex $[\text{V}^{\text{IV}}(\text{bdt})_3]^{2-}$ was doped at 0.5% in its isostructural analogue $[\text{PPh}_4]_2[\text{Ti}^{\text{IV}}(\text{bdt})_3]$ as well as the bis complex $[\text{Cu}^{\text{II}}(\text{bdt})_2]^{2-}$, in its analogue $[\text{PPh}_4]_2[\text{Ni}^{\text{II}}(\text{bdt})_2]$ at 0.5% doping to investigate the effects on T_1 . The postulation was that if the electron resides in a non-bonding orbital of predominantly metal character and its spin-lattice relaxation time is dictated by the lattice and molecular vibrations isolating the SOMO from other orbitals should increase T_1 . Chemically this is realised going from V^{IV} with its non-bonding d_{z^2} SOMO to Cu^{II} with an antibonding, highly covalent $d_{x^2-y^2}$ SOMO, the expectation is that a higher

level of covalency would be deleterious to T_1 as there are more involved atoms as well as T_2 as the spin is delocalised across the molecule and more susceptible to nuclear flip-flops. The spin Hamiltonian parameters for $[\text{V}^{\text{IV}}(\text{bdt})_3]^{2-}$ give $g_{\parallel} = 1.9878$, $g_{\perp} = 1.9698$ and a highly anisotropic hyperfine coupling of $A_{\parallel} = 0$ and $A_x = 258$ MHz, $A_y = 264$ MHz consistent with a trigonally symmetric pseudo-octahedral vanadium complex with an unpaired electron of metal orbital character. $[\text{PPh}_4]_2[\text{Cu}^{\text{II}}(\text{bdt})]^{2-}$ gives an axial g splitting $g_{\parallel} = 2.085$ and $g_{\perp} = 2.019$. These values are closer to the free electron value than $g = \sim 2.11$ commonly found for copper ions with predominantly metal character, indicating a high degree of covalency. Hyperfine values are again axial with $A_{\parallel} = 500$ MHz and $A_{\perp} = 115$ MHz consistent with related copper complexes. DFT gives good results in corroborating the EPR interpretations with spin densities of $M = 0.935$ and $E = 0.008$ for V^{IV} , where M is the spin density on the metal and E is the spin density across the chalcogenide donors, and $M = 0.756$ and $E = 0.059$ for Cu^{II} . At lower temperatures $[\text{V}^{\text{IV}}(\text{bdt})_3]^{2-}$ was found to possess a marginally larger coherence time $T_M = 2.81$ μs than its copper counterpart $T_M = 2.48$ μs peaking at 20 K. However beyond 100 K $[\text{V}^{\text{IV}}(\text{bdt})_3]^{2-}$ shows no spin echo while $[\text{Cu}^{\text{II}}(\text{bdt})]^{2-}$ persists up to 280 K with $T_M = 0.51$ μs . To investigate this further the Freedman group synthesised the benzene-1,2-diselenolate (bds) ligand analogues $[\text{V}^{\text{IV}}(\text{bds})_3]^{2-}$ and $[\text{Cu}^{\text{II}}(\text{bds})]^{2-}$. $[\text{PPh}_4]_2[\text{V}^{\text{IV}}(\text{bds})_3]^{2-}$ possesses much lower g values than $[\text{PPh}_4]_2[\text{V}^{\text{IV}}(\text{bdt})_3]^{2-}$ and a slight degree of rhombicity in g with $g_x = 1.950$, $g_y = 1.960$, and $g_z = 1.955$ but with almost identical

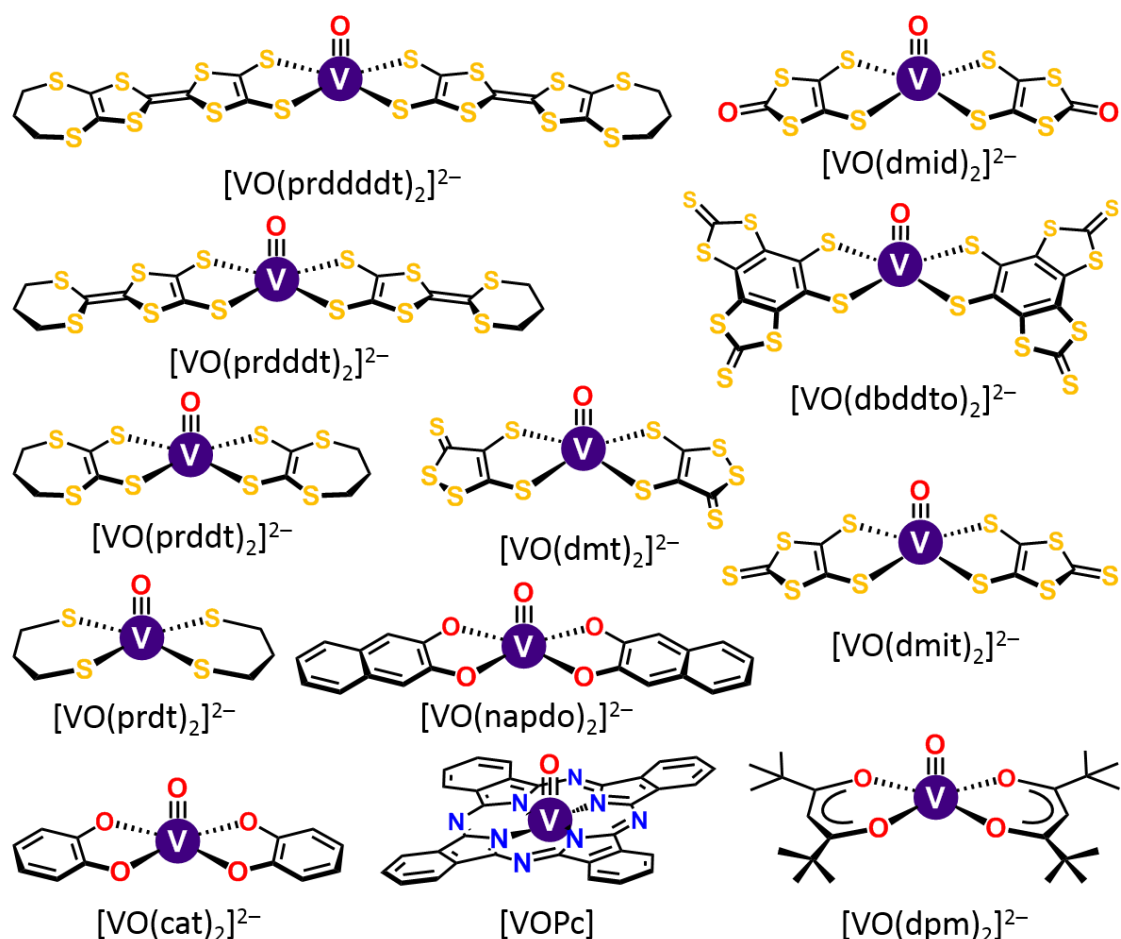


Figure 1.8. All bis(vanadyl) monospin molecular electron-spin qubits

hyperfine values of $A_{||} = 0$ and $A_x = 258$ MHz, $A_y = 264$ MHz. Lower g values indicate the environment of the unpaired electron is even more localised on the V^{IV} centre and is corroborated with spin density values of $M = 0.949$ and $E = 0.007$. In contrast to this the SOMO of $[Cu^{II}(bds)]^{2-}$ displays even higher degrees of covalency with $g_{||} = 2.082$, $g_{\perp} = 2.018$, $A_{||} = 460$ MHz and $A_{\perp} = 145$ MHz and spin densities of $M = 0.732$ and $E = 0.065$. Doped at 0.5% in $[PPh_4]_2[Ti^{IV}(bds)_3]$ and $[PPh_4]_2[Ni^{II}(bds)]$ the selenium analogues display the same temperature dependency as the thiolates but with suitably longer $T_M = 5.06$ μ s, and 5.318 μ s for V^{IV} and Cu^{II} respectively. 280 K $[Cu^{II}(bds)]^{2-}$ shows a decreased T_M of 0.194 μ s. This is attributed to the larger number of phonon modes induced by the larger selenium atoms than sulfur impacting T_1 at higher temperatures limiting T_2 . Conversely, to the initial hypothesis it was found that covalency increases T_1 and allows its persistence at higher temperature regimes despite T_M being lower at lower temperatures.

Sessoli et al have studied the effects of T_1 on vanadium and vanadyl systems, and what potentially causes them, using AC susceptometry and THz spectroscopy.³¹ Four complexes were employed in this study, two bis(vanadyl) species $[V^{IV}O(cat)_2]^{2-}$ and $[V^{IV}O(napdo)_2]^{2-}$ and two tris(vanadium species) $[V^{IV}(cat)_3]^{2-}$ and $[V^{IV}(napdo)_3]^{2-}$. The ligands used here are catecholate, $(cat)^{2-}$, IUPAC benzene-1,2-diolate and 2,3-naphthalenediol, $(napdo)^{2-}$. Both

are structurally rigid due to the aromatic ring system with the fused ring system of napdo offering more rigidity than cat. T_1 for the square pyramidal vanadyl species were found to be $T_1 = 10.989$ ms and 9.675 ms at 10 K for cat and napdo respectively: almost an order of magnitude higher than the octahedral tris species with $T_1 = 3.3$ ms and 3.675 ms at 5 K from neat polycrystalline samples. Increasing the temperature gives $T_1 = 0.06$ ms and 0.04 ms at 75 K and $T_1 = 0.072$ ms and 0.05 ms for $[\text{V}^{\text{IV}}\text{O}(\text{cat})_2]^{2-}$, $[\text{V}^{\text{IV}}\text{O}(\text{napdo})_2]^{2-}$, $[\text{V}^{\text{IV}}(\text{cat})_3]^{2-}$, and $[\text{V}^{\text{IV}}(\text{napdo})_3]^{2-}$ respectively. One mechanism by which mediates T_1 is its interaction with vibrational modes known as phonons. These low frequency oscillations form different energy modes which interact with the electron spin providing a pathway to release energy and therefore promote spin-lattice relaxation. THz spectroscopy in the range $100\text{--}20\text{ cm}^{-1}$ can directly measure all these bands which are observed under IR selection rules though not all are implicit in spin-lattice relaxation phenomena. Magnetic analysis suggests the phonons that cause magnetic relaxation are of the energies 48 and 34 cm^{-1} for $[\text{V}^{\text{IV}}\text{O}(\text{cat})_2]^{2-}$ and $[\text{V}^{\text{IV}}\text{O}(\text{napdo})_2]^{2-}$ which were both observed in the THz spectra. For $[\text{V}^{\text{IV}}(\text{cat})_3]^{2-}$ and $[\text{V}^{\text{IV}}(\text{napdo})_3]^{2-}$ these modes are expected at 12 and 20 cm^{-1} and 18 and 32 cm^{-1} respectively and observed at 22 and 28 cm^{-1} and 20 and 33 cm^{-1} . Unfortunately, at room temperature, these spectra are very broad and no information as to structure or potential rotational coupling could be observed. While no clear relation could be extracted due to the spectral complexity of the complexes it is clear that the symmetry of the species dictates T_1 by some factor going from square pyramidal to octahedral crystal field splitting arrangements. It is suggested by the authors that ro-vibrational coupling may induce the differences in T_1 going from cat to napdo but further studies at lower temperatures is required. Nevertheless, Sessoli et al made headway in quantitatively analysing these methods of relaxation beyond the conventional fit data from which relaxation times are extracted and made the first steps to developing an understanding of how these very low energy, but highly impactful, vibrational modes dictate relaxation within a molecular framework.

1.2.2.1.2. Group 6

Moving to group 6 sees a drastic drop in the number of qubits analysed thus far (Figure 1.9.). This is due to two factors: the available oxidation states and the prevalence of first row transition metals over second and third. The most common magnetic oxidation states of chromium are $\text{Cr}^{\text{II}} [\text{Ar}] d^4$ and $\text{Cr}^{\text{III}} [\text{Ar}] d^3$. While $\text{Cr}^{\text{V}} [\text{Ar}] d^1$ is known in the oxochromium species none have been investigated as qubits. As EPR requires the ground state to be a non-integer value to be observed all monospin chromium qubits are Cr^{III} , which ubiquitously exhibits a highly symmetric octahedral coordination environment. All chromium qubits are high spin $S = 3/2$ which presents a larger spin manifold than for a monospin complex. An advantage of which being that excitations can be made between the $m_{s,l}$ spin states to act as individual qubits. Nuclear isotopes of chromium are almost entirely $I = 0$ with only ^{53}Cr

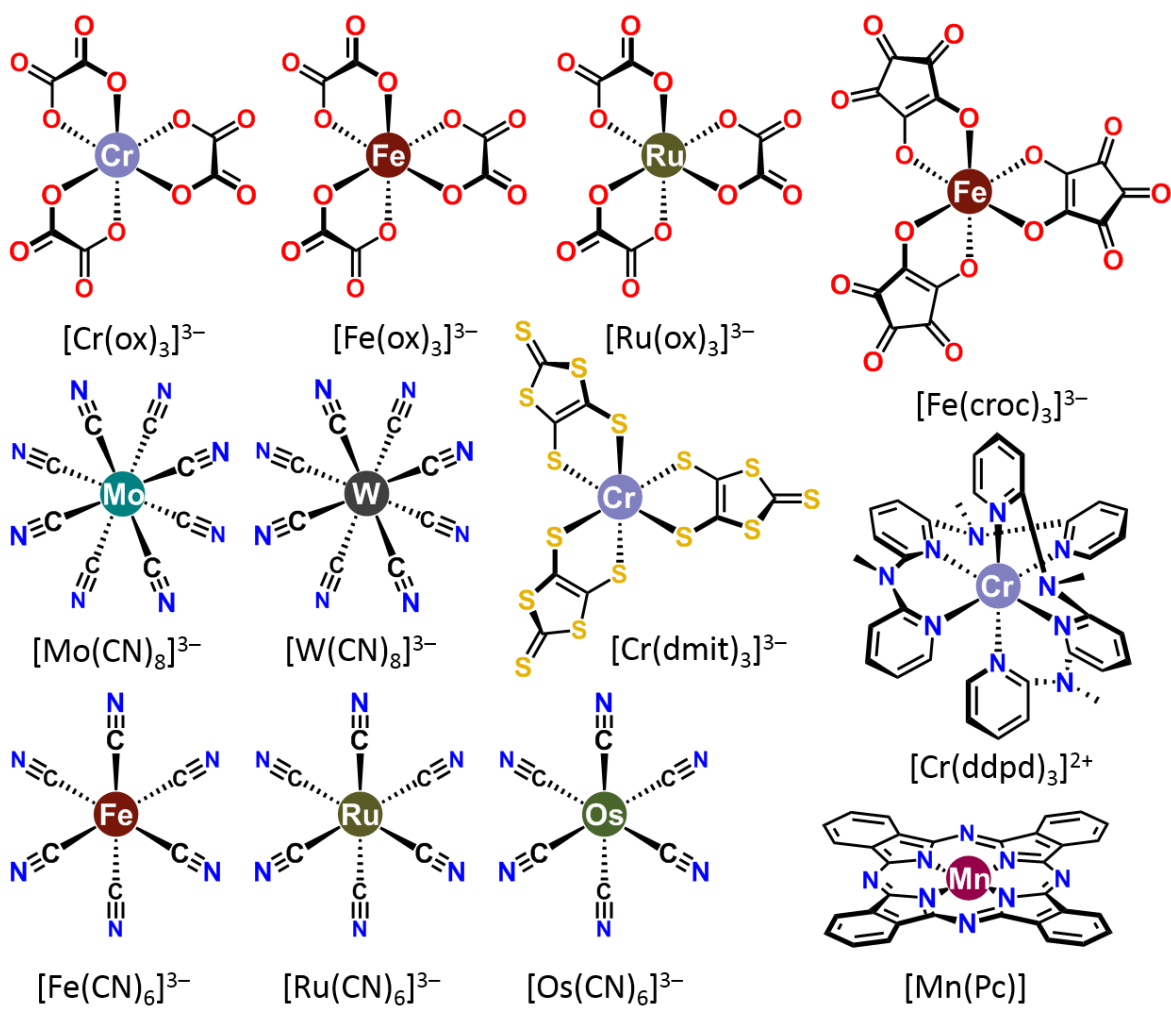


Figure 1.9. All group 6, 7, and 8 monospin molecular electron-spin qubits

possessing $I = 3/2$ magnetic nuclei at 9.5% abundance. Molybdenum and tungsten being second and third row respectively form exclusively low spin complexes with the only oxidation states investigated being Mo^{V} $[\text{Kr}] 4d^1$ and W^{V} $[\text{Xe}] 5d^1$. Molybdenum and tungsten show a range of coordination geometries: square pyramidal, octahedral, trigonal prismatic, trigonal bipyramidal, and square antiprismatic only the latter of which have been investigated. The magnetic isotopes of molybdenum are ^{95}Mo $I = 5/2$ (15.9% abundance) and ^{97}Mo $I = 5/2$ (9.6% abundance); both have a very low nuclear magnetic moment. The only magnetic isotope of tungsten is ^{183}W $I = 1/2$ at 14.3% which also has a very low nuclear magnetic moment.

The first monospin chromium qubit to ever be analysed was $[\text{Cr}(\text{ox})_3]^{3-}$ by the Freedman group as part of the series $[\text{M}(\text{ox})_3]^{3-}$ where $(\text{ox})^{2-}$ is the ligand oxalate, the conjugate of oxalic acid and a nuclear spin free ligand.³² The metals selected were Ru^{III} , Cr^{III} , and Fe^{III} with spin ground states $S = 1/2$, $S = 3/2$, and $S = 5/2$ respectively. T_2 was found to decrease upon increasing spin state due to the increased number of pathways to dissipate energy going from 3.4 μs , 1.79 μs , to 1.83 μs with increasing spin state at 4.7 K in 1 mM 1:1 H_2O /glycerol. The impact of spin state on T_2 was therefore found to be largely insignificant

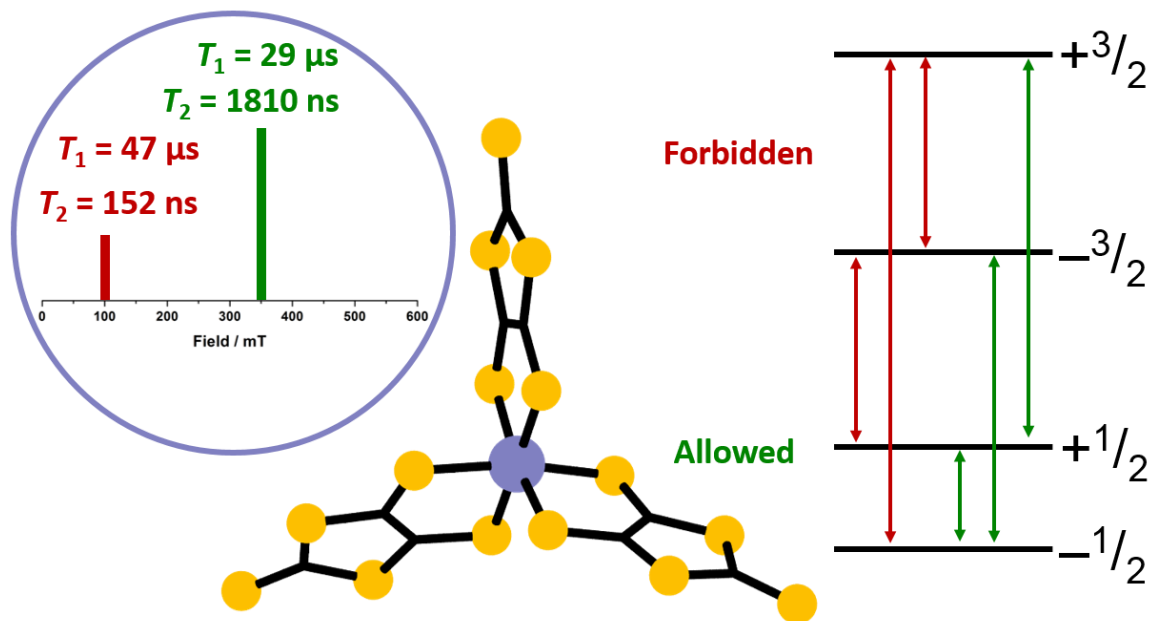


Figure 1.10. Top left, stick plot of the EPR spectrum of $[\text{Cr}(\text{dmit})_3]^{3-}$ at X-band with the forbidden transitions in red and allowed in green with associated T_1 and T_2 . Middle, the structure of $[\text{Cr}(\text{dmit})_3]^{3-}$. Right, the spin manifold of $[\text{Cr}(\text{dmit})_3]^{3-}$ with $S = 3/2$ with forbidden and allowed transitions

and exemplifies the potential to form qubits with multiple qubit sites on one spin centre by manipulating zero-field splitting.

This was further pursued by the Freedman group with the octahedral complex $[\text{Cr}(\text{dmit})_3]^{3-}$ with $(t_{2g})^3$ electronic configuration.³³ From cw EPR the complex was found to have a low $D = 0.326 \text{ cm}^{-1}$ and an almost completely rhombic field $|E/D| = -0.328$. This high rhombicity moves $g = (1.99, 2.02, 1.96)$ to their effective positions in a low D field and allows for the observation of the first superposition of a forbidden $m_s = -3/2 \rightarrow +3/2$ transition at an accessible resonant field position of 100 mT, and the allowed $m_s = -3/2 \rightarrow -1/2$ transition at 350 mT at X-band frequencies (Figure 1.10.). Pulsed EPR gave $T_2 = 1.81 \mu\text{s}$ and $0.15 \mu\text{s}$ for the allowed and forbidden transitions respectively when $[\text{PPh}_4-d_{20}]_3[\text{Cr}(\text{dmit})_3]$ was doped at 1% into $[\text{PPh}_4-d_{20}]_3[\text{Ga}(\text{dmit})_3]$ and Rabi oscillations were observed at each transition. This was the first recorded entry of a high spin magnetic centre with Rabi oscillations, showing that $S \geq 1/2$ are viable candidates as molecular spin qubits.

More recently Slageren et al have demonstrated greater coherence times in a D_{2d} octahedral complex $[\text{Cr}(\text{ddpd})_2]^{3+}$ and the partially deuterated analogue $[\text{Cr}(\text{ddpd}-d_9)_2]^{3+}$.³⁴ (ddpd) is the ligand *N,N'*-dimethyl-*N,N'*-dipyridine-2-yl-pyridine-2,6-diamine and consists of three pyridines bonded through a tertiary methyl amine on the *ortho* position to the pyridyl nitrogen. It is synthesised in excellent yields from the reaction of 2,6-dibromo-pyridine and *N*-methyl-2-pyridinamine in the presence of a strong base.³⁵⁻³⁶ Reaction of (ddpd) with D_2O and a palladium on carbon catalyst under microwave irradiation gives the ~50% deuterated

(ddpd- d_9) which shows a statistical pattern of deuteration pictured in Figure 1.11. This electron rich tridentate ligand is a strong σ -donor and a weak π -acceptor and has a large bite angle when complexing metals with N—M—N equalling 90° . In the strong field induced by (ddpd) Cr^{III} displays long lived luminescence of 2.3 ms at room temperature. This is due to the strong field rendering the non-emissive $^4\text{T}_{2g}$ state thermally inaccessible from the emissive $^2\text{E}_g$ and $^2\text{T}_{1g}$ states. The complex itself has a lower zero-field splitting than $[\text{Cr}(\text{dmit})_3]^{3-}$ with $D = +0.18$ and the maximum possible rhombicity for $|E/D|$ along with an almost isotropic $g = (1.98, 1.98, 1.99)$. The isolation of the $^4\text{T}_{2g}$ state is also particularly favourable for qubits giving a T_2 value of $8.4 \mu\text{s}$ and $6.629 \mu\text{s}$ for $[\text{Cr}(\text{ddpd})_2]^{3+}$ and $[\text{Cr}(\text{ddpd}-d_9)_2]^{3+}$ respectively in 1 mM 1:1 $\text{D}_2\text{O}/\text{glycerol}-d_8$ at 7 K. The authors attribute this increase in coherence times not to the decrease in D but to the very high-energy excited quartet state, which is inaccessible in a highly rhombic field, which forces a small D . The similarities in coherence times between the complexes in deuterated media is attributed to the hydrogens in $[\text{Cr}(\text{ddpd})_2]^{3+}$ and deuterons in $[\text{Cr}(\text{ddpd}-d_9)_2]^{3+}$ being within the spin diffusion barrier and too few to constitute parts of the spin bath, thus resulting in very similar values. Measurements of $[\text{Cr}(\text{ddpd})_2]^{3+}$ and $[\text{Cr}(\text{ddpd}-d_9)_2]^{3+}$ in protonated media gave $T_M = 4.24 \mu\text{s}$ and $4.47 \mu\text{s}$ respectively. Typically the discrepancy between deuterated and protonated medium T_2 values is a factor of six. However in this case a factor of no more than two when going from a protonated medium to deuterated is observed. In addition, at slightly higher temperatures, T_M values for each complex in each solvent become the same within experimental error, attributed to T_1 becoming the same order of magnitude as T_2 around 35 K. While this could be attributed to deuteration in $[\text{Cr}(\text{ddpd}-d_9)_2]^{3+}$ being only partial it was suggested that the difference is incurred by the stretch factor k of the stretched exponential. For protonated media, k is ~ 2 whereas for deuterated k is unity. This means both samples initially have very similar coherence times but then the decay of the protonated media accelerates. To better visualise this Slageren et al utilised $T_{M,10\%}$, the time for 90% of the echo signal to disappear. By using $T_{M,10\%}$ instead of T_M the discrepancies between different decay profiles become more pronounced. It is typically used in magnetic imaging or biological distance measurements where labelling spins are surrounded by protonated media and decohere quickly but information on environment is discerned through decay rate.³⁷ $T_{M,10\%}$ allows for a phenomenological snapshot of these biological systems and is here appropriated to do the same for $[\text{Cr}(\text{ddpd})_2]^{3+}$ and $[\text{Cr}(\text{ddpd}-d_9)_2]^{3+}$ in deuterated and

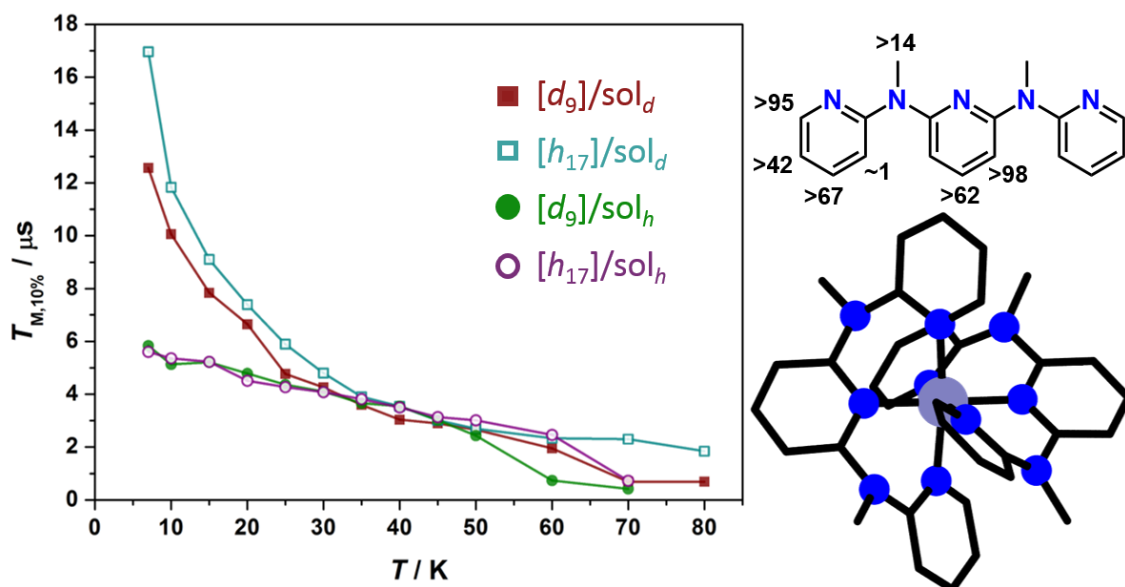


Figure 1.11. Left, $T_{M,10\%}$ at variable temperatures for the complexes $[Cr(ddpd)_2]^{3+}$ and $[Cr(ddpd-d_9)_2]^{3+}$ in protonated and deuterated media. Top right, experimentally observed percentages of deuteration for $(ddpd-d_9)$. Bottom right, the structure of $[Cr(ddpd)_2]^{3+}$.

non-deuterated solvent mixtures giving a direct visualisation of decay as opposed to inference through correlation of T_M and k (Figure 1.11.).

Continuing down group 6 the octacyanometallate qubits $[Mo^V(CN)_8]^{3-}$ and $[W^V(CN)_8]^{3-}$ were investigated by the Freedman group.³⁸ Homoleptic cyanometallates have long been studied for their magnetic properties and are known to form solid state arrays.³⁹⁻⁴⁰ As such they are ideal candidates to form spatially distributed and controllable qubit motifs. $[Mo^V(CN)_8]^{3-}$ and $[W^V(CN)_8]^{3-}$ both exhibit square anti-prismatic geometries splitting a cubic ligand field into the doubly degenerate E_2 and E_3 states with the unpaired electron occupying a low energy isolated d_{z^2} orbital with A_1 symmetry. At cryogenic temperatures these complexes display completely isotropic g values of 1.973 and 1.963 and hyperfine values of 103 MHz and 185 MHz respectively. These ground state $S = 1/2$ complexes display phenomenal T_1 values of 1.05 s and 0.63 s at 5 K in 0.5 mM PrCN respectively and the structural similarities between the two allow for a direct comparison of the effects of spin-orbit coupling on T_1 . Spin-lattice relaxation is known to be mediated by a direct process, Raman process, and local vibrational modes and the rate of decay is described by the fit equation;

$$\frac{1}{T_1} = A_{dir}T + A_{ram} \left(\frac{T}{\theta_D}\right)^9 J_8 \left(\frac{\theta_D}{T}\right) + A_{loc} \frac{e^{\Delta_{loc}/T}}{(e^{\Delta_{loc}/T} - 1)^2}$$

Where A_{dir} , A_{ram} , and A_{loc} are the direct, Raman, and local mode coefficients respectively, θ_D is the Debye temperature and J_8 is the transport integral

$$J_8 \left(\frac{\theta_D}{T}\right) = \int_0^{\theta_D/T} x^8 \frac{e^x}{(e^x - 1)^2}$$

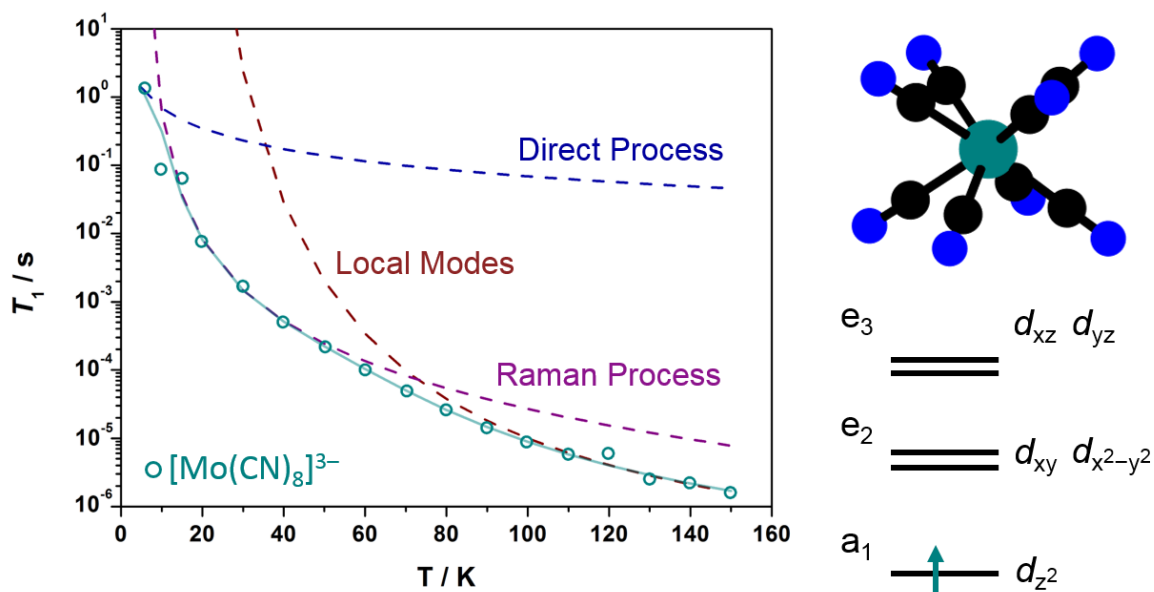


Figure 1.12. Left, T_1 at variable temperature for $[\text{Mo}(\text{CN})_8]^{3-}$ with fit data for the direct process, Raman process, and local vibrational modes. Top right, the structure of $[\text{Mo}(\text{CN})_8]^{3-}$. Bottom right, d-orbital splitting and symmetry terms for a square antiprismatic d^1 complex.

and Δ_{loc} is the energy of the local mode vibrations (Figure 1.12.). At temperatures below 10 K the direct process dominates. This represents a single phonon-induced spin flip and is a formally forbidden process. Some form of hyperfine field usually mediates its occurrence. Above this till 60 K the Raman process is dominant, a two-phonon event in which a phonon is absorbed to form an excited state which then emits a phonon to decay analogous to the Raman photon spectroscopy from which it derives its name. Above 60 K local vibrational modes dominate relaxation and are specific to the immediate environment around the qubit as opposed to the long-range phonon modes that are involved in the Raman and direct process. Interestingly in cyanooctametalates of molybdenum and tungsten at 5 K the direct process is suppressed preventing efficient relaxation of the spin and allowing for extremely long spin-lattice coherence times. Comparing the two metals the first divergence with increasing temperature occurs at 20 K as the Raman process begins to dominate. This is consistent with the spin-orbit coupling of Mo and W being $\xi = 900 \text{ cm}^{-1}$ and $\xi = 2700 \text{ cm}^{-1}$ respectively as spin-orbit coupling provides an efficient mediation between the spin and both long range and local vibrational modes, the A_{ram} value for tungsten being almost double that of molybdenum. Unfortunately, neither of these complexes display a measurable T_2 echo due to a coincidental cancellation conditional X-band $A_{iso} = 2\nu_1$ where ν_1 is the nuclear Larmor-frequency and so could only be compared as T_R , the ratio between T_2 at T and T_2 at 5 K which displayed a normal dependence to temperature down to 30 K where it becomes T_1 limited.

Table 1.1. Spin Hamiltonian Parameters and Coherence Times for $S = 1/2$ Transition Metal Qubits.

Complex	Medium	$g_{x,y,z}$	$A_{x,y,z} / \text{MHz}$	T_1 / ms	$T_2 / \mu\text{s}$	T / K	Ref.
[PPh ₄ -d ₂₀] ₂ [V ^{IV} (dbddto) ₃]	0.01 mM CS ₂	1.968	-261	20.4	675	10	28
		1.970	-269				
		1.990	46				
[PPh ₄] ₂ [V ^{IV} (dbddto) ₃]	0.5 mM 1:1 DMF- <i>d</i> ₇ /toluene- <i>d</i> ₈	1.968	-261	10.8	6.5	10	28
		1.970	-269				
		1.990	46				
[NEt ₄] ₂ [V ^{IV} (dbddto) ₃]	1 mM PrCN	1.972	-258	1.5	1.5	20	29
		1.972	-258				
		1.992	6				
[PPh ₄] ₂ [V ^{IV} (dmit) ₃]	0.5 mM 1:1 DMF- <i>d</i> ₇ /toluene- <i>d</i> ₈	1.959	-348	2.4	6.0	10	28
		1.958	-310				
		1.980	46				
[PPh ₄] ₂ [V ^{IV} (dmt) ₃]	0.5 mM 1:1 DMF- <i>d</i> ₇ /toluene- <i>d</i> ₈	1.956	-342	1.2	6.1	10	28
		1.954	-338				
		1.986	65				
[PPh ₄] ₂ [V ^{IV} (dmid) ₃]	0.5 mM 1:1 DMF- <i>d</i> ₇ /toluene- <i>d</i> ₈	1.960	-319	1.1	6.3	10	28
		1.964	-341				
		1.981	57				
K ₂ [V ^{IV} (prddt) ₃]	0.32 mM 45 vol % DMF- <i>d</i> ₇ /toluene- <i>d</i> ₈	1.972	321	8.0	7.21	10	26
		1.988	43				
		1.995	5				

Complex	Medium	$g_{x,y,z}$	$A_{x,y,z} / \text{MHz}$	T_1 / ms	$T_2 / \mu\text{s}$	T / K	Ref.
$\text{K}_2[\text{V}^{\text{IV}}(\text{prdddt})_3]$	0.32 mM 45 vol % DMF- d_7 /toluene- d_8	1.962	337	5.9	1.48	10	26
		1.983	73				
		1.992	6				
$\text{K}_2[\text{V}^{\text{IV}}(\text{prdddt})_3]$	0.32 mM 45 vol % DMF- d_7 /toluene- d_8	1.960	343	5.3	6.89	10	26
		1.986	57				
		1.993	7				
$[\text{PPh}_4]_2[\text{V}^{\text{IV}}(\text{cat})_3]$	neat polycrystalline solid	1.945	330	3.3	—	5	31
		1.945	330				
		1.989	65				
$[\text{PPh}_4]_2[\text{V}^{\text{IV}}(\text{bdt})_3]$	0.5% $[\text{PPh}_4]_2[\text{Ti}^{\text{IV}}(\text{bdt})_3]$	1.9698	258	45	2.156	5	30
		1.9698	264				
		1.9878	0				
$[\text{PPh}_4]_2[\text{V}^{\text{IV}}(\text{bds})_3]$	0.5% $[\text{PPh}_4]_2[\text{Ti}^{\text{IV}}(\text{bds})_3]$	1.960	255	205	3.820	5	30
		1.955	265				
		1.950	0				
$[\text{PPh}_4]_2[\text{V}^{\text{IV}}(\text{napdo})_3]$	neat polycrystalline solid	1.914	394	3.79	—	5	31
		1.927	245				
		2.001	30				
$[\text{PPh}_4]_2[\text{V}^{\text{IV}}\text{O}(\text{dbddto})_2]$	0.5 mM 1:1 DMF- d_7 /toluene- d_8	1.975	411	16.72	3.2	10	41
		1.957	411				
		1.990	131				
$[\text{PPh}_4]_2[\text{V}^{\text{IV}}\text{O}(\text{dmit})_2]$	0.5 mM 1:1 DMF- d_7 /toluene- d_8	1.972	418	17.42	2.95	10	41
		1.972	418				
		1.989	132				

Complex	Medium	$g_{x,y,z}$	$A_{x,y,z} / \text{MHz}$	T_1 / ms	$T_2 / \mu\text{s}$	T / K	Ref.
[PPh ₄] ₂ [V ^{IV} O(dmt) ₂]	0.5 mM 1:1 DMF- <i>d</i> ₇ /toluene- <i>d</i> ₈	1.971	414	17.05	2.3	10	41
		1.971	414				
		1.990	131				
[PPh ₄] ₂ [V ^{IV} O(dmid) ₂]	0.5 mM 1:1 DMF- <i>d</i> ₇ /toluene- <i>d</i> ₈	1.974	415	17.89	2.6	10	41
		1.974	415				
		1.990	131				
[PPh ₄] ₂ [V ^{IV} O(prdt) ₂]	0.32 mM 45 vol % DMF- <i>d</i> ₇ /toluene- <i>d</i> ₈	1.975	418	17.5	10.11	10	27
		1.975	418				
		1.982	125				
[PPh ₄] ₂ [V ^{IV} O(prddt) ₂]	0.32 mM 45 vol % DMF- <i>d</i> ₇ /toluene- <i>d</i> ₈	1.978	395	16.5	6.02	10	27
		1.978	395				
		1.986	120				
[PPh ₄] ₂ [V ^{IV} O(prddd) ₂]	0.32 mM 45 vol % DMF- <i>d</i> ₇ /toluene- <i>d</i> ₈	1.970	416	11.3	6.59	10	27
		1.970	416				
		1.986	129				
[PPh ₄] ₂ [V ^{IV} O(prddd) ₂]	0.32 mM 45 vol % DMF- <i>d</i> ₇ /toluene- <i>d</i> ₈	1.969	417	12.3	5.95	10	27
		1.969	417				
		1.986	129				
[PPh ₄] ₂ [V ^{IV} O(cat) ₂]	1.0 mM 3:1 CH ₂ Cl ₂ /benzene	1.980	159	40	3.6	4.5	31
		1.988	126				
		1.956	465				
[PPh ₄] ₂ [V ^{IV} O(napdo) ₂]	1.0 mM 3:1 CH ₂ Cl ₂ /benzene	1.979	156	20	4.2	4.5	31
		1.988	127				
		1.955	465				

Complex	Medium	$g_{x,y,z}$	$A_{x,y,z} / \text{MHz}$	T_1 / ms	$T_2 / \mu\text{s}$	T / K	Ref.
[V ^{IV} O(Pc)]	0.1% [Ti ^{IV} O(Pc)]	1.987	168	14	3.4	4.3	42
		1.987	168				
		1.966	477				
[V ^{IV} O(dpm) ₂]	0.5 mM D ₂ SO ₄	1.9760	480	2405	22	7	43
		1.9760	220				
		1.9975	85				
[V ^{IV} O(dpm) ₂]	1 mM 2:3 CH ₂ Cl ₂ /toluene	1.9980	168	50	2.7	4	44
		1.9815	190				
		1.9490	510				
[HNBu ₃] ₂ [Mo ^V (CN) ₈]	0.5 mM PrCN	1.973	103	1050	—	5	38
[HNBu ₃] ₂ [W ^V (CN) ₈]	0.5 mM PrCN	1.963	185	630	—	5	38
[Mn ^{II} (Pc)]	0.5 mM D ₂ SO ₄	2.0000	0	0.69	14	7	43
		1.9978	288				
		1.9978	278				
[PPh ₄] ₃ [Fe ^{III} (CN) ₆]	1 mM 1:1 H ₂ O/glycerol	2.34	—	—	2.4	4.7	32
		2.10					
		0.915					
[PPh ₄] ₃ [Ru ^{III} (CN) ₆]	1 mM 1:1 H ₂ O/glycerol	1.976	—	—	2.6	4.7	32
		1.991					
		2.003					
K ₃ [Ru ^{III} (ox) ₃]	1 mM 1:1 H ₂ O/glycerol	2.473	—	—	3.4	4.7	32
[PPh ₄] ₃ [Os ^{III} (CN) ₆]	1 mM 1:1 H ₂ O/glycerol	1.82	—	—	4.1	4.6	32

Complex	Medium	$g_{x,y,z}$	$A_{x,y,z} / \text{MHz}$	T_1 / ms	$T_2 / \mu\text{s}$	T / K	Ref.
[Co ^{II} (tmc)(MeCN)][PF ₆] ₂	0.5% [Zn ^{II} (tmc)(MeCN)][PF ₆] ₂ ^a	2.022	286 ^c	1.43	0.913	5	45
		2.022	286 ^c				
		2.337	68 ^c				
[Co ^{II} (Pc)]	0.5 mM D ₂ SO ₄	2.2830	60	11.1	9.4	7	43
		2.2830	60				
		2.0232	259				
[PPh ₄ -d ₂₀][Ni ^{III} (mnt) ₂]	1 mM 1:1 CD ₂ Cl ₂ /CS ₂	1.9935	—	8.5	38.7	7	46
		2.0404					
		2.1390					
[PPh ₄ -d ₂₀][Ni ^{III} (mnt) ₂]	0.01% [PPh ₄] ₂ [Ni ^{II} (mnt) ₂]	1.9935	—	0.93	20.2	7	46
		2.0404					
		2.1390					
[PPh ₄ -d ₂₀][Ni ^{III} (mnt) ₂]	0.01% [PPh ₄ -d ₂₀] ₂ [Ni ^{II} (mnt) ₂]	1.9935	—	0.79	7.78	7	46
		2.0404					
		2.1390					
[HNEt ₃][Ni ^{III} (dip) ₂]	1 mM 1:1 CD ₂ Cl ₂ /CS ₂	2.0075	—	4.04	11.0	7	46
		2.0405					
		2.1725					
[Cu ^{II} (acac)]	1 mM 1:1 CD ₂ Cl ₂ /CS ₂	2.26	520	0.9	2.8	7	47
		2.26	520				
		2.040	85				

Complex	Medium	$g_{x,y,z}$	$A_{x,y,z} / \text{MHz}$	T_1 / ms	$T_2 / \mu\text{s}$	T / K	Ref.
[Cu ^{II} (tfacac)]	1 mM 1:1 CD ₂ Cl ₂ /CS ₂	2.266	520	0.47	4.75	7	47
		2.266	520				
		2.052	70				
[Cu ^{II} (hfac)]	1 mM 1:1 CD ₂ Cl ₂ /CS ₂	2.31	500	1.17	5.0	7	47
		2.31	500				
		2.060	0				
[Cu ^{II} (fod)]	1 mM 1:1 CD ₂ Cl ₂ /CS ₂	2.26	550	1.1	1.7	7	47
		2.26	550				
		2.057	0				
[Cu ^{II} (bzac)]	1 mM 1:1 CD ₂ Cl ₂ /CS ₂	2.255	550	0.7	2.20	7	47
		2.255	550				
		2.052	70				
[Cu ^{II} (dbm)]	1 mM 1:1 CD ₂ Cl ₂ /CS ₂	2.258	550	1.3	4.2	7	47
		2.258	550				
		2.051	80				
[PPh ₄] ₂ [Cu ^{II} (bdt)]	0.5% [PPh ₄] ₂ [Ni ^{II} (bdt)]	2.085	500	30.7	2.048	5	30
		2.019	115				
		2.019	115				
[PPh ₄] ₂ [Cu ^{II} (bds)]	0.5% [PPh ₄] ₂ [Ni ^{II} (bds)]	2.082	460	91.4	3.183	5	30
		2.018	145				
		2.018	145				
[PPh ₄] ₂ [Cu ^{II} (mnt)]	0.001% [PPh ₄] ₂ [Ni ^{II} (mnt)]	2.0227	118	87.4	9.2	7	48
		2.0227	118				
		2.0925	500				

Complex	Medium	$g_{x,y,z}$	$A_{x,y,z} / \text{MHz}$	T_1 / ms	$T_2 / \mu\text{s}$	T / K	Ref.	
[PPh ₄ -d ₂₀] ₂ [Cu ^{II} (mnt)]	0.01% [PPh ₄ -d ₂₀] ₂ [Ni ^{II} (mnt)]	2.0227	118	96.2	68	7	48	
		2.0227	118					
		2.0925	500					
[Cu ^{II} (Pc)]	0.5 mM H ₂ SO ₄	2.0496	15	85	7.8	7	43	
		2.0496	15					
		2.1990	630					
[Cu ^{II} (Pc)]	0.5 mM D ₂ SO ₄	2.0502	30	103	41	7	43	
		2.0502	30					
		2.1965	610					
[Cu ^{II} Pc ^F]	0.5 mM D ₂ SO ₄	2.0470	15	60	40	7	43	
		2.0470	15					
		2.1925	630					
[Cu ^{II} (Pc ^{Cl})]	0.5 mM D ₂ SO ₄	2.0525	30	140	43	7	43	
		2.0525	30					
		2.2050	620					
[K(2.2.2.cryptand)][Y(Cp') ₃]	10 mM THF	1.986	100.8	41.27	2.85	5	49	
		1.986	100.8					
		2.001	98.6					
	0.2% [K(2.2.2.cryptand)][Yb(Cp') ₃]	1.986	1.986	100.8	17.95	2.68	5	49
			1.986	100.8				
			2.001	98.6				

^a measured parallel to the magnetic field, ^b measured perpendicular to the magnetic field, ^c hyperfine interaction of ⁵⁹Co $I = 7/2$, ^d hyperfine interaction of ¹⁴N $I = 1$.

1.2.2.1.3. Group 7

Manganese is the only member of group 7 to be incorporated in a qubit and despite manganese cluster compounds seeing much attention in the field of SMMs there exists only one monospin molecular qubit. This is surprising given the varied stable oxidation states manganese possesses: Mn^{II} [Ar] $3d^5$, Mn^{III} [Ar] $3d^4$, Mn^{IV} [Ar] $3d^3$, Mn^{V} [Ar] $3d^2$, and Mn^{VI} [Ar] $3d^1$ are all known in air-stable compounds. Manganese is a monoisotopic element with ^{55}Mn having $I = 5/2$. This coupled with, for example, Mn^{II} high spin $S = 5/2$ would give a qubit with six accessible nuclear spin states and five allowed electronic transitions on each nuclear resonance amounting to a whopping thirty available qubits. Instead what we have is the meagrely performing [Mn(Pc)] in which manganese adopts an intermediate spin state $S = 3/2$ from complexation with the strong-field phthalocyanine ligand.⁴³ The complex has an axial g value with $g_z = 2.0000$ and $g_y = g_x = 1.9978$ and an axial hyperfine component $A_z = 0$ $A_y = A_x = 278$ MHz. In 0.5 mM D_2SO_4 at 7 K $T_1 = 0.69$ ms and $T_M = 14.0$ μs . T_1 is two degrees of magnitude lower than that of $[\text{V}^{\text{IV}}\text{O}(\text{Pc})]$ and T_2 is almost half, this is attributed to at least one unpaired electron being in an orbital perpendicular to the molecular plane allowing for more spin-spin interactions with no electronic shielding.

1.2.2.1.4. Group 8

The group 8 elements iron, ruthenium and osmium comprise a series investigated by the Freedman group conducted in parallel with their investigation of the effect of spin states on T_2 , this time assessing spin-orbit coupling.³² The spin-orbit coupling series consisted of archetypal hexacyano complexes with spin-orbit coupling constants of 464, 880, and 3100 cm^{-1} for each element going down the group respectively. With each metal in the +III oxidation state the strong ligand field induced by the cyanide ligand an $S = 1/2$ ground state, T_2 actually increased with increasing spin-orbit coupling, $\text{Fe} < \text{Ru} < \text{Os}$ (Table 1). This is unanticipated given spin-orbit coupling arbitrates spin-lattice relaxation which in turn limits T_2 . However, at the very low measurement temperature of 5 K, T_1 is far longer T_2 , and therefore removes the influence of spin-orbit coupling on the coherence time. Though, as expected, by increasing temperature between 13 and 22 K T_2 is shortened to a far greater degree for Os than either Fe or Ru. Overall Ru is the least effected by temperature.

Continuing their investigations of high spin d-block element qubits the Freedman group turned to $[\text{Fe}(\text{croc})_3]^{3-}$ where $(\text{croc})^{2-}$ is the conjugate of the five-membered ring containing croconic acid.⁵⁰ The $S = 5/2$ ferric ion shows the characteristic effective g -value of 4.3 arising from the rhombicity of the system with a small contribution from D . Simulation of the X-band spectrum at 77 K gave spin-Hamiltonian parameters $g = (2.009, 2.010, 2.011)$, $D = 0.30$ cm^{-1} , and $|E/D| = 0.23$, exemplifying the highly mixed m_s states for this rhombic system. Unfortunately, while Rabi oscillations were observed for a sample with 0.2% dilution in the corresponding gallium analogue the decoherence time of 0.72 μs is limited by the short T_1

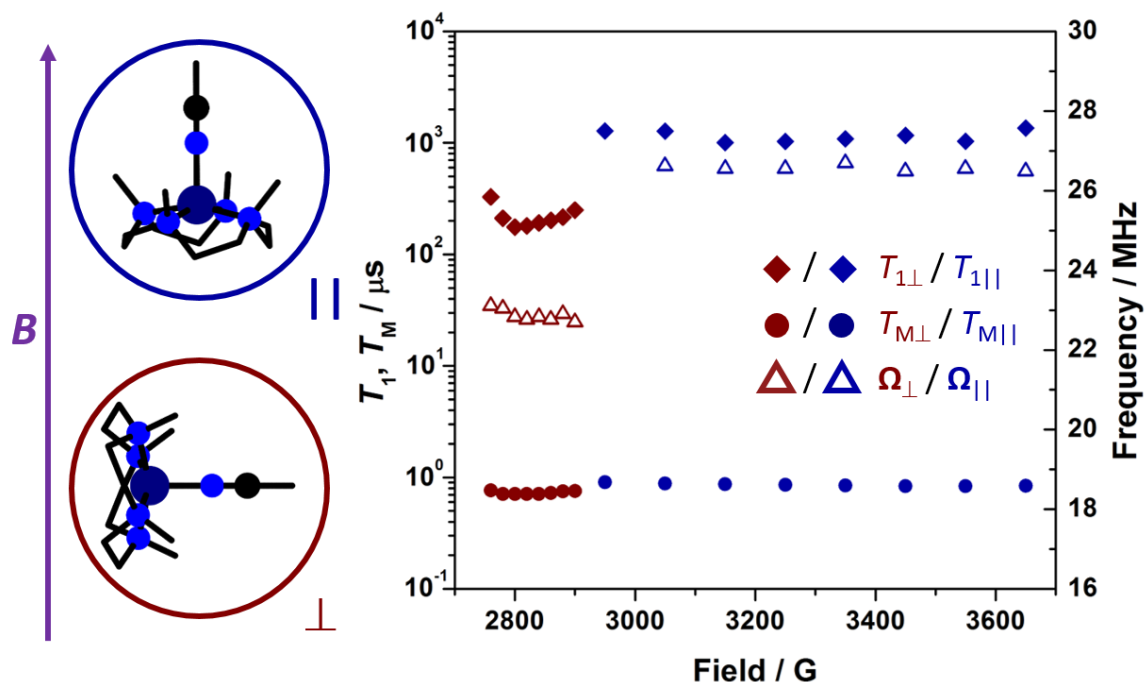


Figure 1.13. [Co(tmc)(MeCN)]²⁺ parallel and perpendicular to the magnetic field. Right, T_1 and T_M at field positions corresponding to the eight hyperfine transitions and their Rabi frequencies.

of 11.3 μs measured at 5 K, emphasising the importance of T_1 on the performance of any molecular spin qubit.

1.2.2.1.5. Group 9

Cobalt is the sole member of group 9 for qubits (Figure 1.14.). Typically cobalt is associated with single-molecule magnets with Co^{II} [Ar] 3d⁷ in a tetrahedral field $S = 3/2$ displaying a large D as a result of each each excitation of the ground state being a spin conserving transition.⁵¹ It displays magnetic hysteresis and slow magnetic relaxation in the absence of a field. To convert this to a qubit requires the tetrahedral symmetry to be broken and transformed to a distorted D_{2d} or into D_{4h} symmetry at which point it would adopt a $S = 1/2$ configuration in square pyramidal or square planar geometry. Freedman and co-workers altered the counteranion paired with [Co(dmit)₂]²⁻ to convert it from a single-molecule magnet to a potential qubit.⁵² The four counteranions: NBu₄⁺, PPh₄⁺, [(Ph₃P)₂N]⁺, and [K(18-crown-6)]⁺ were employed. The greatest deviation of the [Co(dmit)₂]²⁻ from D_{2d} symmetry was enforced by the smaller, more flexible cation, NBu₄⁺ cation. This departure from D_{2d} spurred an increase in the rhombicity of the zero-field interaction, as observed in the absence of hysteresis in coercive field susceptibility measurements. The mixing of m_s states driven by rhombicity brings the allowed transition of the effective $S = 1/2$ system into a resonant field accessible at L-band frequency providing a new point of access to quantum transitions in high spin transition metal complexes.

Following through to full D_{4h} symmetry is $[\text{Co}(\text{Pc})]$ investigated by Bader et al.⁴³ The square planar complex has an $S = 1/2$ ground state with axial g and A values (Table 1) where the SOMO is in an orbital with some z character. Thus, similarly to $[\text{Mn}(\text{Pc})]$, $[\text{Co}(\text{Pc})]$ suffers in coherence times compared to its vanadyl and copper brethren with $T_1 = 11.1$ ms and $T_M = 9.44$ μs .

Gao et al measured the Rabi oscillations of the complex $[\text{Co}^{\text{II}}(\text{tmc})(\text{MeCN})]^{2+}$ doped into a single crystal of $[\text{Zn}^{\text{II}}(\text{tmc})(\text{MeCN})]^{2+}$ parallel and perpendicular to the magnetic field (Figure 1.13).⁴⁵ The ligand (tmc) is a tetradentate N-donor macrocycle where each donor atom is joined by an ethylene group and topped with a methyl to form a tertiary amine. Co^{II} sits above the plane of the ligand in a square pyramidal geometry capped by an apical acetonitrile. In the C_{4v} symmetry complex Co^{II} is low-spin $S = 1/2$ below 250 K and possesses highly anisotropic g and A values (Table 1). The ^{59}Co $I = 7/2$ nucleus splits the spectrum into eight lines and has the most striking effect on the anisotropy of the system with the parallel alignment well-spaced at higher fields and the perpendicular alignment contracted and at lower fields. The octet is split into triplets by hyperfine contributions from the ^{14}N $I = 1$ donor atom of MeCN confirming the SOMO to be of d_{z^2} character. The complex crystallises in a tetragonal space group with the magnetic centre on the 4-fold axis with the uniaxial principal axes of the axial \mathbf{g} , \mathbf{A}_{Co} and \mathbf{A}_{N} tensors collinear with the crystallographic \mathbf{c} axis. T_1 , T_M were measured and transient nutation performed on each octet peak for the parallel and perpendicular alignments. T_M was not affected by a change in field direction. However, T_1 decreases by an order of magnitude when the field is perpendicular to the magnetic axis. This is attributed to the mixing of closer magnetic states in the perpendicular direction allowing for lower energy relaxation pathways. Transient nutation showed a linear relation to power at each field position confirming coherent manipulation of spins. Interestingly, the Rabi frequency decreased from 26.5 MHz in the parallel field to 23.0 MHz in the perpendicular, and is dependant on the anisotropy of the molecule to the field. The authors suggest that this phenomenon is caused by the spin mixing with nuclear forbidden transitions via the highly anisotropic hyperfine couplings and highlight the possibility of using magnetic anisotropy to tune the properties of a molecular qubit.

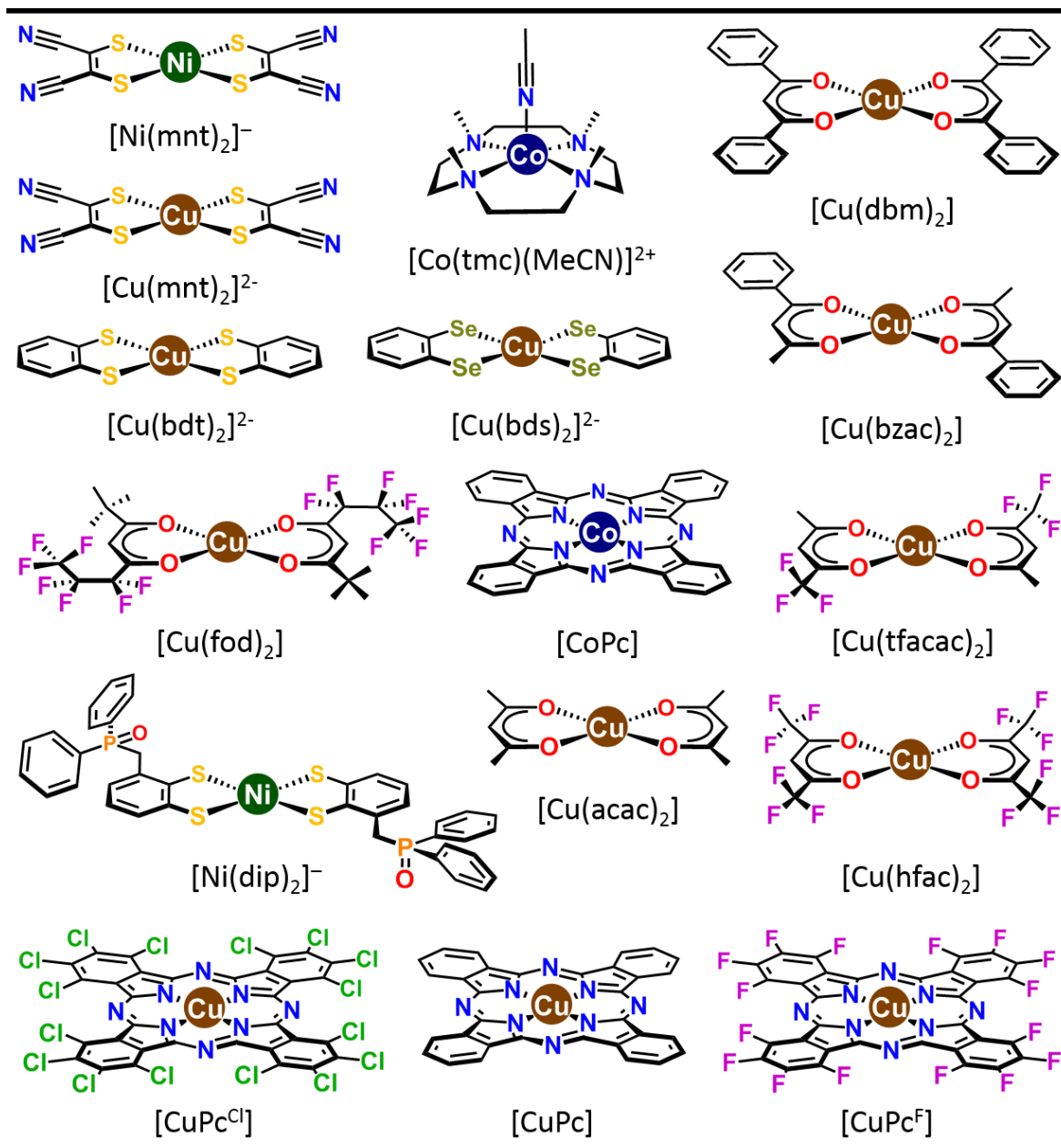


Figure 1.14. All group 9, 10, and 11 monospin molecular electron spin qubits.

1.2.2.1.6. Group 10

Group 10 is infamous for its stable square planar 16 electron complexes. None so are more ubiquitous than bis(dithiolene) complexes which show rich multiple electron transfer series. Van Slageren and co-workers utilised two of these, $[\text{Ni}^{\text{III}}(\text{mnt})_2]^-$ and $[\text{Ni}^{\text{III}}(\text{dip})_2]^-$, to investigate what they attribute as a formal Ni^{III} oxidation state with $S = 1/2$ in the strong field produced by the sulfur chelates (Figure 1.14.).⁴⁶ Dithiolene ligands form five-membered metallo-rings through a cis arrangement of two sulfur donors, as is the case for 1,2-cyanoethylene-1,2-dithiolate ($\text{mnt})^{2-}$ which earns its monicker for its structural similarities to maleonitrile, where the other double bond substituents are strongly electron withdrawing cyanides. Two ortho sulfur donors on a benzene ring also afford a dithiolene ligand such as

3-(diphenylphosphoryl)-methylbenzene-1,2-dithiolate, shortened to (dip)²⁻, which has a diphenylphosphinomethylene substituted to the 3-position of the benzene-1,2-dithiolate ring. Nickel is nuclear spin free so the ground state SOMO of nickel bis(dithiolenes) is described entirely by a rhombic *g* value (Table 1.1.). Both complexes gave respectable *T_M* values of 38.7 and 11 μs for (mnt)²⁻ and (dip)²⁻ respectively in 1:1 DCM-*d*₂/CS₂ at 7 K with the nuclear spin free (mnt)²⁻ providing the longer coherence times as expected.

1.2.2.1.7. Group 11

Prior to investigating the monoanionic nickel bis(dithiolenes) as qubits Van Slageren and coworkers had found success with the dianionic copper bis(dithiolenes) (Figure 1.14.).⁴⁸ The square planar structure of bis(dithiolenes) persists for all the late transition metals, with [Cu^{II}(mnt)₂]²⁻ exhibiting axial *g* and *A* values (Table 1). In a fully deuterated system [PPh₄-*d*₂₀]₂[Cu^{II}(mnt)₂] was doped at 0.01% into the corresponding [PPh₄-*d*₂₀]₂[Ni^{II}(mnt)₂] diamagnetic matrix yielded a *T₁* of 96 ms and *T₂* of 68 μs at 7 K using a Q-band spectrometer. *T₂* approached 1 μs at room temperature giving the first example of room temperature quantum coherence for inorganic molecular electron spin qubits.

Van Slageren et al also investigated a series of charge neutral Cu^{II} β-diketonate complexes (Figure 1.14.).⁴⁷ The β-diketonates are monoanionic oxygen donor ligands and form a six-membered metallo-ring with their complexed metal, which is resonance stabilised. Varying the substituents on the α-position of each carbonyl has minimal effect on the *g* and *A* values of the copper centre but introduces a unique nuclear spin environment to investigate *T₁* and *T_M* (Table 1). The best performing non-fluorinated qubit [Cu^{II}(dbm)₂] has exclusively phenyl substituents and a *T_M* of 4.2 μs in a 1 mM frozen solution of 1:1 CD₂Cl₂/CS₂. The Slageren group set out to build a model by which they could quantitatively predict nuclear-spin-diffusion limited coherence times of copper qubits in the solid state stemming from similar work done on phosphorous atoms doped in silicon.³⁷ This model takes all proton nuclear spin pairs within a 30 Å radius from the copper centre in the molecular *xy* plane (as the Hahn echo is experimentally measured at the *g*_⊥ resonance field position) and calculates for each possible proton nuclear spin pair, its contribution to the decoherence of the copper spin by the equation;

$$v_E^{(2)}(\tau) = \exp\left(\sum_{n>m} 1 - v_{nm}(\tau)\right)$$

Where *v_E⁽²⁾(τ)* is the intensity of the Hahn echo, *τ* is the pulse delay time and *v_{nm}(τ)* is the pair contribution. Excellent correlation is to experimental data is found for the *T_M* decay of [Cu^{II}(dbm)₂] doped at 0.001% into the diamagnetic [Ni^{II}(dbm)₂] which has *T_M* = 7.74 μs at 7 K. This model requires only the crystal structure of the copper compound, but has only so far been adapted to compute the effects of proton nuclear spins on copper spin-hosts.

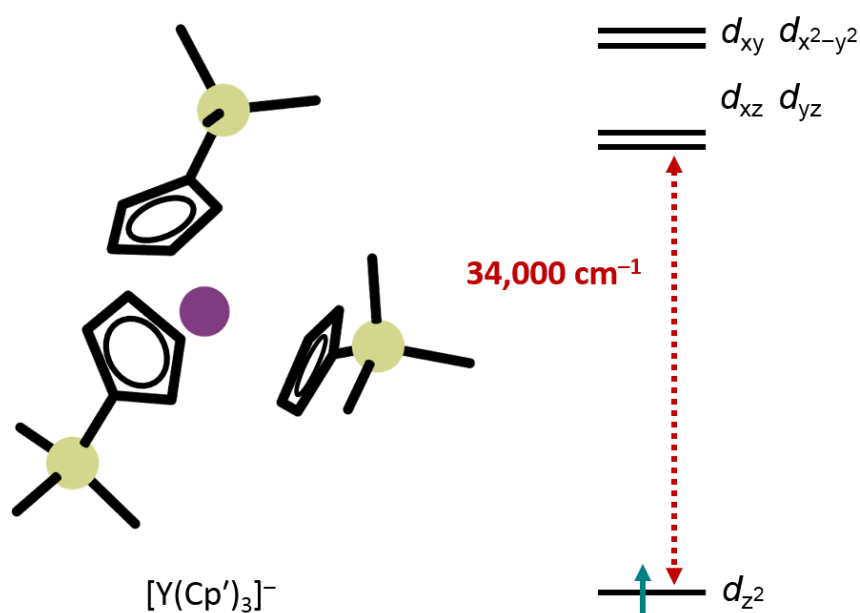


Figure 1.15. Left, the structure of $[\text{Y}(\text{Cp}')_3]^-$. Right, the d-orbital splitting of Y^{II} d^1 in a trigonal field with energy of the first transition in wavenumbers.

1.2.2.2. Rare-earth Metal Compounds

The rare earth elements encompass group 3 of the transition metals and the f-block, grouped together as they exhibit incredibly similar chemical properties. Indeed, the rare earths are found in nature as highly mixed metal ores and are separated with great difficulty. The stable members of the rare earth family commonly exhibit a +III oxidation state with few exceptions. One such exception was exploited by Ariciu et al with a series of group 3 trigonal coordination geometry complexes with a +II oxidation state.⁴⁹ Making use of the sterically encumbered ligands 1-(trimethylsilyl)-2,4-cyclopentadien-1-yl and 1,1,1-trimethyl-*N*-(trimethylsilyl)-silanamine, known colloquially as Cp' and "big N" respectively, the researchers were able to stabilise and isolate the elusive +II oxidation states. The trigonal complexes of scandium, yttrium, lanthanum and lutetium have axial g and A albeit with very small anisotropic distortions: the largest anisotropy is in the lutetium complex with $g = (1.945, 1.945, 1.975)$ and $A = (1121, 1121, 1070)$ MHz and the smallest in yttrium with $g = (1.986, 1.986, 2.001)$ and $A = (100.8, 100.8, 98.6)$ MHz. Pulsed EPR of $[\text{Y}(\text{Cp}')_3]^-$ doped at 2% in the diamagnetic $[\text{K}(2.2.2\text{-cryptand})][\text{Yb}(\text{Cp}')_3]$ gave $T_1 = 17.95$ ms and $T_M = 2.07$ μs at the first resonant field position from the splitting of the 100% abundant ^{89}Y $I = 1/2$ nucleus. The authors boldly claim a ^2S ground state for these complexes and attribute these 'long' coherence times to the fidelity of that state despite being predominantly d_{z^2} in character. Another, more reasonable, postulate put forward by the authors comes from corroboration with computational analysis of the molecular orbitals. They found the complex to consist of nine non-bonding ligand-character orbitals between the SOMO and the next highest metal

orbital, a $34,000\text{ cm}^{-1}$ energy gap, which sufficiently separates the ground state (Figure 1.15.).

The chemistry of the f-block elements has seen great advancement in recent years due largely to their weighty influence in the field of molecular magnetism. In single molecule magnets their large spin states and enormous spin-orbit coupling gives a large magnetic anisotropy. While these features do typically prove to be deleterious to the relaxation performance of a qubit, optimised systems on high spin transition metal systems have proved to be fortuitous and the large spin manifolds presented by lanthanides provide a convenient way to access multiple qubit states.

$\text{Gd}^{\text{III}} [\text{Xe}] 4f^7$ has a half-filled shell with a $S = 7/2$ ground state and exhibits comparable features to transition metal elements with half-filled levels, such as Mn^{II} and Fe^{III} , both $S = 5/2$. The principle contributor to large D comes from spin-conserving transitions that are spin-forbidden in half-shell configurations— as such, small ZFS parameters are inherent to these isotropic ions. The Coronado group have specialised in lanthanide molecular spin qubits within cluster compounds. One such entry in their archives is $[\text{GdW}_{30}\text{P}_5\text{O}_{110}(\text{H}_2\text{O})]^{14-}$, an isotropic Gd^{III} ion with C_5 symmetry complexed by a polyoxometalate (POM) torus and topped with an apical water ligand.⁵³ POMs typically consist of molybdenum, tungsten and chalcogenides and so, with their low nuclear magnetic spin abundance are considered nuclear spin free. A powder sample of the polyoxometalate complex (Figure 1.16.), doped at 1% and 0.1% in its diamagnetic yttrium counterpart, displayed Rabi oscillations signifying coherent spin control. By tuning the Rabi frequency to the proton Larmour frequency (15 MHz at X-band; $B_0 = 349.6\text{ mT}$), it was demonstrated that the long-term oscillations were dependent on the static field (B_0) as opposed to the microwave power. This indicated

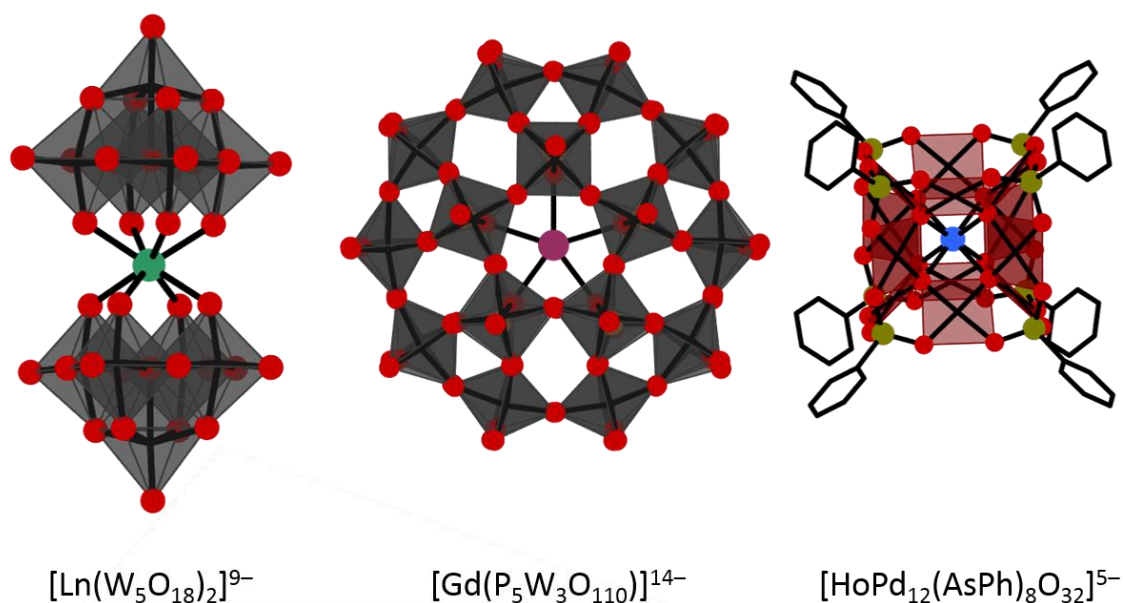


Figure 1.16. Left, the structure of $[\text{Ln}(\text{W}_5\text{O}_{18})_2]^{9-}$. Middle, the structure of $[\text{GdW}_{30}\text{P}_5\text{O}_{110}(\text{H}_2\text{O})]^{14-}$, viewed from the C_5 axis with water ligand omitted. Right, the structure of $[\text{LnPd}_{12}(\text{AsPh})_8\text{O}_{32}]^{5-}$.

coherence between the predominantly $m_s \pm 5/2 \rightarrow \pm 3/2$ transition and the proton nuclear spin incident on the coordinated water molecule.

Using this same feature of the field dependency of the Rabi oscillation frequency Coronado and co-workers suppressed the dipolar contributions from protons that comprise the spin bath leading to short decoherence times.⁵³ They utilised a series of complexes of the form $[\text{LnPd}_{12}(\text{AsPh})_8\text{O}_{32}]^{5-}$; where the lanthanoid ion is encapsulated within a polyoxopalladate, the selected f-elements – Tb, Dy, Ho, Er, Tm – give a selection of Kramers and non-Kramers ions with an opulent energy level structure in this highly symmetric, near-cubic ligand field. For the Ho complex, a temperate axial compression of 1% caused by a small applied magnetic field of 410 mT fashioned a setting where the electron spins of the lanthanide became invisible to the nuclear spins that constitute the spin bath. This removes the need to chemically impede the decohering nuclear spin bath and arises from the incidence of sizeable tunnelling splittings inherent to lanthanoid molecular magnets.

Another entry in the choice field of lanthanide molecular qubits are those of $[\text{Ln}(\text{W}_5\text{O}_{18})_2]^{9-}$, also provided by Coronado et al.⁵⁴ The qubits consist of an 8-coordinate lanthanide ion with square antiprismatic geometry fixed between two tungsten polyoxometalate ligands. Rabi oscillations detected from the holmium analogue, $[\text{Ho}(\text{W}_5\text{O}_{18})_2]^{9-}$ indicated a long decoherence time sustained by the aforementioned tunnelling splitting of the ground state, even at high concentration (25% diluted in the Y analogue). The $m_J = 4$ ground state of this square anti-prismatic Ho single-ion magnet with D_{4d} point symmetry is split by the 100% abundant ^{165}Ho $I = 7/2$ nuclear spin. This large tunnelling splitting gave rise to atomic clock transitions, which earn their name from atomic clocks, which are composed of similarly

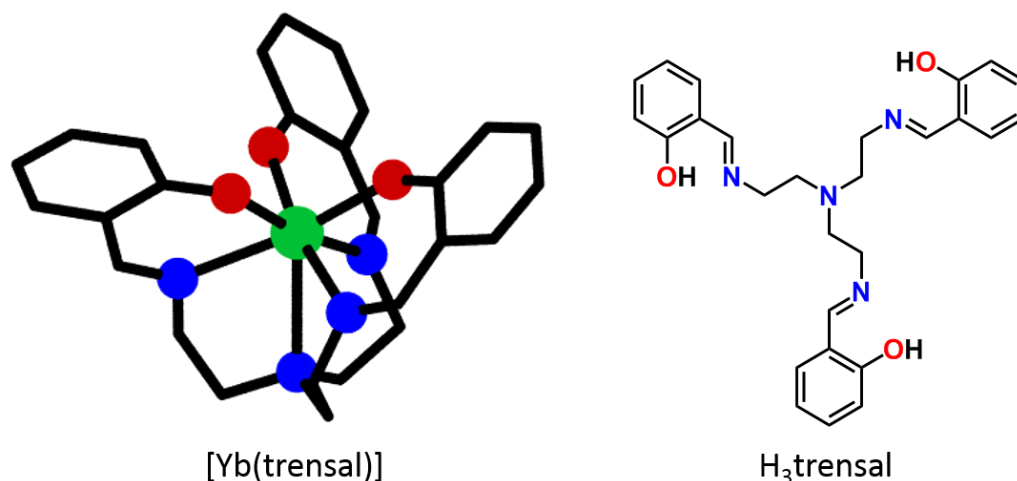


Figure 1.17. Left, the structure of [Yb(trensal)]. Right, the protonated tripodal ligand H₃trensal.

isolated ions that are impervious to magnetic field variations and other environmental factors rendering them exceptional timekeepers. The transitions are those within the m_l levels of Ho, where at specific field positions the electron spin flipping between the spin-up and spin-down manifolds ($DMI = 0$) is isolated from the surrounding environment. The coherence time measured at one of these atomic clock transitions was 8.4 μ s at 5 K.

Pedersen and coworkers characterised the molecular spin qubit [Yb(trensal)].⁵⁵⁻⁵⁶ The organic tripodal Schiff-base ligand trensal allows for the complexation of a +III ion in a C_3 field resulting in a charge neutral complex. It is formed in high yields from the condensation of salicylic acid and tris(2-aminoethyl)amine (Figure 1.17.). As the complex is charge neutral, it is sublimable: allowing for scaling up by thermal or vapour deposition on appropriate substrates. The EPR spectrum of single crystals of the diamagnetic [Lu(trensal)] doped with 7% [Yb(trensal)] is $^2F_{7/2}$ and simulated as an effective $S = 1/2$ system with $g_{||} = 4.3$ and $g_{\perp} = 2.9$. The long T_1 of 10 ms at 3.5 K also yields a modest T_2 of 0.5 ms at a field position corresponding to the $l = 0$ EPR transition in the Hahn-echo for B_{\perp} to the C_3 axis of the complex.

1.3. Multispin Molecular Electron Spin Qubits

1.3.1. Organic Systems

In the instances of multiple paramagnetic centred qubits the nitroxyl radicals of the Takui group paved the way in designer qubits.²⁰ The Takui utilised the fact that the coherent manipulation of more than one electron in a multiple paramagnetic centred molecule was indistinguishable if the molecule possessed a centre of inversion (meaning that the g -tensors of each electron are identical with respect to each other). This, is the concept of g -engineering. At its core the concept is simple, the g -tensors of multiple electron spin host molecules must be different relative to each other to be distinguishable and individually

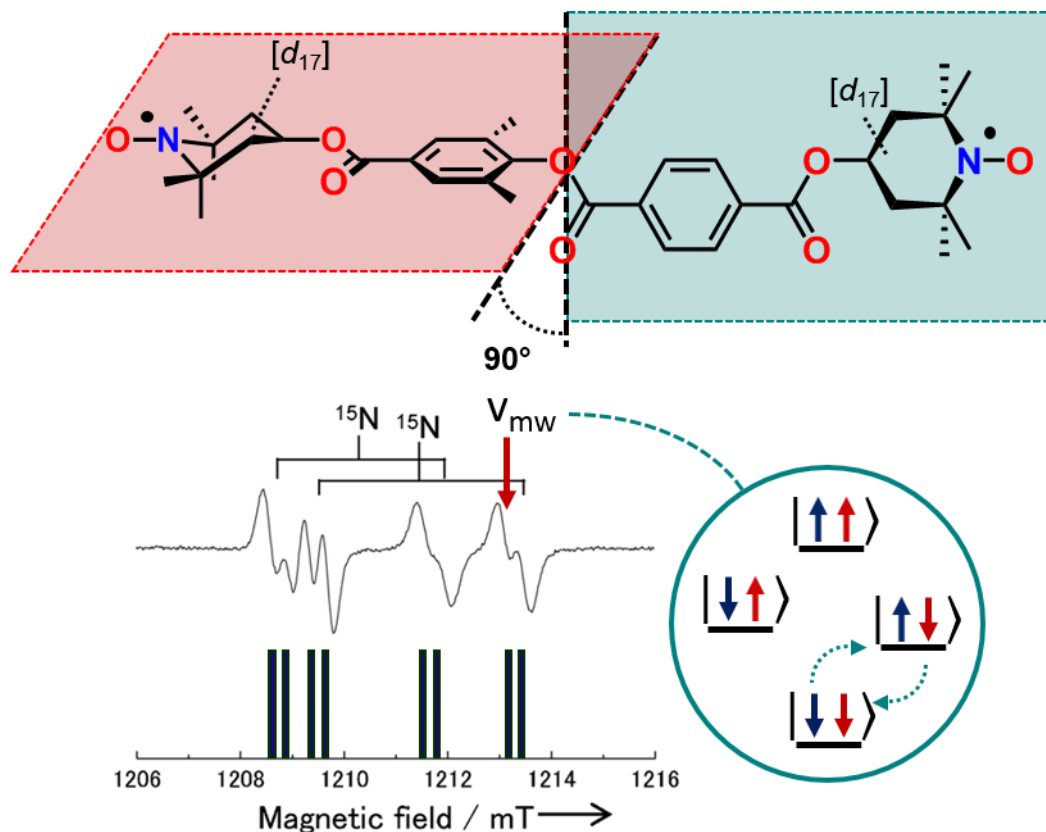


Figure 1.18. Top, molecular structure of the nitroxyl biradical exhibiting the orthogonality induced by the sterically encumbered dimethyl phenyl. Bottom, stick plot and the specified resonant field position pulsed to implement a CNOT gate.

manipulable. This can be manifested by 1) The use of electrons with intrinsically different g -values, dubbed heterospin g -engineering 2) The use of electron spins that are the same but orientated in different directions in space, named homospin g -engineering and 3) The introduction of different hyperfine couplings to each radical, this is technically speaking A -engineering but is referred to as pseudo g -engineering. It is through homospin g -engineering of TEMPO biradicals that yields the most impressive results, the pinnacle of which is the [2,2,6,6-tetramethylpiperidin-N-oxyl-4-yl]-3,5-dimethylbenzoate-4-yl terephthalate biradical. The two methyl groups in the ortho positions to the carboxylic ester in the central linkage enforces orthogonality between the two TEMPO radical moieties. This change in the local g -frame is accompanied by a shift in the resonant field positions. The biradical, with deuterated TEMPO groups and a ^{15}N ($I = 1/2$) nucleus gives rise to the cw EPR spectrum shown in Figure 1.18. With pulse EPR and pumping a microwave pulse at the specified frequency the second spin is flipped enacting a CNOT gate operation which is confirmed by observation of Rabi oscillations in transient nutation experiments.

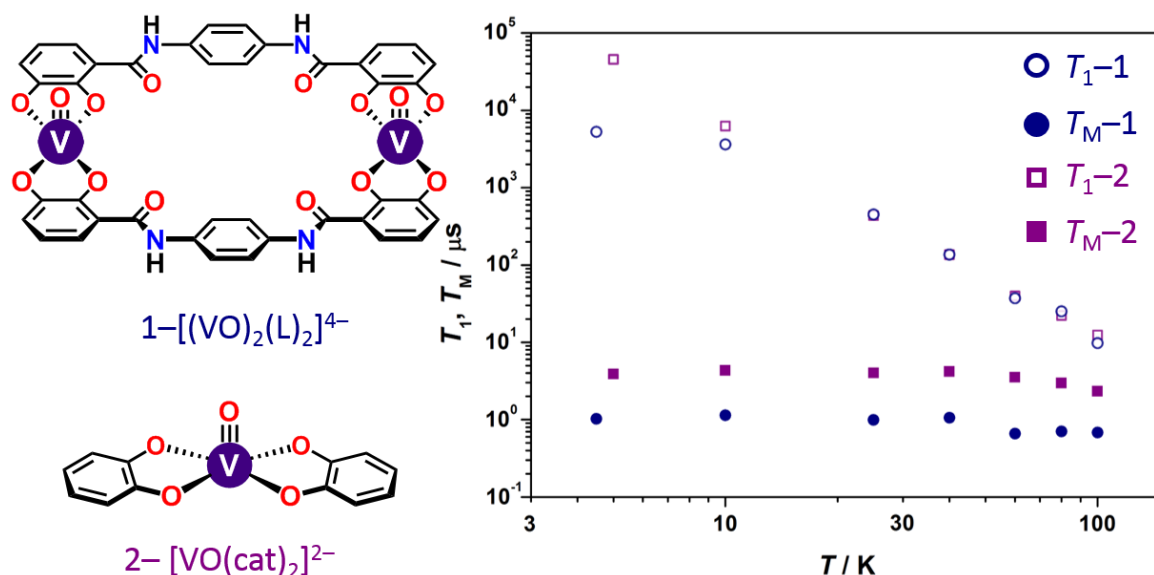


Figure 1.19. Left, the structures of the bimetallic and monometallic vanadyl bis(catecholate) systems labelled 1 and 2 respectively. Right, T_1 and T_M of 1 and 2 at variable temperature.

1.3.2. Coordination Systems

Multispin qubit systems of coordination compounds are dominated by the octametallc NiCr₇ rings of Winpenny and coworkers. However, as these species and structures have been discussed *ad nauseam* the reader is directed to the multiple review articles present in the literature.⁵⁷⁻⁶⁵ Instead, this thesis will focus on the smaller group of well-defined transition metal and lanthanide complexes that exhibit far greater coherence times and rational design.

Sessoli and coworkers utilised the bound bis(catechol) ligand *N,N*-bis(2,3-dihydroxybenzoyl)-1,4-phenylenediamine complexing vanadyl to construct a two-qubit gate (Figure 1.19). Two bis(catecholate)s bind two vanadyl ions to form a bridged complex.¹¹ The ligands are of sufficient length to minimise through bond *J*-coupling and the dominant interaction is through space resulting in a purely dipolar coupling between the 5 Å separated vanadyl electron spins. Solution state cwEPR spectroscopy gave the spin Hamiltonian parameters $g = (1.982, 1.941, 1.982)$, $A = (186, 498, 182)$ MHz and $J = -1.65 \times 10^3$ cm⁻¹ for the $S = 1$ molecule. Using Electron nuclear double resonance (ENDOR) Sessoli and coworkers were able to employ the molecule as a universal control-Z (CZ) gate. Assigning the ⁵¹V nuclear transitions $|m_I = 7/2\rangle$ and $|m_I = 5/2\rangle$ as the logical $|0\rangle$ and $|1\rangle$ states of the qubit respectively a simple radiofrequency pulse can be used to rotate between the states. These states are then coupled by the electron spin-spin interaction governed by *J*. A microwave pulse from $|00\rangle |M_s = -1\rangle \rightarrow |00\rangle |M_s = 0\rangle$ preceded by a full Rabi oscillation adds a π phase to only the $|00\rangle$ component of the wave-function, as such implementing the CZ gate. The gate was used to simulate a simple parabolic curve with 98% fidelity. 99.99% is the fidelity

required for operational use. Of course, the limiting factor within this system is the decoherence introduced by T_M which was found to be 1 μ s at 4.5 K. The research previously performed on bis(vanadyl) species into optimising T_M underpins the decision process in assembling this qubit system, and thus, the realisation of this excellent result.

With a similar approach to complex structure Slageren and coworkers used a bis- β -diketone derivative of bis(thiophenyl)cyclopentene in two equivalents to complex late transition metal ions.⁶⁶ This gives the four metal containing homometallic compounds $[M_4L_2(py)_6]$ ($M = Co, Ni, Cu, Zn$) and the heterometallic $[M_2M'L_2(py)_6]$ ($M = Cu, Co, M' = Ni; M = Co, M' = Cu; M = Cu, Ni, M' = Zn$) where the bis- β -diketone ligands bridge between two MM' units and the coordination spheres of the metal ions are completed by pyridines to form 5-coordinate external sites and octahedral central sites. The ligand shows selectivity with smaller ionic radius metal ions occupying the central site except in the case of the nickel containing heterometallics, which exclusively feature nickel in the central position. The $[CuZn]$ complex has an effective $S = 1/2$ ground state due to a weak isotropic $J = -0.24 \text{ cm}^{-1}$, resulting from the long 16 Å $M-M$ distance, with spin Hamiltonian parameters $g = (2.307, 2.307, 2.067)$ and $A = (470, 470, 60) \text{ MHz}$. The complex $[CuNi]$ exhibits a quartet state at room temperature which on cooling below 40 K is completely depopulated to form an $S = 1/2$ ground state. Pulsed EPR of $[CuNi]$ and $[CuZn]$ gives T_1 values of 0.99 and 2.11 ms respectively. As temperature increases T_1 decreases faster for $[CuNi]$ as expected with its $S = 3/2$ excited state providing additional relaxation pathways. T_M values of 3.59 and 6.03 μ s are found for $[CuNi]$ and $[CuZn]$ respectively, which are excellent for multiqubit systems. The bridging ligand employed by Slageren et al may also be used as a photoactive switch. The dithienylethene photochromic unit is known to undergo photocyclisation in the solid state (Figure 1.20.) and has precedence as a switch for magnetostructural interactions in solid state magnetic materials.⁶⁷⁻⁷¹ This is an ideal switch for a qubit system as it provides a means of optically addressing the system to switch between different states. The ring system is 'closed' under exposure to ultra-violet light and 'opened' in visible, which theoretically allows for a shorter through bond J interaction in the 'closed' conformation. Thus far, these complexes have not been used for gate operations but highlight the scope of tunability offered in a molecular multiqubit system.

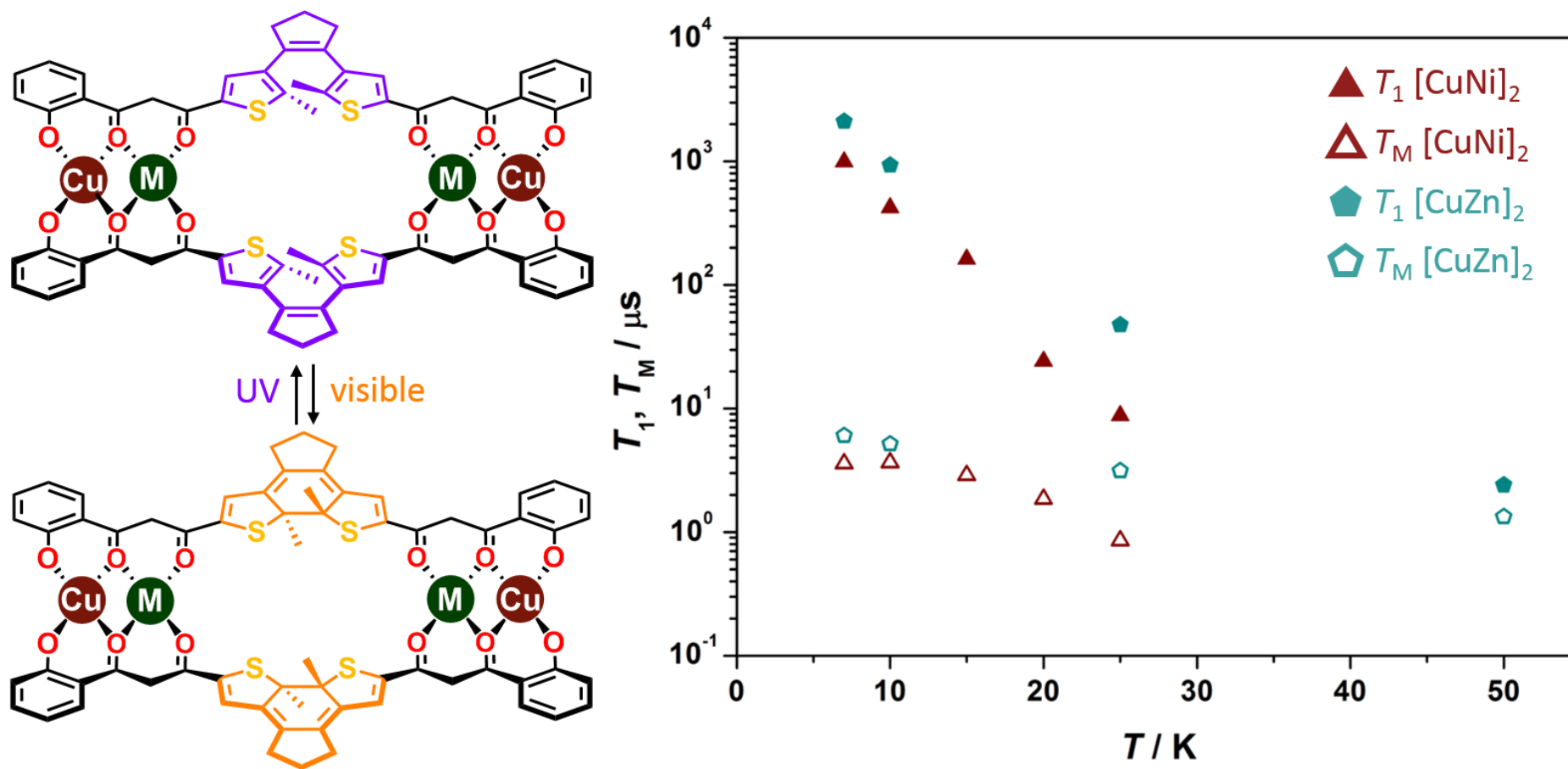


Figure 1.20. Left, the 'open' form of [CuM] depicted in purple with the photocyclisation to the 'closed' form depicted in orange. Right, The T_1 , and T_M variable temperature dependence of [CuNi] and [CuZn].

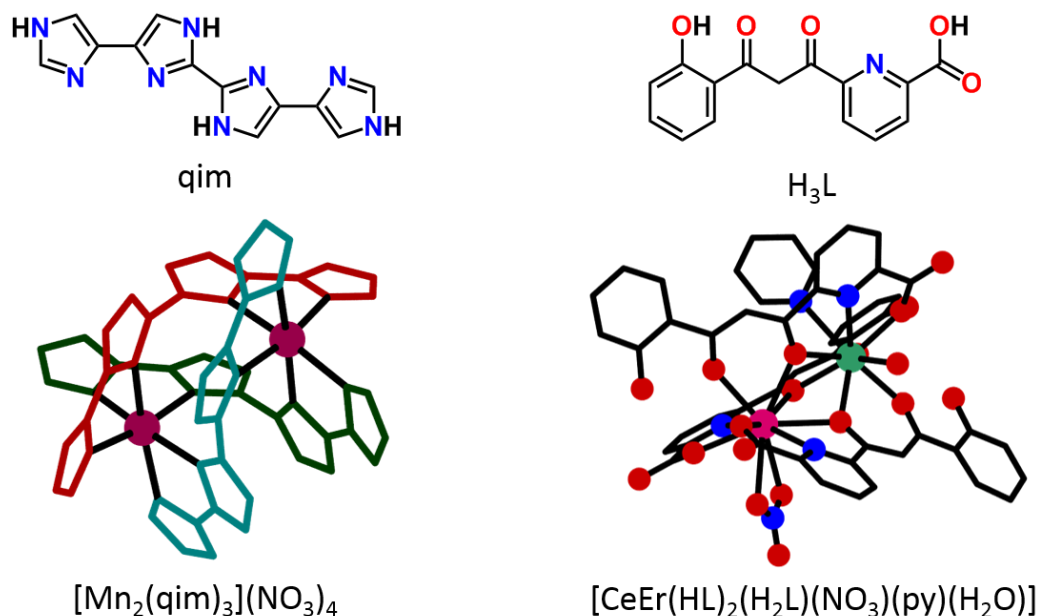


Figure 1.21. Top left, the structure of the α -diimine (qim). Bottom left the structure of the trihelicate $[\text{Mn}_2(\text{qim})_3]^{4+}$ with each (qim) ligand represented as a different colour; crimson, cyan, emerald, for clarity. Top right, the structure of Aromi *et al.*'s polydentate ligand. Bottom right, the heterometallic [CeEr] complex.

Takui and coworkers ventured into the field of coordination chemistry with the homobimetallic trihelicate $[\text{Mn}_2(\text{qim})_3]^{4+}$.⁷² The ligand qim is 4,4':2'',2''':4'',4'''-quaterimidazole which complexes two Mn^{II} $S = 5/2$ ions through the two α -diimine functionality pockets (Figure 1.21). Another two (qim) ligands complete the pseudo-octahedral geometry around each Mn^{II} centre resulting in two Mn^{II} ions with distinctly different g -tensors. This makes $[\text{Mn}_2(\text{qim})_3]^{4+}$ a model for an electron-spin Lloyds $(\text{ABC})_n$ qubit.⁷³ Lloyd's model of open-shell qubits in a spatially defined system is a realisation of g -engineering and in the C_3 helically symmetric system would give rise to three non-equivalent g -tensors. This model system containing only two open-shell centres in 2-fold helical symmetry gives two non-equivalent g tensors which were measured by cwEPR to give $g_1 = (2.00524, 2.00466, 2.00404)$ and $g_2 = (2.0073, 2.0041, 1.99984)$. Each centre has an isotropic $A = 251$ MHz and exhibits an immeasurably weak Mn—Mn coupling as a result of the greater than 5 Å distance between them. This was the first example of g -engineering applied to electron spin qubits and while it lacks complete evaluation in the form of relaxation studies it highlighted the versatility in coordination systems that could be used to satisfy conditions from previously only theoretical models.

Aromi *et al* conceived a multidentate ligand that has led to the development of a two-qubit lanthanide system.^{12, 74} Three of these asymmetric ligands, composed of different functional donor types, ketone, alcohol, and amine (Figure 1.21.), serendipitously leads to the formation of different sized coordination pockets that differentiate lanthanoids based on their

ionic radius. This forms the family of general formula $[\text{LnLn}'(\text{HL})_2(\text{H}_2\text{L})]^+$, for $\text{Ln} = \text{La}, \text{Ce}$, $\text{Ln}' = \text{Er}$; $\text{Ln} = \text{Ce}, \text{Ln}' = \text{Y}$; $\text{Ln} = \text{Ln}' = \text{Y}$ (where Y is not a lanthanide but exhibits remarkably similar chemical properties). Solvent molecules of water, pyridine and nitrate counterions complete the coordination sphere. The ligands ability to guide the positioning of early and late period lanthanoids gave the two-qubit system $[\text{CeEr}]$ (Figure 1.21). Both ions are in the +III oxidation state. The larger $\text{Ce}^{\text{III}} 4f^1$ ion is characterised by $J = 15/2$ and $g_J = 6/5$, while the smaller $\text{Er}^{\text{III}} 4f^{11}$ has $J = 5/2$ and $g_J = 6/7$. These Kramers ions are treated as effective spin $S = 1/2$ at low temperatures, validated by magnetic susceptibility measurements, and are described by a simple spin-doublet Hamiltonian. By pairing each with a diamagnetic ion in the adjacent site: Er with La, and Ce with Y, the electronic structure of the two spin hosts, Ce^{III} and Er^{III} , was obtained. The sum of these values then describes the magnetic properties of the $[\text{CeEr}]$ complex. In a similar manner as was experimentally demonstrated with Takui *et al.*'s nitroxyl biradical, these two effective $S = 1/2$ ions combined constitutes a two-qubit logic gate. The differing g -values allow the addressability of each individual spin site with a minute exchange coupling of $J = 0.01 \text{ cm}^{-1}$. An auspicious coherence time for f-block systems of $0.4 \mu\text{s}$ was recorded at 5 K.

1.4.Scope of Thesis

This thesis looks at electron spin qubits of intermediate organic-inorganic spin complexes. This is done via the use of radical ligands complexed to diamagnetic metal ions. In chapter 2 the focus is on group 10 bis(dithiolene)s and phosphine heteroleptics. The series **2.1a–2.3a** are the neutral diamagnetic bis(dithiolene)s of Ni, Pd, and Pt respectively with the ligand adt (anisyl dithiolene). Reduction yields the monoanionic $S = 1/2$ species **2.1b–2.3b** which are charge balanced by tetraphenylphosphonium. T_M and T_1 relaxation times are discussed with respect to the electronic structures of the complex. Excellent T_M values are recorded for the species at low temperature exceeding those of other state-of-the-art V and Cu qubits with nuclear spins removed from the system. Heteroleptic species of the adt ligand and Ni are then discussed with the monometallic species **2.5** and bimetallic **2.4** compared.

Chapter 3 utilises the same dithiolene ligand adt, this time paired with Au^{III} . The diamagnetic species is now the monoanion **3.1a**, and the radical is the neutral species **3.1b**. The key observations here are the influence of the quadrupolar nucleus of Au $I = 3/2$ on the relaxation times. Two unconventional solvents for pulsed EPR spectroscopy- carbon tetrachloride, and trichloroacetonitrile- were also investigated, alongside a 2% doping of **3.1b** into the diamagnetic **2.1a** to form a molecular semiconductor.

Chapter 4 veers from the focus on relaxation times and looks at the synthesis and isolation of multimetallic complexes with radical ligands. The bifunctional ligand dto (dithiooxalate) is used to form trimetallic species between Ni and a rare earth atom, **4.1a–4.12**. The Y and

Gd neutral complexes are reduced by cobaltocene to give the first reported isolation of the radical anion of dto. Trimetallics of Lu are synthesised with Pd and Pt to provide a greater platform to investigate the localisation of the radical in the trimetallic complex. This is all contrasted against the backdrop of the known trimetallic Sn species **4.15**, which has been shown to undergo a one-electron reduction but evades isolation, facilitating a discussion on stabilisation on the choice of capping ligand.

Table 1.2. Abbreviations List for Compounds in this Thesis.

Abbreviation	Complex
2.1a	$[\text{Ni}^{\text{II}}(\text{adt})_2]^0$
2.1b	$[\text{Ni}^{\text{II}}(\text{adt})_2][\text{PPh}_4]$
2.2a	$[\text{Pd}^{\text{II}}(\text{adt})_2]^0$
2.2b	$[\text{Pd}^{\text{II}}(\text{adt})_2][\text{PPh}_4]$
2.3a	$[\text{Pt}^{\text{II}}(\text{adt})_2]^0$
2.3b	$[\text{Pt}^{\text{II}}(\text{adt})_2][\text{PPh}_4]$
2.4	$\{[\text{Ni}^{\text{II}}(\text{adt})]_2(\text{tpbz})\}^{2+}$
2.5	$[\text{Ni}^{\text{II}}(\text{adt})(\text{dppb})]^+$
3.1a	$[\text{Au}^{\text{III}}(\text{adt})_2][\text{PPh}_4]$
3.1b	$[\text{Au}^{\text{III}}(\text{adt})_2]^0$
4.1a	$[[\text{Ni}^{\text{II}}\{(\text{dto})\text{Y}^{\text{III}}\text{Tp}_2\}_2]$
4.1b	$[[\text{Ni}^{\text{II}}\{(\text{dto})\text{Y}^{\text{III}}\text{Tp}_2\}_2][\text{CoCp}_2]$
4.2	$[[\text{Ni}^{\text{II}}\{(\text{dto})\text{Nd}^{\text{III}}\text{Tp}_2\}_2]$
4.3	$[[\text{Ni}^{\text{II}}\{(\text{dto})\text{Sm}^{\text{III}}\text{Tp}_2\}_2]$
4.4	$[[\text{Ni}^{\text{II}}\{(\text{dto})\text{Eu}^{\text{III}}\text{Tp}_2\}_2]$
4.5a	$[[\text{Ni}^{\text{II}}\{(\text{dto})\text{Gd}^{\text{III}}\text{Tp}_2\}_2]$
4.5b	$[[\text{Ni}^{\text{II}}\{(\text{dto})\text{Gd}^{\text{III}}\text{Tp}_2\}_2][\text{CoCp}_2]$
4.6	$[[\text{Ni}^{\text{II}}\{(\text{dto})\text{Tb}^{\text{III}}\text{Tp}_2\}_2]$
4.7	$[[\text{Ni}^{\text{II}}\{(\text{dto})\text{Dy}^{\text{III}}\text{Tp}_2\}_2]$
4.8	$[[\text{Ni}^{\text{II}}\{(\text{dto})\text{Ho}^{\text{III}}\text{Tp}_2\}_2]$
4.9	$[[\text{Ni}^{\text{II}}\{(\text{dto})\text{Er}^{\text{III}}\text{Tp}_2\}_2]$
4.10	$[[\text{Ni}^{\text{II}}\{(\text{dto})\text{Tm}^{\text{III}}\text{Tp}_2\}_2]$
4.11	$[[\text{Ni}^{\text{II}}\{(\text{dto})\text{Yb}^{\text{III}}\text{Tp}_2\}_2]$
4.12	$[[\text{Ni}^{\text{II}}\{(\text{dto})\text{Lu}^{\text{III}}\text{Tp}_2\}_2]$
4.13	$[[\text{Pd}^{\text{II}}\{(\text{dto})\text{Lu}^{\text{III}}\text{Tp}_2\}_2]$
4.14	$[[\text{Pt}^{\text{II}}\{(\text{dto})\text{Lu}^{\text{III}}\text{Tp}_2\}_2]$
4.15	$[[\text{Ni}^{\text{II}}\{(\text{dto})\text{Sn}^{\text{IV}}\text{Cl}_4\}_2][\text{PPh}_4]_2]$

1.5. References

- 1 Feynman, R. P., *Optics News* **1985**, 11 (2), 11-20.
- 2 Sproules, S., Molecules as electron spin qubits. In *Electron Paramagnetic Resonance: Volume 25*, The Royal Society of Chemistry: 2017; Vol. 25, pp 61-97.
- 3 Tosi, G.; Mohiyaddin, F. A.; Schmitt, V.; Tenberg, S.; Rahman, R.; Klimeck, G.; Morello, A., *Nature Communications* **2017**, 8 (1), 450.
- 4 Lühmann, T.; John, R.; Wunderlich, R.; Meijer, J.; Pezzagna, S., *Nature Communications* **2019**, 10 (1), 4956.
- 5 Hensen, B.; Wei Huang, W.; Yang, C.-H.; Wai Chan, K.; Yoneda, J.; Tantt, T.; Hudson, F. E.; Laucht, A.; Itoh, K. M.; Ladd, T. D.; Morello, A.; Dzurak, A. S., *Nature Nanotechnology* **2020**, 15 (1), 13-17.
- 6 Cory, D. G.; Fahmy, A. F.; Havel, T. F., *Proceedings of the National Academy of Sciences* **1997**, 94 (5), 1634.
- 7 Gershenfeld, N. A.; Chuang, I. L., *Science* **1997**, 275 (5298), 350.
- 8 Gaita-Ariño, A.; Luis, F.; Hill, S.; Coronado, E., *Nature Chemistry* **2019**, 11 (4), 301-309.
- 9 Bloch, F., *Physical Review* **1946**, 70 (7-8), 460-474.
- 10 DiVincenzo, D. P., *Fortschritte der Physik* **2000**, 48 (9-11), 771-783.
- 11 Atzori, M.; Chiesa, A.; Morra, E.; Chiesa, M.; Sorace, L.; Carretta, S.; Sessoli, R., *Chemical Science* **2018**, 9 (29), 6183-6192.
- 12 Luis, F.; Repollés, A.; Martínez-Pérez, M. J.; Aguilà, D.; Roubeau, O.; Zueco, D.; Alonso, P. J.; Evangelisti, M.; Camón, A.; Sesé, J.; Barrios, L. A.; Aromí, G., *Physical Review Letters* **2011**, 107 (11), 117203.
- 13 Eaton, S. S., Eaton, G. R., *Biological Magnetic Resonance* **2000**, 19, 29.
- 14 Rabi, I. I., *Physical Review* **1937**, 51, 652.
- 15 Nelson, J. N.; Zhang, J.; Zhou, J.; Rugg, B. K.; Krzyaniak, M. D.; Wasielewski, M. R., *The Journal of Physical Chemistry A* **2018**, 122 (49), 9392-9402.
- 16 Wu, Y.; Zhou, J.; Nelson, J. N.; Young, R. M.; Krzyaniak, M. D.; Wasielewski, M. R., *Journal of the American Chemical Society* **2018**, 140 (40), 13011-13021.
- 17 Ciccullo, F.; Calzolari, A.; Bader, K.; Neugebauer, P.; Gallagher, N. M.; Rajca, A.; van Slageren, J.; Casu, M. B., *ACS Applied Materials & Interfaces* **2019**, 11 (1), 1571-1578.
- 18 Lenz, S.; Kern, B.; Schneider, M.; van Slageren, J., *Chemical Communications* **2019**, 55 (50), 7163-7166.
- 19 Morton, J. J. L.; Tyryshkin, A. M.; Ardavan, A.; Porfyrakis, K.; Lyon, S. A.; Briggs, G. A. D., *The Journal of Chemical Physics* **2006**, 124 (1), 014508.

- 20 Nakazawa, S.; Nishida, S.; Ise, T.; Yoshino, T.; Mori, N.; Rahimi, R. D.; Sato, K.; Morita, Y.; Toyota, K.; Shiomi, D.; Kitagawa, M.; Hara, H.; Carl, P.; Höfer, P.; Takui, T., *Angewandte Chemie International Edition* **2012**, *51* (39), 9860-9864.
- 21 Atsumi, H.; Maekawa, K.; Nakazawa, S.; Shiomi, D.; Sato, K.; Kitagawa, M.; Takui, T.; Nakatani, K., *Chemistry – A European Journal* **2012**, *18* (1), 178-183.
- 22 Ayabe, K.; Sato, K.; Nakazawa, S.; Nishida, S.; Sugisaki, K.; Ise, T.; Morita, Y.; Toyota, K.; Shiomi, D.; Kitagawa, M.; Suzuki, S.; Okada, K.; Takui, T., *Molecular Physics* **2013**, *111* (18-19), 2767-2787.
- 23 Yamamoto, S.; Nakazawa, S.; Sugisaki, K.; Sato, K.; Toyota, K.; Shiomi, D.; Takui, T., *Physical Chemistry Chemical Physics* **2015**, *17* (4), 2742-2749.
- 24 Ueda, A.; Suzuki, S.; Yoshida, K.; Fukui, K.; Sato, K.; Takui, T.; Nakasuji, K.; Morita, Y., *Angewandte Chemie International Edition* **2013**, *52* (18), 4795-4799.
- 25 Ueda, A.; Wasa, H.; Suzuki, S.; Okada, K.; Sato, K.; Takui, T.; Morita, Y., *Angewandte Chemie International Edition* **2012**, *51* (27), 6691-6695.
- 26 Graham, M. J.; Krzyaniak, M. D.; Wasielewski, M. R.; Freedman, D. E., *Inorganic Chemistry* **2017**, *56* (14), 8106-8113.
- 27 Graham, M. J.; Yu, C.-J.; Krzyaniak, M. D.; Wasielewski, M. R.; Freedman, D. E., *Journal of the American Chemical Society* **2017**, *139* (8), 3196-3201.
- 28 Zadrozny, J. M.; Niklas, J.; Poluektov, O. G.; Freedman, D. E., *ACS Central Science* **2015**, *1* (9), 488-492.
- 29 Zadrozny, J. M.; Niklas, J.; Poluektov, O. G.; Freedman, D. E., *Journal of the American Chemical Society* **2014**, *136* (45), 15841-15844.
- 30 Fataftah, M. S.; Krzyaniak, M. D.; Vlasisavljevich, B.; Wasielewski, M. R.; Zadrozny, J. M.; Freedman, D. E., *Chemical Science* **2019**, *10* (27), 6707-6714.
- 31 Atzori, M.; Benci, S.; Morra, E.; Tesi, L.; Chiesa, M.; Torre, R.; Sorace, L.; Sessoli, R., *Inorganic Chemistry* **2018**, *57* (2), 731-740.
- 32 Graham, M. J.; Zadrozny, J. M.; Shiddiq, M.; Anderson, J. S.; Fataftah, M. S.; Hill, S.; Freedman, D. E., *Journal of the American Chemical Society* **2014**, *136* (21), 7623-7626.
- 33 Fataftah, M. S.; Zadrozny, J. M.; Coste, S. C.; Graham, M. J.; Rogers, D. M.; Freedman, D. E., *Journal of the American Chemical Society* **2016**, *138* (4), 1344-1348.
- 34 Lenz, S.; Bamberger, H.; Hallmen, P. P.; Thiebes, Y.; Otto, S.; Heinze, K.; van Slageren, J., *Physical Chemistry Chemical Physics* **2019**, *21* (13), 6976-6983.
- 35 Otto, S.; Grabolle, M.; Förster, C.; Kreitner, C.; Resch-Genger, U.; Heinze, K., *Angewandte Chemie International Edition* **2015**, *54* (39), 11572-11576.

- 36 Wang, C.; Otto, S.; Dorn, M.; Kreidt, E.; Lebon, J.; Sršan, L.; Di Martino-Fumo, P.; Gerhards, M.; Resch-Genger, U.; Seitz, M.; Heinze, K., *Angewandte Chemie International Edition* **2018**, *57* (4), 1112-1116.
- 37 Witzel, W. M.; Das Sarma, S., *Physical Review B* **2006**, *74* (3), 035322.
- 38 Pearson, T. J.; Laorenza, D. W.; Krzyaniak, M. D.; Wasielewski, M. R.; Freedman, D. E., *Dalton Transactions* **2018**, *47* (34), 11744-11748.
- 39 Pinkowicz, D.; Southerland, H. I.; Avendaño, C.; Prosvirin, A.; Sanders, C.; Wernsdorfer, W.; Pedersen, K. S.; Dreiser, J.; Clérac, R.; Nehr Korn, J.; Simeoni, G. G.; Schnegg, A.; Holldack, K.; Dunbar, K. R., *Journal of the American Chemical Society* **2015**, *137* (45), 14406-14422.
- 40 Qian, K.; Huang, X.-C.; Zhou, C.; You, X.-Z.; Wang, X.-Y.; Dunbar, K. R., *Journal of the American Chemical Society* **2013**, *135* (36), 13302-13305.
- 41 Yu, C.-J.; Graham, M. J.; Zdrozny, J. M.; Niklas, J.; Krzyaniak, M. D.; Wasielewski, M. R.; Poluektov, O. G.; Freedman, D. E., *Journal of the American Chemical Society* **2016**, *138* (44), 14678-14685.
- 42 Atzori, M.; Tesi, L.; Morra, E.; Chiesa, M.; Sorace, L.; Sessoli, R., *Journal of the American Chemical Society* **2016**, *138* (7), 2154-2157.
- 43 Bader, K.; Winkler, M.; van Slageren, J., *Chemical Communications* **2016**, *52* (18), 3623-3626.
- 44 Tesi, L.; Lucaccini, E.; Cimatti, I.; Perfetti, M.; Mannini, M.; Atzori, M.; Morra, E.; Chiesa, M.; Caneschi, A.; Sorace, L.; Sessoli, R., *Chemical Science* **2016**, *7* (3), 2074-2083.
- 45 Xu, M.-X.; Liu, Z.; Dong, B.-W.; Cui, H.-H.; Wang, Y.-X.; Su, J.; Wang, Z.; Song, Y.; Chen, X.-T.; Jiang, S.-D.; Gao, S., *Inorganic Chemistry* **2019**, *58* (4), 2330-2335.
- 46 Bader, K.; Schlindwein, S. H.; Gudat, D.; van Slageren, J., *Physical Chemistry Chemical Physics* **2017**, *19* (3), 2525-2529.
- 47 Lenz, S.; Bader, K.; Bamberger, H.; van Slageren, J., *Chemical Communications* **2017**, *53* (32), 4477-4480.
- 48 Bader, K.; Dengler, D.; Lenz, S.; Endeward, B.; Jiang, S.-D.; Neugebauer, P.; van Slageren, J., *Nature Communications* **2014**, *5* (1), 5304.
- 49 Ariciu, A.-M.; Woen, D. H.; Huh, D. N.; Nodarakı, L. E.; Kostopoulos, A. K.; Goodwin, C. A. P.; Chilton, N. F.; McInnes, E. J. L.; Winpenny, R. E. P.; Evans, W. J.; Tuna, F., *Nature Communications* **2019**, *10* (1), 3330.
- 50 Zdrozny, J. M.; Freedman, D. E., *Inorganic Chemistry* **2015**, *54* (24), 12027-12031.
- 51 Fataftah, M. S.; Zdrozny, J. M.; Rogers, D. M.; Freedman, D. E., *Inorganic Chemistry* **2014**, *53* (19), 10716-10721.
- 52 Fataftah, M. S.; Coste, S. C.; Vlaisavljevich, B.; Zdrozny, J. M.; Freedman, D. E., *Chemical Science* **2016**, *7* (9), 6160-6166.

- 53 Baldoví, J. J.; Cardona-Serra, S.; Clemente-Juan, J. M.; Coronado, E.; Gaita-Ariño, A.; Prima-García, H., *Chemical Communications* **2013**, 49 (79), 8922-8924.
- 54 AlDamen, M. A.; Clemente-Juan, J. M.; Coronado, E.; Martí-Gastaldo, C.; Gaita-Ariño, A., *Journal of the American Chemical Society* **2008**, 130 (28), 8874-8875.
- 55 Hussain, R.; Allodi, G.; Chiesa, A.; Garlatti, E.; Mitcov, D.; Konstantatos, A.; Pedersen, K. S.; De Renzi, R.; Piligkos, S.; Carretta, S., *Journal of the American Chemical Society* **2018**, 140 (31), 9814-9818.
- 56 Pedersen, K. S.; Ariciu, A.-M.; McAdams, S.; Weihe, H.; Bendix, J.; Tuna, F.; Piligkos, S., *Journal of the American Chemical Society* **2016**, 138 (18), 5801-5804.
- 57 Affronte, M.; Troiani, F.; Ghirri, A.; Carretta, S.; Santini, P.; Corradini, V.; Schuecker, R.; Muryn, C.; Timco, G.; Winpenny, R. E., *Dalton Transactions* **2006**, (23), 2810-2817.
- 58 Affronte, M.; Troiani, F.; Ghirri, A.; Carretta, S.; Santini, P.; Schuecker, R.; Timco, G.; Winpenny, R. E. P., *Journal of Magnetism and Magnetic Materials* **2007**, 310 (2, Part 2), e501-e502.
- 59 Boulon, M.-E.; Fernandez, A.; Moreno Pineda, E.; Chilton, N. F.; Timco, G.; Fielding, A. J.; Winpenny, R. E. P., *Angewandte Chemie International Edition* **2017**, 56 (14), 3876-3879.
- 60 Candini, A.; Lorusso, G.; Troiani, F.; Ghirri, A.; Carretta, S.; Santini, P.; Amoretti, G.; Muryn, C.; Tuna, F.; Timco, G.; McInnes, E. J. L.; Winpenny, R. E. P.; Wernsdorfer, W.; Affronte, M., *Physical Review Letters* **2010**, 104 (3), 037203.
- 61 Fernandez, A.; Ferrando-Soria, J.; Pineda, E. M.; Tuna, F.; Vitorica-Yrezabal, I. J.; Knappe, C.; Ujma, J.; Muryn, C. A.; Timco, G. A.; Barran, P. E.; Ardavan, A.; Winpenny, R. E. P., *Nature Communications* **2016**, 7 (1), 10240.
- 62 Fernandez, A.; Moreno Pineda, E.; Muryn, C. A.; Sproules, S.; Moro, F.; Timco, G. A.; McInnes, E. J. L.; Winpenny, R. E. P., *Angewandte Chemie International Edition* **2015**, 54 (37), 10858-10861.
- 63 Timco, G. A.; Carretta, S.; Troiani, F.; Tuna, F.; Pritchard, R. J.; Muryn, C. A.; McInnes, E. J. L.; Ghirri, A.; Candini, A.; Santini, P.; Amoretti, G.; Affronte, M.; Winpenny, R. E. P., *Nature Nanotechnology* **2009**, 4 (3), 173-178.
- 64 Wedge, C. J.; Timco, G. A.; Spielberg, E. T.; George, R. E.; Tuna, F.; Rigby, S.; McInnes, E. J. L.; Winpenny, R. E. P.; Blundell, S. J.; Ardavan, A., *Physical Review Letters* **2012**, 108 (10), 107204.
- 65 Whitehead, G. F. S.; Ferrando-Soria, J.; Carthy, L.; Pritchard, R. G.; Teat, S. J.; Timco, G. A.; Winpenny, R. E. P., *Dalton Transactions* **2016**, 45 (4), 1638-1647.
- 66 Uber, J. S.; Estrader, M.; Garcia, J.; Lloyd-Williams, P.; Sadurní, A.; Dengler, D.; van Slageren, J.; Chilton, N. F.; Roubeau, O.; Teat, S. J.; Ribas-Ariño, J.; Aromí, G., *Chemistry – A European Journal* **2017**, 23 (55), 13648-13659.

- 67 S n chal-David, K.; Zaman, N.; Walko, M.; Halza, E.; Riv re, E.; Guillot, R.; Feringa, B. L.; Boillot, M. L., *Dalton Transactions* **2008**, (14), 1932-1936.
- 68 Han, J.; Maekawa, M.; Suenaga, Y.; Ebisu, H.; Nabei, A.; Kuroda-Sowa, T.; Munakata, M., *Inorganic Chemistry* **2007**, *46* (8), 3313-3321.
- 69 Munakata, M.; Han, J.; Maekawa, M.; Suenaga, Y.; Kuroda-Sowa, T.; Nabei, A.; Ebisu, H., *Inorganica Chimica Acta* **2007**, *360* (8), 2792-2796.
- 70 Morimoto, M.; Miyasaka, H.; Yamashita, M.; Irie, M., *Journal of the American Chemical Society* **2009**, *131* (28), 9823-9835.
- 71 Pinkowicz, D.; Ren, M.; Zheng, L.-M.; Sato, S.; Hasegawa, M.; Morimoto, M.; Irie, M.; Breedlove, B. K.; Cosquer, G.; Katoh, K.; Yamashita, M., *Chemistry – A European Journal* **2014**, *20* (39), 12502-12513.
- 72 Morita, Y.; Yakiyama, Y.; Nakazawa, S.; Murata, T.; Ise, T.; Hashizume, D.; Shiomi, D.; Sato, K.; Kitagawa, M.; Nakasuji, K.; Takui, T., *Journal of the American Chemical Society* **2010**, *132* (20), 6944-6946.
- 73 Lloyd, S., *Sci. Am.* **1995**, *73*, 140.
- 74 Aguil , D.; Barrios, L. A.; Velasco, V.; Roubeau, O.; Repoll s, A.; Alonso, P. J.; Ses , J.; Teat, S. J.; Luis, F.; Arom , G., *Journal of the American Chemical Society* **2014**, *136* (40), 14215-14222.

2.Chapter 2: Group 10 Dithiolene Radical Magnetic Relaxation

2.1.Introduction

2.1.1.Innocence and Non-innocence in Coordination Compounds

The terms "innocent" and "suspect" were first used to describe ligands by Jørgensen and pertain directly to their implicitness in the oxidation state of a metal. Ligands are described as innocent when they allow oxidation states of the central atoms to be defined. Suspect ligands— also referred to as non-innocent— partake in some degree of valence transfer where the oxidation state of the system becomes ambiguous. One of the simplest non-innocent ligands is nitroxide (NO) which can be described as a cationic, neutral, or anionic ligand when bound to a metal centre. The NO ligand itself is redox active which means that it can undergo electron-transfer processes. Not all redox-active ligands are inherently non-innocent and not all non-innocent ligands are necessarily redox active. In fact, the case must be made on an individual basis and is influenced by: the identity of the coordinating metal, coordination number and geometry around the metal, any substituents on the ligand, and other ligands. It has not been uncommon to have research groups pitted against each other on the classification of ligands, the most important being the dithiolene.

2.1.2.Dithiolene Ligands

Transition metal dithiolene chemistry dates back to the 1930s, where toluene-3,4-dithiol and 1-chlorobenzene-3,4-dithiol were found to be useful as metal sequestration agents.¹⁻² However, it was another 30 years before the unique properties of dithiolene complexes were apprehended.³ The isolation of square planar bis(dithiolene) complexes of late transition metals and the formation of trigonal prismatic tris(dithiolene) coordination complexes of early transition metals in the 1960s initiated studies of transition metal dithiolene complexes, and since then the field has thrived.

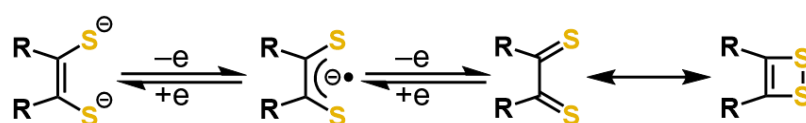


Figure 2.1. Valence bond description of the canonical dithiolene forms. One electron oxidation of the dianionic ene-1,2-dithiolate results in the formation of the monoanionic ligand radical. Further one electron oxidation results in formation of the 1,2-dithione and 1,2-dithiete resonance forms.

These compounds were first prepared by Schrauzer at Munich⁴, Davison and Holm at Harvard,⁵⁻⁶ and Gray at Columbia,⁷ and their properties explored. Focus centred on the extraordinary reversible redox properties of these complexes. Davison *et al.* first

demonstrated the two-electron difference between the neutral complex of Schrauzer *et al.*, and Gray's dianionic species; suggesting that it should be possible to oxidise the dianion to a neutral species— or reduce the neutral compound to a dianionic complex— via an intermediate monoanionic complex, and isolated several different paramagnetic monoanions; $[M(S_2C_2R_2)_2]^-$ ($M = Cu, Co, Ni, Pd, Pt, Au$; $R = CN$; $M = Ni$; $R = Ph, CF_3$).

The traditional description of metal complexes as composed of a central metal atom or ion bound to ligands with a defined electronic disposition was no longer a satisfactory model. The structure of a bis(dithiolene) complex is best described as a resonance hybrid of the limiting structures displayed in Figure 2.2.⁸

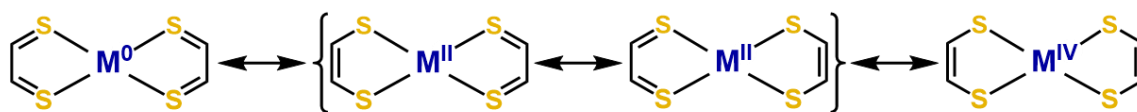


Figure 2.2. Resonance hybrid limiting structures of metallo-bis(dithiolene) complexes.

The π -orbitals of the ligand mix with metal d orbitals to give frontier molecular orbitals of mixed ligand and metal character, inducing extensive delocalisation throughout the metal dithiolene moiety which exhibits a degree of aromaticity. The name “dithiolene” is nebulously used to describe these complexes giving no bias toward any of the limiting structures. Thus, the dithiolene can be regarded as two extreme forms; the dianionic ene-1,2-dithiolate and the neutral 1,2-dithione or 1,2-dithiete form (Figure 2.2.).

The essential difference between these two established forms is the number of π -electrons in the C_2S_2 unit. This amounts to four for the neutral form and six for the dianionic form. Depending on which canonical form of the dithiolene ligand is coordinated, the metal can have a 4+, 2+ or 0 oxidation state (Figure 2.1). Two-electron oxidation of the dianionic ene-1,2-dithiolate forms the 1,2-dithione and 1,2-dithiete resonance forms.

2.1.2.1. Group 10 Homoleptic Bis Chelates

Coordination geometries, coordination numbers, and propensity for dimerization of homoleptic dithiolenes show few trends in relation to group in the early transition metals.⁹ The most structurally consistent group is that of the platinum metals; nickel, palladium, platinum, which are exclusively square planar bis chelates: an unremarkable feature for a d^8 metal ion. The identity of the metal determines covalency, electronic structure, and reactivity for these complexes but is typically outshone by the contributions from the dithiolene ligand which may produce much more pronounced changes on subtle structural variation.¹⁰

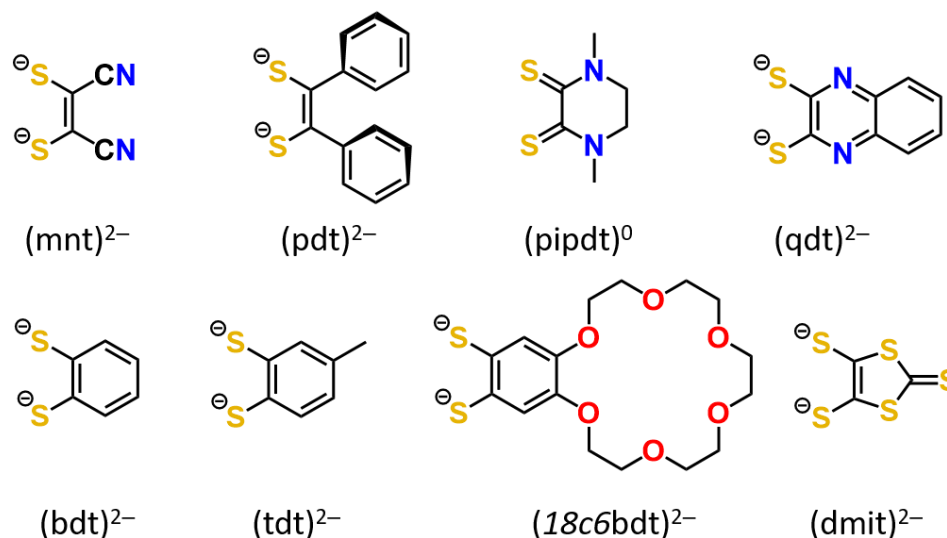


Figure 2.3. Selected dithiolene ligands.

The distinguishing feature of a dithiolene ligand is the substituent, displayed in Figure 2.3. The electronic properties of this group define the electronic structure and susceptibility to reduction and oxidation of the ligand and thus the entire complex. These broadly fall into five categories; electron withdrawing (e.g. CN and CO₂Me), electron donating by induction (e.g. alkyl and aryl substituents), electron donating (e.g. dimethylethylenediamine), aromatic (e.g. 1,2-benzene), and cyclic non-aromatic (e.g. dithiocroconate and 1,2-trithiocarbonate).

Electron withdrawing groups form weak field dithiolene ligands that have the lowest degree of covalency. These ligands are typically in the 2⁻ oxidation state at standard potential and require mild oxidation to access the radical monoanionic form of the ligand as discovered by Davison et al. The electron withdrawing or donating ability of the group is directly manifested in the reduction potential $E_{1/2}$ between members of the electron transfer series. [Ni(mnt)₂] has $E_{1/2} = -0.14$ V vs Fc^{0/+} for the 2⁻ → 1⁻ oxidation, the lowest reduction potential for the dianion to monoanion electron transfer for all bis(dithiolene)s. In fact, it may even be reduced to the trianion [Ni^I(mnt)₂]³⁻ at $E_{1/2} = -1.97$ V vs Fc^{0/+}. As each of the (mnt)²⁻ ligands are in their fully reduced forms the complex is described best with a formal Ni^I oxidation state, corroborated with a g value of 2.116. Oxidation to the neutral species [Ni^{II}(mnt⁻)₂]⁰ occurs at a difficult $E_{1/2} = +0.82$ V vs Fc^{0/+}.

Table 2.1. Reduction Potentials for Selected Group 10 Homoleptic Bis(dithiolene) Complexes.

Complex	S₂C₂R₁R₂	Medium	Redox events (V vs Fc^{0/+})	Ref
[Ni ^{II} (mnt) ₂]	CN	1.0 mM in 0.1 M NaClO ₄ MeCN	-1.94 -0.14 +0.82	11
[Pd ^{II} (mnt) ₂]	CN	1.0 mM in 0.1 M NaClO ₄ MeCN	-2.17 +0.04 +0.48	11
[Pt ^{II} (mnt) ₂]	CN	1.0 mM in 0.1 M NaClO ₄ MeCN	-2.68 -0.16 +0.72	11
[Ni ^{II} (pdt) ₂]	Ph	1.0 mM in 0.1 M <i>n</i> Bu ₄ NPF ₆ CH ₂ Cl ₂	-1.26 -0.34 +0.69	12
[Pd ^{II} (pdt) ₂]	Ph	1.0 mM in 0.1 M <i>n</i> Bu ₄ NPF ₆ CH ₂ Cl ₂	-1.07 -0.37 +0.71	12
[Pt ^{II} (pdt) ₂]	Ph	1.0 mM in 0.1 M <i>n</i> Bu ₄ NPF ₆ CH ₂ Cl ₂	-1.26 -0.38 +0.74	12
[Ni ^{II} (pipdt) ₂]	—N(Me)C ₂ H ₄ N(Me)—	1.0 mM in 0.1 M <i>n</i> Bu ₄ NClO ₄ MeCN	-1.45 -1.14 -0.58 -0.29	13

Complex	S ₂ C ₂ R ₁ R ₂	Medium	Redox events (V vs Fc ^{0/+})	Ref
[Ni ^{II} (bdt) ₂]	—C ₆ H ₄ —	1.0 mM in 0.1 M <i>n</i> Bu ₄ NPF ₆ DMF	-0.95 -0.03 —	14
[Ni ^{II} (tdt) ₂]	—C ₆ H ₃ (Me)—	1.0 mM in 0.1 M <i>n</i> Et ₄ NPF ₆ MeCN	-0.87 +0.04	14
[Ni ^{II} (15c5-bdt) ₂]	—C ₆ H ₂ (15c5)—	1.0 mM in 0.2 M <i>n</i> Bu ₄ NBF ₄ MeCN	-1.07 -0.27 —	15
		1.0 mM in 0.2 M LiClO ₄ MeCN	— -0.29 —	15
		1.0 mM in 0.2 M NaClO ₄ MeCN	-1.07 -0.24 —	15
		1.0 mM in 0.2 M KBF ₄ MeCN	-1.11 -0.31 —	15
[Ni ^{II} (qdt) ₂]	—NC ₆ H ₄ N—	1.0 mM in 0.1 M <i>n</i> Et ₄ NClO ₄ DMF	-0.28 — —	16
[Ni ^{II} (dmit) ₂]	—S(C=S)S—	1.0 mM in 0.1 M <i>n</i> Bu ₄ NClO ₄ MeCN	-0.53 +0.11 ^{irr} —	17

The dithiolenes discovered in parallel by Schrauzer et al. have substituents that are electron donating by induction. These ligands show a much higher degree of covalency than their electron withdrawing counterparts reflected in their reduction potentials, with the phenyl substituted $[\text{Ni}^{\text{II}}(\text{pdt}^-)_2]^0$ reducing at $E_{1/2} = -0.34 \text{ V vs Fc}^{0/+}$, and are synthesized in air to give the radical monoanionic form of the dithiolene in neutral complexes that are almost black in colour. This intensity comes from an intraligand valence transfer that is now spin allowed within the complex due to the half-populated HOMO b_{2g} orbital. The valence form of these complexes form the electron transfer series $[\text{M}^{\text{I}}(\text{L}^{2-})_2]^{3-} \rightleftharpoons [\text{M}^{\text{II}}(\text{L}^{2-})_2]^{2-} \rightleftharpoons [\text{M}^{\text{II}}(\text{L}^{2-})(\text{L}^{\cdot-})]^- \rightleftharpoons [\text{M}^{\text{II}}(\text{L}^{\cdot-})_2]^0$ with $S = 0$, $S = 1/2$ and $S = 0$ respectively. The diamagnetism of the diradical stems from the incredibly strong exchange interaction between both radical ligands which has been experimentally verified in isovalent bis(iminosemiquinone)s to be 2400 cm^{-1} , 1800 cm^{-1} and over 2800 cm^{-1} for Ni, Pd, and Pt respectively.¹⁸

Electron donating groups follow suit and form neutral dithione type dithiolene ligands. Tacking on to the end of the established electron series $[\text{M}^{\text{I}}(\text{L}^{2-})_2]^{3-} \rightleftharpoons [\text{M}^{\text{II}}(\text{L}^{2-})_2]^{2-} \rightleftharpoons [\text{M}^{\text{II}}(\text{L}^{2-})(\text{L}^{\cdot-})]^- \rightleftharpoons [\text{M}^{\text{II}}(\text{L}^{\cdot-})_2]^0 \rightleftharpoons [\text{M}^{\text{II}}(\text{L}^0)(\text{L}^{\cdot-})]^+ \rightleftharpoons [\text{M}^{\text{II}}(\text{L}^0)_2]^{2+}$ with $S = 1/2$, 0 , $1/2$, 0 , $1/2$ and 0 respectively. Donating groups incorporated into dithiolene ligands are rare with derivatives of $(\text{pipdt})^0$ being the sole members of this class, the complex $[\text{Ni}^{\text{II}}(\text{pipdt})_2]^{2+}$ is unique in its ability to undergo four consecutive reductions to $[\text{Ni}^{\text{II}}(\text{pipdt})_2]^{2-}$ which is the greatest number of electron transfer series members to be achievable within accessible electrochemical windows (Table 2.1.).

Aromatic dithiolene ligands encompass mostly 1,2-dithiobenzene derivatives with some nitrogen or sulfur containing heterocycles such as quinoxalinedithiolate or thiophene. These ligands favour the 2- and 1- oxidation states and are influenced by the secondary substitution around the aromatic ring, and identity and position of any hetero atoms. This is exemplified by the crown ether containing benzenedithiolate derivative $[\text{Ni}^{\text{II}}(\text{pipdt})_2]^{2-}$ which experiences mild perturbation of its reduction potentials depending on the identity of the ion complexed by the crown ether moiety.

The final cyclic non-aromatic ligands behave somewhat anomalously to the conventional dithiolenes, for example the ligand $(\text{dmit})^{2-}$ binds iron and cobalt in a D_{2d} distorted tetrahedral arrangement rather than the conventional square pyramidal dimers FeS_4C_4 and CoS_4C_4 species form. For group 10 metals there is no structural variation with the d^8 square planar arrangement prevailing but there is anomalous redox behavior. $[\text{Ni}(\text{dmit})_2]^{2-}$ and $[\text{Ni}(\text{dmit})_2]^-$ regularly form composite mixtures on oxidation from the dianion despite the use of an oxidant that should result in pure monoanion, and oxidation to the neutral species does not show reversible behavior in solution. Other ligands of this class exhibit similar difficulties in oxidation to the monoanionic and neutral complexes.

Reactivity of these complexes may occur on either the dithiolene ligand or the metal centre.¹⁹⁻²⁰ The former is out-with the scope of this thesis and only a brief discussion of ligand substitution is present here. Two factors dictate ligand metathesis from group 10 bis(dithiolenes); the charge of the dithiolene ligand and the identity of the metal. Bis(dithiolenes) of the form $[M^{II}(L^{2-})_2]^{2-}$ can undergo ligand scrambling with neutral group 10 bis(dithiocarbamates) to give dimeric $[[M^{II}(dtc)(L^{2-})]_2]^{2-}$ with five coordinate square pyramidal geometry around the metal centre. The negative charge on the fully reduced dithiolene ligand allows the ligand to act as the apical ligand of the paired heteroleptic complex. By far more common is the introduction of a sigma donating ligand. The smaller Ni^{II} metal ion can undergo substitution of one dithiolene ligand by an incoming sigma donating ligand such as an isonitrile, sterically unencumbered phosphine, or bipyridine derivative. The results of these reactions are, with one exception, all neutral four-coordinate square planar heteroleptic complexes of the type $[Ni(PR_3)(L^{2-})]^{0}$ where the dithiolene ligand is in its fully reduced form. The larger Pd^{II} and Pt^{II} ions can facilitate more sterically encumbered phosphines into their coordination sphere and can also undergo a two-electron oxidation to Pd^{IV} and Pt^{IV} and adopt a six-coordinate octahedral coordination geometry. However, the most common arrangement is still square planar for both metals. One of the most studied classes of this compound are platinum dithiolate alpha(diimines) owing to their strong interligand charge transfer. These complexes are known for their non-linear optical properties. Only phosphine species will be discussed from here on out.

2.1.2.2. Heteroleptic Chelates with Phosphines

Phosphine ligands are ubiquitous in coordination and organometallic chemistry. They are most often encountered in their simplest form PR_3 where R is an alkyl, aryl, alkoxide or phenoxide. The phosphine being second of the pnictogens and 3+ oxidation state adopts the same trigonal pyramidal structure as ammonia, a lone pair occupying the apical position. In the spectroelectrochemical series phosphines are among the strongest of the strong field ligands, comparable to cyanide and carbon monoxide. In a molecular orbital theory setting phosphines are best described as strong sigma donors. It is commonly taught that they also possess the ability to participate in π -backbonding due to an empty 4d orbital set, however, this set is rather high in energy and alternative explanations— such as the formation of three-centered two-electron bonds— run amok in the literature. Conveniently none of this actually matters and the explanation that phosphines are simply very good neutral sigma donors suffices for anything we will be using them for as, π -backbonding or not, phosphines are innocent, typically redox inert ligands, and thus will not facilitate the passing of charge.

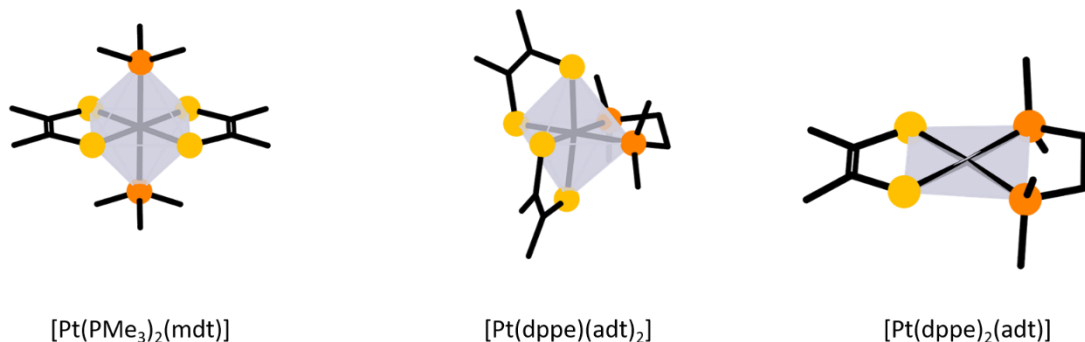


Figure 2.4. Depiction of the octahedral geometry of platinum bis(dithiolene) complexes on addition of monodentate and bidentate phosphine ligands and the thermodynamic sink, the squareplanar heteroleptic.

Phosphine ligated group 10 dithiolene complexes are the earliest examples of heteroleptic dithiolene chelates, being synthesized by Schrauzer et al in 1960. Schrauzer et al had intended for the triaryl phosphine to scavenge the metal and sulfur from the complex to yield a route to substituted thiophenes. However, the strongly sigma-donating properties of the phosphine outshone their propensity to oxidatively eliminate sulfur giving the sparingly characterized series $[\text{Pt}^{\text{IV}}(\text{pdt})_2(\text{PPh}_3)_2]$ where $(\text{pdt})^{2-}$ is the ligand diphenyldithiolate. While numerous other phosphine heteroleptics were synthesized since then Schrauzer et al's complex remained uninvestigated till 2014 when the Donahue group produced the platinum and palladium analogues of Schrauzer along with a clarification on the heteroleptic complexes possible.²¹ Examining the reaction of $[\text{Pt}^{\text{II}}(\text{adt})_2]^0$ with a stoichiometric amount of phosphines; PPh_3 , $(\text{dppe})^0$ and $(\text{dppb})^0$ Donahue et al isolated the uncharacterized compounds of Schrauzer and clarified the mechanism of ligand metathesis. The ligation of two phosphorous to form a six-membered complex is accompanied with a simultaneous oxidation from Pt^{II} to Pt^{IV} and reduction of both ligands from their radical anionic form to their dianionic form. If the ligating phosphorous atoms belong to two discrete species, as is the case with PPh_3 , the phosphines adopt a trans-conformation in the octahedral complex. Use of the structurally fused phosphines in $(\text{dppb})^0$ results in the adoption of the cis-conformer. Further reaction at room temperature or above results in the elimination of one of the dithiolenes concomitant with the reduction of Pt^{IV} to Pt^{II} and yields the most encountered square planar form of a heteroleptic phosphine dithiolene $[\text{Pt}^{\text{II}}(\text{adt})(\text{dppb})]$.

Table 2.2. Reduction Potentials for Selected Heteroleptic Group 10 Dithiolene Phosphine Complexes.

Complex	$PR_1R_2R_3$	Ring size	P—M—P	Medium	$E_{1/2}^{1^{st} red}$	$E_{1/2}^{1^{st} ox}$	$E_{1/2}^{2^{nd} ox}$	Ref
[Ni ^{II} (dppa-e)(mnt)]	<i>Ph, Ph, —</i>	4	73.45	1.0 mM in 0.1 M <i>n</i> Bu ₄ NPF ₆ MeCN	-1.54	+0.60	—	22
[Ni ^{II} (dppa-e)(bdt)]	<i>Ph, Ph, —</i>	4	73.80	1.0 mM in 0.1 M <i>n</i> Bu ₄ NPF ₆ CH ₂ Cl ₂	-2.13	+0.20	—	23
[Ni ^{II} (dppa-e)(tdt)]	<i>Ph, Ph, —</i>	4	—	1.0 mM in 0.1 M <i>n</i> Bu ₄ NPF ₆ CH ₂ Cl ₂	-2.13	+0.28	—	23
[Ni ^{II} (dppb)(adt)]	<i>Ph, Ph, —</i>	5	88.92	1.0 mM in 0.1 M <i>n</i> Bu ₄ NPF ₆ CH ₂ Cl ₂ ^a	—	-0.15	+0.44	24
[Pd ^{II} (dppb)(adt)]	<i>Ph, Ph, —</i>	5	86.032	1.0 mM in 0.1 M <i>n</i> Bu ₄ NPF ₆ CH ₂ Cl ₂ ^a	—	-0.20	+0.40	24
[Pt ^{II} (dppb)(adt)]	<i>Ph, Ph, —</i>	5	—	1.0 mM in 0.1 M <i>n</i> Bu ₄ NPF ₆ CH ₂ Cl ₂ ^a	—	-0.10	+0.53	24
[Pt ^{II} (PMe ₃) ₂ (adt) ₂]	<i>Me, Me, Me</i>	—	179.437	1.0 mM in 0.1 M <i>n</i> Bu ₄ NPF ₆ CH ₂ Cl ₂	-0.08	+0.40	—	21
[Pt ^{II} (dppe)(adt) ₂]	<i>Ph, Ph, —</i>	5	86.41	1.0 mM in 0.1 M <i>n</i> Bu ₄ NPF ₆ CH ₂ Cl ₂	+0.13	+0.58	—	21

Complex	$PR_1R_2R_3$	Ring size	P—M—P	Medium	$E_{1/2}^{1^{st} red}$ $E_{1/2}^{1^{st} ox}$ $E_{1/2}^{2^{nd} ox}$	Ref
[Pt ^{II} (dppe)(adt)]	<i>Ph, Ph, —</i>	5	86.18	1.0 mM in 0.1 M <i>n</i> Bu ₄ NPF ₆ CH ₂ Cl ₂	-0.01 +0.61 —	21
[Ni ^{II} (dppe)(mnt)]	<i>Ph, Ph, —</i>	5		1.0 mM in 0.1 M <i>n</i> Bu ₄ NPF ₆ CH ₂ Cl ₂	-1.20 — —	25
[Ni ^{II} (dppm)(mnt)]	<i>Ph, Ph, —</i>	5		1.0 mM in 0.1 M <i>n</i> Bu ₄ NPF ₆ CH ₂ Cl ₂	-1.08 — —	25
[Ni ^{II} (dppb)(mnt)]	<i>Ph, Ph, —</i>	5		1.0 mM in 0.1 M <i>n</i> Bu ₄ NPF ₆ CH ₂ Cl ₂	-1.06 — —	24
[Ni ^{II} (dppe)(dmobdt)]	<i>Ph, Ph, —</i>	5		1.0 mM in 0.2 M <i>n</i> Bu ₄ NBF ₄ MeCN	-1.94 +0.09 —	15
				1.0 mM in 0.2 M LiClO ₄ MeCN	-2.07 -0.05 —	15
				1.0 mM in 0.2 M NaClO ₄ MeCN	-2.06 -0.06 —	15
				1.0 mM in 0.2 M KBF ₄ MeCN	-2.03 -0.01 —	15

Complex	$PR_1R_2R_3$	Ring size	P—M—P	Medium	$E_{1/2}^{red}$ $E_{1/2}^{1^{st} ox}$ $E_{1/2}^{2^{nd} ox}$	Ref
[Ni ^{II} (dppe)(15c5-bdt)]	<i>Ph, Ph, —</i>	5		1.0 mM in 0.2 M <i>n</i> Bu ₄ NBF ₄ MeCN	-1.94 +0.13 —	15
				1.0 mM in 0.2 M LiClO ₄ MeCN	-2.05 +0.05 —	15
				1.0 mM in 0.2 M NaClO ₄ MeCN	-2.03 +0.04 —	15
	<i>Ph, Ph, —</i>	5		1.0 mM in 0.2 M KBF ₄ MeCN	-2.03 +0.07 —	15
[Ni ^{II} (dppee)(mnt)]	<i>Ph, Ph, —</i>	5		1.0 mM in 0.1 M <i>n</i> Bu ₄ NPF ₆ CH ₂ Cl ₂ ^d	-1.07 — —	26
[Ni ^{II} (dpmppb)(mnt)]	<i>Ph, Ph, —; Me, Ph, —</i>	5		1.0 mM in 0.1 M <i>n</i> Bu ₄ NPF ₆ CH ₂ Cl ₂ ^d	-1.16 — —	26
[Ni ^{II} (mppb)(mnt)]	<i>Me, Ph, —</i>	5		1.0 mM in 0.1 M <i>n</i> Bu ₄ NPF ₆ CH ₂ Cl ₂ ^d	-1.23 — —	26
[Ni ^{II} (bpdppb)(mnt)]	<i>Ph, Ph, —; nBu, Ph, —</i>	5		1.0 mM in 0.1 M <i>n</i> Bu ₄ NPF ₆ CH ₂ Cl ₂ ^d	-1.22 — —	26

Complex	$PR_1R_2R_3$	Ring size	P—M—P	Medium	$E_{1/2}^{red}$	$E_{1/2}^{1^{st} ox}$	$E_{1/2}^{2^{nd} ox}$	Ref
[Ni ^{II} (dppee)(pdt)]	<i>Ph, Ph, —</i>	5		1.0 mM in 0.1 M <i>n</i> Bu ₄ NPF ₆ CH ₂ Cl ₂ ^d	-1.79	—	—	26
[Ni ^{II} (dpmppb)(pdt)]	<i>Ph, Ph, —; Me, Ph, —</i>	5		1.0 mM in 0.1 M <i>n</i> Bu ₄ NPF ₆ CH ₂ Cl ₂ ^d	-1.66	—	—	26
[Ni ^{II} (mppb)(pdt)]	<i>Me, Ph, —</i>	5		1.0 mM in 0.1 M <i>n</i> Bu ₄ NPF ₆ CH ₂ Cl ₂ ^d	-1.74	—	—	26
[Ni ^{II} (bpdppb)(pdt)]	<i>Ph, Ph, —; nBu, Ph, —</i>	5		1.0 mM in 0.1 M <i>n</i> Bu ₄ NPF ₆ CH ₂ Cl ₂ ^d	-1.73	—	—	26
[Ni ^{II} (dmdppb)(pdt)]	<i>Me, Me, —;</i> <i>Ph, Ph, —</i>	5		1.0 mM in 0.1 M <i>n</i> Bu ₄ NPF ₆ CH ₂ Cl ₂ ^d	-1.34	—	—	26
[Ni ^{II} (PPh ₃) ₂ (mnt)]	<i>Ph, Ph, Ph</i>	—		1.0 mM in 0.1 M <i>n</i> Bu ₄ NPF ₆ CH ₂ Cl ₂	-0.74	—	—	26
[Ni ^{II} (PMePh ₂) ₂ (mnt)]	<i>Me, Ph, Ph</i>	—		1.0 mM in 0.1 M <i>n</i> Bu ₄ NPF ₆ CH ₂ Cl ₂	-0.93	—	—	26
[Ni ^{II} (P <i>n</i> BuPh ₂) ₂ (mnt)]	<i>nBu, Ph, Ph</i>	—		1.0 mM in 0.1 M <i>n</i> Bu ₄ NPF ₆ CH ₂ Cl ₂	-0.82	—	—	26

Complex	$PR_1R_2R_3$	Ring size	P—M—P	Medium	$E_{1/2}$ 1 st red $E_{1/2}$ 1 st ox $E_{1/2}$ 2 nd ox	Ref
[{Ni ^{II} (mnt)} ₂ (μ-tpbz)]	<i>Ph, Ph, —</i>	5	88.59		— — —	24
[{Ni ^{II} (mdt)} ₂ (μ-tpbz)]	<i>Ph, Ph, —</i>	5	88.48	1.0 mM in 0.1 M <i>n</i> Bu ₄ NPF ₆ CH ₂ Cl ₂ ^a	-2.10 -0.03 +0.61	24
[{Pd ^{II} (mdt)} ₂ (μ-tpbz)]	<i>Ph, Ph, —</i>	5	87.17	1.0 mM in 0.1 M <i>n</i> Bu ₄ NPF ₆ CH ₂ Cl ₂ ^a	-1.99 -0.10 +0.68	24
[{Pt ^{II} (mdt)} ₂ (μ-tpbz)]	<i>Ph, Ph, —</i>	5	86.76	1.0 mM in 0.1 M <i>n</i> Bu ₄ NPF ₆ CH ₂ Cl ₂ ^a	-2.07 -0.04 +0.75	24
[{Ni ^{II} (pdt)} ₂ (μ-tpbz)]	<i>Ph, Ph, —</i>	5	89.12	1.0 mM in 0.1 M <i>n</i> Bu ₄ NPF ₆ CH ₂ Cl ₂ ^a	-2.02 +0.07 +0.66	24
[Pd ^{II} (pdt)} ₂ (μ-tpbz)]	<i>Ph, Ph, —</i>	5	85.82	1.0 mM in 0.1 M <i>n</i> Bu ₄ NPF ₆ CH ₂ Cl ₂ ^a	-1.96 +0.02 +0.73	24
[Pt ^{II} (pdt)} ₂ (μ-tpbz)]	<i>Ph, Ph, —</i>	5	87.30	1.0 mM in 0.1 M <i>n</i> Bu ₄ NPF ₆ CH ₂ Cl ₂ ^a	-2.05 -0.04 +0.49	24

Complex	$PR_1R_2R_3$	Ring size	P—M—P	Medium	$E_{1/2}$ 1 st red $E_{1/2}$ 1 st ox $E_{1/2}$ 2 nd ox	Ref
[{Ni ^{II} (adt)} ₂ (μ -tpbz)]	<i>Ph, Ph, —</i>	5	89.17	1.0 mM in 0.1 M <i>n</i> Bu ₄ NPF ₆ CH ₂ Cl ₂ ^a	-2.05 -0.04 +0.49	24
[Pd ^{II} (adt)} ₂ (μ -tpbz)]	<i>Ph, Ph, —</i>	5	85.23	1.0 mM in 0.1 M <i>n</i> Bu ₄ NPF ₆ CH ₂ Cl ₂ ^a	-1.97 -0.04 +0.50	24
[Pt ^{II} (adt)} ₂ (μ -tpbz)]	<i>Ph, Ph, —</i>	5	84.52	1.0 mM in 0.1 M <i>n</i> Bu ₄ NPF ₆ CH ₂ Cl ₂ ^a	-2.09 -0.02 +0.53	24
[{Ni ^{II} (dppe)} ₃ (hbdt)]	<i>Ph, Ph, —</i>	5		1.0 mM in 0.1 M <i>n</i> Bu ₄ NPF ₆ CH ₂ Cl ₂ ^a	-0.50 +0.03 —	27
[{Ni ^{II} (dppe)} ₂ (tti)]	<i>Ph, Ph, —</i>	5	87.07	1.0 mM in 0.01 M Na(BArF ₂₄) 5:4:1 CH ₂ Cl ₂ :anisole:THF	— -0.44 +0.25	28
[{Ni ^{II} (dppee)} ₂ (tti)]	<i>Ph, Ph, —</i>	5	87.50	1.0 mM in 0.01 M Na(BArF ₂₄) 5:4:1 CH ₂ Cl ₂ :anisole:THF	— -0.34 —	28
[{Ni ^{II} (dppb)} ₂ (tti)]	<i>Ph, Ph, —</i>	5	88.45	1.0 mM in 0.01 M Na(BArF ₂₄) 5:4:1 CH ₂ Cl ₂ :anisole:THF	— -0.37 +0.38	28
[{Ni ^{II} (dcpe)} ₂ (tti)]	<i>Ph, Ph, —</i>	5	87.73	1.0 mM in 0.01 M Na(BArF ₂₄) 5:4:1 CH ₂ Cl ₂ :anisole:THF	— -0.51 +0.21	28

Complex	$PR_1R_2R_3$	Ring size	P—M—P	Medium	$E_{1/2}$ 1 st red	$E_{1/2}$ 1 st ox	$E_{1/2}$ 2 nd ox	Ref
[{Pd ^{II} (bdt)} ₂ (dppac) ₂]	<i>Ph, Ph, —</i>	10	95.12	1.0 mM in 0.1 M <i>n</i> Bu ₄ NPF ₆ CH ₂ Cl ₂	—	+0.296	+0.404	29
[{Pd ^{II} (tdt)} ₂ (dppac) ₂]	<i>Ph, Ph, —</i>	10	95.16	1.0 mM in 0.1 M <i>n</i> Bu ₄ NPF ₆ CH ₂ Cl ₂	—	+0.285	+0.343	29
[{Pd ^{II} (docbdt)} ₂ (dppac) ₂]	<i>Ph, Ph, —</i>	10	96.78	1.0 mM in 0.1 M <i>n</i> Bu ₄ NPF ₆ CH ₂ Cl ₂	—	+0.455	+0.684	29
[{Pt ^{II} (bdt)} ₂ (dppac) ₂]	<i>Ph, Ph, —</i>	10	94.18	1.0 mM in 0.1 M <i>n</i> Bu ₄ NPF ₆ CH ₂ Cl ₂	—	+0.386	+0.56	29
[{Pt ^{II} (tdt)} ₂ (dppac) ₂]	<i>Ph, Ph, —</i>	10	95.39	1.0 mM in 0.1 M <i>n</i> Bu ₄ NPF ₆ CH ₂ Cl ₂	—	+0.359	+0.517	29
[{Pt ^{II} (docbdt)} ₂ (dppac) ₂]	<i>Ph, Ph, —</i>	10	97.34	1.0 mM in 0.1 M <i>n</i> Bu ₄ NPF ₆ CH ₂ Cl ₂	—	+0.543	+0.793	29
[{Pt ^{II} (dddtd)} ₂ (dppac) ₂]	<i>Ph, Ph, —</i>	10		1.0 mM in 0.1 M <i>n</i> Bu ₄ NBF ₄ CH ₂ Cl ₂ ^a	—	+0.33(2e)	—	30
[{Pt ^{II} (dtmdt)} ₂ (dppac) ₂]	<i>Ph, Ph, —</i>	10		1.0 mM in 0.1 M <i>n</i> Bu ₄ NBF ₄ CH ₂ Cl ₂ ^a	—	+0.33(2e)	—	30

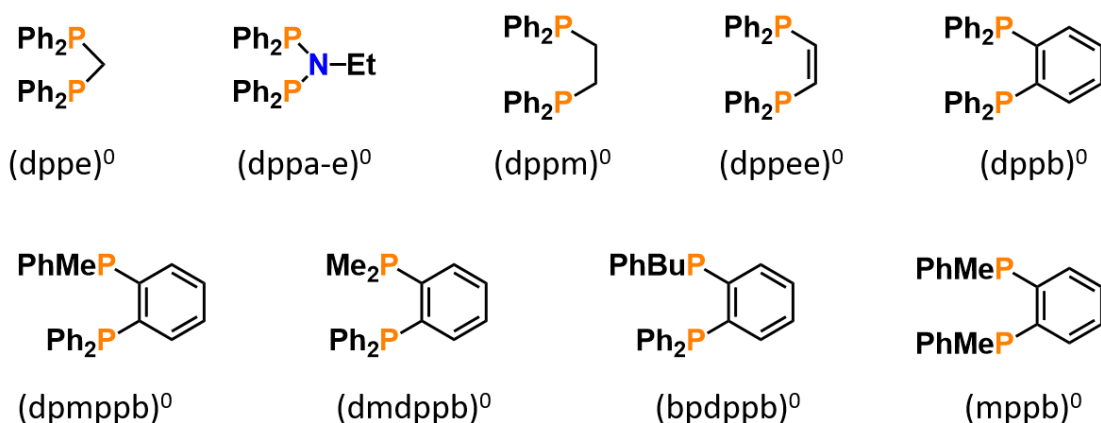


Figure 2.5. Selected phosphine ligands.

The most abundant class of phosphine ligated group 10 dithiolene complexes are the four-coordinate square planar structures. As synthesized these complexes are neutral charge with two neutral phosphorus donor atoms and a dianionic dithiolene ligand. The metal (if nickel) may be reduced once and the dithiolene ligand may be oxidized twice to form the electron transfer series $[M^I(L^{2-})(P-P)]^- \rightleftharpoons [M^{II}(L^{2-})(P-P)]^0 \rightleftharpoons [M^{II}(L^-)(P-P)]^+ \rightleftharpoons [M^{II}(L^0)(P-P)]^{2+}$. The dependence on the substituents of the dithiolene ligand are still the principle factor in determining the reduction potential as illustrated by the complexes $[Ni(dppb)(mnt)]$ and $[Ni(dppb)(mdt)]$ where $(dppb)^0$ is the ligand 1,2-bis(diphenylphosphino)benzene with 0/+ couples of $E_{1/2} = -1.43$ V and -0.20 V vs ferrocene (Fc) respectively. The contribution from the phosphine is slightly more subtle. Olefinic phosphines have been shown to stabilize higher oxidation states of coordinated metals in homoleptic complexes and heteroleptic phosphine-halide complexes. However, there is no experimental verification of this effect in heteroleptic phosphine-dithiolene complexes; only the observation that olefinic phosphines facilitate milder reduction to the Ni^I species (Table 2.2.).

Phosphine ligands are commonly found as bidentate chelates being joined by an alkyl or aryl group such as 1,2-bis(diphenylphosphino)ethane $(dppe)^0$, and $(dppb)^0$. When complexed these structures form a five-membered ring metallocycle which offers great stability.²⁴ Homologues of $(dppe)^0$ such as 1,2-bis(diphenylphosphino)methane $(dppm)^0$ and 1,2-bis(diphenylphosphino)propane $(dppp)^0$ give four-membered and six-membered metallocycles respectively. These ring structures enforce the direction of the lone pairs on phosphorus and enforce ligand bite angles. The four membered metallocycle formed by $(dppm)^0$ facilitates an easier reduction to the Ni^I species than the corresponding saturated five and six-membered homologous (Table 2.2.).

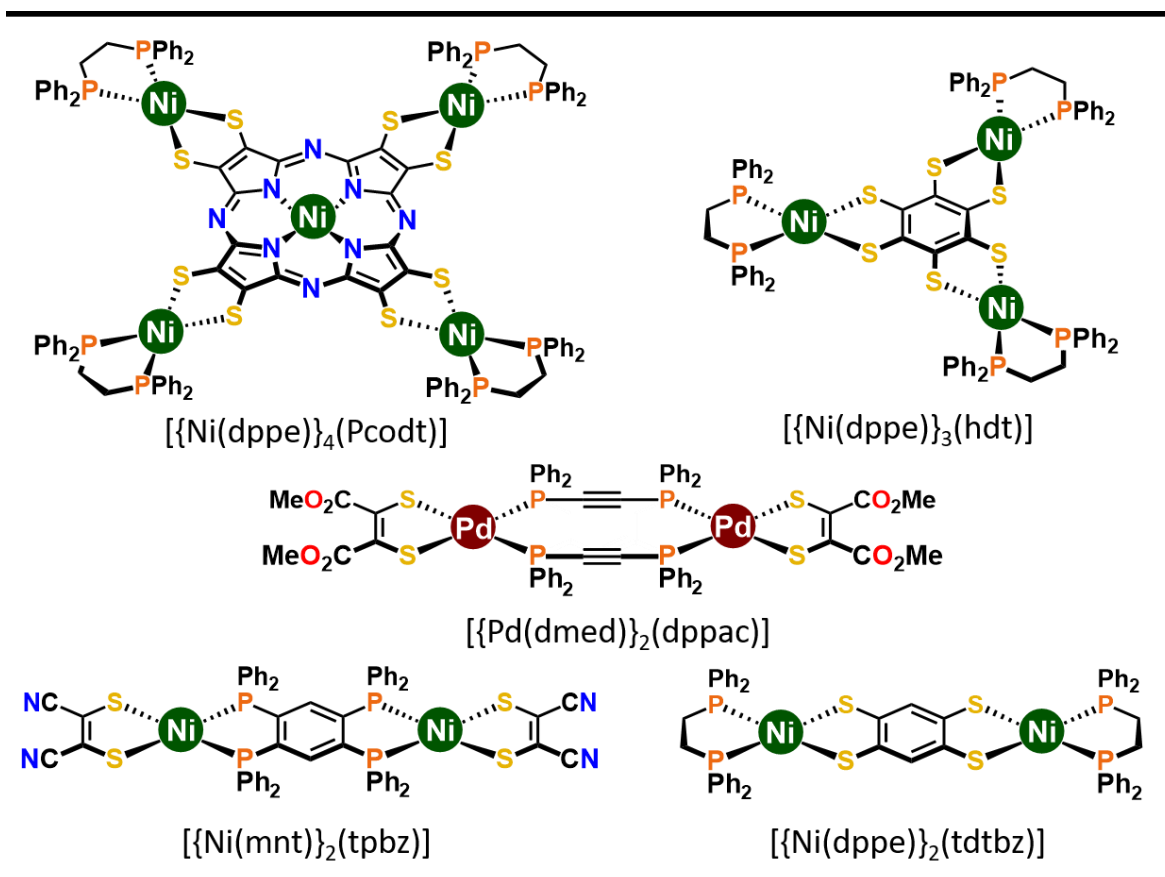


Figure 2.6. Selected multimetallic phosphine dithiolene containing heteroleptics.

The customizability of both phosphine and dithiolene ligands has resulted in the inception of many multimetallic systems. These can be separated into two categories; those with bridging dithiolenes and those with bridging phosphines. The ligand $(\text{tti})^{4-}$ (1,2,4,5-tetrathiobenzene) conjoins two Ni bis(phosphine) moieties to form a series of centrosymmetric complexes of the form $[\{\text{Ni}^{\text{II}}(\text{P}-\text{P})\}_2(\text{tti})]$. The phosphines $(\text{dppe})^0$, $(\text{dppb})^0$, and $(\text{dcpe})^0$, where dcpe is bis(dicyclohexylphosphino)ethane, provide reduction potentials for $0 \rightarrow 1+$ in the range -0.51 to -0.37 V and for $1+ \rightarrow 2+$ between $+0.21$ and $+0.38$ V. This comfortably establishes the complex as the radical monocationic form at 0 V with mild reduction or oxidation to the diamagnetic neutral and dicationic forms. Further substitution of the benzene ring with sulfur yields the hexathiobenzene ligand $(\text{hbdt})^{6-}$. This has been incorporated into the trimetallic complex $[\{\text{Ni}^{\text{II}}(\text{dppe})\}_3(\text{hbdt})]$ which can similarly be oxidised to access the radical ligand form.

Far more common is the use of a phosphine as a bridging ligand. The four donor atom ligand $(\text{tpbz})^0$, 1,2,4,5-tetra(diphenylphosphino)benzene, and the two donor atom ligand $(\text{dppac})^0$, bis(diphenylphosphino)acetylene, comprise the majority of bimetallic phosphine bridged structures with either one bridging moiety in the case of $(\text{tpbz})^0$ and two for $(\text{dppac})^0$. Simultaneous reversible or quasireversible electron transfer oxidation processes occur for complexes of $(\text{tpbz})^0$. These two electron processes are the oxidation of the two dithiolene

ligands. The proximity and overall charge dictate that these oxidations occur simultaneously opposed to sequentially.

2.1.3. Scope of Chapter

Compounds of interest **2.1** – **2.3** were synthesized in high yield via one-electron reduction of the parent neutral complexes using PPh_4BH_4 . To expand the utility of the radical ligand as a spin host, we have developed a series of heteroleptic metallodithiolene complexes as a platform for implementing two-qubit quantum gates.³¹⁻³⁴ The central design strategy involves $\{\text{MS}_2\text{P}_2\}$ building blocks where the metal is coordinated by a redox-active dithiolene ligand on one side and a redox-inert diphosphine ligand on the other. The latter serves as the vector of propagation, and we have synthesized complexes with two metallodithiolene units linked via a tetraphosphine bridge,^{31, 33} which can be further elaborated into what can be considered multi-qubit polymers.³⁵ The synthesis is highly modular, where metals and ligands are selectively installed and positioned in a way that infuses the system with an unprecedented degree of control that fosters single qubit addressability. We can demonstrate this potential with the compound $[\{\text{Ni}(\text{adt})\}_2(\mu\text{-tpbz})]$ (**2.4**). Essentially this is an expanded bis(dithiolene) complex, where the metal ions in **2.1** – **2.3** are now replaced by the $\{\text{M}(\mu\text{-tpbz})\text{M}\}$ spacer that separates the terminal dithiolene ligands by ca. 1 nm.³¹

2.2.Synthesis

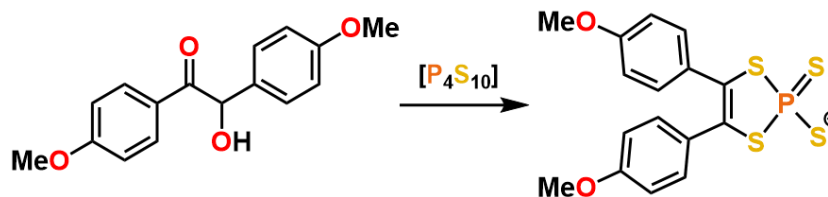


Figure 2.7. Formation of the operative thiophosphoric ester in Schrauzer's method for preparation of dithiolenes.

The neutral group 10 complexes $[M(\text{adt})_2]^0$ where synthesized via Schrauzer's methodology. An acyloin, a ketyl functionality with an alpha hydroxy, is refluxed in dioxane with an excess of phosphorous pentasulfide. The reaction results in the formation of many odorous species, the one of utility is the thiophosphoric ester of the selected acyloin, in this case anisoin, on which the acyloin functionality is appended by anisyl substituents. This thiophosphoric ester is produced in approximately 13% yield and is present in the filtrate of the first step. To the filtrate is then added an aqueous solution of a group 10 metal chloride salt; $\text{NiCl}_2 \cdot 6\text{H}_2\text{O}$, $\text{K}_2[\text{PdCl}_4]$, $\text{K}_2[\text{PtCl}_4]$, in equivalence to the expected 13% thiophosphoric ester to prevent precious metal waste, and the resulting solution is refluxed for a further 2 hours. Upon heating the colour of this reaction drastically changes from a transparent red to obsidian with hints of emerald, ruby, or sapphire for Ni, Pd, Pt, respectively. The evolution of a black hue is the telltale sign of a radical ligand complex that forms from oxidation of the $[M^{\text{II}}(\text{adt})_2]^{2-}$ formed as the acidic and thiophilic transition metals remove and replace the thiophosphoric ester functionality. Cooling results in a black precipitate which is filtered and purified by Soxhlet extraction.

2.3.X-ray Crystallographic Structure

The molecular structures of **2.1** – **2.3** have been characterized by X-ray diffractometry; a representative structure is shown in Figure 1. The central metal ion adopts a square planar geometry with the $\{\text{NiS}_4\}$ unit in **2.1** – **2.3** exhibiting the largest drift toward tetrahedral ($\alpha = 17.6^\circ$). This is a consequence of crystal packing as evidenced by the perfectly planar geometry ($\alpha = 0^\circ$) of the complex ion with a $[\text{NEt}_4]^+$ counterion.³⁶ The anisyl substituents are rotated relative to the $\{\text{S}_2\text{C}_2\}$ plane at angles ranging $42 - 86^\circ$ across the series. Therefore via induction, the anisyl group is electron donating reflecting the softer, more polarizable sulfur atoms compared with aromatic dithiolenes or maleonitrile dithiolate, mnt.³⁷ An important consideration for the forgoing examination of the spin dynamics of this molecular building block is the presence of protons on the periphery of the ligand. Despite the absence of conjugation that ensures the spin density is confined to the $\{\text{S}_2\text{C}_2\}$ core, the vocal nuclear spin of protons presents an efficient decoherence pathway driven by dipolar coupling.³⁸⁻³⁹

The three types of proton in the ligand – two aromatic and one methyl – are on average 3.4 Å, 5.5 Å and 7.5 Å, respectively, away from the spin barycenter (Figure 1). The orbital parentage manifests in the intraligand bond distances for **2.1** – **2.3**. The average S–C bond distance of ca. 1.74 Å and average C–C distance of ca. 1.37 Å are shorter and longer, respectively, than the corresponding bond lengths in the dianionic dithiolate form of the ligand (Table S2). This is characteristic of an oxidized dithiolene, which due to the centrosymmetry of each complex, is distributed over both ligands. The electronic structure of **2.1** – **2.3** is defined as $[M^{II}(L_2^{3-})]^{1-}$ (L = dithiolene), which is an abridged description derived from the limiting resonance forms $[M^{II}(L^{2-})(L^{-})]^{1-} \leftrightarrow [M^{II}(L^{-})(L^{2-})]^{1-}$.⁴⁰⁻⁴¹

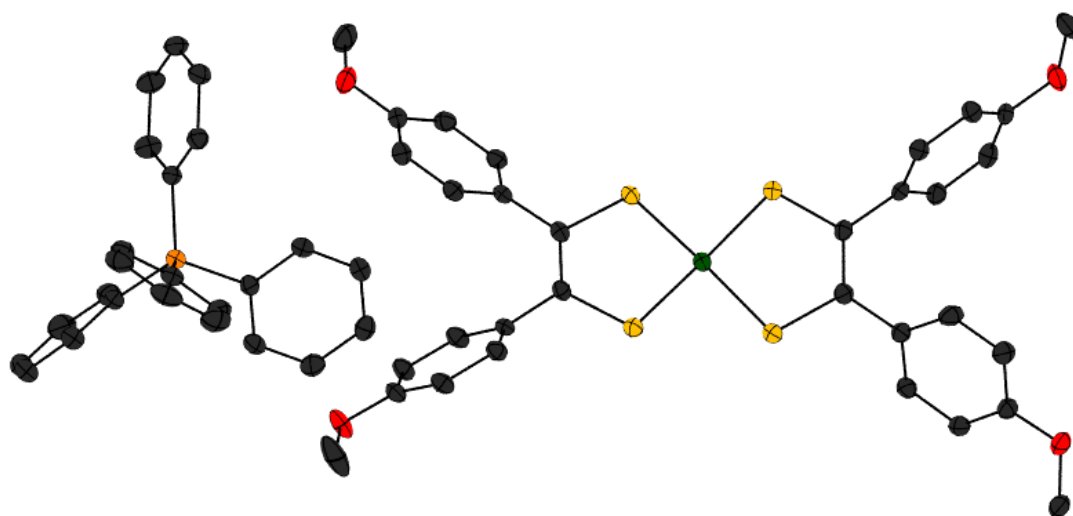


Figure 2.8. Molecular structure of $[PPh_4][Ni(adt)_2]$.

Table 2.3. Comparison of Calculated and Experimental Metric Parameters^[a]

	2.1		2.2		2.3	
	Exptl	Calcd	Exptl	Calcd	Exptl	Calcd
avg. M–S	2.1561(9)	2.154	2.278(1)	2.298	2.270(2)	2.295
avg. S–C	1.748(2)	1.752	1.742(2)	1.751	1.741(7)	1.753
avg. C–C	1.366(2)	1.382	1.372(3)	1.384	1.366(9)	1.382
avg. S–M–S	91.01(3)	90.4	88.46(2)	87.3	87.90(6)	87.3
$\alpha^{[b]}$	17.6	0.2	3.3	1.7	0	1.3

[a] Distances in angstrom; angles in degrees. [b] Dihedral angle between mean MS₂ planes.

2.4. Electronic Structure

2.4.1. Electronic Spectra

The integrity of the sample was conveniently tracked with electronic spectroscopy, as the prominent band is distinct both in energy and intensity when comparing the monoanionic and neutral members that constituent each electron transfer series (Figure S1). The characteristic absorption band is diagnostic of the electronic structure of these bis(dithiolene) species where the low-energy yet high intensity is defined as an intervalence charge transfer (IVCT) transition to the highest occupied molecular orbital (HOMO), which is singly occupied (SOMO) b_{2g} MO in D_{2h} symmetry, from the b_{1u} HOMO-1, which are ligand-based.⁴⁰⁻⁴¹ In the case of the neutral parent compounds the HOMO is the unoccupied b_{2g} . The electronic transitions in question are found in the near-infra-red (NIR) region of the electronic spectra. Ligand radicals in bis(dithiolene) complexes are characterized by an intense transition of $\epsilon \sim 25,000 \text{ M}^{-1} \text{ cm}^{-1}$ in the NIR region. For the neutral complexes this transition occurs for both ligand radicals at 900, 950, and 850 nm for Ni, Pd, and Pt respectively. On reduction the intensity of this transition is halved and shifted further into the NIR region as there is now an electron present in the HOMO which means one of the electrons in HOMO-1 cannot have an allowed transition by the Pauli principle and the energy of the receiving orbital has been reduced by occupation resulting in a lower energy of transition. The IVCT transitions for the monoanions are 1000, 1270, and 1000 nm for Ni, Pd, Pt respectively. The largest deviation is found in the Pd complex.

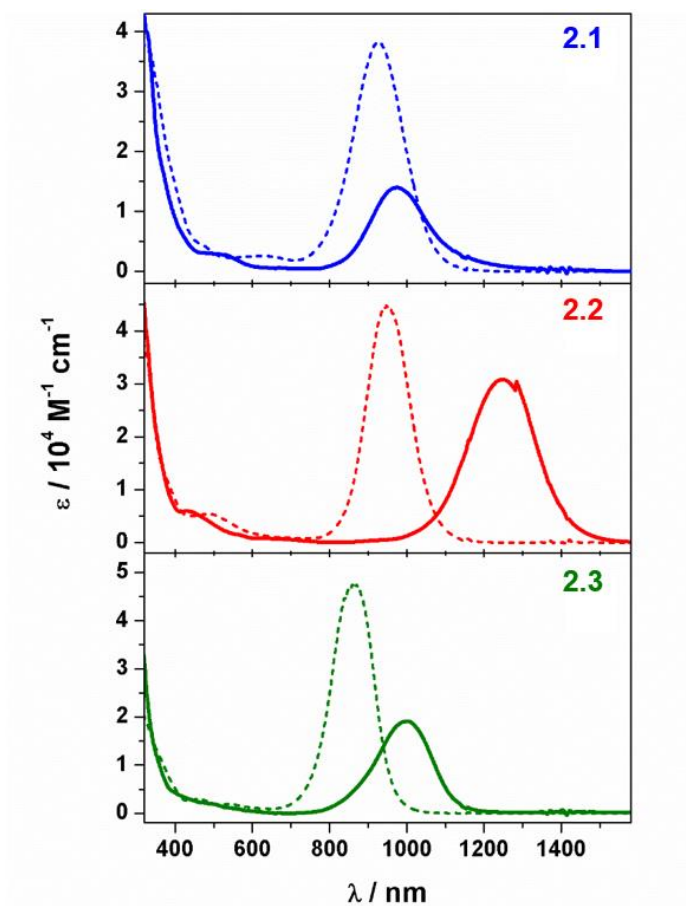


Figure 2.9. Electronic spectra for the neutral $[M(\text{adt})_2]$ ($M = \text{Ni}$ (blue), Pd (red), and Pt (green)) represented by the dashed line and their radical anionic form represented by the solid line.

2.4.2. Continuous Wave EPR

Electron paramagnetic (or spin) resonance spectroscopy is a technique applied to species with one or more unpaired electrons. It is founded on the resonance absorption of microwave radiation associated with transitions between energy levels of the electronic term split by the external magnetic field, B . The removal of degeneracy of energy levels in a magnetic field is known as the Zeeman effect, and occurs because of the difference in energy of an electron whose magnetic moment is aligned parallel or antiparallel to the magnetic field. Continuous wave EPR spectroscopy is an experiment in which a constant microwave frequency is applied while the magnetic field strength is varied. The absorption of the microwave radiation is measured and the first differential of the spectrum of absorbance versus the magnetic field is plotted as the lower signal to noise ratio provides better spectral resolution. Several different, but invariant, frequencies, also known as bands (a remnant of world war II), are used in EPR experiments, and are listed in Table 2.4.

Table 2.4. Microwave frequency bands available for EPR studies.

Microwave band	Frequency (GHz)
L	1.1
S	3.0
X	9.75
K	25.0
Q	34.0
W	94.0

The energy gap between the two spin states (Figure 2.10) and the magnetic Field are related according to Equation 2.3.;

$$\Delta E = h\nu = g\mu_B B$$

where μ_B is the Bohr magneton and g is the g -value. The g -value is a dimensionless parameter that corresponds to the strength of the magnetic field at which the microwave frequency and the energy gap between the spin states are in resonance. Its value for a free electron in a vacuum, g_e , is 2.0023. When the electron is in a molecular orbital it is susceptible to the effects of spin-orbit coupling and zero-field splitting and so different values of g are expected for transition metal compounds. The g -value does not vary across spectra of the same sample recorded at various microwave bands as it is independent of microwave frequency.

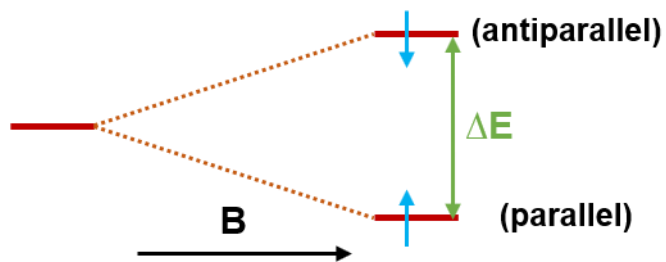


Figure 2.10. Pictorial representation of the energy difference (ΔE) of the two electron spin energy levels in a magnetic field (B).

Interactions between the magnetic field of the electron and the nuclear magnetic moment generate hyperfine splitting, parametrised by the A tensor. This is a magnetic dipole-dipole interaction and leads to a small perturbation in the energy levels of transition metal complexes. This is used to determine the position of the unpaired electron in the metal d orbitals and disclose the extent of the association with a particular metal d orbital. Interaction of the unpaired electron with surrounding nuclei of the ligands perturbs the energy levels further as superhyperfine splitting. The evaluation of g - and A -tensors provides detailed information about the symmetry and electronic environment of metal centres.

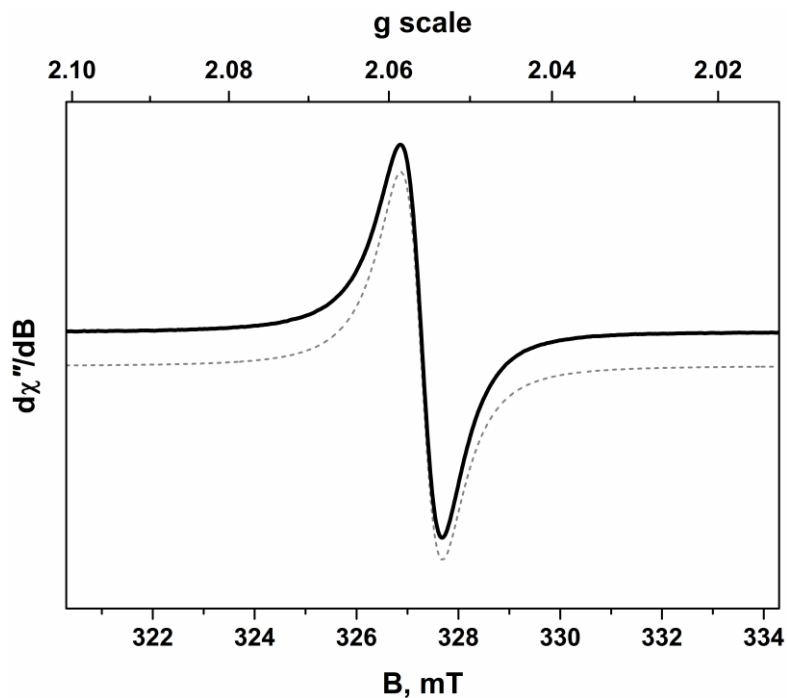


Figure 2.11. X-band EPR spectrum of **2.1** recorded in CH_2Cl_2 solution at 293 K (experimental conditions: frequency, 9.4176 GHz; power, 0.063 mW; modulation, 0.1 mT). Experimental data are represented by the black line; simulation is depicted by the dashed trace.

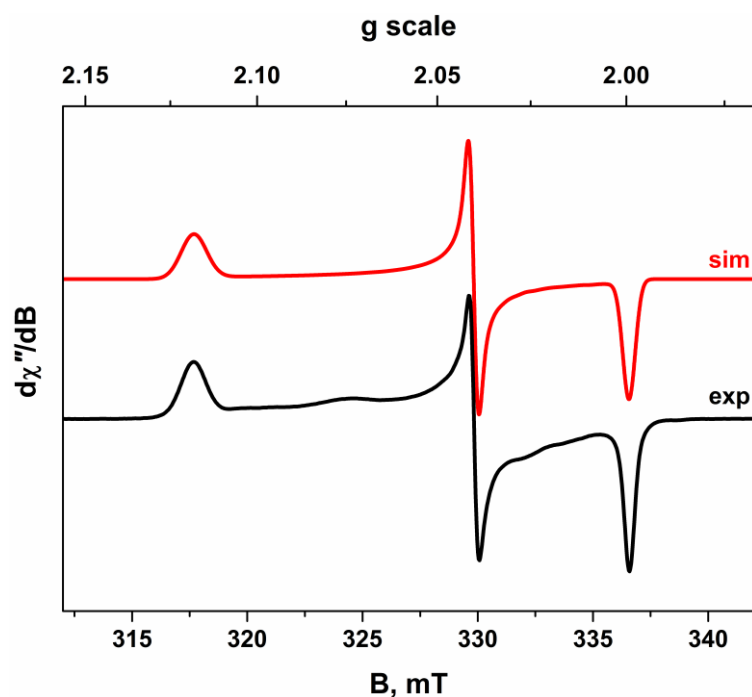


Figure 2.12. X-band EPR spectrum of **2.1** recorded in $\text{CH}_2\text{Cl}_2/\text{DMF}$ solution at 130 K (experimental conditions: frequency, 9.4180 GHz; power, 0.63 mW; modulation, 0.2 mT). Experimental data are represented by the black line; simulation is depicted by the red trace.

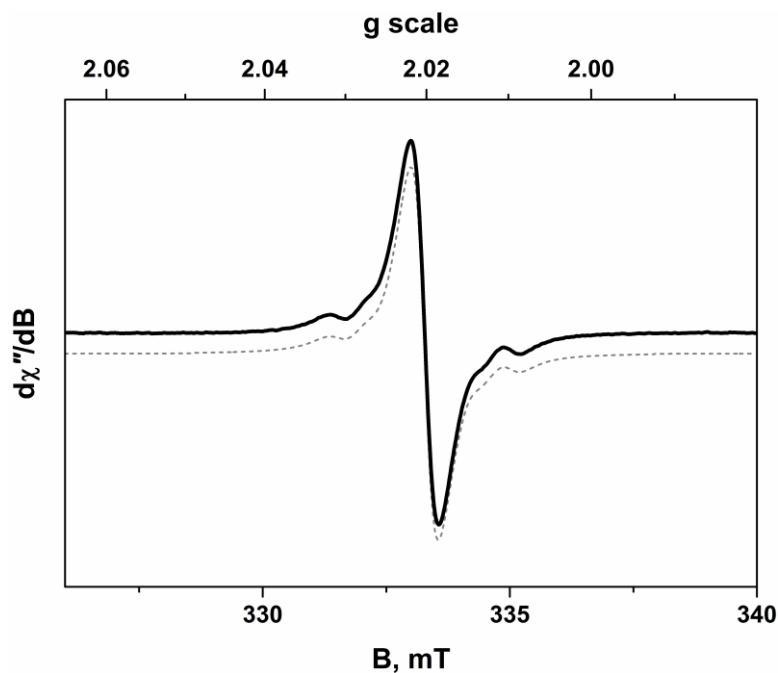


Figure 2.13. X-band EPR spectrum of **2.2** recorded in CH_2Cl_2 solution at 293 K (experimental conditions: frequency, 9.4236 GHz; power, 0.63 mW; modulation, 0.1 mT). Experimental data are represented by the black line; simulation is depicted by the dashed trace.

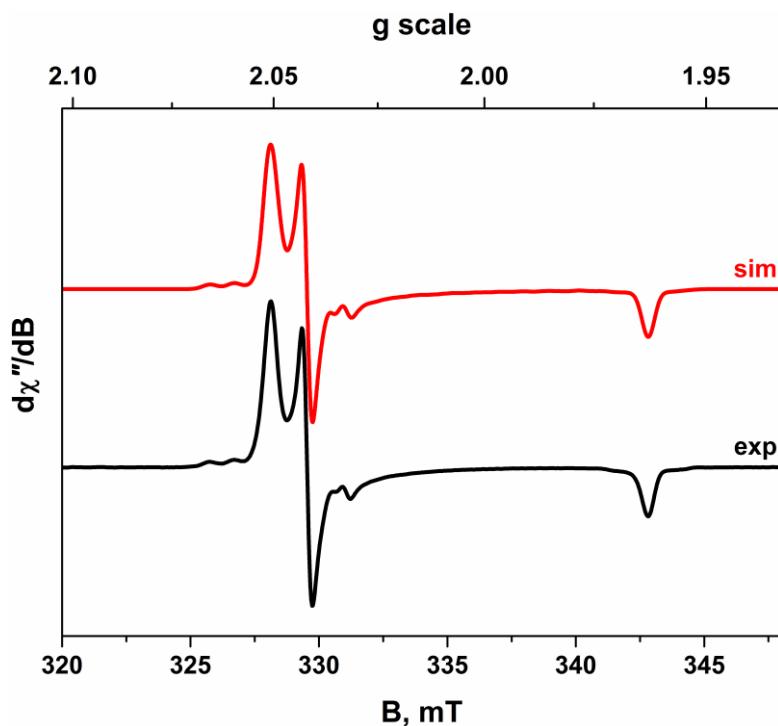


Figure 2.14. X-band EPR spectrum of **2.2** recorded in $\text{CH}_2\text{Cl}_2/\text{DMF}$ solution at 130 K (experimental conditions: frequency, 9.4178 GHz; power, 0.2 mW; modulation, 0.3 mT). Experimental data are represented by the black line; simulation is depicted by the red trace.

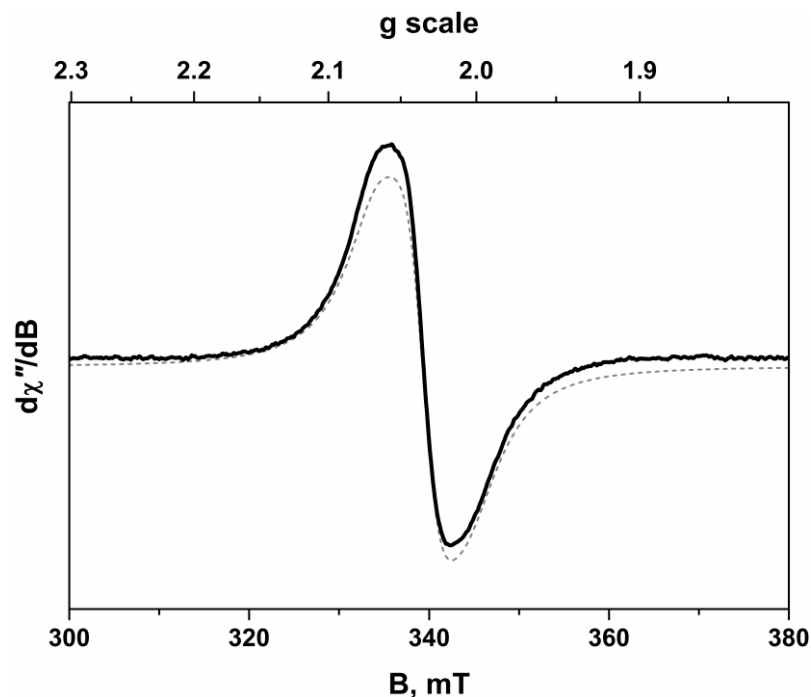


Figure 2.15. X-band EPR spectrum of **2.3** recorded in CH_2Cl_2 solution at 293 K (experimental conditions: frequency, 9.6647 GHz; power, 0.63 mW; modulation, 0.3 mT). Experimental data are represented by the black line; simulation is depicted by the dashed trace.

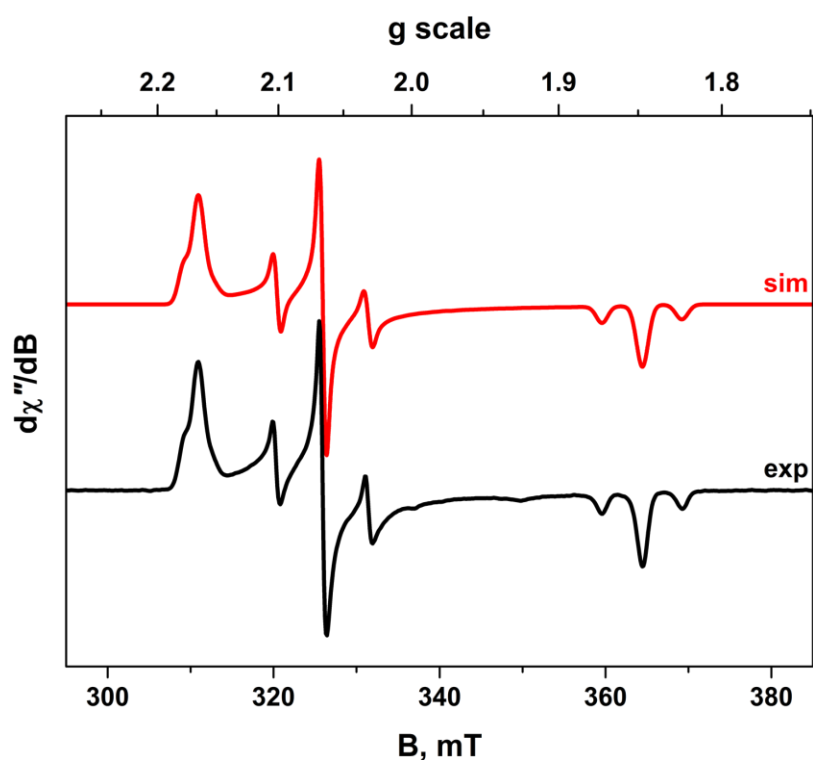


Figure 2.16. X-band EPR spectrum of **2.3** recorded in $\text{CH}_2\text{Cl}_2/\text{CH}_3\text{CN}$ solution at 130 K (experimental conditions: frequency, 9.4230 GHz; power, 0.63 mW; modulation, 0.3 mT). Experimental data are represented by the black line; simulation is depicted by the red trace.

The cw X-band EPR spectra of **2.1** – **2.3** recorded in frozen CH₂Cl₂/DMF solution at 130 K display signals typical of an $S = 1/2$ system with rhombic g -values in agreement with those reported in the literature (Table 1).⁴² The profiles for all three spectra are similar with $g_1 > g_2 > g_3$. The spectrum of **2** exhibits weak shoulders about each g -value indicating the presence of hyperfine splitting from ¹⁰⁵Pd ($I = 5/2$, 22.2% abundant), which are most pronounced on the low-field lines (Figure 2.14.). Spectral simulation was achieved with $A = (9.0, 5.9, 4.6) \times 10^{-4} \text{ cm}^{-1}$. A more prominent hyperfine interaction is observed in the spectrum of **2.3**, where coupling to the ¹⁹⁵Pt ($I = 1/2$, 33.8% abundant) isotope yielded $A = (-33, -106, -83) \times 10^{-4} \text{ cm}^{-1}$ (Figure 2.16.). The larger coupling in **2.3** is a direct consequence of the nuclear g -value of ¹⁹⁵Pt ($g_N = 1.219$) which is roughly 5 times larger than that of ¹⁰⁵Pd ($g_N = -0.256$). The more meaningful measure of metal content of the magnetic orbital is the rhombicity of the g -values which ranges from 0.10 for **2.2** to 0.66 for **2.1** (Table 1). This parameter reflects the metal contribution to the magnetic orbital (%M). The low rhombicity as well as the low isotropic part of the magnetic hyperfine coupling, indicates that the metal contribution to the SOMO is smallest for **2.2**. Conversely, **2.1** being the most rhombic has the largest metal contribution to its magnetic orbital. The anisotropy of the g -values stems from the spin-orbit coupling (SOC) constant of the metal center tempered by its contribution to the ground state. As SOC commutes as Z^4 ,⁴³ the largest g -anisotropy is observed for **2.3** because of the greater SOC constant of platinum ($Z = 78$). The equivalent g -anisotropy for **2.1** and **2.2** reflects the smaller palladium content to the SOMO in the latter despite having the larger SOC constant. Interestingly, the metal content as assessed by g -anisotropy is also modulated by the dithiolene ligand, being larger for aromatic-type dithiolenes such that a more significant proportion of the spin resides on the alkyl dithiolene variant used here.³⁷

44

Table 2.5. Summary of Experimental and Calculated Data^[a] for **2.1 – 2.3**

	2.1	2.2	2.3
M	Ni	Pd	Pt
$\zeta_{nd} / \text{cm}^{-1}$ ^[b]	700	1300	3400
%M ^[a]	25.2	12.8	18.9
ρ_M ^[a]	0.25	0.11	0.14
g_1	2.1182 (2.0979)	2.0508 (2.0521)	2.1653 (2.1864)
g_2	2.0402 (2.0650)	2.0419 (2.0487)	2.0654 (2.1062)
g_3	1.9993 (2.0013)	1.9628 (1.9671)	1.8472 (1.8644)
R_g ^[c]	0.66	0.10	0.31
Δg ^[d]	0.1189	0.0880	0.3181
B_0 / mT	340.6	343.3	339.1 344.5
$T_{1,s} / \text{ms}$ ^[e]	6.31(3)	4.99(1)	1.64(2) 1.72(2)
$T_{M,s} / \mu\text{s}$ ^[e]	4.89(1)	2.07(2)	3.63(2) 3.64(2)
Ω_R / MHz ^[f]	13.6	15.5	14.5

^[a] From ZORA-PBE0 level of theory (calculated g -values in parenthesis); ^[b] Values taken from ref. ⁴⁵; ^[c] Rhombicity, $R_g = (g_1 - g_2)/(g_1 - g_3)$; ^[d] g -anisotropy, $\Delta g = g_1 - g_3$; ^[e] Relaxation time at 10 K (error given in parenthesis); ^[f] Rabi frequency from nutation experiment at 10 K and 6 dB microwave attenuation.

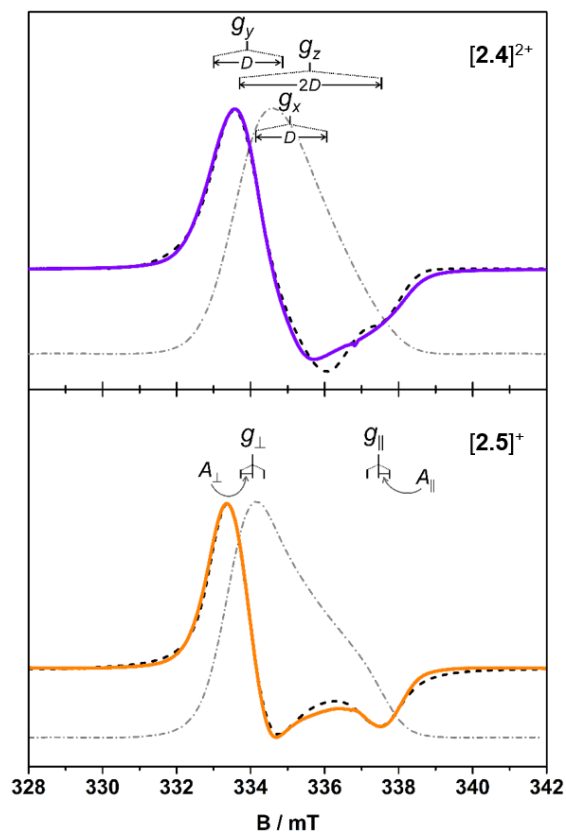


Figure 2.17. X-band EPR spectra of $[2.4]^{2+}$ (top) and $[2.5]^{1+}$ (bottom) recorded in CH_2Cl_2 solution at 130 K. Experimental data are shown as the solid line in each case, with the absorption spectrum shown beneath as a dashed grey line to indicate the field position of maximum intensity for pulsed EPR measurements. Simulations of each spectrum are depicted by the dashed black line with markings at field positions that correspond to the key spin-Hamiltonian parameters. For $[2.4]^{2+}$ $S = 1$: $g_{x,y,z} = (2.010, 2.017, 2.007)$, $D = -18 \times 10^{-4} \text{ cm}^{-1}$, $E/D = 0.005$; $A_{x,y,z} = (3, 1, 1) \times 10^{-4} \text{ cm}^{-1}$ ($4 \times {}^{31}\text{P}$ $I = 1/2$, 100% abundant – not resolved but used to improve the lineshape). For $[2.5]^{1+}$ $S = 1/2$: $g_{x,y,z} = (2.0205, 2.0158, 1.9954)$, $A_{x,y,z} = (3.0, 3.5, 3.5) \times 10^{-4} \text{ cm}^{-1}$ ($2 \times {}^{31}\text{P}$).

The cw EPR spectrum of $[2.4]^{2+}$ is characterized with miniscule anisotropy ($g = 2.010, 2.017, 2.007$) and a vanishingly small zero-field splitting of the $S = 1$ state of $D = 0.0018 \text{ cm}^{-1}$ and negligible rhombicity ($E/D = 0.005$).³¹ Broken symmetry DFT calculations estimate $J = -3.1 \text{ cm}^{-1}$, underscoring the near degenerate singlet-triplet ground state in $[2.4]^{2+}$ (Figure 2.17.).

2.5. Electrochemistry

Central to dithiolene complexes are electron transfer processes. Molecular electrochemistry in solution is a vehicle that allows for greater insight into these processes. Typical cell set up will involve a working electrode which delivers electrons into the electrochemical cell, an electrolyte in the solvent medium that facilitates ion transport through the cell to the counter electrode, which completes the cell. This is typically bolstered by a reference electrode; a second reference compound may also be added. Either the potential or current is changed at the working electrode and the response in the current or potential is measured at the counter electrode or reference electrode respectively, these two modes of operation are called potentiometric or coulometric respectively. The most widely applicable electrochemical technique for coordination complexes is cyclic voltammetry as it reveals not only the standard reduction potentials but also degrees of reversibility under electrochemical conditions. Electron transfer in an electrochemical cell is heterogeneous between the electrode surface and the molecular species, and how effectively an electron is transferred to from one medium to another is called reversibility. Cyclic voltammetry is a potentiometric technique and measures the current response as the potential is swept across a range of values and back again at a set, but variable, scan rate, measured in volts per second. Electrochemical events appear as peaks that are parameterised at their zenith for the forward and backward scans. Going toward negative potentials (cathodically) reduction events are labelled with $E_{p,c}$ and $I_{p,c}$ for their potential and current respectively; toward positive potential (anodically) denoted $E_{p,a}$ and $I_{p,a}$. The relationship between these parameters determines reversibility. For full reversibility the separation between $E_{p,c}$ and $E_{p,a}$ must not be greater than 57 mV for one-electron; integration of the current density $I_{p,a}$ must be equal to that of $I_{p,c}$; the peak currents must increase linearly with the square root of the scan rate for solution based measurements; $E_{1/2}$ must be invariant to scan rate. Deviation from any of these deems the system irreversible, however, quasi-reversibility is a term frequently used to describe systems close to full reversibility. What qualifies as 'close' varies author to author and the term is not explicitly defined but generally refers to systems that are chemically reversible but cannot be shown under electrochemical conditions to be electrochemically reversible. Chemical reversibility is simply the ability to perform the electron transfer from one chemical species to another and chemically react in both the reductive and oxidative directions.

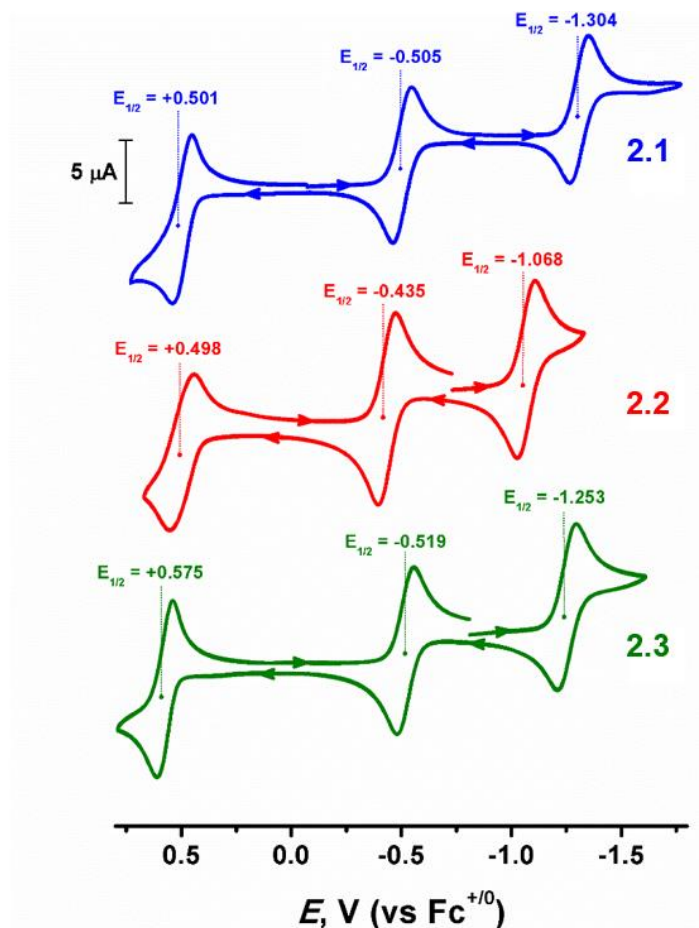


Figure 2.18. Cyclic voltammograms of **2.1** – **2.3** in CH_2Cl_2 solution 0.10 M $[\text{N}(\text{tBu})_4]\text{PF}_6$ supporting electrolyte at 22 °C at a scan rate of 100 mV s^{-1} . Potentials are referenced versus the $\text{Fc}^{+/0}$ couple.

Cyclic voltammograms were recorded for $[\text{M}(\text{adt})_2]$ ($\text{M} = \text{Ni}, \text{Pd}, \text{Pt}$) using the method described in section 2.2.2. Each compound was dissolved in dichloromethane containing 0.1 M $[\text{nBu}_4\text{N}][\text{PF}_6]$ as supporting electrolyte and measurements were recorded at room temperature. All complexes displayed one oxidation process at positive potentials and two reduction processes at negative potentials, versus Fc . Oxidation and reduction potentials for each complex are presented in Figure 2.18. The cathodic and anodic processes displayed well resolved sets of peaks corresponding to a reversible, one-electron reduction of the molecule. This is defined as the ligand based reduction $[\text{M}^{\text{II}}(\text{adt}^-)_2]^0 \rightleftharpoons [\text{M}^{\text{II}}(\text{adt}^{2-})(\text{adt}^-)]^-$. In all cases peak current ratios ($I_{\text{pa}}/I_{\text{pc}}$) were close to unity at scan rates of 50, 100, 200, 400, and 500 mV s^{-1} .

Charge-neutral **2.4** is readily oxidized at very mild potential; the two-electron event produces the diradical $[\mathbf{2.4}]^{2+}$ where each dithiolene now possess an unpaired spin giving near degenerate singlet-triplet ground state. The optimized structure exhibits the same intraligand bond distances consistent with a coordinated dithienyl radical. Aside from the

inherent air stability of this diradical, it is the first cationic molecular spin qubit whose electrostatic field perturbs the interaction with decohering hydrogens in the solvent shell compared with its anionic counterparts.⁴⁶ The importance of electrostatics and charge distribution on spin relaxation lifetimes has recently been investigated by Freedman and co-workers.³⁸

2.6.DFT Calculations

The geometry-optimized structures for the complex anions in **2.1** – **2.3** are in excellent agreement with the experimental data, with the metal-sulfur and intraligand bond distances and angles accurately reproduced (Table 2.3.). Moreover the structures are strictly planar demonstrating the modest tetrahedralization about the nickel ion in **2.1** is a consequence of crystal packing. Inspection of the frontier MOs reveals four metal d orbitals lower in energy than the ligand-based b_{2g} and b_{3g} (D_{2h} point group) which undergo symmetry-allowed π interactions with metal d orbitals.⁴⁰⁻⁴¹ The b_{2g} symmetric SOMO is ligand-centered such that the electronic structure is best represented as $[M^{II}(L_2^{3-\cdot})]^{1-}$. The unpaired spin is delocalized across both ligands as regulated by the metal ion, whose contribution trends Ni > Pt > Pd across the series (Table 1). As a consequence **2.2** has a low spin density of 0.11 at the Pd(II) ion indicating an almost negligible contribution from the Pd(III) configuration to the ground state. In contrast, the 0.25 spin density at nickel shows enhanced Ni(III) character in **2.1** that accounts for its EPR spectral profile. The electronic structure has been verified by very accurate calculation of the g -values for **2.1** – **2.3** (Table 1). This level of precision allows for meaningful insight that correlates composition and electronic structure factors on the spin dynamics of molecular qubits based on coordination complexes.

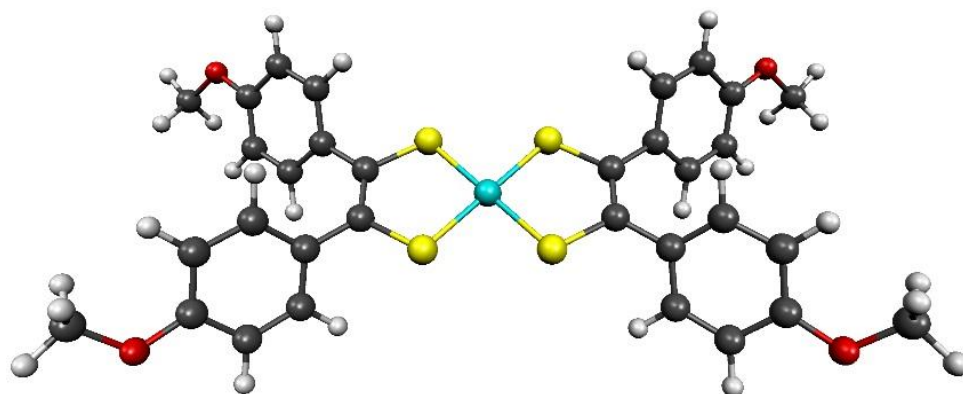


Figure 2.19. Geometry-optimized structure of [Ni(adt)₂]¹⁻

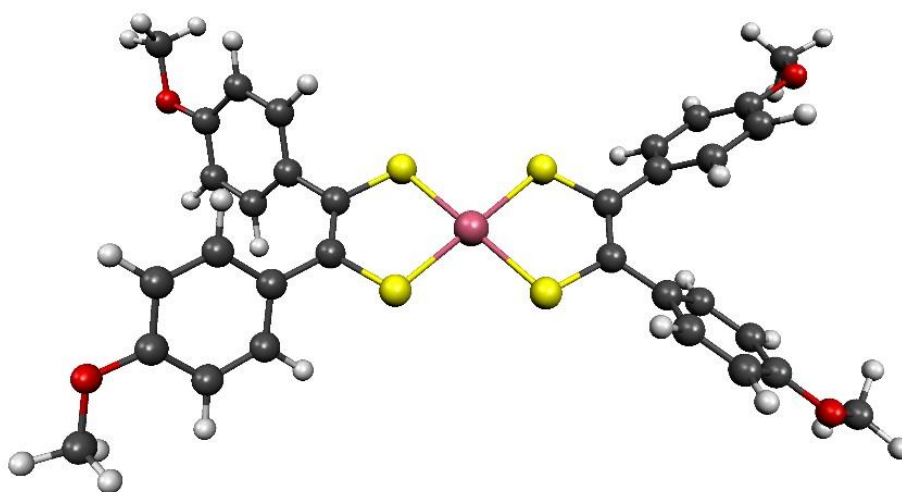


Figure 2.20. Geometry-optimized structure of [Pd(adt)₂]¹⁻

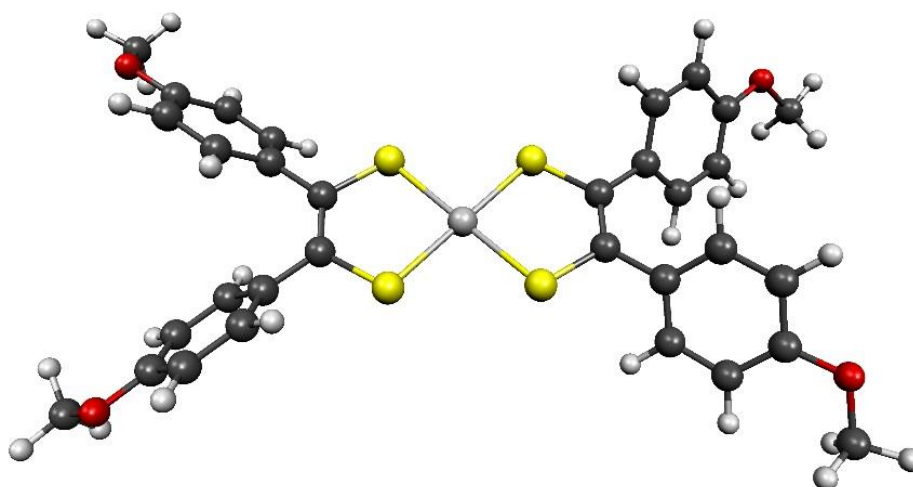


Figure 2.21. Geometry-optimized structure of [Pt(adt)₂]¹⁻

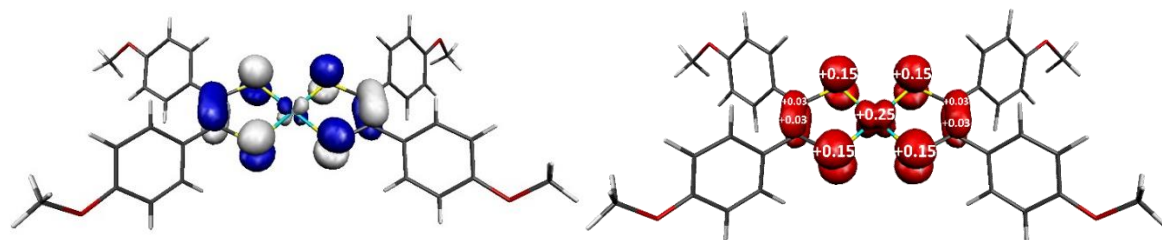


Figure 2.22. Depiction of the singly-occupied molecular orbital (left) and Mulliken spin population analysis (right) of [Ni(adt)₂]¹⁻

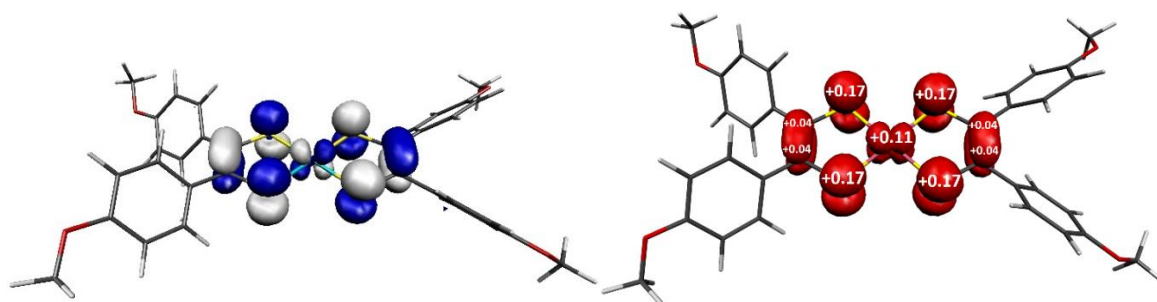


Figure 2.23. Depiction of the singly-occupied molecular orbital (left) and Mulliken spin population analysis (right) of [Pd(adt)₂]¹⁻

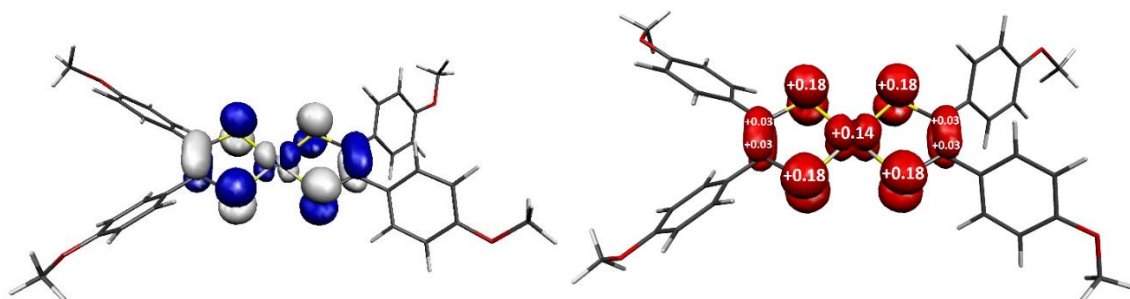


Figure 2.24. Depiction of the singly-occupied molecular orbital (left) and Mulliken spin population analysis (right) of [Pt(adt)₂]¹⁻

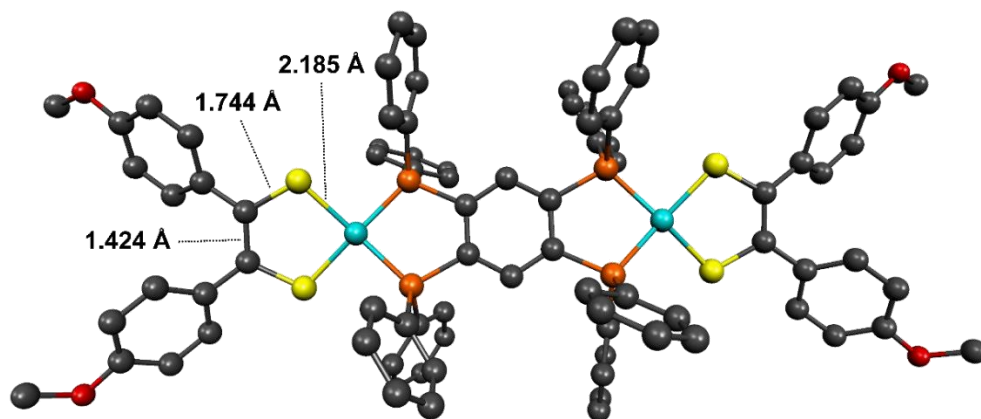


Figure 2.25. Geometry-optimized structure of [2.4]²⁺

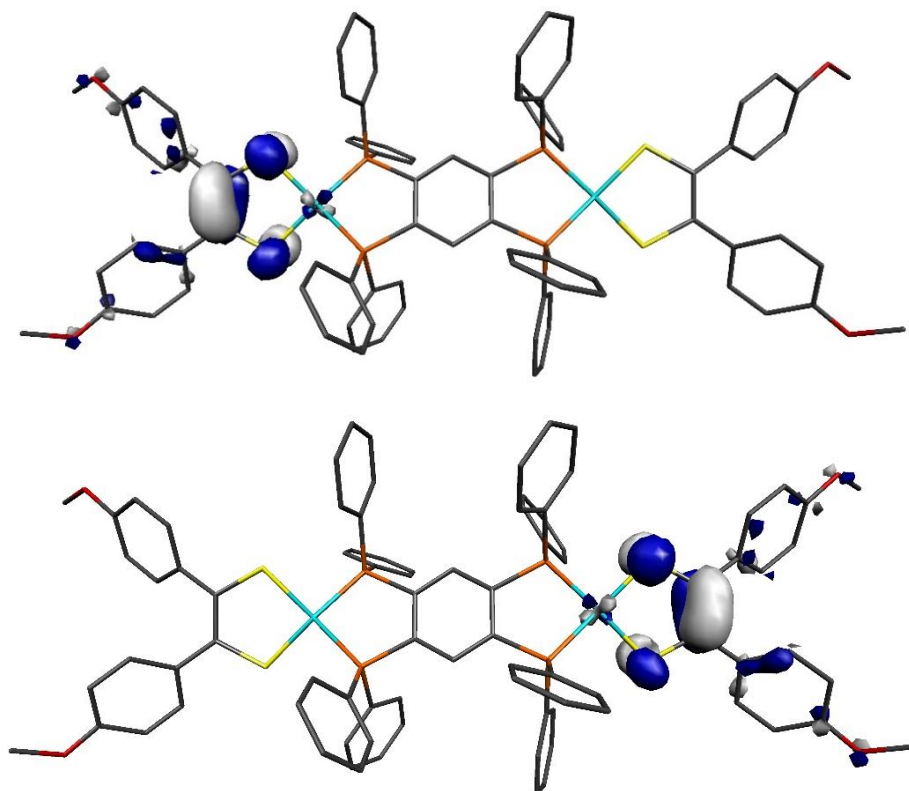


Figure 2.26. Depiction of the magnetic orbitals of [2.4]²⁺

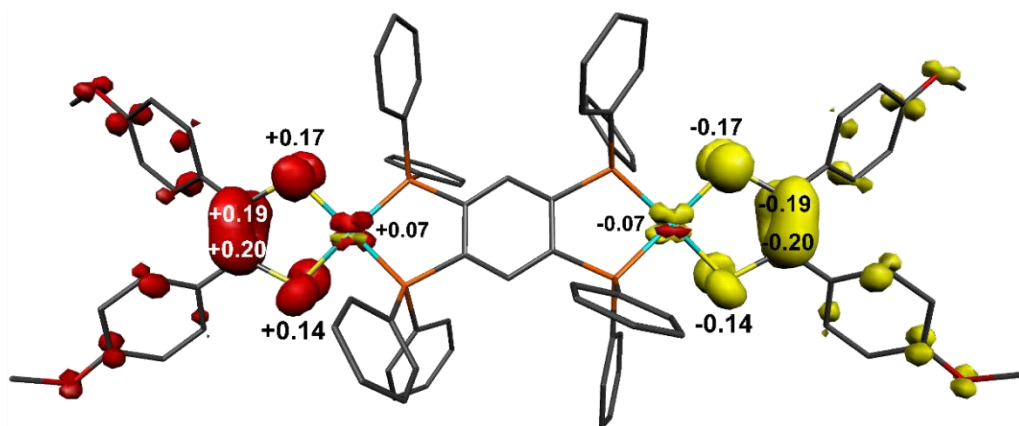


Figure 2.27. Mulliken spin distribution for [2.4]²⁺

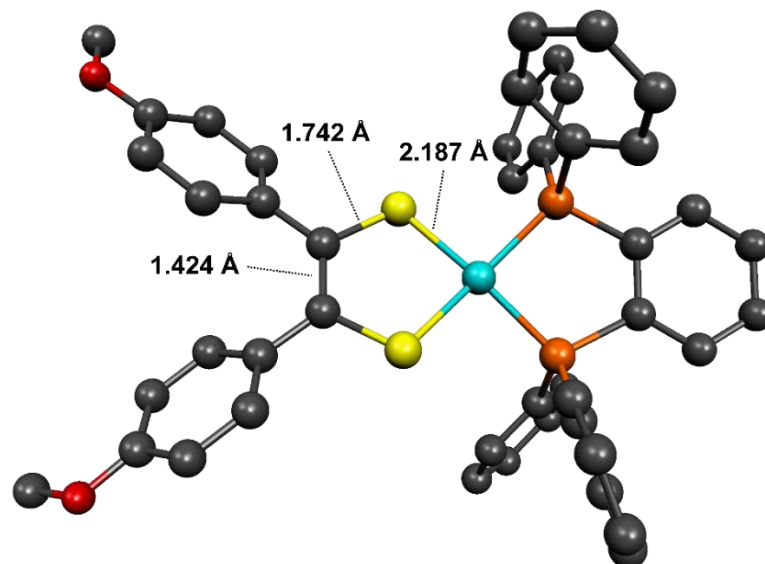


Figure 2.28. Geometry-optimized structure of [2.5]¹⁺

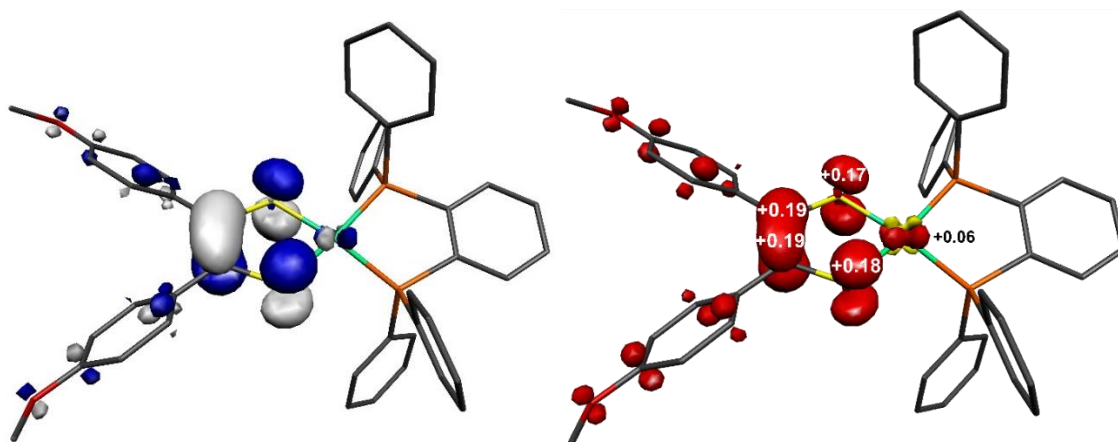


Figure 2.29. Depiction of the singly-occupied molecular orbital (left) and Mulliken spin population analysis (right) of [2.5]¹⁺

2.7. Relaxation Phenomena

2.7.1. Spin-Lattice Relaxation

Spin-lattice relaxation times for **2.1** – **2.3** have been obtained from a three-pulse inversion recovery experiment. A biexponential fit applied to the data yielded fast ($T_{1,f}$) and slow ($T_{1,s}$) relaxation processes, where the former is attributed to spectral diffusion and the latter assigned as the spin-lattice relaxation time. Overall the $T_{1,s}$ times at 10 K are 2–3 orders of magnitude longer than the phase memory time (Table 2.5.). The difference in $T_{1,s}$ across the series represents the most unambiguous demonstration of the intrinsic electronic properties of the atomic constituents of the qubit on its performance. Specifically, the $T_{1,s}$ time is directly correlated to the SOC constant of the metal ion as group 10 is descended. This is the same trend observed in the g -anisotropy of the cw EPR spectra and the intensity of the signature electronic transition in these complexes. The significance of SOC has been previously shown to impact on spin-lattice times when comparing first- and second-row metals in systems where the metal is the spin host.⁴⁷⁻⁴⁹ Here, with an unpaired electron predominantly on the ligand, the metal ion presents a heavy-atom effect – a phenomenon that has been exploited in a range of materials, most notably enhancing the performance of semiconductors in spintronic devices.⁵⁰⁻⁵² At the measurement temperature, a direct spin relaxation process is dominant,⁵³ but as the temperature increases the Raman mechanism takes precedence⁵⁴ and becomes more efficient with increasing SOC.⁵⁵ While relaxation times cannot be directly computed, we have used the calculated electronic structure parameters to estimate $T_{1,s}$ for **2.1** and **2.2** compared with **2.3**. The calculation is based on the ratio of the SOC constant and the parentage of the spin in the molecule, and underscores the high correlation between spin-lattice relaxation and SOC which is relevant to all proposed constructs for implementing quantum computing. We have begun to explore using these molecules as an alternative to metal dichalcogenides in graphene-based heterostructures.⁵⁶⁻⁵⁸

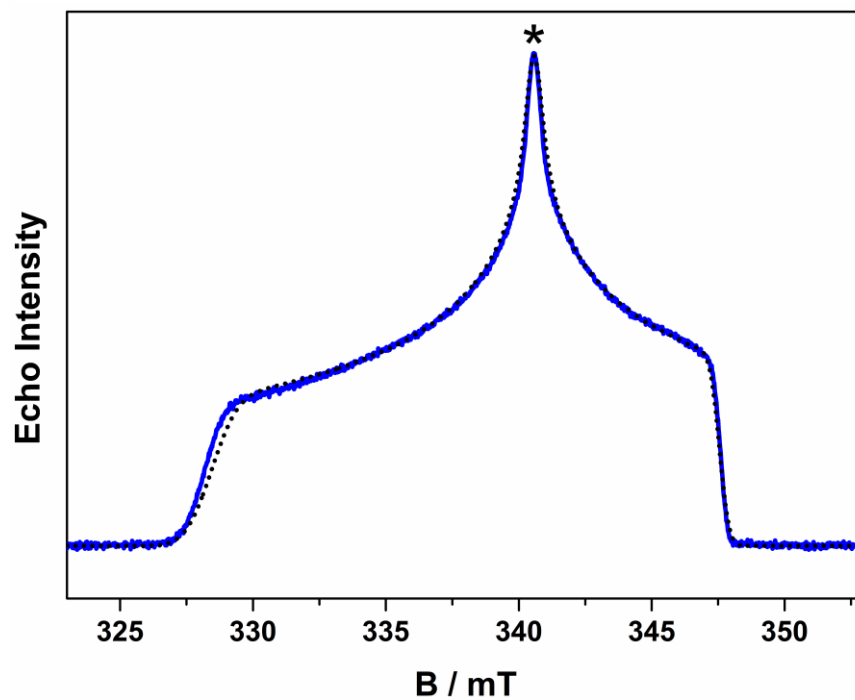


Figure 2.30. ESE detected EPR spectrum (blue line) and simulation (dashed line) of a 1 mM solution of **2.1** in 2% DMF- d_7 /CD $_2$ Cl $_2$ recorded at 10 K and 9.7437 GHz. Asterisk indicates field position for relaxation measurements.

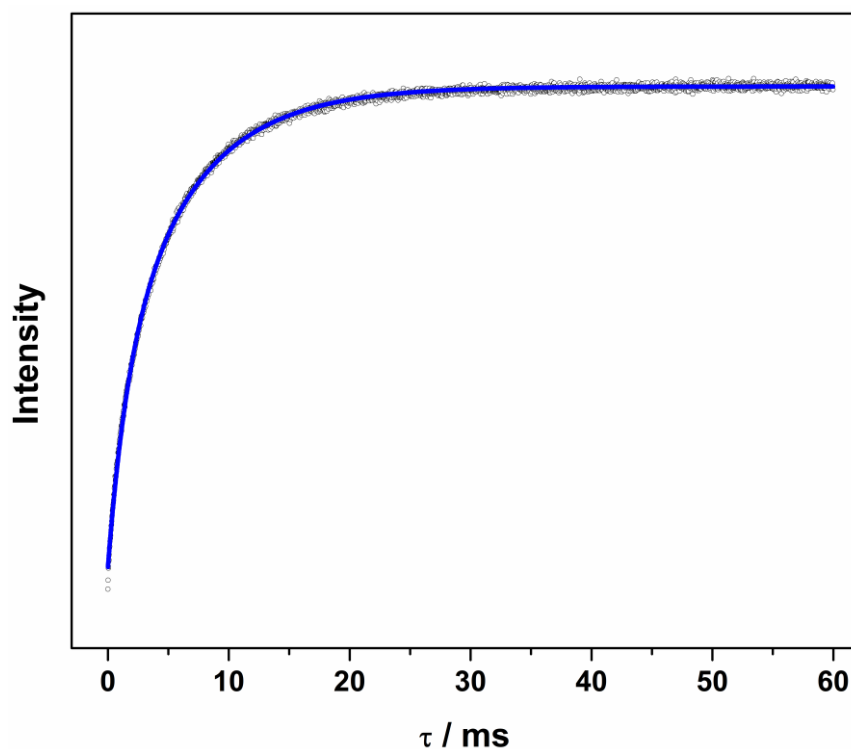


Figure 2.31. Inversion recovery data (open circles) and biexponential fit (blue line) of a 1 mM solution of **2.1** in 2% DMF- d_7 /CD $_2$ Cl $_2$ recorded at 10 K and 340.6 mT. Fit parameters: $A_f = -0.23 \pm 0.02$, $T_{1,f} = 1.60 \pm 0.02$ ms, $A_s = -0.42 \pm 0.03$, $T_{1,s} = 6.31 \pm 0.03$ ms.

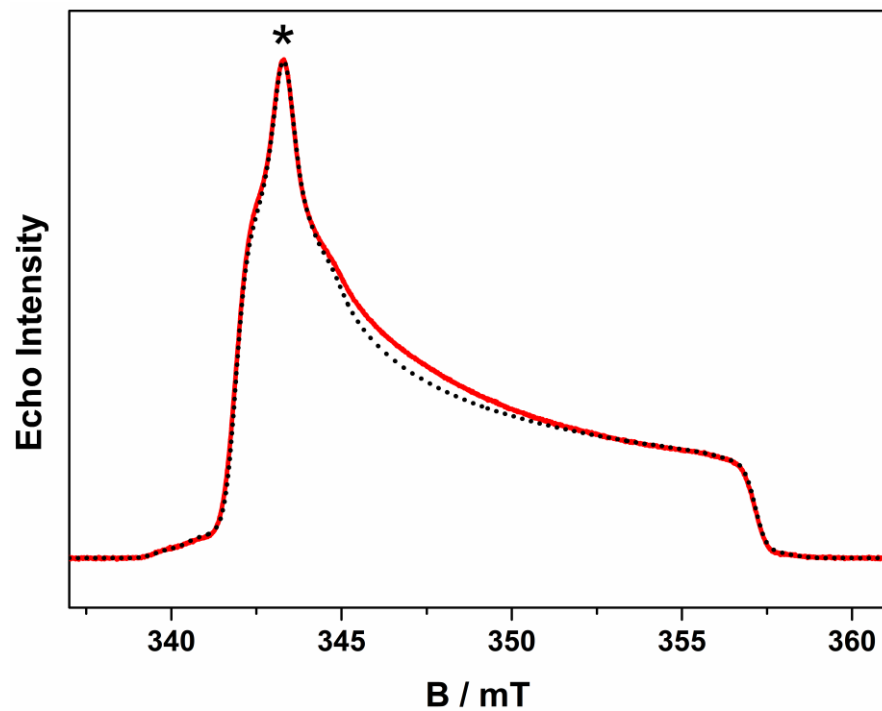


Figure 2.32. ESE detected EPR spectrum (red line) and simulation (dashed line) of a 1 mM solution of **2.2** in 2% DMF- d_7 /CD $_2$ Cl $_2$ recorded at 10 K and 9.8314 GHz. Asterisk indicates field position for relaxation measurements.

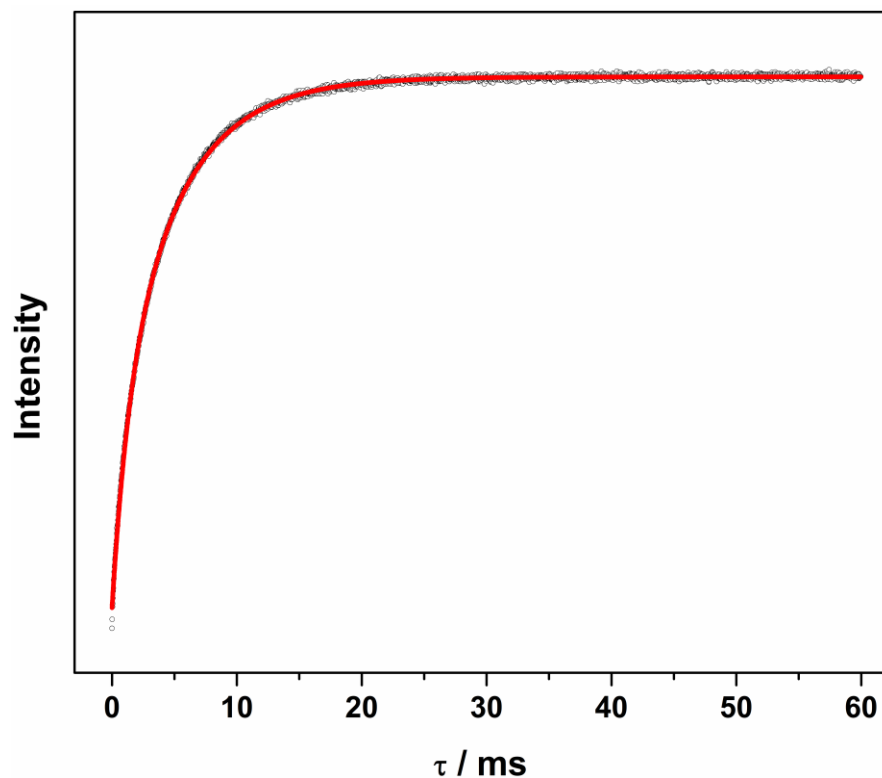


Figure 2.33. Inversion recovery data (open circles) and biexponential fit (red line) of a 1 mM solution of **2.2** in 2% DMF- d_7 /CD $_2$ Cl $_2$ recorded at 10 K and 343.3 mT. Fit parameters: $A_f = -0.28 \pm 0.02$, $T_{1,f} = 1.32 \pm 0.02$ ms, $A_s = -0.57 \pm 0.01$, $T_{1,s} = 4.99 \pm 0.02$ ms.

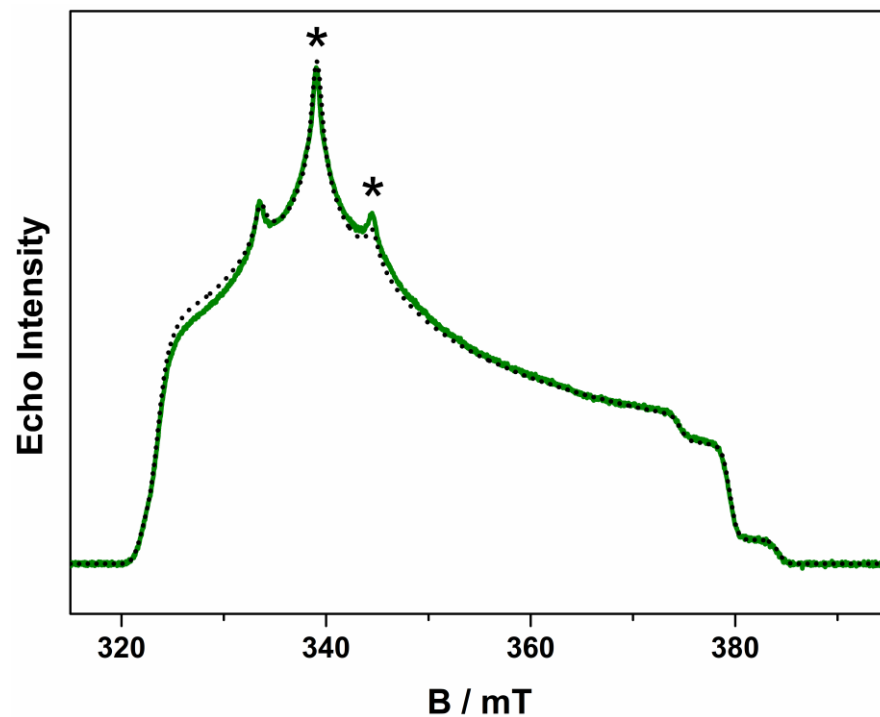


Figure 2.34. ESE detected EPR spectrum (green line) and simulation (dashed line) of a 1 mM solution of **2.3** in 2% DMF- d_7 /CD $_2$ Cl $_2$ recorded at 10 K and 9.8346 GHz. Asterisks indicate field positions for relaxation measurements.

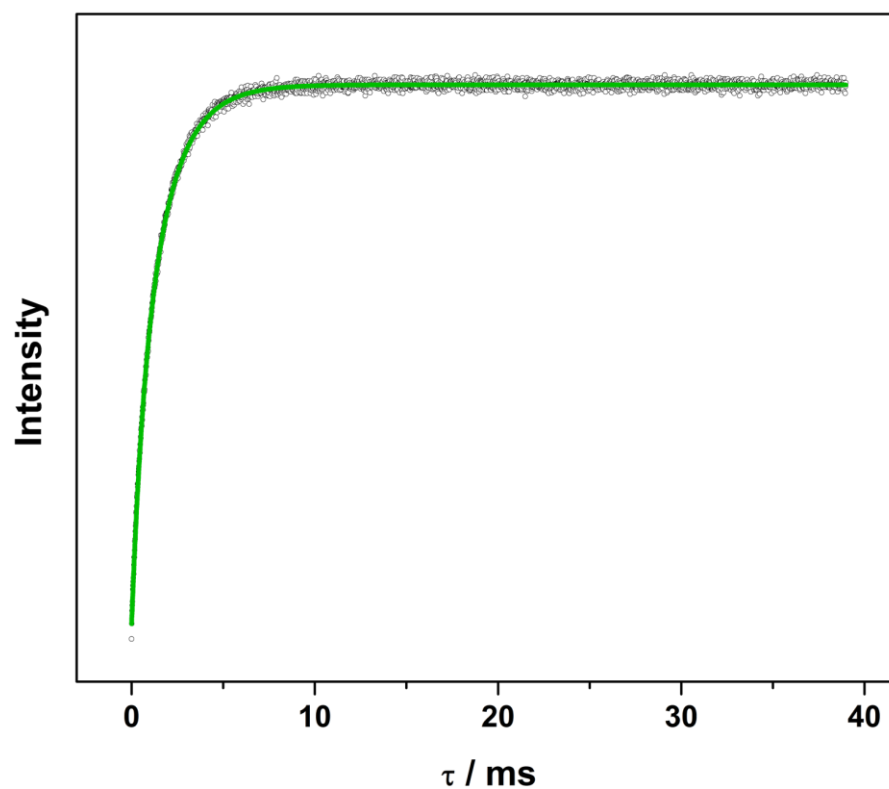


Figure 2.35. Inversion recovery data (open circles) and biexponential fit (red line) of a 1 mM solution of **2.3** in 2% DMF- d_7 /CD $_2$ Cl $_2$ recorded at 10 K and 339.1 mT. Fit parameters: $A_f = -0.18 \pm 0.01$, $T_{1,f} = 0.56 \pm 0.03$ ms, $A_s = -0.53 \pm 0.01$, $T_{1,s} = 1.64 \pm 0.02$ ms.

2.7.2. Spin-Spin Relaxation

The decoherence of the spin superposition as quantified by the phase memory time was investigated for **2.1** – **2.3** over the temperature range 5 – 120 K on 1 mM solutions in 2% CD₂Cl₂/DMF-*d*₇. The decay of the Hahn echo measured at the magnetic field corresponding to the absorption maxima (g_2) in the EPR spectrum follows a biexponential profile; the temperature dependence for **2.1** is shown in Figure 2.35. The biexponential fit gives an estimate for the fast ($T_{M,f}$) and slow ($T_{M,s}$) relaxation processes, with the latter used as the qubit's decoherence parameter. The slow component is longest for **2.1** at 4.89(1) μ s, shortest for **2.2** at 2.07(2) μ s with **2.3** residing between these times at 3.63(2) μ s. These times are equal to or eclipse a swathe of $S = 1/2$ coordination complexes reported recently,⁴⁶ the few with phase memory times that surpass this have their composition and environment purged of nuclear spins.^{44, 59-61} The phase memory time displays no orientation dependence nor does it correlate with g -anisotropy as observed previously.^{44, 47} The variation within the series of **2.1** > **2.3** > **2.2** is directly correlated to the spin density at the metal center (vide supra). The major contributor to spin decoherence is electron-nuclear spin interaction, which is the dominant factor at very low temperatures (<30 K). The nuclear spin bath comprises protons on the anisyl substituents of the dithiolene ligand spin host, the protons and phosphorus atom (³¹P $I = 1/2$, 100% abundant) of the PPh₄⁺ counterion, and the ²H nuclei present in the solvent glass. The electronic structure of **2.1** – **2.3** differ in the degree of spin density distributed on the S₂C₂ unit of the dithiolene as opposed to the superchange center that is the metal ion. The pitch of the proton laden anisyl substituents to a non-conjugated orientation with the dithiolene core ensures ¹H interaction is dipolar and governed by the interspin distance. Here with the locus of the spin on the ligand, only the methoxy groups lie beyond the spin-diffusion barrier.³⁸⁻³⁹ As this distance is identical across the series, interactions from the ligand protons are essentially the same for all complexes. Likewise the metal hyperfine interaction observed in the cw spectra for **2.2** and **2.3** has negligible impact on $T_{M,s}$, as ¹⁹⁵Pt has the largest coupling but not the shortest decoherence time. Furthermore, shifting to the high-field hyperfine component about g_2 ($B_0 = 344.5$ mT) does not alter $T_{M,s}$ within experimental error (Table 2.5.). The distribution of spin density away from the metal ion and the disposition of the SOMO orthogonal to the plane of the complex facilitates greater interaction with the solvent medium. This can be described as an electrostatic interaction between deuterons and the electronegative S₂C₂ core of the spin host, as evidenced by the modulation in the Hahn echo decay (Figure 2.36.). This effect would be eliminated by solid dilution of these paramagnetic species, where co-crystallization of the paramagnetic complex in a diamagnetic analogue will cull the number of spin-active nuclei in the vicinity of the paramagnetic species.^{59, 62-64}

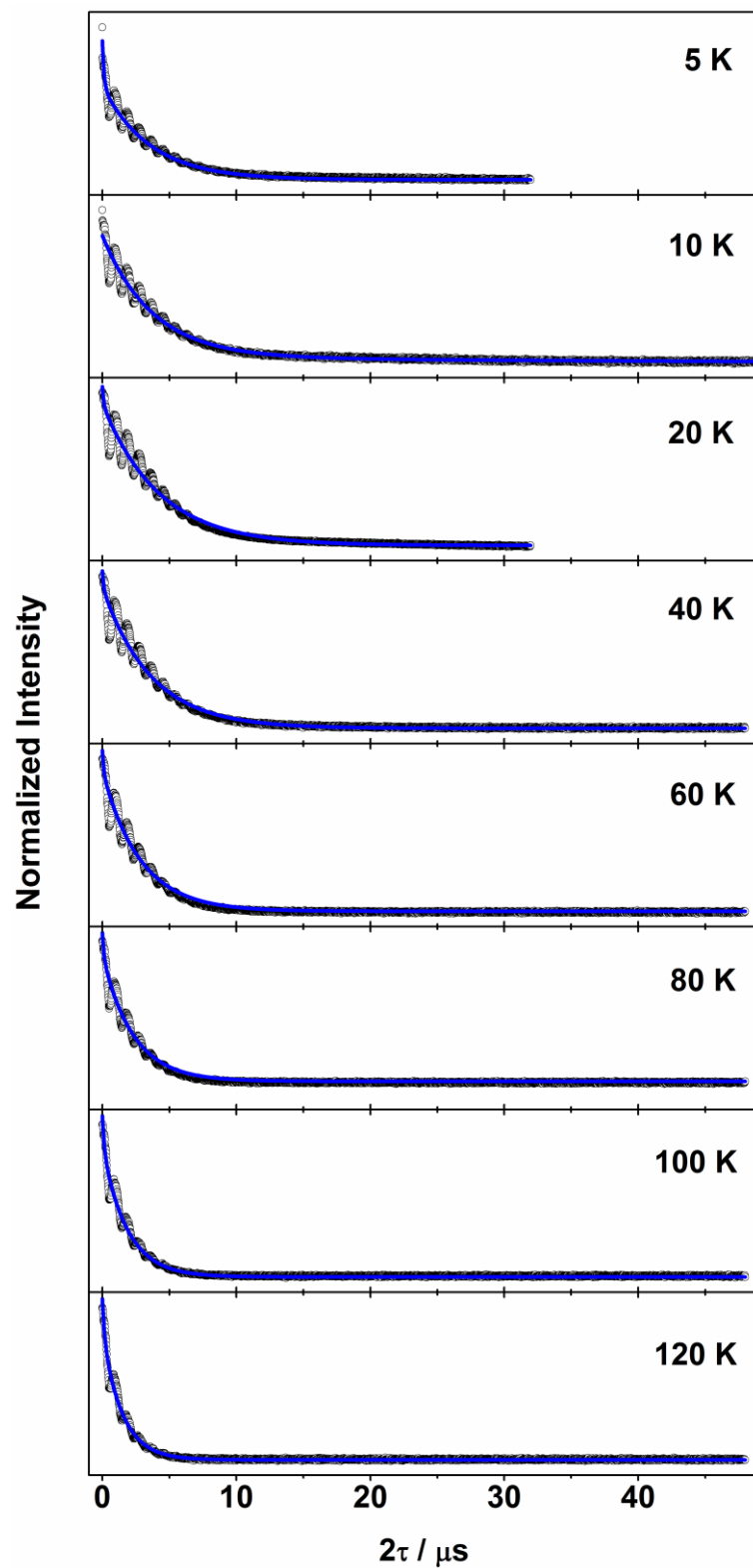


Figure 2.36. Hahn-echo decay curves (black line) and biexponential fit (blue line) of a 1 mM solution of **2.1** in 2% DMF- d_7 /CD $_2$ Cl $_2$ recorded at over the temperature range 5 – 120 K. Fit parameters are given in Table S6.

Table 2.6. Parameters of the biexponential fit functions for Hahn echo decay curves of 2.1, $B_0 = 340.6$ mT

T	A_f	$T_{M,f} / \mu\text{s}$	A_s	$T_{M,s} / \mu\text{s}$
5	0.65(3)	0.13(1)	1.344(8)	3.58(3)
10	0.089(6)	0.09(1)	0.512(1)	4.89(1)
20	0.30(4)	0.10(2)	2.540(6)	4.23(1)
40	0.14(2)	0.10(2)	1.181(4)	3.66(2)
60	0.30(3)	0.11(2)	2.026(8)	2.84(1)
80	0.41(3)	0.13(2)	2.27(1)	2.32(1)
100	1.05(4)	0.15(1)	4.38(2)	1.86(1)
120	1.33(5)	0.17(1)	4.94(3)	1.49(1)

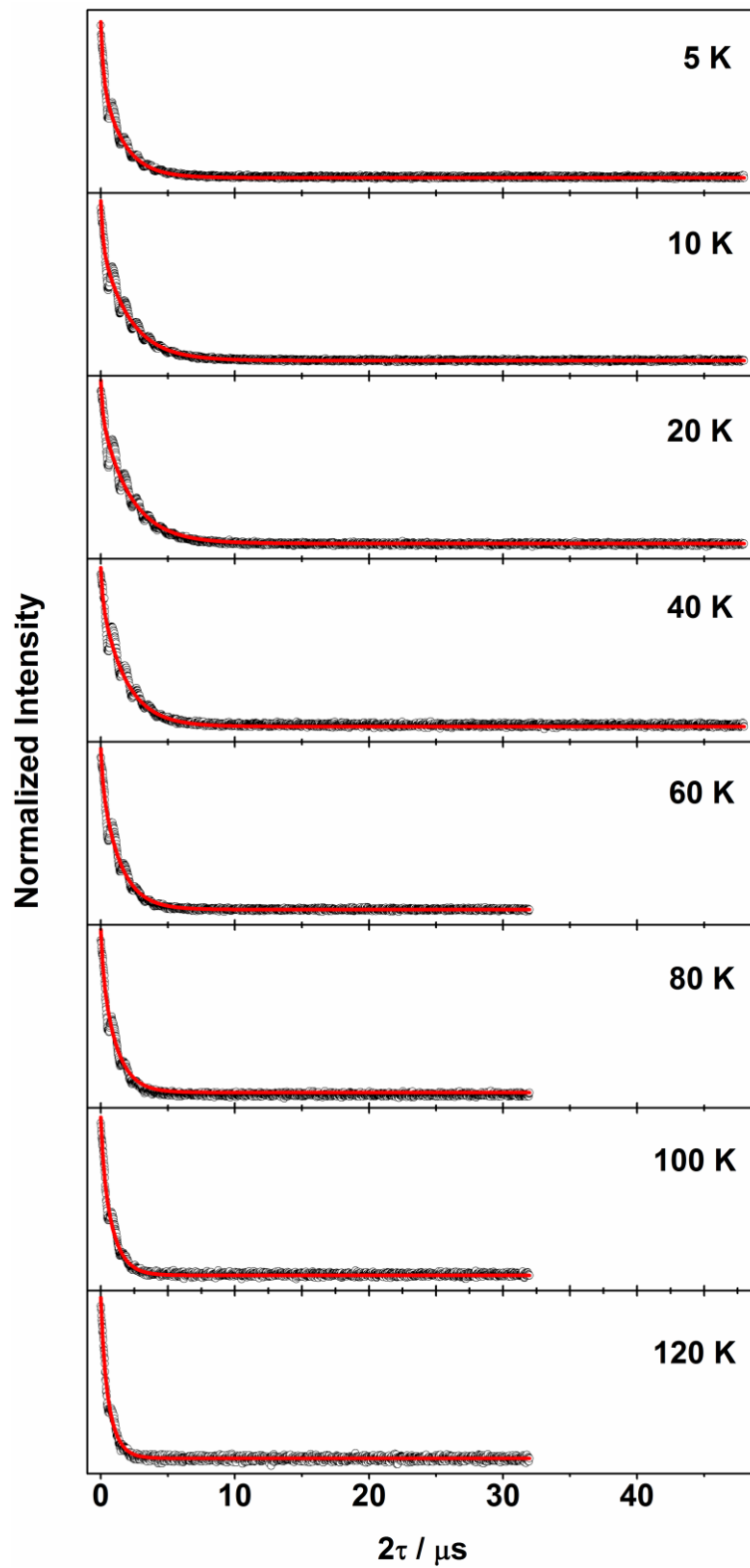


Figure 2.37. Hahn-echo decay curves (black line) and biexponential fit (blue line) of a 1 mM solution of **2.2** in 2% DMF- d_7 /CD $_2$ Cl $_2$ recorded at over the temperature range 5 – 120 K. Fit parameters are given in Table S7.

Table 2.7. Parameters of the biexponential fit functions for Hahn echo decay curves of 2.2, $B_0 = 343.3$ mT

T	A_f	$T_{M,f} / \mu\text{s}$	A_s	$T_{M,s} / \mu\text{s}$
5	0.374(8)	0.181(8)	0.707(6)	1.61(1)
10	0.31(1)	0.15(1)	0.887(5)	2.08(1)
20	0.19(1)	0.14(1)	0.763(5)	2.17(1)
40	0.136(7)	0.14(1)	0.631(3)	1.81(1)
60	0.36(2)	0.15(2)	1.68(2)	1.39(1)
80	0.30(2)	0.17(2)	1.25(2)	1.13(1)
100	0.37(3)	0.19(2)	1.40(3)	0.91(1)
120	0.44(6)	0.23(3)	1.29(6)	0.73(2)

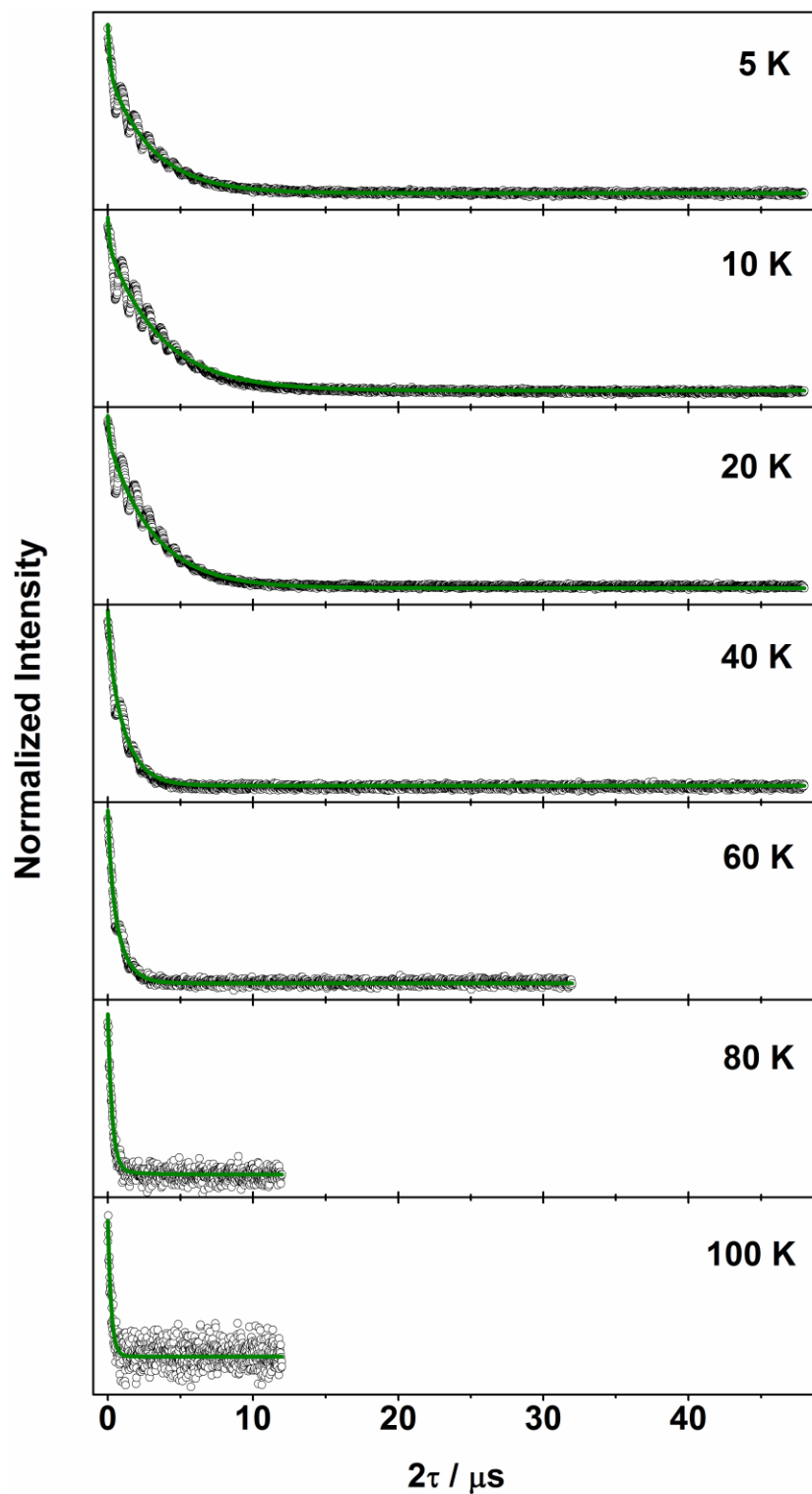


Figure 2.38. Hahn-echo decay curves (black line) and biexponential fit (green line) of a 1 mM solution of **2.3** in 2% DMF- d_7 /CD $_2$ Cl $_2$ recorded at $B_0 = 339.1$ mT over the temperature range 5 – 100 K. Fit parameters are given in Table S8.

Table 2.8. Parameters of the biexponential fit functions for Hahn echo decay curves of **2.3**, $B_0 = 339.1$ mT

T	A_f	$T_{M,f} / \mu\text{s}$	A_s	$T_{M,s} / \mu\text{s}$
5	0.167(6)	0.15(1)	0.450(2)	2.89(2)
10	0.092(8)	0.12(2)	0.491(2)	3.63(2)
20	0.12(1)	0.11(2)	0.825(3)	3.09(2)
40	0.36(2)	0.17(2)	1.56(2)	1.20(1)
60	0.81(7)	0.23(2)	1.90(8)	0.85(2)
80	1.03(6)	0.30(1)	3.0(3)	0.34(2)
100	1.54(4)	0.2(3)	4.0(2)	0.26(2)

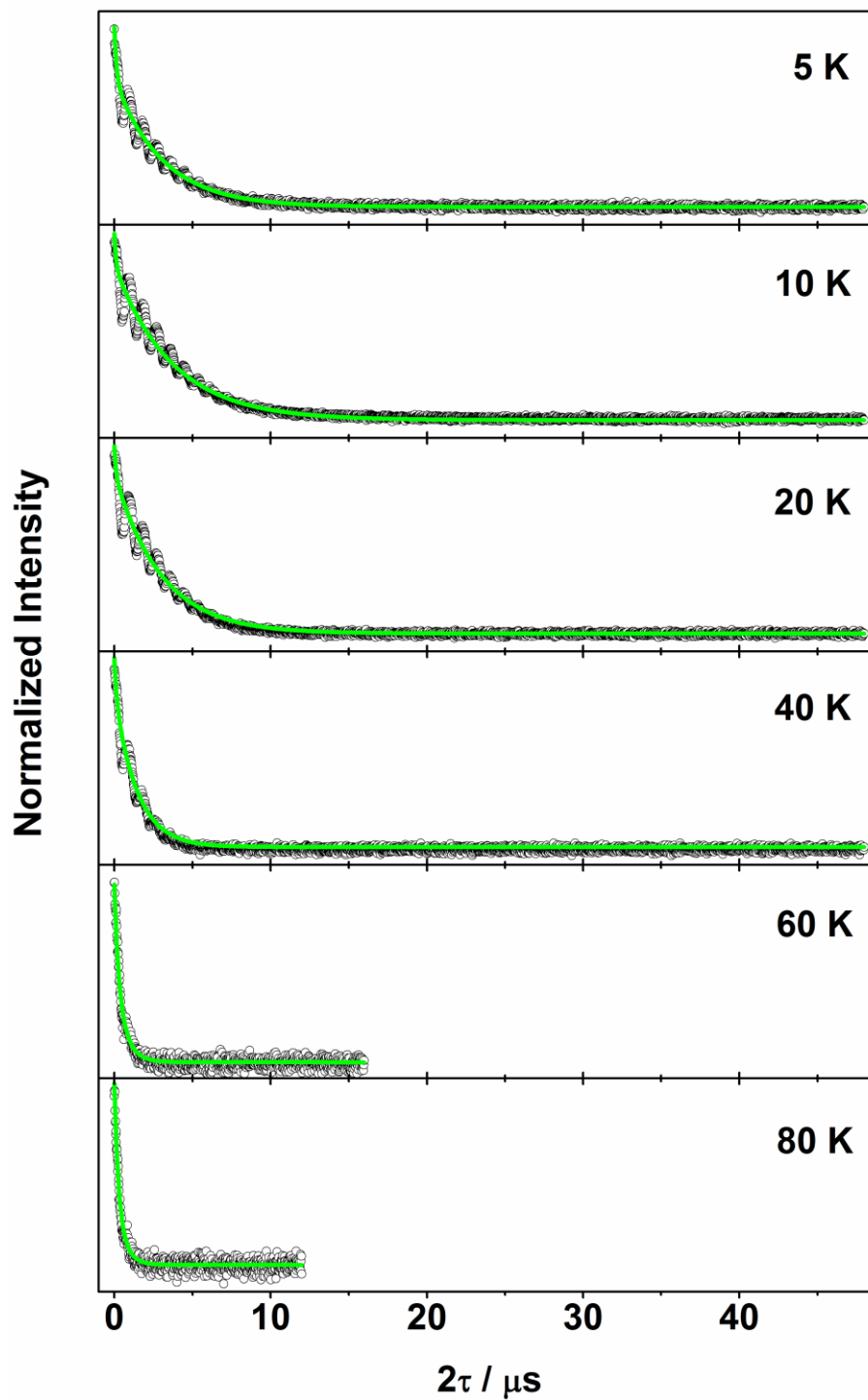


Figure 2.39. Hahn-echo decay curves (black line) and biexponential fit (green line) of a 1 mM solution of **2.3** in 2% DMF- d_7 /CD $_2$ Cl $_2$ recorded at $B_0 = 344.5$ mT over the temperature range 5 – 80 K. Fit parameters are given in Table S9.

Table 2.9. Parameters of the biexponential fit functions for Hahn echo decay curves of **2.3**, $B_0 = 344.5$ mT

T	A_f	$T_{M,f} / \mu\text{s}$	A_s	$T_{M,s} / \mu\text{s}$
5	0.157(6)	0.15(1)	0.386(2)	3.08(2)
10	0.099(8)	0.11(2)	0.491(2)	3.64(2)
20	0.15(2)	0.11(2)	1.068(4)	2.99(2)
40	0.29(2)	0.14(2)	1.33(1)	1.44(1)
60	0.36(2)	0.28(2)	3.11(8)	0.67(1)
80	6.0(2)	0.28(5)	3.0(2)	0.6(2)

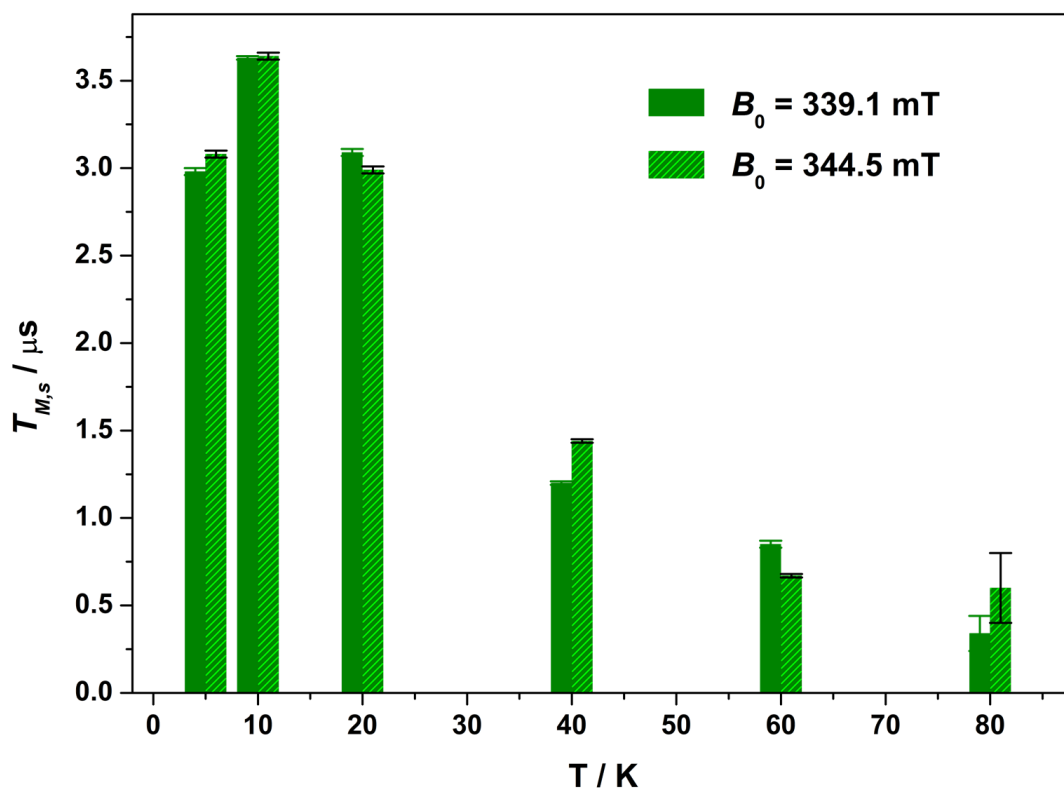


Figure 2.40. Temperature dependence of $T_{M,s}$ values for **2.3** comparing the $B_0 = 339.1$ mT corresponding to the maximum in the powder pattern (g_2) with $B_0 = 344.5$ mT corresponding to the high field hyperfine line of g_2 (see Figure S16). Error bars represent the standard deviation of the fit.

There is an overall increase in the relaxation rate with increasing temperature; however, the temperature dependence is markedly different for **2.3** compared to **2.1** and **2.2**. Although all exhibit a shorter $T_{M,s}$ at 5 K than 10 K due to a loss of solubility leading to inhomogeneity in the glass, there is a dramatic decrease for **2.3** above 20 K. Molecular motion, principally methyl group rotation is touted as the source of decoherence above 40 K where the frequency aligns with the experimental timescale, however this will be uniform across this series. Rather, the shortening of $T_{M,s}$ of **2.3** is driven by a comparable reduction in the spin-lattice relaxation time which is the ultimate limit for $T_{M,s}$.⁶⁵ This striking decrease in spin-lattice relaxation leads to $T_{M,f}$ and $T_{M,s}$ approaching parity and prevents measurement of the Hahn echo decay above 100 K.

The effect of the intramolecular spin coupling (J and D) on the phase memory time of the dicationic complex **[2.4]²⁺** has been measured at 20 K on a 1 mM sample of the complex electrochemically generated in CH_2Cl_2 solution containing 0.1 M $[\text{N}(\text{tBu}_4)]\text{PF}_6$ as electrolyte, i.e. a fully protiated environment. The result is compared to the corresponding monospin species, $[\text{Ni}(\text{adt})(\text{dppb})]^{1+}$, **[2.5]¹⁺**, which is a simplified representation of the bipartite system sans intramolecular spin coupling. A biexponential fit to the Hahn echo decay yielded $T_{M,s}$ of 3.39(4) μs for **[2.4]²⁺** $S = 1$ and 5.16(6) μs for **[2.5]¹⁺** $S = 1/2$, where the impact of intramolecular spin coupling in the former results in ca. 30% reduction of the phase memory time. The longer time for **[2.5]¹⁺** compared with **2.1** is consequence of the miniscule spin density (6%) on the nickel ion.

2.7.3. Rabi Oscillations

To demonstrate coherent spin control, echo-detected nutation experiments were performed by applying a microwave pulse of duration t_p to produce Rabi-like oscillations between two states that correspond to arbitrary superpositions of the electron spin. Confirmation that these are Rabi oscillations comes from the linear dependence of the oscillation frequency (Ω_R) with the applied microwave amplitude (B_1), which was varied by selecting microwave attenuations of 6, 10 and 14 dB. Changes in the oscillations were observed at $t_p > 400$ ns which were independent of the microwave attenuation and arise from the electron spin interacting with surrounding protons.⁶⁶ Interestingly, the Rabi frequency varies across the series in the order **2.2** > **2.3** > **2.1**, and possibly reflects the different static fields (B_0), however the difference is not significantly large to draw any meaningful conclusions.

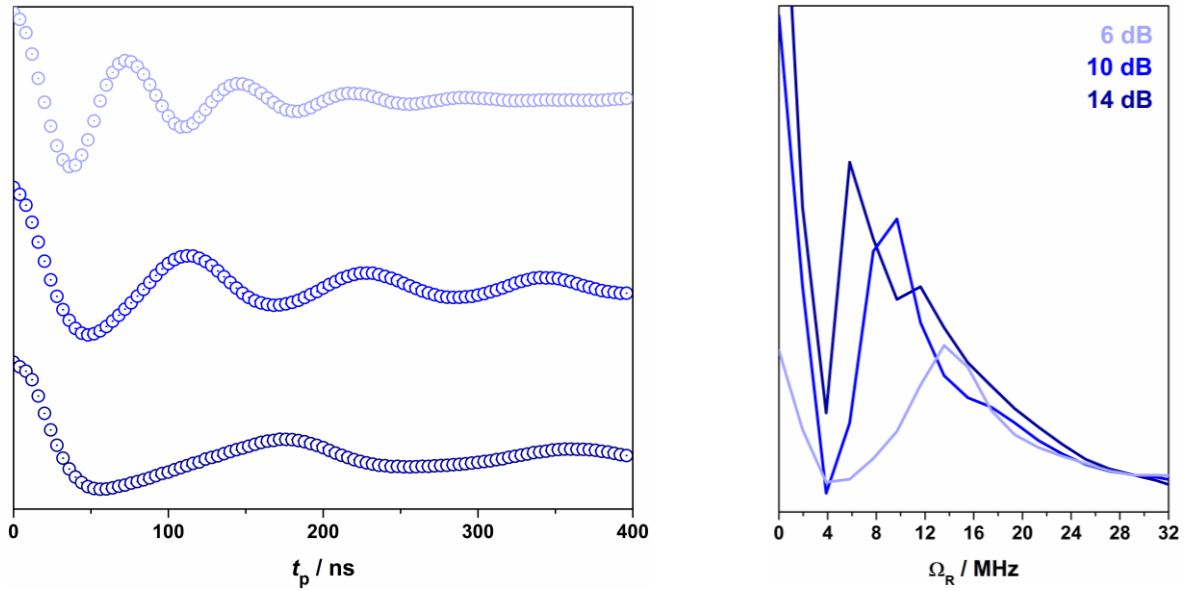


Figure 2.41. Rabi oscillations (left) and corresponding Rabi frequencies (right) for **2.1** $B_0 = 340.6$ mT and 10 K recorded variable power nutation measurements.

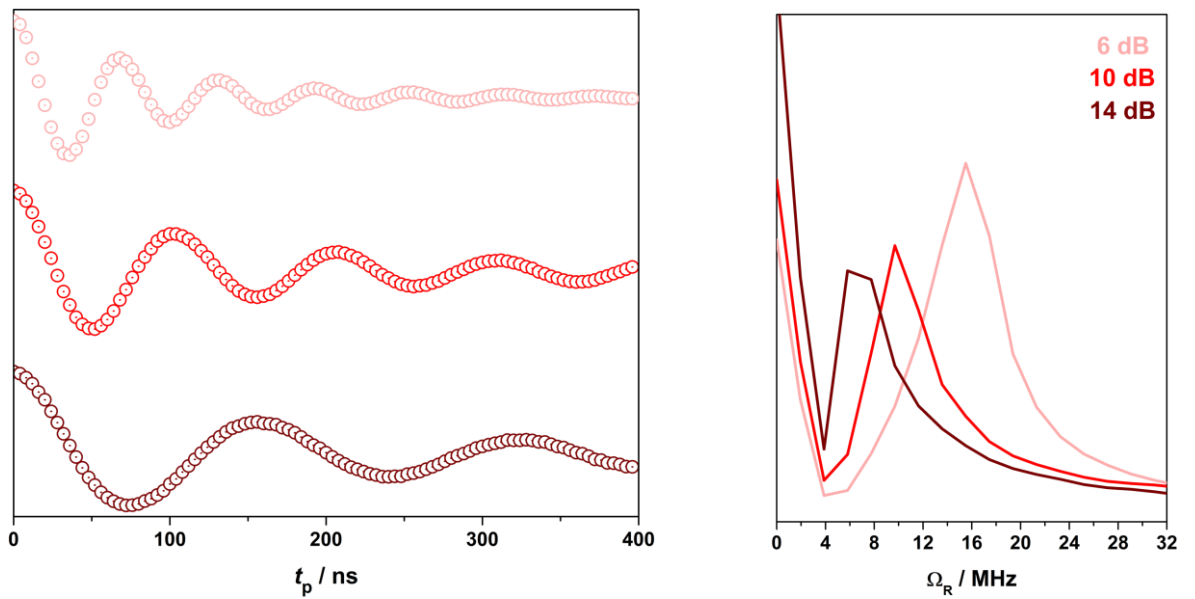


Figure 2.42. Rabi oscillations (left) and corresponding Rabi frequencies (right) for **2.2** $B_0 = 343.3$ mT and 10 K recorded variable power nutation measurements.

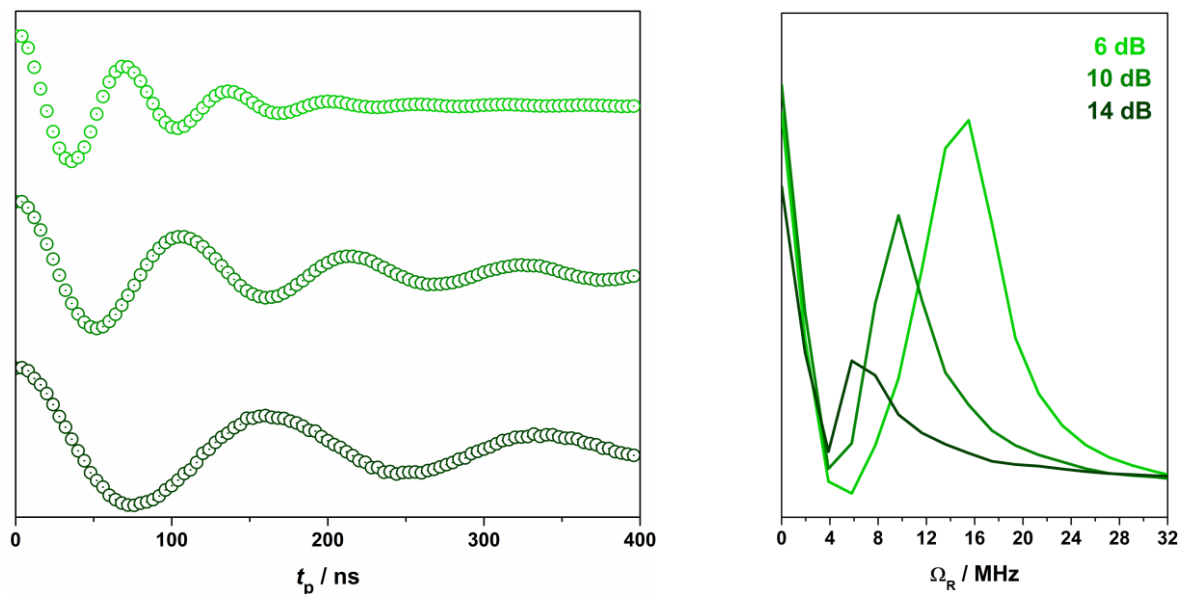


Figure 2.43. Rabi oscillations (left) and corresponding Rabi frequencies (right) for **2.3** at $B_0 = 339.1$ mT and 10 K recorded variable power nutation measurements.

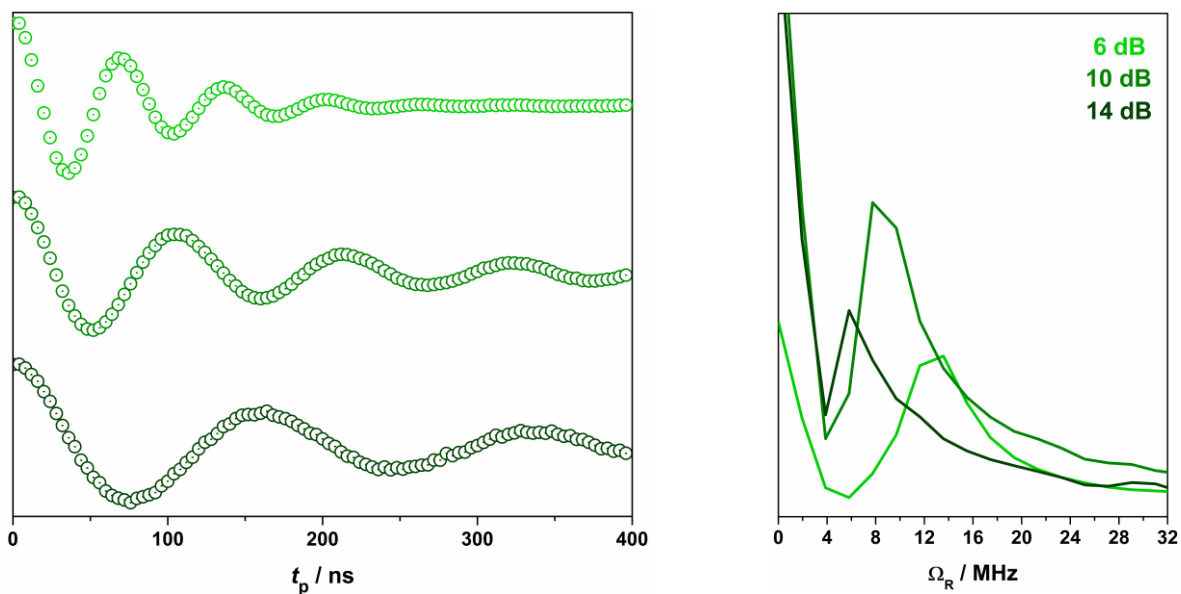


Figure 2.44. Rabi oscillations (left) and corresponding Rabi frequencies (right) for **2.3** at $B_0 = 344.5$ mT (corresponding to the high-field hyperfine line of g_2 ; Figure S16) and 10 K recorded variable power nutation measurements.

2.8. Conclusions

This work represents the first study that utilizes the organic component of a coordination complex – the ligand – as the spin host in a potential electron spin qubit. The redox-active dithiolene ligand bearing a nuclear-spin-free core affords long phase memory times approaching 5 μ s that are equal to or exceed those reported for related $S = 1/2$ complexes typically with V(IV) and Cu(II) paramagnetic ions.⁴⁶ The temperature dependence of the phase memory time is limited by spin-lattice relaxation, which is dramatically shortened when descending group 10 with the concomitant increase in the SOC constant for the diamagnetic metal ion. The efficacy of the dithiolene radical as a spin host was extended to heteroleptic complexes, which present a convenient synthetic route to preparing multi-qubit ensembles. The long phase memory time for the prototype two-qubit complex **[2.4]**²⁺ exceeds that for all other transition-metal-based two-qubit species at an equivalent temperature.⁶⁷⁻⁷² Moreover this molecular system delivers sufficiently long relaxation times negating any need to optimize the surrounding environment. Key to the challenge of single qubit addressability, we demonstrate electrochemical activation of the spin qubit which is an effective handle to switch the qubit “on” and “off” by applying an appropriate potential, which occurs on a timescale orders of magnitude faster than the lifetime of the superposition state.⁷³⁻⁷⁴ The ability to electrically activate individual qubits is achieved by altering the metal and ligand components of the molecule, and therein lies the ability to switch between various spin states and entanglement scenarios.

2.9.Experimental

2.9.1.Synthesis

The compounds $[M(\text{adt})_2]$ ($M = \text{Ni}, \text{Pd}, \text{Pt}$) were prepared following the procedure of Schrauzer and Mayweg.⁷⁵ $[\text{PPh}_4][\text{BH}_4]$ was synthesized following the literature method.⁷⁶ Solvents either were dried with a system of drying columns from the Glass Contour Company (CH_2Cl_2 , hexanes) or freshly distilled according to standard procedures (CH_3OH).⁷⁷ Dichloromethane- d_2 and N,N -dimethylformamide- d_7 were degassed by six successive freeze pump thaw cycles and dried over 3 Å molecular sieves prior to use.

$[\text{PPh}_4][M(\text{adt})_2]$ { $M = \text{Ni}$ (2.1), Pd (2.2), Pt (2.3)}. A 50 mL Schlenk flask containing $[M(\text{adt})_2]$ (0.1 mmol) dissolved in CH_2Cl_2 (10 mL) was treated with $[\text{PPh}_4][\text{BH}_4]$ (0.1 mmol) and stirred for 30 min at ambient temperature. The solvent was removed under reduced pressure, and the residue was recrystallized from $\text{CH}_2\text{Cl}_2/\text{CH}_3\text{OH}$ to give a microcrystalline product. Yield: 84% (2.1), 89% (2.2), 87% (2.3). ESI mass spectrometry confirmed the complex ion $[M]^-$ in the negative ion mode which was accompanied with the singular presence of PPh_4^+ in the positive ion mode. Purity was confirmed by recording the electronic spectra of 2.1 – 2.3 which are distinct from their charge-neutral precursors (Figure 2.9).

2.9.2.Physical Characterization and Theoretical

X-ray Crystallographic Data Collection and Structure Refinement. Diffraction quality crystals of 2.1 – 2.3 were obtained by slow diffusion of hexanes into a concentrated dichloromethane solution of the complex. The crystals were coated with paratone oil and mounted on the end of a nylon loop attached to the end of the goniometer. Data were collected with a Bruker SMART APEX CCD diffractometer equipped with a Kryoflex attachment supplying a nitrogen stream at 150 K. Structure solution and refinement were carried out with SHELXS-97⁷⁸ and SHELXL-97⁷⁹ using the WinGX⁸⁰ software package. Corrections for incident and diffracted beam absorption effects were applied using empirical absorption corrections.⁸¹ All non-hydrogen atoms were refined with anisotropic thermal parameters. The positions of hydrogen atoms of PPh_4^+ counterions and disordered CH_2Cl_2 solvent content were calculated based on stereochemical considerations and refined isotropically. The disordered H_2O content was identified in the DF map and refined with isotropic thermal parameters. However, the hydrogen atoms associated with the H_2O content were not possible to be located from the DF map and have been omitted from the refinement cycles. Final unit cell data and refinement statistics are collected in Table 2.10. CCDC numbers 1851991–1851993 contains the supplementary crystallographic data for 2.1 – 2.3. These data can be obtained free of charge from The Cambridge Crystallographic Data Center via www.ccdc.cam.ac.uk/data_request/cif.

Table 2.10. Crystallographic Data for compounds in Chapter 2

compound	PPh ₄ [Ni(adt) ₂]	PPh ₄ [Pd(adt) ₂]	PPh ₄ [Pt(adt) ₂].CH ₂ Cl ₂ .2H ₂ O
formula	C ₅₆ H ₄₈ O ₄ PS ₄ Ni	C ₅₆ H ₄₈ O ₄ PS ₄ Pd	C ₅₇ H ₅₄ O ₆ PS ₄ Pt
fw	1002.86	1050.55	1260.20
T, K	150(2)	150(2)	150(2)
λ, Å	0.71073	0.71073	0.71073
2θ range, deg	2.72 – 52.88	1.64 – 52.74	1.62 – 52.98
crystal system	triclinic	triclinic	triclinic
space group	<i>P</i> $\bar{1}$	<i>P</i> $\bar{1}$	<i>P</i> $\bar{1}$
a, Å	11.935(5)	14.424(5)	13.832(3)
b, Å	13.947(6)	15.323(6)	15.761(4)
c, Å	15.696(7)	25.029(9)	16.441(4)
α, deg	82.077(5)	86.403(5)	71.074(3)
β, deg	73.662(5)	89.534(5)	83.128(3)
γ, deg	79.995(5)	64.752(4)	80.342(3)
V, Å ³	2458(2)	4992(3)	3334(1)
Z	2	4	2
ρ, g cm ⁻³	1.355	1.398	1.255
μ, mm ⁻¹	0.644	0.617	2.374
crystal size	0.08 × 0.10 × 0.20	0.15 × 0.17 × 0.18	0.05 × 0.05 × 0.10
color, habit	green block	orange block	orange block
reflections collected	35536	60789	56198
independent data	10095	20329	13795
restraints	0	0	0
parameters refined	595	1197	663
GoF ^[a]	1.077	1.047	1.061
R1, ^[b,c] wR2 ^[c,d]	0.0262, 0.0704	0.0315, 0.0771	0.0577, 0.1866
R1, ^[b,e] wR2 ^[d,e]	0.0325, 0.0784	0.0466, 0.0853	0.0713, 0.2031
largest diff. peak, e Å ⁻³	0.390	0.920	3.443
largest diff. hole, e Å ⁻³	-0.257	-0.493	-0.608

^[a] GoF = $\{\sum[w(F_o^2 - F_c^2)^2]/(n - p)\}^{1/2}$, where n = number of reflections and p is the total number of parameters refined. ^[b] R1 = $\sum||F_o| - |F_c||/\sum|F_o|$. ^[c] R indices for data cut off at $I > 2\sigma(I)$. ^[d] wR2 = $\{\sum[w(F_o^2 - F_c^2)^2]/\sum[w(F_o^2)^2]\}^{1/2}$, where $w = 1/[\sigma^2(F_o^2) + (aP)^2 + bP]$, $P = (F_o^2 + 2F_c^2)/3$. ^[e] R indices for all data.

EPR Spectroscopy. Continuous wave X-band EPR spectra was recorded on a Bruker ELEXSYS E500 spectrometer. Spectra were simulated using the simulation package XSOPHE;⁸² fluid solution spectra using the spin-Hamiltonian $\hat{H} = g\mu_B BS + aSI$, and frozen solution spectra using the spin-Hamiltonian $\hat{H} = \mu_B \mathbf{B} \cdot \mathbf{g} \cdot \mathbf{S} + \mathbf{S} \cdot \mathbf{A} \cdot \mathbf{I}$, where \mathbf{g} and \mathbf{A} are the 3×3 electron Zeeman and magnetic hyperfine interaction matrices, respectively. A Gaussian lineshape and distribution of g - and A -values (strain) were employed to account for the linewidth variation.

Pulsed X-band EPR data were measured using a Bruker ELEXSYS E580 spectrometer equipped with an Oxford Instruments CF935 continuous Helium flow cryostat. Samples were prepared by dissolving **2.1** – **2.3** in CD_2Cl_2 to a concentration of 1 mM, loading into 3.8 mm o.d. quartz EPR tubes and adding 2% (v/v) $\text{DMF-}d_7$ to aid glassing. The solution samples were degassed via three freeze-pump-thaw cycles, followed by flame sealing. Samples of **2.4** and **2.5** were prepared by bulk electrolysis of a 1 mM dichloromethane solution containing 0.2 M $[\text{N}(^n\text{Bu})_4]\text{PF}_6$ as electrolyte. The electrochemical cell was degassed prior to the experiment and the electrolysis conducted under an inert atmosphere. ESE-detected EPR spectra were collected at 10 K (**2.1** – **2.3**) and 20 K (**2.4** and **2.5**) using a Hahn echo pulse sequence ($\pi/2 - \tau - \pi - \tau - \text{echo}$) with a 4-step phase cycle, where $\pi/2 = 16$ ns, $\pi = 32$ ns and $\tau = 400$ ns. Simulations were performed as using XSOPHE⁸² using the aforementioned spin-Hamiltonian. Phase memory times (T_M) were also measured with a Hahn echo pulse sequence. Decay curves were collected at field positions indicated on ESE spectra. Acquisition times were set to capture the top half of the spin echo and the acquired echo was integrated. The data were phased by maximizing the sum of the data points in the real components of the spectrum and fit to the biexponential function $I(\tau) = y_0 + A_f \exp(-\tau/T_{M,f}) + A_s \exp(-\tau/T_{M,s})$, where f and s indicate fast and slow processes, respectively. Spin-lattice relaxation times (T_1) for **2.1** – **2.3** were collect at 10 K following the inversion recovery sequence ($\pi - T - \pi/2 - \tau - \pi - \tau - \text{echo}$) with 4-step phase cycling in which $\pi/2 = 16$ ns, $\pi = 32$ ns, and T incremented from a starting value of 100 ns. The value of τ was selected to correspond to the maximum in the ESEEM at 400 ns. Acquisition times were set to capture the top half of the spin echo and the acquired echo was integrated. The data were phased by maximizing the sum of the data points in the real components of the spectrum and fit to the biexponential function $I(\tau) = y_0 + A_f \exp(-\tau/T_{1,f}) + A_s \exp(-\tau/T_{1,s})$. Nutation measurements were performed at three different microwave powers with a nutation pulse of variable length (tipping) pulse followed by a Hahn echo sequence ($t_p - T - \pi/2 - \tau - \pi - \tau - \text{echo}$). Data were collected employing 4-phase cycling, in which in which $\pi/2 = 16$ ns, $\pi = 32$ ns and $\tau = 400$ ns for nutation pulse lengths $T = 400$ ns and 1800 ns. The tipping pulse, t_p , is augmented in 4 ns increments from a starting value of 4 ns. Nutation data was processed by subtracting a stretched exponential baseline from the echo decay,

then zero-filling with 1024 or 2048 points, followed by a Fourier transform with a Hamming window.

Other Physical Methods. Cyclic voltammogrammetry measurements were performed with a Metrohm Autolab P128 potentiostat. The electrode configuration consisted of a 2 mm glassy carbon working electrode, a platinum auxiliary electrode and a reference electrode consisting of Ag/AgNO₃ (0.01 M in MeCN) incorporated into a salt bridge containing supporting electrolyte (to minimize Ag⁺ leakage). Solutions of the complexes (1–2 mM) were prepared in dichloromethane containing 0.1 M [N(ⁿBu)₄]PF₆ as electrolyte. All reduction potentials are referenced versus the ferrocenium/ferrocene (Fc⁺⁰) couple. Electronic absorption spectra were recorded on a Shimadzu UVA 3600 spectrophotometer (range 200–1600 nm). Electrospray ionization (ESI) mass spectra were obtained on a Bruker micrOTOF-Q mass spectrometer.

Calculations. All calculations in this work were performed with the electronic structure program ORCA.⁸³ Geometry optimizations were carried out using the BP86 functional with dichloromethane as solvent.⁸⁴⁻⁸⁵ A segmented all-electron relativistically contracted basis set of triple- ζ -quality (def2-TZVPP) was used for all atoms.⁸⁶ A scalar relativistic correction was applied using the zeroth-order regular approximation (ZORA) method⁸⁷⁻⁸⁹ as implemented by van Wüllen.⁹⁰ In the context of ZORA, a one center approximation has been shown to introduce only minor errors to the final geometries. Auxiliary basis sets for all complexes used to expand the electron density in the calculations were chosen to match the orbital basis. The conductor like screening model (COSMO) was used for all calculations.⁹¹ The self-consistent field calculations were tightly converged ($1 \times 10^{-8} E_h$ in energy, $1 \times 10^{-7} E_h$ in the density change, and 1×10^{-7} in the maximum element of the DIIS⁹²⁻⁹³ error vector). The geometry search for all complexes was carried out in redundant internal coordinates without imposing geometry constraints. The property calculations at the optimized geometries were done with the PBE0 hybrid functional⁹⁴⁻⁹⁵ and the RIJCOSX algorithm to expedite calculation of the Hartree-Fock exchange.⁹⁶⁻⁹⁷ In this case the same basis sets were used but with enhanced integration accuracy (SPECIALGRIDINTACC 10) for the metal and sulfur atoms. Calculation of the **g**-matrix included a larger the integration grid (Grid5) and fully decontracted basis sets.⁹⁸⁻⁹⁹

We used the broken symmetry (BS) approach to describe our computational result of [2.4]²⁺.¹⁰⁰⁻¹⁰⁴ We adopt the following notation: the given system was divided into two fragments. The notation BS(*m*,*n*) refers then to a broken symmetry state with *m* unpaired α -spin electrons essentially on fragment 1 and *n* unpaired β -spin electrons localized on fragment 2. In most cases, fragments 1 and 2 correspond to the metal and the ligands, respectively. In this notation the standard high-spin, open-shell solution is written as BS(*m*

+ $n,0$). The BS(m,n) notation refers to the initial guess to the wave function. The variational process does, however, have the freedom to converge to a solution of the form BS($m - n,0$) in which effectively the $n\beta$ -spin electrons pair up with $n < m\alpha$ -spin electrons on the partner fragment. Such a solution is then a standard $M_s \equiv (m - n)/2$ spin-unrestricted Kohn-Sham solution. As explained elsewhere,¹⁰⁵ the nature of the solution is investigated from the corresponding orbital transformation (COT) which, from the corresponding orbital overlaps, displays whether the system should be described as a spin-coupled or a closed-shell solution. The exchange coupling constant J was calculated on broken-symmetry geometries using Eq. 1,¹⁰⁶⁻¹⁰⁷ and assuming the spin-Hamiltonian Eq. 2 is valid.

$$J = \frac{E_{HS} - E_{BS}}{\langle \hat{S}^2 \rangle_{HS} - \langle \hat{S}^2 \rangle_{BS}} \quad (1)$$

$$\hat{H} = -2J\hat{S}_A \cdot \hat{S}_B \quad (2)$$

Corresponding¹⁰⁵ canonical orbitals and density plots were constructed using the program Molekel.¹⁰⁸

2.10.References

1. Clark, R. E. D., *Analyst* **1936**, 61 (721), 242-245.
2. Clark, R. E. D., *Analyst* **1937**, 62 (738), 661-663.
3. Metal 1,2-Dithiolene and Related Complexes. In *Progress in Inorganic Chemistry*, 1968; pp 49-221.
4. Schrauzer, G. N.; Mayweg, V., *Journal of the American Chemical Society* **1962**, 84 (16), 3221-3221.
5. Davison, A.; Edelstein, N.; Holm, R. H.; Maki, A. H., *Journal of the American Chemical Society* **1963**, 85 (13), 2029-2030.
6. Davison, A.; Edelstein, N.; Holm, R. H.; Maki, A. H., *Inorganic Chemistry* **1963**, 2 (6), 1227-1232.
7. Gray, H. B.; Williams, R.; Bernal, I.; Billig, E., *Journal of the American Chemical Society* **1962**, 84 (18), 3596-3597.
8. Electrochemical and Chemical Reactivity of Dithiolene Complexes. In *Dithiolene Chemistry*, 2003; pp 267-314.
9. Structures and Structural Trends in Homoleptic Dithiolene Complexes. In *Dithiolene Chemistry*, 2003; pp 55-110.
10. The Electronic Structure and Spectroscopy of Metallo-Dithiolene Complexes. In *Dithiolene Chemistry*, 2003; pp 111-212.
11. Geiger, W. E.; Barrière, F.; LeSuer, R. J.; Trupia, S., *Inorganic Chemistry* **2001**, 40 (11), 2472-2473.
12. Nomura, M.; Takayama, C.; Kajitani, M., *Inorganica Chimica Acta* **2004**, 357 (8), 2294-2300.
13. Mogesa, B.; Perera, E.; Rhoda, H. M.; Gibson, J. K.; Oomens, J.; Berden, G.; van Stipdonk, M. J.; Nemykin, V. N.; Basu, P., *Inorganic Chemistry* **2015**, 54 (16), 7703-7716.
14. Pilia, L.; Marinotto, D.; Pizzotti, M.; Tessore, F.; Robertson, N., *The Journal of Physical Chemistry C* **2016**, 120 (34), 19286-19294.
15. Lowe, N. D.; Garner, C. D., *Journal of the Chemical Society, Dalton Transactions* **1993**, (22), 3333-3340.
16. Mukhopadhyay, S.; Ray, D., *Journal of the Chemical Society, Dalton Transactions* **1993**, (7), 1159-1162.
17. Lieffrig, J.; Jeannin, O.; Auban-Senzier, P.; Fourmigué, M., *Inorganic Chemistry* **2012**, 51 (13), 7144-7152.
18. Conner, K. M.; Perugini, A. L.; Malabute, M.; Brown, S. N., *Inorganic Chemistry* **2018**, 57 (6), 3272-3286.

19. Obanda, A.; Valerius, K.; Mague, J. T.; Sproules, S.; Donahue, J. P., *Organometallics* **2020**, *39* (15), 2854-2870.
20. Obanda, A.; Martinez, K.; Schmehl, R. H.; Mague, J. T.; Rubtsov, I. V.; MacMillan, S. N.; Lancaster, K. M.; Sproules, S.; Donahue, J. P., *Inorganic Chemistry* **2017**, *56* (17), 10257-10267.
21. Chandrasekaran, P.; Greene, A. F.; Lillich, K.; Capone, S.; Mague, J. T.; DeBeer, S.; Donahue, J. P., *Inorganic Chemistry* **2014**, *53* (17), 9192-9205.
22. Mou, W.-Y.; Li, T.; Xie, B.; Zhang, D.-L.; Lai, C.; Deng, C.-L.; Cao, J.-X.; Bai, X.-X.; Liu, X.-Q., *Inorganica Chimica Acta* **2020**, *507*, 119587.
23. Liu, X.-F.; Li, R.-X.; Ren, X.-T.; Yin, Y.-B.; Mei, S.-K.; Liu, T.; Yan, J., *Journal of Catalysis* **2017**, *348*, 314-320.
24. Arumugam, K.; Selvachandran, M.; Obanda, A.; Shaw, M. C.; Chandrasekaran, P.; Caston Good, S. L.; Mague, J. T.; Sproules, S.; Donahue, J. P., *Inorganic Chemistry* **2018**, *57* (7), 4023-4038.
25. Bowmaker, G. A.; Boyd, P. D. W.; Campbell, G. K., *Inorganic Chemistry* **1982**, *21* (6), 2403-2412.
26. Bowmaker, G. A.; Williams, J. P., *Journal of the Chemical Society, Dalton Transactions* **1993**, (23), 3593-3600.
27. Kambe, T.; Tsukada, S.; Sakamoto, R.; Nishihara, H., *Inorganic Chemistry* **2011**, *50* (15), 6856-6858.
28. Arumugam, K.; Shaw, M. C.; Chandrasekaran, P.; Villagrán, D.; Gray, T. G.; Mague, J. T.; Donahue, J. P., *Inorganic Chemistry* **2009**, *48* (22), 10591-10607.
29. Shin, K.-S.; Son, K.-I.; Kim, J. I.; Hong, C. S.; Suh, M.; Noh, D.-Y., *Dalton Transactions* **2009**, (10), 1767-1775.
30. Shin, K.-S.; Noh, D.-Y., *Bulletin of the Korean Chemical Society* **2004**, *25* (1), 130-132.
31. Arumugam, K.; Selvachandran, M.; Obanda, A.; Shaw, M. C.; Chandrasekaran, P.; Caston Good, S. L.; Mague, J. T.; Sproules, S.; Donahue, J. P., *Inorgic Chemistry* **2018**, *57*, 4023.
32. Arumugam, K.; Shaw, M. C.; Chandrasekaran, P.; Villagrán, D.; Gray, T. G.; Mague, J. T.; Donahue, J. P., *Inorgic Chemistry* **2009**, *48*, 10591.
33. Arumugam, K.; Shaw, M. C.; Mague, J. T.; Bill, E.; Sproules, S.; Donahue, J. P., *Inorgic Chemistry* **2011**, *50*, 2995.
34. Arumugam, K.; Yu, R.; Villagrán, D.; Gray, T. G.; Mague, J. T.; Donahue, J. P., *Inorgic Chemistry* **2008**, *47*, 5570.
35. Fox, M. A.; Chandler, D. A., *Advanced Materials* **1991**, *3*, 381.
36. Zardadoulas, A.; Field, M. J.; Papatriantafyllopoulou, C.; Fize, J.; Artero, V.; Mitsopoulou, C. A., *Inorgic Chemistry* **2016**, *55*, 432.

37. Sproules, S.; Banerjee, P.; Weyhermüller, T.; Yan, Y.; Donahue, J. P.; Wieghardt, K., *Inorgic Chemistry* **2011**, *50*, 7106.
38. Graham, M. J.; Krzyaniak, M.; Wasieleski, M. R.; Freedman, D. E., *Inorgic Chemistry* **2017**, *56*, 8106.
39. Graham, M. J.; Yu, C.; Krzyaniak, M.; Wasieleski, M. R.; Freedman, D. E., *Journal of the American Chemical Society* **2017**, *139*, 3196.
40. Ray, K.; Petrenko, T.; Wieghardt, K.; Neese, F., *Dalton Transactions* **2007**, 1552.
41. Sproules, S.; Wieghardt, K., *Coordination Chemistry Reviews* **2011**, *255*, 837.
42. Kirmse, R.; Möller, E.; Seitz, C.; Reinhold, J., *Zeitschrift für Anorganische und Allgemeine Chemie* **1997**, *627*, 159.
43. Sarma, D. D., *Proc. Indian Academic Society (Chem. Sci.)* **1981**, *90*, 19.
44. Bader, K.; Schlindein, S. H.; Gudat, D.; van Slageren, J., *Physical Chemistry Chemical Physics* **2017**, *19*, 2525.
45. Bendix, J.; Brorson, M.; Schäffer, C. E., *Inorgic Chemistry* **1993**, *32*, 2838.
46. Sproules, S., Molecules as Electron Spin Qubits. In *Electron Paramagnetic Resonance*, Chechik, V.; Murphy, D. M., Eds. The Royal Society of Chemistry: Cambridge, UK, 2017; Vol. 25, pp 61-97.
47. Du, J.-L.; Eaton, G. R.; Eaton, S. S., *Applied Magnetic Resonance* **1994**, *6*, 373.
48. Du, J.-L.; Eaton, G. R.; Eaton, S. S., *Journal of Magnetic Resonance Series A* **1996**, *119*, 240.
49. Husted, R.; Du, J.-L.; Eaton, G. R.; Eaton, S. S., *Magnetic Resonance Chemistry* **1995**, *33*, S66.
50. Kato, Y.; Myers, R. C.; Gossard, A. C.; Awschalom, D. D., *Science* **2003**, *306*, 1910.
51. Liu, L.; Pai, C.-F.; Li, Y.; Tseng, H. W.; Ralph, D. C.; Burhman, R. A., *Science* **2012**, *336*, 555.
52. Ganichev, S. D.; Ivchenko, E. L.; Bel'kov, V. V.; Tarasenko, S. A.; Sollinger, M.; Weiss, D.; Wegscheider, W.; Prettl, W., *Nature* **2002**, *417*, 153.
53. Lunghi, A.; Totti, F.; Sessoli, R.; Sanvito, S., *Nature Communications* **2017**, *8*, 14620.
54. Kirmse, R.; Stach, J.; Dietzsch, W.; Steimecke, G.; Hoyer, E., *Inorgic Chemistry* **1980**, *19*, 2679.
55. Sato, H.; Kathirvelu, V.; Fielding, A. J.; Blinco, J. P.; Micallef, A. S.; Bottle, S. E.; Eaton, S. S.; Eaton, G. R., *Molecular Physics* **2007**, *105*, 2137.
56. Benítez, L. A.; Sierra, J. F.; Saverio Torres, W.; Arrighi, A.; Bonell, F.; Costache, M. V.; Valenzuela, S. O., *Nature Physics* **2018**, *14*, 303.
57. Yan, W.; Txoperena, O.; Llopis, R.; Dery, H.; Hueso, L. E.; Casanova, F., *Nature Communications* **2016**, *7*, 13372.

58. Garcia, J. H.; Vila, M.; Cummings, A. W.; Roche, S., *Chemical Society Reviews* **2018**, *47*, 3359.
59. Bader, K.; Dengler, D.; Lenz, S.; Endeward, B.; Jiang, S.-D.; Neugebauer, P.; van Slageren, J., *Nature Communications* **2014**, *5*, 5304.
60. Zadrozny, J. M.; Niklas, J.; Poluektov, O. G.; Freedman, D. E., *ACS Central Science* **2015**, *1*, 488.
61. Yu, C.; Graham, M. J.; Zadrozny, J. M.; Niklas, J.; Krzyaniak, M.; Wasieleski, M. R.; Poluektov, O. G.; Freedman, D. E., *Journal of the American Chemical Society* **2016**, *138*, 14678.
62. Atzori, M.; Morra, E.; Tesi, L.; Albino, A.; Chiesa, M.; Sorace, L.; Sessoli, R., *Journal of the American Chemical Society* **2016**, *138*, 11234.
63. Atzori, M.; Tesi, L.; Morra, E.; Chiesa, M.; Sorace, L.; Sessoli, R., *Journal of the American Chemical Society* **2016**, *138*, 2154.
64. Lenz, S.; Bader, K.; Bamberger, H.; van Slageren, J., *Chemical Communications* **2017**, *53*, 4477.
65. Warner, M.; Din, S.; Tupitsyn, I. S.; Morley, G. W.; Stoneham, A. M.; Gardener, J. A.; Wu, Z.; Fisher, A. J.; Heutz, S.; Kay, C. W. M.; Aeppli, G., *Nature* **2013**, *503*, 504.
66. Hartmann, S. R.; Hahn, E. L., *Physical Reviews* **1962**, *128*, 2042.
67. Fernandez, A.; Moreno Pineda, E.; Muryn, C. A.; Sproules, S.; Moro, F.; Timco, G. A.; McInnes, E. J. L.; Winpenny, R. E. P., *Angewandte Chemie International Edition* **2015**, *54*, 10858.
68. Ferrando-Soria, J.; Magee, S. A.; Chiesa, A.; Caretta, S.; Santini, P.; Vitorica-Yrezabal, I. J.; Tuna, F.; Whitehead, G. F. S.; Sproules, S.; Lancaster, K. M.; Barra, A.-L.; Timco, G. A.; McInnes, E. J. L.; Winpenny, R. E. P., *Chem* **2016**, *1*, 727.
69. Ferrando-Soria, J.; Moreno Pineda, E.; Chiesa, A.; Fernandez, A.; Magee, S. A.; Caretta, S.; Santini, P.; Vitorica-Yrezabal, I. J.; Tuna, F.; Timco, G. A.; McInnes, E. J. L.; Winpenny, R. E. P., *Nature Communications* **2016**, *7*, 11377.
70. Lutz, P.; Marx, R.; Dengler, D.; Kromer, A.; van Slageren, J., *Molecular Physics* **2013**, *111*, 2897.
71. Aguilà, D.; Barrios, L. A.; Velasco, V.; Roubeau, O.; Repollés, A.; Alonso, P. J.; Sesé, J.; Teat, S. J.; Luis, F.; Aromí, G., *Journal of the American Chemical Society* **2014**, *136*, 14215.
72. Salinas Uber, J.; Estrader, M.; Garcia, J.; Lloyd-Williams, P.; Sadurní, A.; Dengler, D.; van Slageren, J.; Chilton, N. F.; Roubeau, O.; Teat, S. J.; Ribas-Ariño, J.; Aromí, G., *Chemistry-A European Journal* **2017**, *23*, 13648.
73. Lehmann, J.; Gaita-Ariño, A.; Coronado, E.; Loss, D., *Nature Nanotechnology* **2007**, *2*, 312.

74. Meier, F.; Levy, J.; Loss, D., *Physical Review Letters* **2003**, *90*, 047901.
75. Schrauzer, G. N.; Mayweg, V. P., *Journal of the American Chemical Society* **1965**, *87*, 1483.
76. Makhaev, V. D.; Borisov, A. P.; Karpova, T. P.; Lobkovskii, E. B.; Tarasov, B. P.; Chekhlov, A. N., *Bulletin of the Academy of Sciences of the USSR, Division of Chemistry* **1989**, *38*, 377.
77. Armarego, W. L. F.; Perrin, D. D., *Purification of Laboratory Chemicals*. 4th ed.; Butterworth-Heinemann: Oxford, U.K., 2000.
78. Sheldrick, G. M., *Acta Crystallographica Section A* **1990**, *46*, 467.
79. Sheldrick, G. M., *Acta Crystallographica Section A* **2008**, *64*, 112.
80. Farrugia, L. J., *Journal of Applied Crystallography* **1999**, *32*, 837.
81. Clark, R. C.; Reid, J. S., *Acta Crystallographica Section A* **1995**, *51*, 887.
82. Hanson, G. R.; Gates, K. E.; Noble, C. J.; Griffin, M.; Mitchell, A.; Benson, S., *J. Inorganic Biochemistry* **2004**, *98*, 903.
83. Neese, F., *WIREs Computational Molecular Science* **2012**, *2*, 73-78.
84. Becke, A. D., *Journal of Chemical Physics* **1988**, *84*, 4524.
85. Perdew, J. P., *Physical Reviews B* **1986**, *33*, 8822.
86. Pantazis, D. A.; Chen, X.-Y.; Landis, C. R.; Neese, F., *Journal of Chemical Theory and Computation* **2008**, *4*, 908.
87. van Lenthe, E.; Snijders, J. G.; Baerends, E. J., *Journal of Chemical Physics* **1996**, *105*, 6505-6516.
88. van Lenthe, E.; van der Avoird, A.; Wormer, P. E. S., *Journal of Chemical Physics* **1998**, *108*, 4783-4796.
89. van Lenthe, J. H.; Faas, S.; Snijders, J. G., *Chemical Physics Letters* **2000**, *328*, 107-112.
90. van Wüllen, C. J., *Journal of Chemical Physics* **1998**, *109*, 392-399.
91. Klamt, A.; Schüürmann, G., *Journal of the Chemical Society, Perkin Transactions 2* **1993**, 799.
92. Pulay, P., *Chemical Physics Letters* **1980**, *73*, 393.
93. Pulay, P., *Journal of Computational Chemistry* **1982**, *3*, 556.
94. Perdew, J. P.; Burke, K.; Ernzerhof, M., *Physical Review Letters* **1996**, *77*, 3865.
95. Adamo, C.; Barone, V., *Journal of Chemical Physics* **1999**, *110*, 6158.
96. Neese, F.; Wennmohs, F.; Hansen, A.; Becker, U., *Chemical Physics* **2009**, *356*, 98-109.
97. Izsák, R.; Neese, F., *Journal of Chemical Physics* **2011**, *135*, 144105.
98. Neese, F., *Journal of Chemical Physics* **2001**, *115*, 11080.
99. Neese, F., *Journal of Chemical Physics* **2003**, *118*, 3939.
100. Noodleman, L., *Journal of Chemical Physics* **1981**, *74*, 5737-5743.

101. Noodleman, L.; Case, D. A.; Aizman, A., *Journal of the American Chemical Society* **1988**, *110*, 1001-1005.
102. Noodleman, L.; Davidson, E. R., *Chemical Physics* **1986**, *109*, 131-143.
103. Noodleman, L.; Norman, J. G.; Osborne, J. H.; Aizman, A.; Case, D. A., *Journal of the American Chemical Society* **1985**, *107*, 3418-3426.
104. Noodleman, L.; Peng, C. Y.; Case, D. A.; Monesca, J. M., *Coordination Chemistry Reviews* **1995**, *144*, 199-244.
105. Neese, F., *Journal of Physics and Chemistry of Solids* **2004**, *65*, 781-785.
106. Soda, T.; Kitagawa, Y.; Onishi, T.; Takano, Y.; Shigetou, Y.; Nagao, H.; Yoshioka, Y.; Yamaguchi, K., *Chemical Physics Letters* **2000**, *319*, 223.
107. Yamaguchi, K.; Takahara, Y.; Fueno, T., In *Applied Quantum Chemistry*, Smith, V. H., Ed. Reidel: Dordrecht, The Netherlands, 1986; p p. 155.
108. *Molekel*, Advanced Interactive 3D-Graphics for Molecular Sciences, Swiss National Supercomputing Center. <https://ugovaretto.github.io/molekel/>.

3.Chapter 3: Gold Bis(dithiolene) Magnetic Relaxation

3.1.Introduction

3.1.1.Electron Transfer Series

Bis(dithiolene) complexes of Au^{III} have been investigated in parallel with the group 10 metals since the advent of dithiolenes, resultant of the remarkably similar chemistry induced by the isoelectronic d⁸ metal configuration. As the charge of the central metal is varied by 1 between group 10 and 11 the paramagnetism and diamagnetism for the members of the electron transfer series of gold bis(dithiolene)s is the inverse of its group 10 counterparts, i.e. group 10 bis(dithiolene)s with odd charge are $S = 1/2$ and even charge are $S = 0$, group 11 bis(dithiolene)s with even charge are $S = 1/2$ and odd charge are $S = 0$.

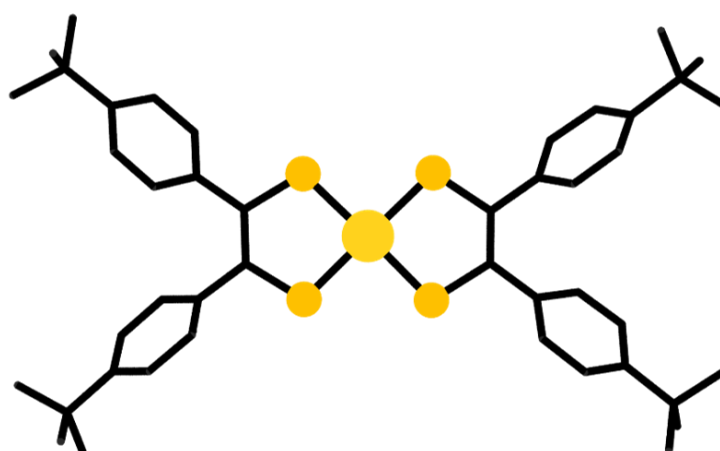


Figure 3.1. Molecular structure of $[\text{Au}^{\text{III}}(\text{dtbpdt})_2]^0$ with sulfur atoms coloured mustard and gold atoms canary.

The series is capped by the dianionic form $[\text{Au}^{\text{I}}(\text{L}^{2-})_2]^{2-}$ which can be achieved with aromatic ligands. Wieghardt *et al.* utilised Sellman's 3,5-di-tert-butylbenzodithiolate ligand $(\text{dtbbdt})^{2-}$ to give $[\text{Au}^{\text{I}}(\text{dtbbdt})_2]^{2-}$ upon one electron reduction of $[\text{Au}^{\text{III}}(\text{dtbbdt})_2]^-$ at a very low -2.28 V vs $\text{Fc}^{+/0}$ in CH_2Cl_2 and 0.1 M $[\text{nBu}_4\text{N}][\text{PF}_6]$ electrolyte.¹ The $+1/0$ couple is achieved at a much milder $+0.07$ V. Wieghardt *et al.* expanded their contribution to gold bis(dithiolenes) with the 1,2-di(4-tert-butylphenyl)ethylene-1,2-dithiolato ligand $(\text{dtbpdt})^{2-}$ (Figure 3.1.) which allows access to the dianionic, monoanionic, neutral, and monocationic forms with fully reversible events at -2.09 , -0.11 , and $+0.54$ V vs $\text{Fc}^{+/0}$ exposing each achievable member of the series. This series allows ready access to the most interesting neutral radical member of the series.

3.1.2. Neutral Radical Gold Bis(dithiolene)s

Complexes of the form $[\text{Au}^{\text{III}}(\text{L}^{2-})(\text{L}^{\cdot-})]$ are isoelectronic with the group 10 monoanions $[\text{M}^{\text{II}}(\text{L}^{2-})(\text{L}^{\cdot-})]^-$ yet the particular arrangement of the gold atom provides some fascinating electronic differences. Firstly, the gold atom is a heavy atom, with large diffuse orbitals and in its neutral form is the first element that induces relativistic effects on the electron in its 6s orbital by virtue of its size.² In dithiolene complexes this results in a miniscule contribution to the open shell SOMO from Au^{III} d orbitals due to the difference in size in spite of the sulfurphilicity of gold. Secondly, the square planar coordination environment around Au^{III} d^8 that results in a highly anisotropic electric field interacts with the 100% nuclear abundant ^{197}Au nucleus $I = 3/2$ to generate a colossal quadrupolar splitting. Gold and rhenium are the only two elements to form homoleptic dithiolene complexes with quadrupolar splitting that is visible in the EPR spectra.

3.1.2.1. Robin-Day Classification

Robin-Day classification for mixed valence compounds is a methodology used to clarify the electronic description of a system in which the localization of an electron/or charge is ambiguous.³ For a one electron bis(dithiolene) system there are three possibilities, best visualised as a potential energy curve as a function of electron transfer (Figure 3.3.). In the first case the electronic coupling (H_{ab}) between the two ligands is weak or non-existent so there are two separate, decoupled diabatic redox states and fully localised redox centres, designated class I. Complexes such as permanganate and Werner ions are examples of class I compounds. As strength of the electronic coupling increases there lies two possibilities defined by the relation of $2H_{\text{ab}}$ to the Marcus reorganisation energy, λ . The Marcus reorganisation energy is vertical reorganizational energy covering structural reorganisation, solvation effect, etc on electron transfer. If $2H_{\text{ab}}$ is less than λ there arises a partially localised double-well adiabatic ground state with partially localised charges and a barrier for thermal electron transfer. Complexes falling into this category are named class II. If $2H_{\text{ab}}$ is greater than or equal to λ only one ground state minimum occurs without an electron transfer barrier and the electron or charge is distributed across evenly across both centres. This delocalised structure is dubbed class III. Group 10 bis(dithiolene) complexes belong to class III where the IVCT optical transition is much stronger and cannot be satisfied thermally. Au^{III} bis(dithiolene) complexes can be class II or class III depending on the identity of the ligand.

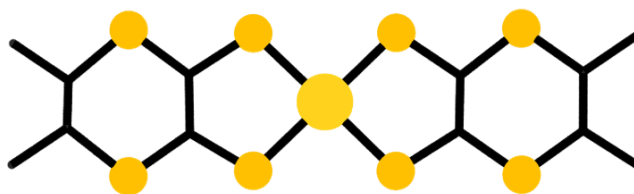


Figure 3.2. Molecular structure of $[\text{Au}^{\text{III}}(\text{dm-dddt})_2]$ with sulfur atoms coloured mustard and gold atoms canary.

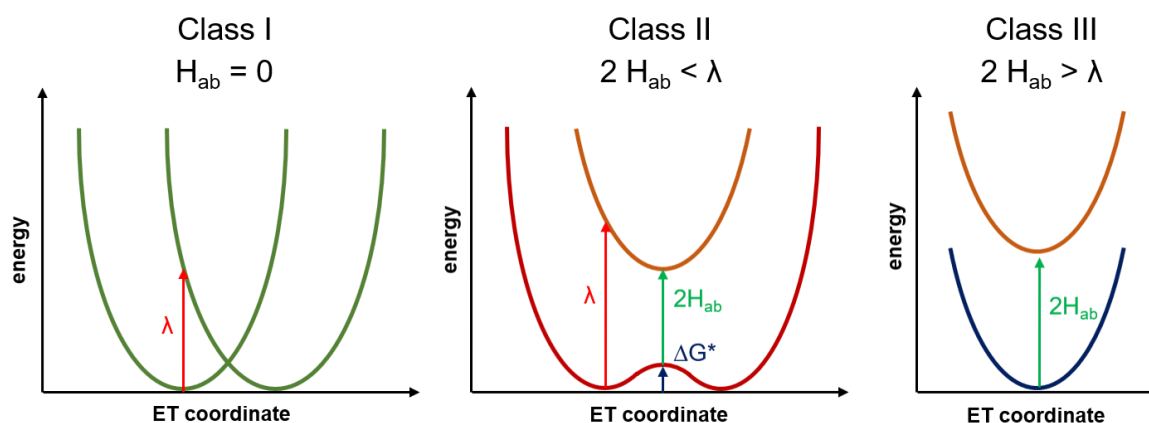


Figure 3.3. Potential energy diagrams versus propensity for electron transfer for class I, II, III coordination compounds in the Robin-Day classification system.

This was explored in detail by Branzea et al comparing Au^{III} and Ni^{II} complexes with various dithiolene ligands in their efforts to predict which systems would allow for single component molecular conductivity.⁴ For the bulk of their investigation they look at the (*S,S*) and (*R,R*) enantiomers of 5,6-dimethyl-5,6-dihydro-1,4-dithiin-2,3-dithiolate (dm-dddt^{2-}) (Figure 3.2.). Crystallisation of the monoanionic nickel species and neutral gold species revealed a dissymmetry between the dithiolene moieties in the gold complex while the nickel species was symmetric. The effect is quite pronounced with C = C bond distances of 1.30 and 1.40 Å for each dithiolene in one $[\text{Au}^{\text{III}}(\text{dm-dddt})_2]$ unit compared to 1.353 and 1.341 Å in its nickel analogue. With extensive modelling the group looked toward theoretically evaluating the distinction between these species, looking to the class II and III Robin-Day classification boundary as the source of the discrepancy. Dispensing with the need for knowing the Marcus reorganisation energy as the approach simply required a qualitative assessment to distinguish between class II and III Branzea et al instead simply looked at the changes in energy for the symmetric distortions of the C = C stretching mode where the value of the C = C bond distance of each C = C bond simultaneously changes. For all the Ni^{II} complexes the symmetric mode was found to be the lowest energy mode and for all Au^{III} the asymmetric, both curves were simulated excellently with a harmonic oscillator;

$$E(d-d_0) = k(d-d_0)^2.$$

The barrier of conversion for the asymmetric gold complexes was found to be 0.25–0.78 kcal/mol. A far larger discrepancy is encountered when calculating the electronic coupling energy. Using two and four electron closed shell occupancy of the two symmetric and asymmetric π -orbital arrangements for the square-planar complexes, to avoid disparities introduced from α and β spins, the energies were computed and contrasted for seven gold complexes, five asymmetric and two, $[\text{Au}^{\text{III}}(\text{bdt})_2]$ and $[\text{Au}^{\text{III}}(\text{ttfdt})_2]$, fully symmetric in the crystal structure versus their nickel analogues. For the asymmetric structures an energetic discrepancy of ~ 0.4 eV was found, an exception being for the symmetric gold complexes which had far smaller discrepancies ~ 0.18 eV, both of which ligands have larger conjugated π -systems incorporated into their ligands. These results point to the gold atom's poorer mediating of electronic coupling across dithiolenes as the source of this shift to class II for particular members of the gold bis(dithiolene) family.

3.3.2.2. Quadrupolar EPR

Wieghardt *et al.* achieved the best resolved quadrupolar splitting in an EPR spectrum with $[\text{Au}^{\text{III}}(\text{dtbpd}^{2-})(\text{dtbpd}^{2-})]$;⁵ $g = (1.944, 2.030, 2.065)$, $A = (-6.8, -6.7, -6.3) \times 10^4 \text{ cm}^{-1}$, $P = (-150, +50, +100) \times 10^4 \text{ cm}^{-1}$ and $[\text{Au}^{\text{III}}(\text{mnt}^{2-})(\text{mnt}^{2-})]$; $g = (1.928, 2.039, 2.075)$, $A = (-8.1, -7.0, -8.1) \times 10^4 \text{ cm}^{-1}$, $P = (-150, +50, +100) \times 10^4 \text{ cm}^{-1}$ where the P -tensor mediates the quadrupolar interaction. The unusual features are manifest as uneven line spacing of the multiplet hyperfine lines in the spectrum. Where the splitting would be expected as an evenly spaced quartet from the ^{197}Au $I = 3/2$ nucleus instead it resembles a triplet and quartet. This is due to a strong electric field gradient at the gold nucleus, imposed by the d^8 square planar geometry and the corresponding strong quadrupolar hyperfine interaction with the principle axes pointing in different directions than the g -matrix or A -tensor.

3.1.3. Molecular Semiconductors

The most explored topic involving gold bis(dithiolene)s is their use as molecular semiconductors. Gold bis(dithiolene)s may conduct as a single component semiconductor or as part of an alloy typically formed by doping with the isoelectronic nickel species. Fully metallic and superconducting states have also been shown to be possible in these crystalline structures. While a greater number of π -interactions are available in solid state packings of the neutral species the monoanionic species will also form molecular semiconductors with adequate counterion choice.⁶ These systems may be favourable in terms of tunability as the counter cation can introduce new properties to the material.

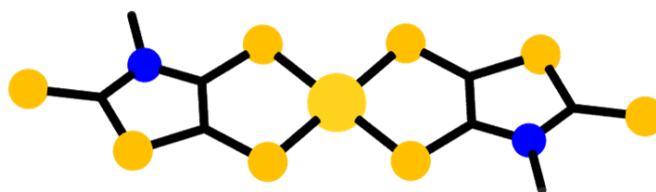


Figure 3.4. Molecular structure of $[\text{Au}^{\text{III}}(\text{Me-thiazdt})_2]$ with sulfur atoms coloured mustard, nitrogen atoms azure, and gold atoms canary.

The chiral $[\text{Au}^{\text{III}}(\text{dm-dddt})_2]$ molecules of Branzea et al are examples of single component semiconductors albeit rather poor ones. The designation of $[\text{Au}^{\text{III}}(\text{dm-dddt})_2]$ as a class II compound is a result of an investigation of the conduction properties afforded by it with a rather poor room temperature conductivity of $0.02\text{--}0.04 \text{ S cm}^{-1}$ and semiconducting activation barrier of 1660 K. This greatly improves under pressure to around 330 K at 11 kbar, however much greater conductivities would be expected on account of those found for similar systems. The π -stacking crystal packing arrangement between the neutral gold and monoanionic nickel species is the same in each structure (albiet with alkylammonium counteractions punctuating the nickel structure). In both, the π -systems orientate with the π -system of one bis(dithiolene) system overlapping with end of the next. In the case of the class II system the overlap between molecules is always between opposite asymmetric orbitals. This results in a pseudo dimerization of adjacent asymmetric molecules where the spins of the open shell moieties will arrange antiferromagnetically. This is illustrated explicitly in the neutral $[\text{Au}^{\text{III}}(\text{dddt})_2]$ which has no EPR spectrum as a powder. The expectation of high conductivity in neutral gold bis(dithiolene) species is exemplified by Lorcy *et al.*'s $[\text{Au}^{\text{III}}(\text{Me-thiazdt})_2]$ and $[\text{Au}^{\text{III}}(\text{Et-thiazdt})_2]$ which display metallic phases and a conductivity of 750 S cm^{-1} at room temperature increasing to 3800 S cm^{-1} at 4 K (Figure 3.4.).^{7, 8}

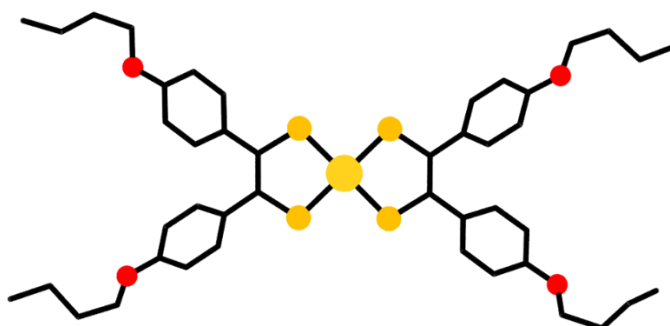
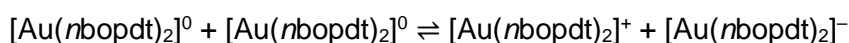
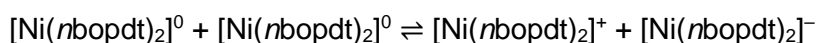
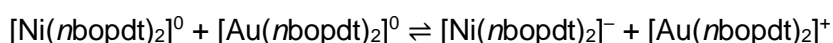
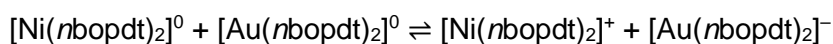


Figure 3.5. Molecular structure of $[\text{Au}(\text{nbopdt})_2]$ with sulfur atoms coloured mustard, oxygen atoms scarlet, and gold atoms canary.

An alternative to a single component molecular semiconductor is a molecular alloy. Fourmigue et al explored the conductive properties of para *n*-butoxy phenyl substituted gold bis(dithiolene)s doped in their nickel analogues at various proportions (Figure 3.5.).⁷ The gold bis(dithiolene)s employed in this study were designated class III evidenced by their symmetric crystal structures. Conductivity was found to increase exponentially with gold content which was increased in measures of 10% with a constant 4200 K activation barrier for semiconduction. However, the highest conduction in the pure [Au(*nbopdt*)₂] complex is a rather low 330 GΩ cm⁻¹, suggesting that despite being predominantly class III there is still a propensity for the open shell moieties to interact and dimerize in the solid. This is corroborated with the magnetic susceptibility data for the pure gold complex as a powder which was found to be below 1.73 μ, the magnetic susceptibility expected for a complex with a single unpaired electron. The exponential increase of conductivity with gold content indicates the sample is not a simple doping band semiconductor which would track linearly. Instead the results are comparable to percolation thresholds found in carbon black particles and carbon nanotubes where the conduction stems from tunnelling via conductive moieties, in this case the gold bis(dithiolene). This behaviour is tentatively rationalized by the group from comparison of the *E*_{1/2} potentials of the matrix and dopant. The nickel species are reduced below -0.1 V and oxidised above +0.87 V, while the same reduction potentials for the gold complex were found to be +0.25 and +0.75 V respectively. Equations for nickel acting as an n-dopant, p-dopant and the disproportionation of each complex are represented by the equations;



The smallest potential difference is found to be 0.5 V in the disproportionation of the neutral gold complex which is therefore the most favourable one to support charge transfer, reinforcing that conduction in the doped species is controlled by a tunnelling barrier between gold segments.

3.1.4.Scope of Chapter

Dissecting the physics of spin decoherence has greatly profited from examination of molecular species.⁹ In particular coordination complexes bearing a paramagnetic metal ion

have produced a bounty of detail about composition and structure, and in particular the impact of nuclear spins on the spin dynamics, and therein the phase memory time.¹⁰⁻²³ The result of these studies has driven phase memory times for coordination complexes to equal or surpasses the best among related matter spin qubits.^{16, 24}

Herein we present a study of the spin dynamics of a square planar bis(dithiolene) gold complex, where the central Au(III) d^8 ion is diamagnetic and the unpaired electron is confined to the dithiolene ligands. This complex was selected for several reasons: i) the charge-neutral state can facilitate surface deposition by vacuum sublimation as a means to scale the system;¹⁸ ii) the anisyl substituents on the dithiolene render the complex highly soluble in a range of esoteric solvents that have either no nuclear spins or nuclei with low magnetogyric ratios; iii) the valence contribution to the electric field gradient (EFG) produces a colossal quadrupolar interaction that dwarfs the hyperfine interaction,²⁵ permitting examination of the impact of quadrupolar coupling on spin dynamics; and iv) there is near negligible metal contribution to the ground state,²⁶ and the complex is thus considered an organic spin qubit. As such it can be tentitively viewed as a model for an organic radical qubit bound to gold surface,^{27, 28} providing a unique opportunity to probe the effect of the materials that ultimately comprise quantum gates where the gold represents the wiring that connects the spin qubit to the rest of the circuitry, and the means, in this setup, to address qubits electrically.^{29, 30} The minuscule gold contribution to the ground state and the charge delivers the longest phase memory time recorded for a third-row transition metal. However, the gold ion presents a heavy atom effect that prevents measurement above 80 K, and underscores the need to engineer the composition of not just the qubit, but all components of the spintronic circuitry.

3.2.Synthesis

Dialkyltin-protected dithiolenes have utility in transmetalation reactions that afford transition-metal dithiolene complexes and result in cleaner synthesis compared to reactions employing the alkali-metal dithiolate salts.³¹⁻³⁶ Dark green $[\text{PPh}_4][\text{Au}(\text{adt})_2]$ is synthesized by the addition of two equivalents $(\text{adt})\text{SnMe}_2$ to potassium tetrachloroaurate in dichloromethane; the SnCl_2Me_2 by-product is conveniently washed away with MeOH. We find this synthetic approach consistently gives excellent yields (90%) and decidedly preferable to the older P_4S_{10} /acyloin method devised by Schrauzer and Mayweg,³⁷ at least with these more expensive noble metals.^{25, 38}

Complex **3.1a** is diamagnetic as was judged from its ^1H NMR spectrum, and its electronic spectrum displays two weak ligand field (LF) transitions in the visible (Figure 3.7); no charge transfer (CT) bands are observed >600 nm in the near-infrared (NIR). Similar spectra have been reported for other diamagnetic, square planar Au^{III} complexes. Electrochemical measurements performed on a solution of **3.1a** in CH_2Cl_2 containing 0.10 M $[\text{N}(\text{tBu})_4]\text{PF}_6$ revealed two reversible one-electron-transfer waves at $E_{1/2} = -0.143$ V and $E_{1/2} = +0.384$ V, relative to the ferrocenium/ferrocene ($\text{Fc}^{+/0}$) couple (Figure 3.6.). The profile and reduction potentials are similar to related aryl-substituted dithiolenes of gold.^{25, 38-43}

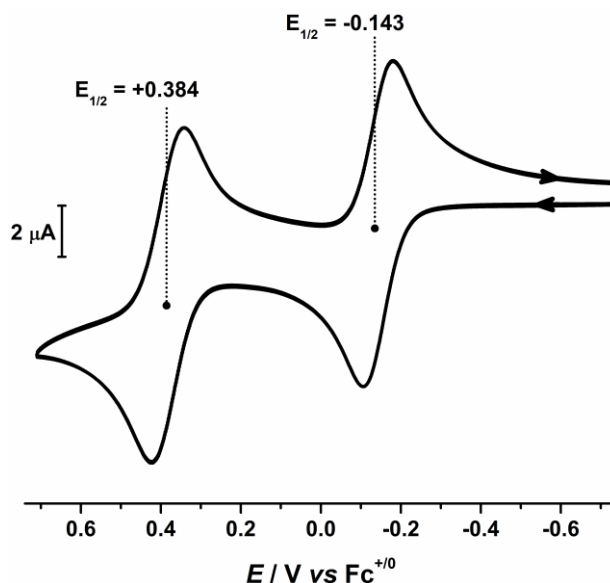


Figure 3.6. Cyclic voltammogram of **3.1a** in CH_2Cl_2 solution (0.10 M $[\text{N}(\text{tBu})_4]\text{PF}_6$ supporting electrolyte) at 22 °C at a scan rate of 100 mV s^{-1} . Potentials are referenced versus the $\text{Fc}^{+/0}$ couple.

The reaction of **3.1a** with 0.5 equiv. of iodine in CH_2Cl_2 yielded dark brown crystals of $[\text{Au}(\text{adt})_2]$ (**3.1b**). This complex is paramagnetic as evinced by its room temperature magnetic moment of $1.72 \mu_{\text{B}}$ (Evans method⁴⁴) indicating an $S = 1/2$ ground state for **3.1b**.

3.3.X-ray Crystallographic Structure

Single-crystal X-ray diffraction revealed the anion in **3.1a** to possess a near square planar {AuS₄} core with a slight twist toward tetrahedral ($\alpha = 14.8^\circ$) ascribed to lattice packing. On the other hand, the coordination environment about the Au ion in **3.1b** is perfectly planar ($\alpha = 0^\circ$). The *p*-anisyl substituents are rotated relative to the {S₂C₂} plane at angles ranging 41 – 72° for both compounds. Therefore via induction, the anisyl group is electron donating reflecting the softer, more polarizable sulfur donor atoms in this ligand. An important consideration relating to the spin dynamics of this molecular spin qubit are the protons on the *p*-anisyl substituents of the dithiolene. Despite the absence of conjugation that ensures the spin density is confined to the {S₂C₂} core, these protons nevertheless present an efficient decoherence pathway through dipolar coupling.^{11, 12} The three types of proton in the ligand – two aromatic and one methyl – are on average 3.4 Å, 5.5 Å and 7.5 Å, respectively, away from the spin locus.

The ligand oxidation level is revealed in the intraligand bond distances for **3.1b** compared with **3.1a**. The average S–C bond distance of 1.739 ± 0.002 Å and average C–C distance of 1.375 ± 0.003 Å are shorter and longer, respectively, than the corresponding bond lengths in the dianionic dithiolate form of the ligand in **3.1a** at 1.767 ± 0.002 Å and 1.351 ± 0.003 Å, respectively (Table 3.1.). This is characteristic of an open-shell dithiolene radical, which due to inversion symmetry, is distributed over both ligands with an electronic structure defined as [Au^{III}(adt₂³⁻)]^{0, 45, 46}. Therefore, the metal ion is +III in both as evinced by the similarity of the average Au–S bond lengths of 2.3165 ± 0.0009 Å in **3.1a** and 2.3006 ± 0.0009 Å in **3.1b**. The observed intraligand metrics are in excellent agreement with a number of monoanionic and neutral aryl-substituted bis(dithiolene)gold complexes.^{25, 38, 39, 42}

Table 3.1. Comparison of Experimental and Calculated Metrics^a

	3.1a		3.1b	
	Exptl	Calcd	Exptl	Calcd
avg. Au–S	2.3165(9)	2.350	2.3006(9)	2.335
avg. S–C	1.767(2)	1.778	1.739(2)	1.747
avg. C–C	1.351(3)	1.363	1.375(3)	1.384
avg. S–Au–S	89.18(3)	87.8	88.81(2)	87.7
α^b	14.8	2.7	0.0	0.4

^a Distances in angstrom; angles in degrees. ^b Dihedral angle between mean AuS₂ planes.

3.4. Electronic Structure

3.4.1. Electronic Spectra

The electronic spectrum displays a very intense absorption maximum in the NIR at 1556 nm ($\epsilon = 1.4 \times 10^4 \text{ M}^{-1} \text{ cm}^{-1}$) which has been previously assigned to an intervalence charge transfer (IVCT) transition of type $[\text{Au}^{\text{III}}(\text{L})(\text{L}')] \leftrightarrow [\text{Au}^{\text{III}}(\text{L}')(\text{L})]$, which corresponds to a spin-allowed excitation from the highest doubly occupied molecular orbital (HOMO-1) to the singly occupied molecular orbital (SOMO) both of which are ligand-centered.²⁶ This IVCT band is observed for all charge-neutral Au^{III} bis(dithiolene) complexes,^{25, 26, 38, 41-43, 47-49} and is diagnostic of a coordinated π radical ligand. The longer wavelength for **3.1b** reflects the ease with which adt is oxidized having softer, more polarizable sulfur donor ligands than its conjugated counterparts.⁵⁰

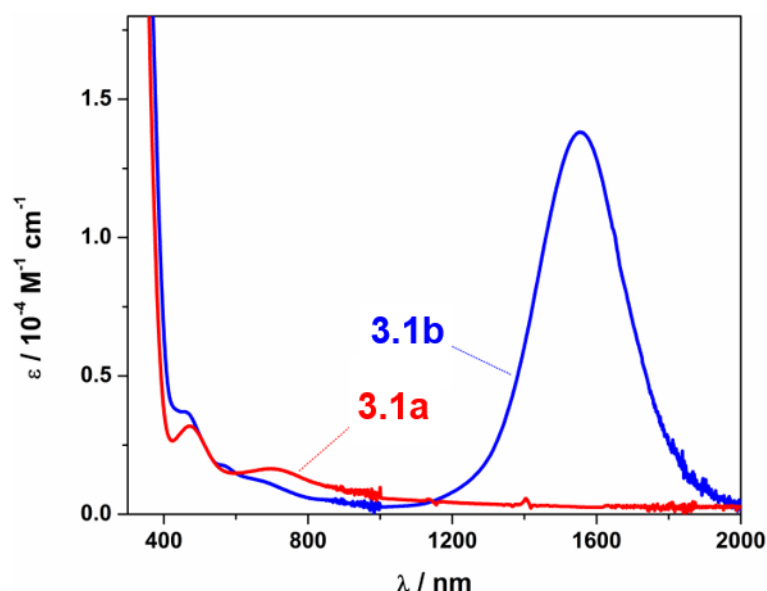


Figure 3.7. Overlay of the electronic spectra of **3.1a** and **3.1b** recorded in CH_2Cl_2 at ambient temperature.

3.4.2. Continuous Wave EPR

The cw X-band EPR spectrum of **3.1b** recorded in THF at 130 K display signals typical of an $S = 1/2$ system with rhombic g -values similar to literature reports of related compounds.^{25, 38, 47-49, 51} The splitting pattern ($g_y > g_x > g_e > g_z$) is the same as observed for isoelectronic bis(dithiolene) monoanions of group 10 metals given an identical ${}^2\text{B}_{2g}$ ground state (vide infra).^{26, 52} The spectrum exhibits a remarkable hyperfine splitting from the ${}^{197}\text{Au}$ nucleus ($I = 3/2$, 100% abundant), where the quartet splitting of each principle g -value manifests with an unusual the spacing and intensity distribution of the hyperfine lines. This outcome is caused by a sizeable EFG at the ${}^{197}\text{Au}$ nucleus that produces the strong quadrupole hyperfine interaction whose principal axes are orientated in a different direction from those

of the g and A matrices. The misalignment of the principle quantization axes leads to mixing of hyperfine levels and emergence of forbidden ($\Delta m_l \neq 0$) transitions in the EPR spectra. This unique situation where the quadrupole interaction is larger than the magnetic hyperfine interaction can only arise if the spin is located on the ligand coordinated to a Au^{III} ion with a $(d_{xz}, yz)^4(d_{zz})^2(d_{xy})^2(d_{x^2-y^2})^0$ electronic configuration. This generates the very large valence contribution to the EFG producing the dominant quadrupole interaction seen in the spectrum. A similar scenario was revealed for neutral tris(dithiolene)rhenium species whose electronic structure was unambiguously defined from its truly exceptional EPR spectrum.⁵³

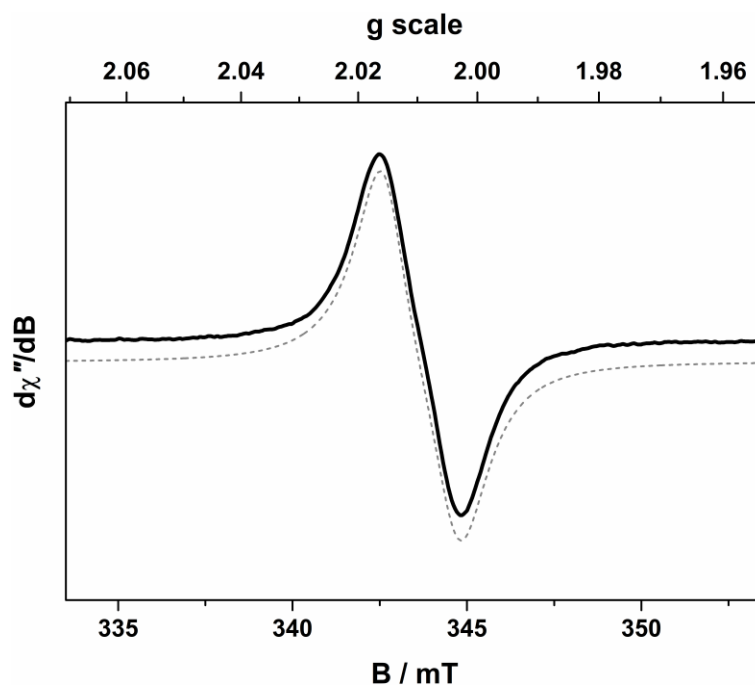


Figure 3.8. X-band EPR spectrum of **3.1b** recorded in CH_2Cl_2 solution at 293 K (experimental conditions: frequency, 9.6657 GHz; power, 6.3 mW; modulation, 0.5 mT). Experimental data are represented by the black line; simulation is depicted by the dashed trace.

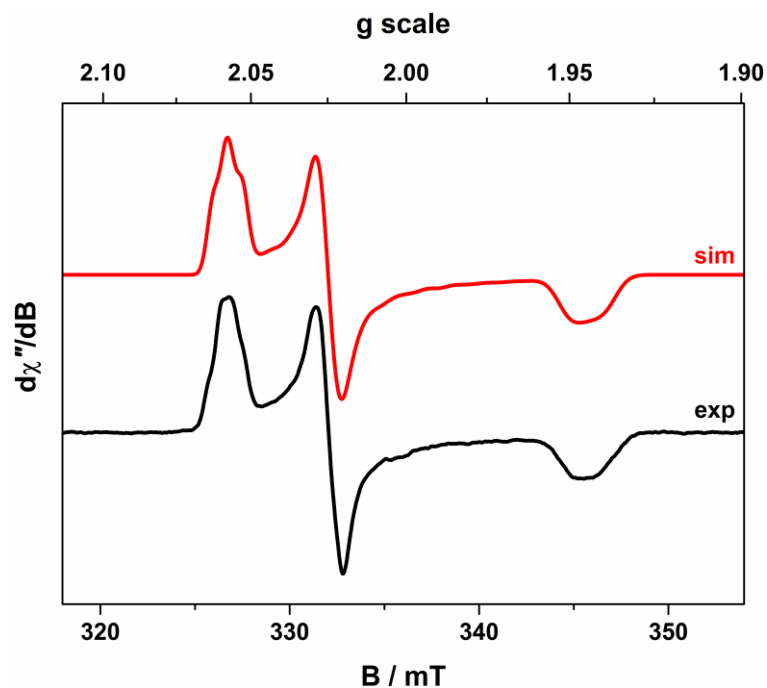


Figure 3.9. X-band EPR spectrum of **3.1b** recorded in THF at 130 K (experimental conditions: frequency, 9.4098 GHz; power, 0.63 mW; modulation, 0.3 mT). Experimental data are represented by the black line; simulation is depicted by the red trace.

An excellent fit was obtained with the g -, A -, and P -values listed in Table 2. Minor details such as the relative rotations of the different principal axes could not be resolved. Each A -value must have the same sign as inferred from the close match of the isotropic value to the average from the anisotropic values. The assignment as negative was derived from the ^{197}Au nuclear g -value assuming a dominant Fermi contact contribution, which is nicely corroborated by DFT calculations (vide infra).

Table 3.2. Summary of Experimental and Calculated Spin-Hamiltonian Parameters for **3.1b**

Parameter	Experimental	Calculated ^a
g_{iso}	2.0094	
g_x	2.0245	2.0294
g_y	2.0575	2.0616
g_z	1.9450	1.9493
$\langle g \rangle^b$	2.0090	2.0134
R_g^c	0.29	0.29
Δg^d	0.1125	0.1123
A_{iso}^e	-5.0	
A_x^e	-3.5	-4.5
A_y^e	-7.0	-4.5
A_z^e	-6.5	-4.7
$\langle A \rangle^{e,f}$	-5.7	-4.6
$P^{e,g}$	-150	
$\eta^{e,h}$	-50	

^a From ZORA-PBE0 DFT calculations. ^b $\langle g \rangle = (g_x + g_y + g_z)/3 \approx g_{\text{iso}}$. ^c Rhombicity, $R_g = (g_y - g_x)/(g_y - g_z)$. ^d g -anisotropy, $\Delta g = g_y - g_z$. ^e In units 10^{-4} cm^{-1} . ^f $\langle A \rangle = (A_x + A_y + A_z)/3 \approx A_{\text{iso}}$. ^g $P = [P_z - (P_x + P_y)/2]/3$. ^h $\eta = (P_x - P_y)/2$.

3.5.DFT Calculations

The geometry-optimized structures for the complex anions in **3.1a** and **3.1b** are in excellent agreement with the experimental data with both the Au–S and intraligand bond distances and angles accurately reproduced (Table 3.1.). Moreover the structures are strictly planar demonstrating the slight tetrahedralization about the Au ion in **3.1a** is a consequence of crystal packing. Inspection of the frontier MOs reveals four metal d orbitals at deeper binding energies than the ligand-based b_{3g} and b_{2g} (D_{2h} point group) which undergo symmetry-allowed π interactions with metal d orbitals.^{45, 46} In both, the HOMO is the b_{2g} symmetric ligand-centered orbital, which is doubly occupied in **3.1a** leading to its assignment as $[\text{Au}^{\text{III}}(\text{adt})_2]^{1-}$. As the redox-active orbital, oxidation of **3.1a** gives the b_{2g} SOMO in **3.1b**, and an electronic structure defined as $[\text{Au}^{\text{III}}(\text{adt}_2^{3-})]^0$ (Figure 3.12.).²⁶ This is consistent with the spin population distribution where the unpaired spin is delocalized across both ligands with miniscule spin residing at the Au^{III} center (Figure 3.12.). The electronic structure of **3.1b** has been verified by very accurate calculation of the g - and A -values (Table 3.2.). This level of precision allows for meaningful insight that correlates composition and electronic structure factors on the spin dynamics of molecular qubits based on coordination complexes.

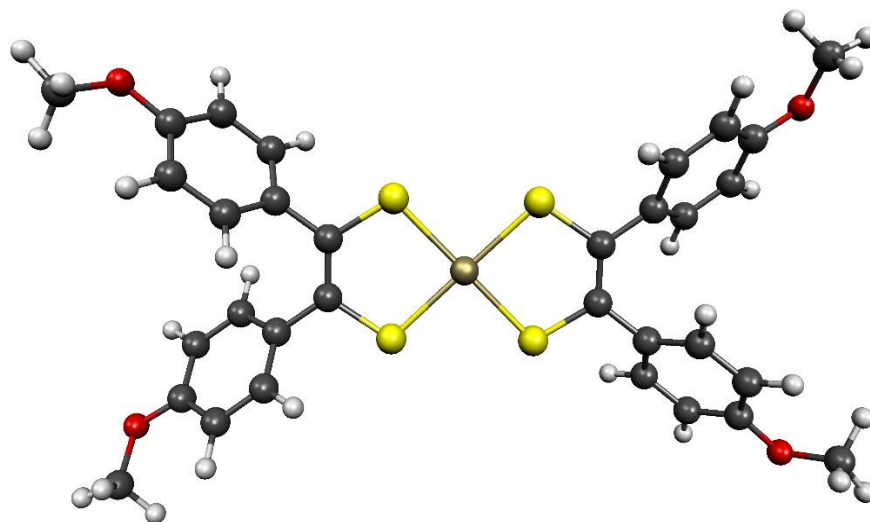


Figure 3.10. Geometry optimized structure of $[\text{Au}(\text{adt})_2]^{1-}$

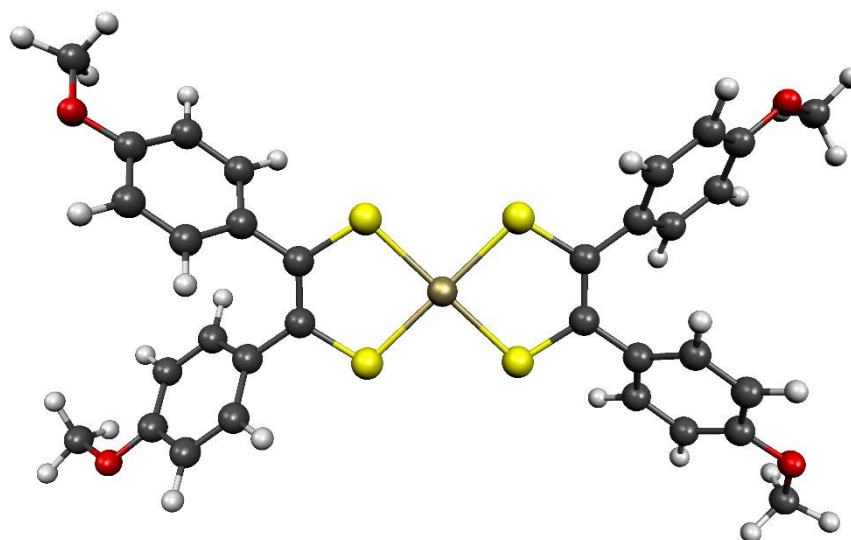


Figure 3.11. Geometry optimized structure of **3.1b**

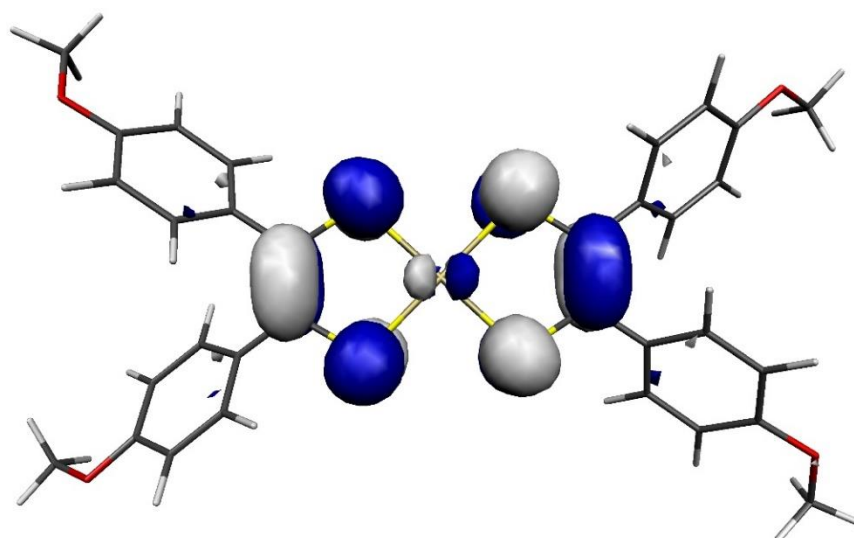


Figure 3.12. Depiction of the b_{2g} magnetic orbital in **3.1b**

3.6.Pulsed EPR

The spin relaxation properties as parameterized by spin-lattice (T_1) and phase memory (T_M) lifetimes were investigated for **3.1b** at field positions corresponding to the most intense resonance lines. The advantage of a charge-neutral molecular qubit with bulky *p*-anisyl substituents allowed us to explore a range of esoteric solvent mixtures. The selection included chloroform-*d* (CDCl_3), carbon tetrachloride (CCl_4), carbon disulfide (CS_2) and trichloroacetonitrile (Cl_3CCN), whose consistent atoms have weak magnetogyric ratios ($^2\text{H} = 4.11 \times 10^{-7}$; $^{14}\text{N} = 1.93 \times 10^{-7}$; $^{35}\text{Cl} = 2.62 \times 10^{-7}$; $^{37}\text{Cl} = 2.17 \times 10^{-7} \text{ T}^{-1} \text{ s}^{-1}$) which are an order of magnitude smaller than for ^1H . In addition, the solvents contain no methyl functionality – CH_3 or CD_3 – whose rotation provide an especially efficient decoherence pathway even at the lowest temperatures.⁵⁴ In order to achieve a good frozen glass, chlorinated solvents were combined with Cl_3CCN as a 4:1 mixture. This ratio was inverted for the Cl_3CCN and CS_2 glassing mixtures in combination with CCl_4 . In contrast to the recent study of isoelectronic complexes, $[\text{PPh}_4][\text{M}(\text{adt})_2]$ ($\text{M} = \text{Ni}, \text{Pd}, \text{Pt}$) in $\text{CD}_2\text{Cl}_2/\text{DMF-}d_7$,⁵² here the only protons and methyl groups are those on the periphery of the dithiolene ligand.

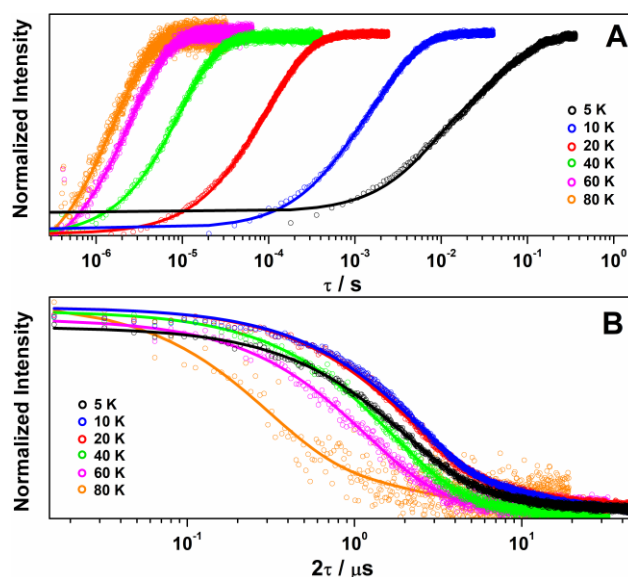


Figure 3.13. Temperature dependence of (a) inversion recovery and (b) Hahn echo decay for **3.1b** in 4:1 $\text{CCl}_4/\text{Cl}_3\text{CCN}$. Experimental data are represented by open circles and corresponding exponential fit depicted by the line.

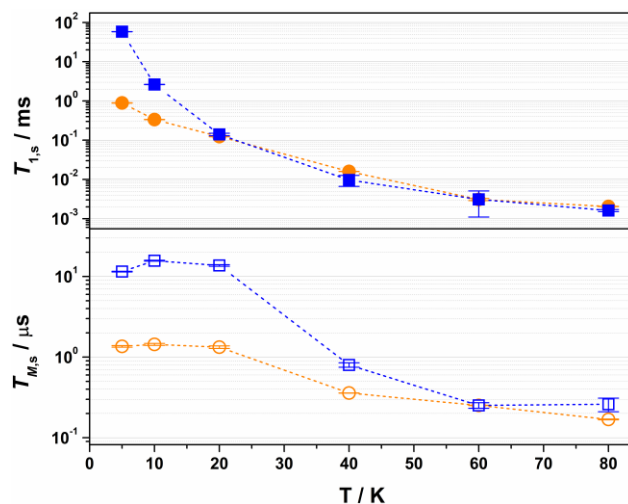


Figure 3.14. Comparison of the temperature dependence of $T_{1,s}$ (top) and $T_{M,s}$ (bottom) relaxation times for **3.1b** diluted in 4:1 $\text{CCl}_4/\text{Cl}_3\text{CCN}$ (blue filled and open squares) and 2% $[\text{Ni}(\text{adt})_2]$ (orange filled and open circles) over the range 5 – 80 K. Error bars are based on the standard deviation of the fit.

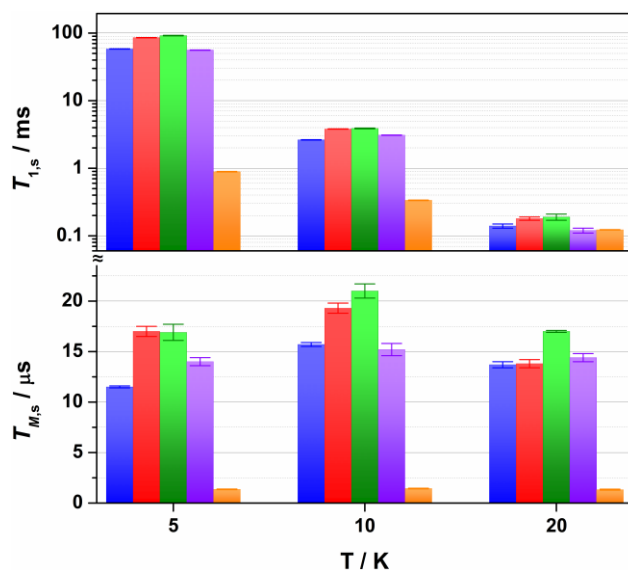


Figure 3.15. Comparison of the temperature dependence of $T_{1,s}$ (top) and $T_{M,s}$ (bottom) for 1 mM solutions of **3.1b** in 4:1 $\text{CCl}_4/\text{Cl}_3\text{CCN}$ (blue), 4:1 $\text{CDCl}_3/\text{Cl}_3\text{CCN}$ (red), 4:1 CS_2/CCl_4 (green), 4:1 $\text{Cl}_3\text{CCN}/\text{CCl}_4$ (violet), and the polycrystalline material (2% in $[\text{Ni}(\text{adt})_2]$, orange) at 5, 10 and 20 K. Error bars are based on the standard deviation of the fit.

3.6.1. Spin-Lattice relaxation

Inversion recovery data were collected on a solution of **3.1b** in 4:1 $\text{CCl}_4/\text{Cl}_3\text{CCN}$ to assess the temperature dependence of spin-lattice relaxation between 5 and 80 K (Figure 3.13.). The curves are modelled with a biexponential function that yielded values for the fast ($T_{1,f}$)

and slow ($T_{1,s}$) relaxation processes, where the former is attributed to spectral diffusion while the latter assigned is the signature spin-lattice relaxation time (Figure 3.14.). The biexponential fit was only applied up to 20 K; beyond this temperature the fast process merged with the spectral noise, and a monoexponential decay curve is sufficient to estimate the slow process until it becomes irretrievable above 80 K. Overall the $T_{1,s}$ decreases exponentially from 58.3 ms at 5 K to the 1.6 ms at 80 K. There is a slight orientation dependence for T_1 with the longest time recorded for $B_0 = 375.7$ mT (g_z) approximately 12% greater than at the other principal g -values. It should be noted that the quadrupole coupling is weakest around g_z ,²⁵ which indicates quadrupolar coupling does attenuate spin relaxation times. The steep decline in the spin-lattice relaxation time is a consequence in the large spin-orbit coupling (SOC) constant of Au at ~ 4500 cm⁻¹. Below 10 K, a direct spin relaxation process is dominant,⁵⁵ but as the temperature increases the Raman mechanism takes precedence,⁵⁶ and becomes more efficient with increasing SOC.¹³ The significance of SOC has been previously shown to impact spin-lattice times when comparing first- and second-row metals in systems where the metal is the spin host.⁵⁷⁻⁵⁹ We recently revealed for this system where the ligand is the spin host anchored by the metal ion, that the latter presents a heavy-atom effect.⁵² The phenomenon is particularly pervasive in this qubit design, and we have begun to explore alternative uses for these molecules to replace dichalcogenides in graphene-based heterostructures.

Altering the solvent medium had a noticeable impact on $T_{1,s}$, as gauged from measurements at 5, 10 and 20 K (Fig. 5). Of the four solvent mixtures tested, the longest time was recorded at 5 K for 4:1 CS₂/CCl₄ of 92 ms – the combination with the least spin-active nuclei (Fig. 5). Slightly shorter times were provided for 4:1 CDCl₃/Cl₃CCN at 86 ms, ahead of 4:1 CCl₄/Cl₃CCN at 58 ms and 4:1 Cl₃CCN/CCl₄ at 56 ms. These lifetimes are among some of the longest recorded for molecular electron spin qubits.⁹ Moreover, they are an order of magnitude longer than their isoelectronic group 10 counterparts, [M(adt)₂]¹⁻ (M= Ni, Pd, Pt),⁵² and related Ni bis(dithiolenes) reported by Bader et al.²¹ This highlights the importance of complex charge – **3.1b** being neutral – and the significantly smaller contribution from Au to the magnetic orbital compared with the group 10 analogues.

The most interesting result is supplied by the solid dilution of **3.1b** in the diamagnetic, charge-neutral [Ni(adt)₂]. As Atzori et al. have shown, the level of dilution has a negligible effect on the relaxation times;⁶³ here we chose 2% in order to give a sufficiently intense Hahn-echo so that the number of averages (scans) was equivalent to the frozen solution samples. The spin-lattice relaxation time measured at 5 K is 0.89 ms, two orders of magnitude smaller than that recorded in frozen solution at an equivalent temperature (Fig. 4). At 20 K and above, the $T_{1,s}$ lifetimes for [Au_{0.02}Ni_{0.98}(adt)₂] match the frozen solution data, and run parallel up to the highest measurement temperature of 80 K. This profile is borne

out of the planar structure of **2** and its diamagnetic host. Neutral gold bis(dithiolenes) are single component semiconductors,^{38, 47, 64-78} and the conductivity is modulated to when doped into the corresponding neutral Ni complex.⁴⁰ The planar molecules stack into dimerized columns with intermolecular distances as short as 3.6 Å, which is the source of the observed singlet-triplet magnetic behaviour in neutral gold bis(dithiolenes).^{40, 70, 76} As detailed by Fourmigué and co-workers, dilution of **3.1b** in [Ni(adt)₂] will give rise to dimers of **3.1b** embedded uniformly in the diamagnetic matrix, where the conductivity derives from tunnelling between gold dimer fragments either along the chain or perpendicular to it. Interestingly, the EPR spectrum of the polycrystalline **3.1b** is identical to the frozen solution spectrum rather than a spin-triplet signal from a dimer moiety, and may suggest that at the low concentration here (2%), that the Ni analogue may disrupt the dimerization. The short intermolecular distances within and between chains provide π -stacking interactions that give rise to semiconductor properties also serve as an efficient pathway for spin-lattice relaxation. This is only noticeable <20 K when compared to frozen solution data, as above this temperature the Raman mechanism prevails as this is driven by SOC and less dependent on intermolecular interactions.

3.6.2. Spin-Spin relaxation

The decay of the Hahn echo measured at the magnetic field corresponding to the absorption maxima (g_x) in the EPR spectrum follows a biexponential profile; the temperature dependence for **3.1b** in 4:1 CCl₄/Cl₃CCN shown in Figure A.2.16. The fit gives an estimate for the fast ($T_{M,f}$) and slow ($T_{M,s}$) relaxation processes, with the latter defined as the phase memory time when measuring qubit performance. An exceedingly long phase memory time of 15.6 μ s is recorded for **3.1b** at 10 K, and this increases to 17.6 μ s when the field position is shifted to 375.7 mT corresponding to g_z , an increase of 12% which aligns with the orientation dependence observed for $T_{1,s}$ (vide supra). This time betters many recently reported $S = 1/2$ coordination complexes.⁹ The few that surpass this time have had their composition and environment rigorously engineered to be devoid of nuclear spins.^{14, 16, 20, 21, 23} Moreover, this is the 4-5 times longer than phase memory times reported for any other second- or third-row transition metals.^{13, 79} The phase memory time is improved by altering the solvent mixture, reaching a maximum of 21 μ s in 4:1 CS₂/CCl₄ – the medium with the fewest nuclear spins (Figure 3.15). The major contributors to spin decoherence are electron-nuclear spin interactions which are the dominant factor at very low temperatures (<30 K). The nuclear spin bath is limited to the protons on the anisyl substituents of the dithiolene ligand; low gyromagnetic ratios for ^{35,37}Cl nuclei in the solvent and ¹⁹⁵Au ensures their contribution is negligible. The pitch of the anisyl substituents to a non-conjugated orientation with the dithiolene core ensures ¹H interaction is dipolar and governed by the interspin distance. Here with the locus of the spin on the ligand, only the methoxy groups

lie beyond the spin-diffusion barrier.^{11, 12} The distribution of spin density away from the metal ion and the disposition of the SOMO orthogonal to the plane of the complex facilitates greater interaction with the solvent medium. There is a slightly stronger interaction between the more polar Cl₃CCN and the electronegative {S₂C₂} core of the dithiolene ligand as evinced by the relaxation times (Figure 3.15.).

There is an overall increase in the relaxation rate with increasing temperature, despite the shorter $T_{M,s}$ at 5 K than 10 K which is due to a loss of solubility leading to inhomogeneity in the glass. The swift decline above 20 K is driven by a comparable reduction in the spin-lattice relaxation time which is the ultimate limit for $T_{M,s}$,⁸⁰ where spin-lattice and spin-spin relaxation approach parity, preventing measurement of the Hahn echo decay above 80 K. The solid dilution of **3.1b** in [Ni(adt)₂] afforded the shortest $T_{M,s}$ of 1.44 μs at 10 K, an order of magnitude smaller than for the frozen solution samples. As $T_{1,s}$ is sufficiently long at 10 K, the short phase memory time is a consequence of the greater population of protons in the spin bath as the dithiolene ligand in the diamagnetic host is fully protiated and the efficient stacking in the solid state brings these decohering spins much closer to the electron spin on the gold complex.

3.6.3.Rabi Oscillations

To demonstrate coherent spin control, echo-detected nutation experiments were performed by applying a microwave pulse of duration t_p to produce Rabi-like oscillations between two states that correspond to arbitrary superpositions of the electron spin (Figure 3.16). The physical origin is confirmed by the linear dependence of the oscillation frequency (Ω_R) with the applied microwave amplitude (B_1), which was varied by selecting microwave attenuations of 3, 6, 9 and 12 dB (Figure 3.16). Changes in the oscillations were observed at $t_p > 400$ ns derived from interaction with ligand protons which are independent of the microwave attenuation.⁸¹ The glassing medium had no bearing on the Rabi frequency with all values within experimental error (Figure 3.16)).

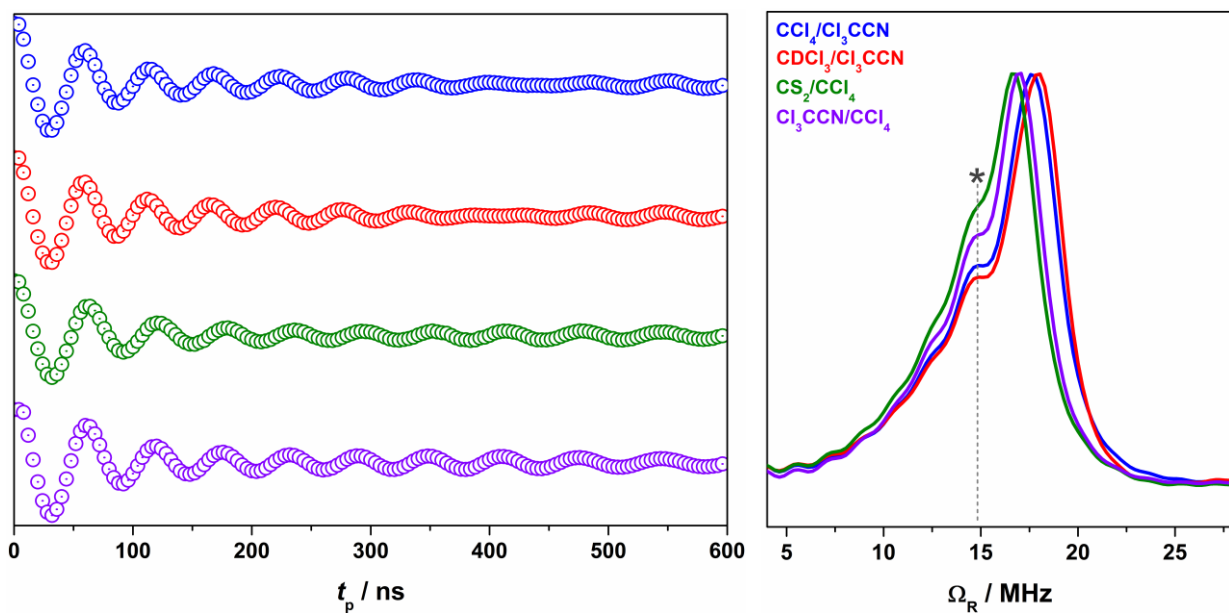


Figure 3.16. Nutation data (left) and Fourier transforms of the data (right) for **3.1b** in 4:1 $\text{CCl}_4/\text{Cl}_3\text{CCN}$ (blue), 4:1 $\text{CDCl}_3/\text{Cl}_3\text{CCN}$ (red), 4:1 CS_2/CCl_4 (green), and 4:1 $\text{Cl}_3\text{CCN}/\text{CCl}_4$ (violet) at 10 K and 343.5 mT. The asterisk in the Fourier transform data indicate the peak matching the Larmor frequency of ^1H (14.6 MHz) within error.⁸¹

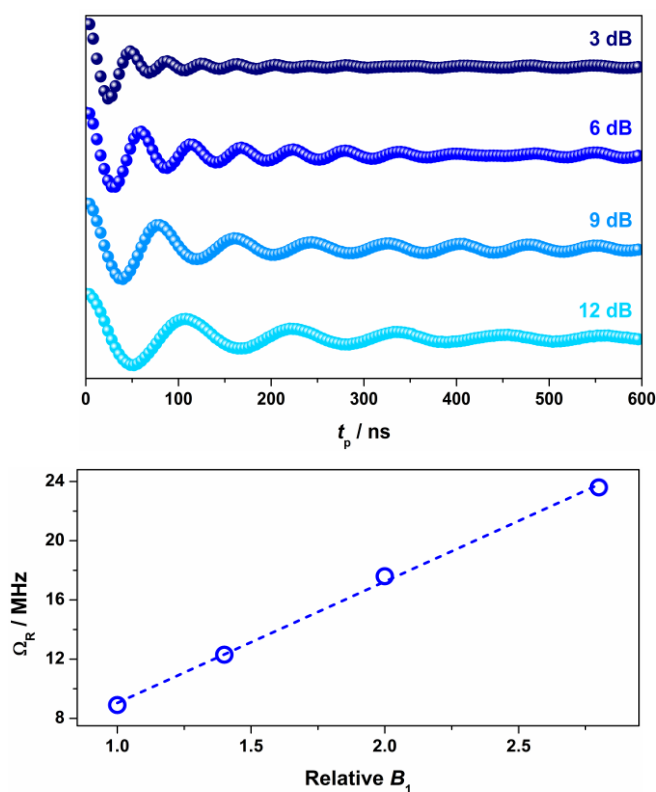


Figure 3.17. Variable power nutation measurements for **3.1b** in 4:1 $\text{CCl}_4/\text{Cl}_3\text{CCN}$ at 10 K and 343.5 mT (top), and linear dependence of Ω_R with respect to the B_1 field (bottom). Dashed trace represents line of best fit.

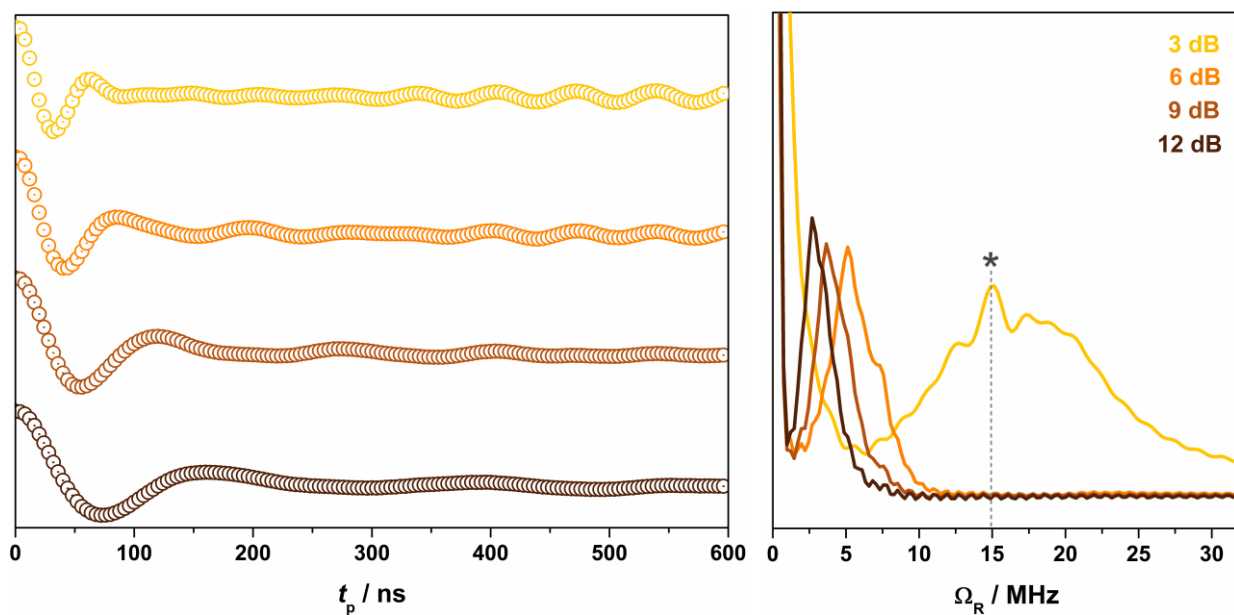


Figure 3.18. Rabi oscillations (left) and corresponding frequencies from the Fourier transfer of the data (right) for **3.1b** in diluted 2% in $[\text{Ni}(\text{adt})_2]$ at 10 K and 348.5 mT from variable power nutation measurements. The Rabi frequency at 3 dB microwave power is obscured in the Fourier transform from coupling to the Larmor frequency of ^1H (14.6 MHz) within error.⁸¹

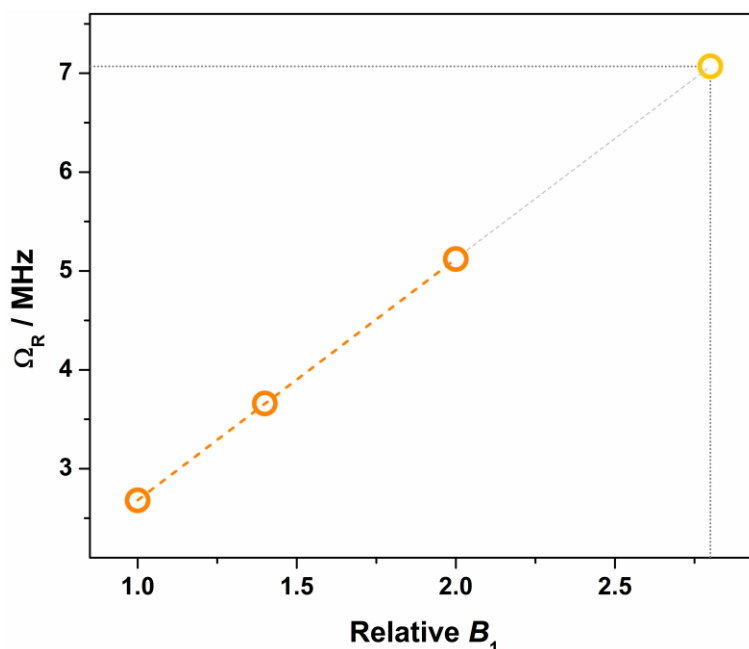


Figure 3.19. Linear dependence of the oscillation frequency (Ω_R) with respect to the B_1 field for polycrystalline **3.1b** diluted 2% in $[\text{Ni}(\text{adt})_2]$. Pumpkin-colored open circles indicate oscillation frequency and the corresponding dashed line the line of best fit. The gray

extrapolation line is used to estimate the Rabi frequency for relative $B_1 = 2.82$ (microwave power = 3 dB) of 7.07 MHz as indicated by sight lines.

The short phase memory time recorded on **3.1b** diluted 2% in $[\text{Ni}(\text{adt})_2]$ similarly leads to short Rabi frequencies (Figure 3.19). The nutation data measured at 6, 9 and 12 dB gave values with the expected linear dependence on the microwave amplitude. However, at 3 dB, the peak is masked in the Fourier transform by features derived by ^1H hyperfine coupling (Figure 3.19.). Nevertheless, the Rabi frequency at 3 dB microwave attenuation is estimated at 7.1 MHz by extrapolation of the linear fit from the plot of Ω_R versus B_1 (Figure 3.19).

3.7. Conclusions

The use of a ligand radical spin host in charge-neutral $[\text{Au}(\text{adt})_2]$ gave an impressive phase memory time of up to 21 μs , which is significantly longer than other qubits based on second- and third-row metals. This lifetime is comparable of the current state of the art in molecule-based systems. The performance of this Au complex when compared to isoelectronic group 10 species,⁵² derives from the combination of the complex charge and the miniscule contribution to the ground state from the Au 5d orbitals. The former facilitated testing of a variety of esoteric solvents comprised of nuclei with low magnetogyric ratios which had not been applied to probing spin dynamics previously. The latter is reflected in the small hyperfine coupling that is dwarfed by the nuclear quadrupolar coupling, and there is an indication from the orientation dependent measurements that quadrupolar interactions also serve to diminish the lifetime of the cohered state. In conjunction with these nuclear characteristics, the colossal SOC supplied by the Au ion precluded measurement above 80 K, following the trend established for $[\text{M}(\text{adt})_2]^{1-}$ ($\text{M} = \text{Ni}, \text{Pd}, \text{Pt}$), as SOC amplifies the Raman process that accelerates spin-lattice relaxation above 20 K.

Relaxation times are markedly shorter for the solid dilution of **3.1b** in the isoelectronic nickel complex on account of the semiconducting properties of the doped mixture. This greatly impacts spin-lattice relaxation, which in turn shortens the phase memory time though this is still 1.44 μs at 10 K. The conductivity provides a unique handle in tackling the next stage in the DiVincenzo criteria,⁸² namely single qubit addressability. Given the persistent square planar geometry adopted by each member of this electron transfer series (monocationic and mononanionic species, $S = 0$; neutral complex, $S = 1/2$) there is no disruption to the stacked structure of the doped material when a potential is applied that can switch the qubit “on” and “off”, and therein the ability to switch between various spin states and entanglement scenarios. We will continue to develop this ligand radical platform with the aim of executing electrically operated multi-qubit quantum gates using molecular semiconducting assemblies.

3.8.Experimental

3.8.1.Synthesis

The compound (adt)SnMe₂ was prepared following the published method.³⁵ Solvents were either dried with a system of drying columns (CH₂Cl₂, MeCN) or degassed by five successive freeze-pump-thaw cycles and dried over 3 Å molecular sieves (CDCl₃, CCl₄, CS₂, Cl₃CCN). All other reagents were used as received.

[PPh₄][Au(adt)₂] (3.1a). A 50 mL Schlenk flask charged with K[AuCl₄] (50 mg; 0.132 mmol), (adt)SnMe₂ (120 mg; 0.267 mmol) and MeCN (20 mL), and stirred at ambient temperature for 1 h. To the dark green reaction mixture was added PPh₄Br (56 mg; 0.132 mmol) in a single portion under a flow of nitrogen, and mixture further stirred for 30 min. The solvent was removed under reduced pressure and the resultant solid was washed with H₂O (3 × 10 mL), MeOH (3 × 10 mL), and Et₂O (3 × 10 mL), and dried under vacuum. Yield: 135 mg (90%). Anal. Calcd for C₅₆H₄₈O₄PS₄Au·0.5CH₂Cl₂: C, 57.33; H, 4.17. Found: C, 57.08; H, 3.95. ¹H NMR (MeCN-*d*₃; δ / ppm): 7.94 (t, 4H, Ph), 7.73 (m, 20H, PPh₄⁺), 7.01 (d, 8H, *J*_{HH} = 8.5 Hz, Ph), 6.55 (d, 8H, *J*_{HH} = 8.5 Hz, Ph), 3.76 (s, 12 H, -OCH₃). ¹³C NMR (DMSO-*d*₆; δ / ppm): 177.40 (s), 157.99 (s), 135.84 (s), 135.10 (s), 134.99 (s), 131.00 (s), 130.87 (s), 113.49 (s), 55.36 (s). Absorption spectrum (CH₂Cl₂; λ_{max} / nm (ε / 10⁻¹ M⁻¹ cm⁻¹)): 472 (0.32), 696 (0.16). ESI mass spectrum (neg. ion): *m/z* 801.04 [M]⁻.

[Au(adt)₂] (3.1b). To a 50 mL Schlenk flask containing **3.1a** (130 mg; 0.114 mmol) in CH₂Cl₂ (20 mL) was added I₂ (29 mg; 0.114 mmol) left to stir at ambient temperature for 1 h. The initial dark green reaction mixture rapidly transitioned to dark brown solution. The solvent was stripped under reduced pressure and the residue washed with H₂O (3 × 10 mL), MeOH (3 × 10 mL), and Et₂O (3 × 10 mL), and dried under vacuum. Yield: 76 mg (83%). Anal. Calcd for C₃₂H₂₈O₄S₄Au: C, 47.90; H, 3.50. Found: C, 47.50; H, 3.45. Absorption spectrum (CH₂Cl₂; λ_{max} / nm (ε / 10⁻⁴ M⁻¹ cm⁻¹)): 455 (0.38), 557 (sh, 0.18), 633 (sh, 0.13), 1556 (1.38). ESI mass spectrum (neg. ion): *m/z* 801.04 [M]⁻.

3.8.2. Physical Characterisation and Theoretical

X-ray Crystallographic Data Collection and Structure Refinement. Diffraction quality crystals of **3.1a** and **3.1b** were obtained by slow diffusion of hexanes into a concentrated dichloromethane solution of the complex. The crystals were coated with paratone oil and mounted on the end of a nylon loop attached to the end of the goniometer. Data were collected with a Bruker SMART APEX CCD diffractometer equipped with a Kryoflex attachment supplying a nitrogen stream at 150 K. Structure solution and refinement were carried out with SHELXS-97⁸³ and SHELXL-97⁸⁴ using the WinGX⁸⁵ software package. Corrections for incident and diffracted beam absorption effects were applied using empirical absorption corrections.⁸⁶ For **3.1a**, all non-hydrogen atoms were refined with anisotropic thermal parameters and the positions of hydrogen atoms of the PPh₄⁺ counterion were calculated based on stereochemical considerations and refined isotropically. For **3.1b**, all non-hydrogen atoms were refined using anisotropic thermal parameters. Additionally, a severely disordered CH₂Cl₂ solvent molecule was refined isotropically, and split over two positions based on the electron density identified by the DF map. Final unit cell data and refinement statistics are collected in Table 3.3. The crystallographic data for **3.1a** and **3.1b** (CCDC 1857516 and 1857517) can be obtained free of charge from the Cambridge Crystallographic Data Centre, 12, Union Road, Cambridge CB2 1EZ; fax:(+44) 1223- 336-033, deposit@ccdc.cam.ac.uk.

Table 3.3. Crystallographic Data for compounds in Chapter 3

compound	PPh ₄ [Au(adt) ₂]	[Au(adt) ₂] ₂ ·CH ₂ Cl ₂
formula	C ₅₆ H ₄₈ O ₄ PS ₄ Au	C ₃₃ H ₃₀ O ₄ S ₄ Cl ₂ Au
fw	1141.12	884.66
T, K	150(2)	150(2)
λ, Å	0.71073	0.71073
2θ range, deg	4.35 – 52.28	4.46 – 53.16
crystal system	triclinic	monoclinic
space group	<i>P</i> $\bar{1}$	<i>P</i> 2 ₁ / <i>c</i>
a, Å	11.913(5)	11.584(4)
b, Å	13.949(5)	15.448(5)
c, Å	15.859(6)	9.441(3)
α, deg	81.424(4)	90
β, deg	72.882(4)	102.511(2)
γ, deg	79.945(4)	90
V, Å ³	2467(2)	1649.5(9)
Z	2	2
ρ, g cm ⁻³	1.536	1.781
μ, mm ⁻¹	3.231	4.913
crystal size	0.08 × 0.12 × 0.13	0.08 × 0.10 × 0.20
color, habit	green block	brown block
reflections	27552	21212
independent data	9442	3449
restraints	0	0
parameters refined	595	216
GoF ^a	1.169	1.062
R1, ^{b,c} wR2 ^{d,c}	0.0151, 0.0427	0.0187, 0.0463
R1, ^{b,e} wR2 ^{d,e}	0.0163, 0.0495	0.0202, 0.0536
largest diff. peak, e Å ⁻²	0.375	1.610
largest diff. hole, e Å ⁻²	-1.020	-0.990

^a GoF = $\{\sum[w(F_o^2 - F_c^2)^2]/(n - p)\}^{1/2}$, where n = number of reflections and p is the total number of parameters refined. ^b R1 = $\sum||F_o| - |F_c||/\sum|F_o|$. ^c R indices for data cut off at $I > 2\sigma(I)$. ^d wR2 = $\{\sum[w(F_o^2 - F_c^2)^2]/\sum[w(F_o^2)^2]\}^{1/2}$, where $w = 1/[\sigma^2(F_o^2) + (aP)^2 + bP]$, $P = (F_o^2 + 2F_c^2)/3$. ^e R indices for all data.

EPR Spectroscopy. Continuous wave X-band EPR spectra was recorded on a Bruker ELEXSYS E500 spectrometer. Spectra were simulated using the simulation package XSOPHE;⁸⁷ fluid solution spectra using the spin-Hamiltonian $\hat{H} = g\mu_B BS + aSI$, and frozen

solution spectra using the spin-Hamiltonian $\hat{H} = \mu_B \mathbf{B} \cdot \mathbf{g} \cdot \mathbf{S} + \mathbf{S} \cdot \mathbf{A} \cdot \mathbf{I} + \mathbf{I} \cdot \mathbf{P} \cdot \mathbf{I} - \mu_n g_n \mathbf{B} \cdot \mathbf{I}$. The symbols have all their usual meanings.

Pulsed X-band EPR data were measured using a Bruker ELEXSYS E580 spectrometer equipped with an Oxford Instruments CF935 continuous Helium flow cryostat. Samples were prepared by dissolving **3.1b** in the selected solvent mixtures (4:1 CDCl₃/Cl₃CCN, 4:1 CCl₄/Cl₃CCN, 4:1 CS₂/Cl₃CCN, 4:1 Cl₃CCN/CDCl₃) to a concentration of 1 mM and loading into 3.8 mm o.d. quartz EPR tubes. The solution samples were degassed via three freeze-pump-thaw cycles, followed by flame sealing. ESE-detected EPR spectra were collected at 10 K using a Hahn echo pulse sequence ($\pi/2 - \tau - \pi - \tau - \text{echo}$) with a 4-step phase cycle, where $\pi/2 = 16$ ns, $\pi = 32$ ns and $\tau = 400$ ns. Simulations were performed as using XSOPHE⁸⁷ using the aforementioned spin-Hamiltonian. Phase memory times (T_M) were also measured with a Hahn echo pulse sequence. Decay curves were collected at field positions indicated on ESE spectra. Acquisition times were set to capture the top half of the spin echo and the acquired echo was integrated to obtain the spectrum. The data were phased by maximizing the sum of the data points in the real components of the spectrum and fit to the biexponential function $I(\tau) = y_0 + A_f \exp(-\tau/T_{M,f}) + A_s \exp(-\tau/T_{M,s})$, where f and s indicate fast and slow processes, respectively. Spin-lattice relaxation times (T_1) were collected at 10 K following the inversion recovery sequence ($\pi - T - \pi/2 - \tau - \pi - \tau - \text{echo}$) with 4-step phase cycling in which $\pi/2 = 16$ ns, $\pi = 32$ ns, and T incremented from a starting value of 100 ns. The value of τ was selected to correspond to the maximum in the ESEEM at 400 ns. Acquisition times were set to capture the top half of the spin echo and the acquired echo was integrated to obtain the spectrum. The data were phased by maximizing the sum of the data points in the real components of the spectrum and fit to the biexponential function $I(\tau) = y_0 + A_f \exp(-\tau/T_{1,f}) + A_s \exp(-\tau/T_{1,s})$. Nutation measurements were performed at three different microwave powers with a nutation pulse of variable length (tipping) pulse followed by a Hahn echo sequence ($t_p - T - \pi/2 - \tau - \pi - \tau - \text{echo}$). Data were collected employing 4-phase cycling, in which in which $\pi/2 = 16$ ns, $\pi = 32$ ns and $\tau = 400$ ns for nutation pulse lengths $T = 600$ ns. The tipping pulse, t_p , is augmented in 4 ns increments from a starting value of 4 ns. Nutation data was processed by subtracting a stretched exponential baseline from the echo decay, then zero-filling with 1024 or 2048 points, followed by a Fourier transform with a Hamming window.

Other Physical Methods. Cyclic voltammetry measurements were performed with a Metrohm Autolab P128 potentiostat. The electrode configuration consisted of a 2 mm glassy carbon working electrode, a platinum auxiliary electrode and a reference electrode consisting of Ag/AgNO₃ (0.01 M in MeCN) incorporated into a salt bridge containing supporting electrolyte (to minimize Ag⁺ leakage). The measurements were collected using a 1 mM solution of **3.1a** dissolved in dichloromethane containing 0.1 M [N(^{*t*}Bu)₄]PF₆ as electrolyte. All reduction potentials are referenced versus the ferrocenium/ferrocene (Fc⁺⁰) couple. Electronic absorption spectra were recorded on a Shimadzu UVA 3600 spectrophotometer (range 200–1600 nm). Electrospray ionization (ESI) mass spectra were obtained on a Bruker micrOTOF-Q mass spectrometer. Elemental analysis were performed using an EA 1110 CHNS, CE-440 Elemental Analyzer.

Calculations. All calculations in this work were performed with the electronic structure program ORCA.⁸⁸ Geometry optimizations were carried out using the BP86 functional with dichloromethane as solvent.^{89, 90} A segmented all-electron relativistically contracted basis set of triple- ζ -quality (def2-TZVPP) was used for all atoms.⁹¹ A scalar relativistic correction was applied using the zeroth-order regular approximation (ZORA) method⁹²⁻⁹⁴ as implemented by van Wüllen.⁹⁵ In the context of ZORA, a one center approximation has been shown to introduce only minor errors to the final geometries. Auxiliary basis sets for all complexes used to expand the electron density in the calculations were chosen to match the orbital basis. The conductor like screening model (COSMO) was used for all calculations.⁹⁶ The self-consistent field calculations were tightly converged ($1 \times 10^{-8} E_h$ in energy, $1 \times 10^{-7} E_h$ in the density change, and 1×10^{-7} in the maximum element of the DIIS^{97, 98} error vector). The geometry search for all complexes was carried out in redundant internal coordinates without imposing geometry constraints. The property calculations at the optimized geometries were done with the PBE0 hybrid functional^{99, 100} and the RIJCOSX algorithm to expedite calculation of the Hartree-Fock exchange.^{101, 102} In this case the same basis sets were used but with enhanced integration accuracy (SPECIALGRIDINTACC 10) for the metal and sulfur atoms. Calculation of spin-Hamiltonian parameters included a larger the integration grid (Grid5) and fully decontracted basis sets.^{103, 104} The use of all-electron calculations using scalar relativistic corrections mandated the effective nuclear charge (Z_{eff}) for Au be adjusted to 27.5, which corresponds to a one-electron spin-orbit coupling constant (ζ_{5d}) of ca. 4500 cm⁻¹. All other effective charges had their default values. Canonical orbitals and density plots were constructed using the program Molekel.

3.9.References

1. K. Ray, T. Weyhermüller, A. Goossens, M. W. J. Crajé and K. Wieghardt, *Inorganic Chemistry*, 2003, **42**, 4082-4087.
2. N. Bartlett, *Gold Bulletin*, 1998, **31**, 22-25.
3. M. Parthey and M. Kaupp, *Chemical Society Reviews*, 2014, **43**, 5067-5088.
4. D. G. Branzea, F. Pop, P. Auban-Senzier, R. Clérac, P. Alemany, E. Canadell and N. Avarvari, *Journal of the American Chemical Society*, 2016, **138**, 6838-6851.
5. S. Kokatam, K. Ray, J. Pap, E. Bill, W. E. Geiger, R. J. LeSuer, P. H. Rieger, T. Weyhermüller, F. Neese and K. Wieghardt, *Inorganic Chemistry*, 2007, **46**, 1100-1111.
6. T. Naito, N. Watanabe, Y. Sakamoto, Y. Miyaji, T. Shirahata, Y. Misaki, S. Kitou and H. Sawa, *Dalton Transactions*, 2019, **48**, 12858-12866.
7. K. Mebrouk, W. Kaddour, P. Auban-Senzier, C. Pasquier, O. Jeannin, F. Camerel and M. Fourmigué, *Inorganic Chemistry*, 2015, **54**, 7454-7460.
8. Y. Le Gal, T. Roisnel, P. Auban-Senzier, N. Bellec, J. Íñiguez, E. Canadell and D. Lorcy, *Journal of the American Chemical Society*, 2018, **140**, 6998-7004.
9. S. Sproules, in *Electron Paramagnetic Resonance*, eds. V. Chechik and D. M. Murphy, The Royal Society of Chemistry, Cambridge, UK, 2017, vol. 25, pp. 61-97.
10. M. S. Fataftah, J. M. Zadrozny, S. C. Coste, M. J. Graham, D. M. Rogers and D. E. Freedman, *Journal of the American Chemical Society*, 2016, **138**, 1344.
11. M. J. Graham, M. Krzyaniak, M. R. Wasieleski and D. E. Freedman, *Inorganic Chemistry*, 2017, **56**, 8106.
12. M. J. Graham, C. Yu, M. Krzyaniak, M. R. Wasieleski and D. E. Freedman, *Journal of the American Chemical Society*, 2017, **139**, 3196.
13. T. J. Pearson, D. W. Laorenza, M. Krzyaniak, M. R. Wasieleski and D. E. Freedman, *Dalton Transactions*, 2018, DOI: 10.1039/c1038dt02312c.
14. C. Yu, M. J. Graham, J. M. Zadrozny, J. Niklas, M. Krzyaniak, M. R. Wasieleski, O. G. Poluektov and D. E. Freedman, *Journal of the American Chemical Society*, 2016, **138**, 14678.
15. J. M. Zadrozny and D. E. Freedman, *Inorganic Chemistry*, 2015, **54**, 12027.
16. J. M. Zadrozny, J. Niklas, O. G. Poluektov and D. E. Freedman, *ACS Central Sciences*, 2015, **1**, 488.
17. M. Atzori, S. Benci, E. Morra, L. Tesi, M. Chiesa, R. Torre, L. Sorace and R. Sessoli, *Inorganic Chemistry*, 2018, **57**, 731.
18. M. Atzori, E. Morra, L. Tesi, A. Albino, M. Chiesa, L. Sorace and R. Sessoli, *Journal of the American Chemical Society*, 2016, **138**, 11234.

19. M. Atzori, L. Tesi, S. Benci, A. Lunghi, R. Righini, A. Taschin, R. Torre, L. Sorace and R. Sessoli, *Journal of the American Chemical Society*, 2017, **139**, 4338.
20. K. Bader, D. Dengler, S. Lenz, B. Endeward, S.-D. Jiang, P. Neugebauer and J. van Slageren, *Nature Communications.*, 2014, **5**, 5304.
21. K. Bader, S. H. Schlindein, D. Gudat and J. van Slageren, *Physical Chemistry Chemical Physics*, 2017, **19**, 2525.
22. K. Bader, M. Winkler and J. van Slageren, *Chemical Communications*, 2016, **52**, 3623.
23. S. Lenz, K. Bader, H. Bamberger and J. van Slageren, *Chemical Communications*, 2017, **53**, 4477.
24. Y. Dai, Z. Shi, Y. Fu, S. Mu, Y. Wu, J.-H. Su, L. Qin, Y.-Q. Zhai, Y.-F. Deng, X. Rong and J. Du, 2017, arXiv:1706.09259v09251 [quant-ph].
25. S. Kokatam, K. Ray, J. Pap, E. Bill, W. E. Geiger, R. J. LeSuer, P. H. Rieger, T. Weyhermüller, F. Neese and K. Wieghardt, *Inorganic Chemistry*, 2007, **46**, 1100.
26. K. Ray, T. Weyhermüller, F. Neese and K. Wieghardt, *Inorganic Chemistry*, 2005, **44**, 5345.
27. R. B. Pontes, F. D. Novaes, A. Fazzio and A. J. R. da Silva, *Journal of the American Chemical Society*, 2006, **128**, 8996.
28. S. Kaneko, D. Murai, S. Marqués-González, H. Nakamura, Y. Komoto, S. Fujii, T. Nishino, K. Ikeda, K. Tsukagoshi and M. Kiguchi, *Journal of the American Chemical Society*, 2016, **138**, 1294.
29. S. Cardonna-Serra and A. Gaita-Ariño, *Dalton Transactions*, 2018, **47**, 5533.
30. M. D. Jenkins, D. Zueco, O. Roubeau, G. Aromí, J. Majer and F. Luis, *Dalton Trans.*, 2016, **45**, 16682.
31. K. Arumugam, M. Selvachandran, A. Obanda, M. C. Shaw, P. Chandrasekaran, S. L. Caston Good, J. T. Mague, S. Sproules and J. P. Donahue, *Inorganic Chemistry*, 2018, **57**, 4023.
32. K. Arumugam, M. C. Shaw, P. Chandrasekaran, D. Villagrán, T. G. Gray, J. T. Mague and J. P. Donahue, *Inorganic Chemistry*, 2009, **48**, 10591.
33. K. Arumugam, M. C. Shaw, J. T. Mague, E. Bill, S. Sproules and J. P. Donahue, *Inorganic Chemistry*, 2011, **50**, 2995.
34. K. Arumugam, R. Yu, D. Villagrán, T. G. Gray, J. T. Mague and J. P. Donahue, *Inorganic Chemistry*, 2008, **47**, 5570.
35. P. Chandrasekaran, A. F. Greene, K. Lillich, S. Capone, J. T. Mague, S. DeBeer and J. P. Donahue, *Inorganic Chemistry*, 2014, **54**, 9192.
36. Y. Yan, C. Keating, P. Chandrasekaran, U. Jayarathne, J. T. Mague, S. DeBeer, K. M. Lancaster, S. Sproules, I. V. Rubtsov and J. P. Donahue, *Inorganic Chemistry*, 2013, **52**, 6743.

37. G. N. Schrauzer and V. P. Mayweg, *Journal of the American Chemical Society*, 1965, **87**, 1483.
38. R. Perochon, L. Piekara-Sady, W. Jurga, R. Clérac and M. Fourmigué, *Dalton Trans.*, 2009, 3052.
39. J. M. Tunney, A. J. Blake, E. S. Davies, J. McMaster, C. Wilson and C. D. Garner, *Polyhedron*, 2006, **25**, 591.
40. K. Mebrouk, W. Kaddour, P. Auban-Senzier, C. Pasquier, O. Jeannin, F. Camerel and M. Fourmigué, *Inorganic Chemistry*, 2015, **54**, 7454.
41. S. Rabaça, A. C. Cerdeira, A. I. S. Neves, S. I. G. Dias, C. Mézière, I. C. Santos, L. C. J. Pereira, M. Fourmigué, R. T. Henriques and M. Almeida, *Polyhedron*, 2009, **28**, 1069.
42. L. Ambrosio, M. C. Aragoni, M. Arca, F. A. Devillanova, M. B. Hursthouse, S. L. Huth, F. Isaia, V. Lippolis, A. Mancini and A. Pintus, *Chemistry- An Asian Journal*, 2010, **5**, 1395.
43. G. C. Papavassiliou, G. C. Anyfantis, C. P. Ratopoulou, V. Psycharis, N. Ioannidis, V. Petrouleas and P. Paraskevopoulou, *Polyhedron*, 2009, **28**, 3368.
44. S. K. Sur, *Journal of Magnetic Resonance*, 1989, **82**, 169-173.
45. K. Ray, T. Petrenko, K. Wieghardt and F. Neese, *Dalton Transactions*, 2007, 1552.
46. S. Sproules and K. Wieghardt, *Coordination Chemistry Reviews*, 2011, **255**, 837.
47. S. Rabaça, A. C. Cerdeira, S. Oliveira, I. C. Santos, R. T. Henriques, L. C. J. Pereira, J. T. Coutinho and M. Almeida, *Polyhedron*, 2012, **39**, 91.
48. R. Perochon, C. Poriel, O. Jeannin, L. Piekara-Sady and M. Fourmigué, *European Journal of Inorganic Chemistry*, 2009, 5413.
49. K. Ray, T. Weyhermüller, A. Goossens, M. W. Crajé and K. Wieghardt, *Inorganic Chemistry*, 2003, **42**, 4082.
50. S. Sproules, P. Banerjee, T. Weyhermüller, Y. Yan, J. P. Donahue and K. Wieghardt, *Inorganic Chemistry*, 2011, **50**, 7106.
51. A. C. Cerdeira, M. L. Afonso, I. C. Santos, L. C. J. Pereira, J. T. Coutinho, S. Rabaça, D. Simão, R. T. Henriques and M. Almeida, *Polyhedron*, 2012, **44**, 228.
52. J. McGuire, H. N. Miras, J. P. Donahue, E. Richards and S. Sproules, *Chemistry- A European Journal*, 2018, **24**, 17598.
53. S. Sproules, F. L. Benedito, E. Bill, T. Weyhermüller, S. DeBeer George and K. Wieghardt, *Inorganic Chemistry*, 2009, **48**, 10926.
54. S. S. Eaton and G. R. Eaton, in *Distance Measurements in Biological Systems by EPR*, eds. L. J. Berliner, G. R. Eaton and S. S. Eaton, Springer US, Boston, MA, 2002, vol. 19, pp. 22-154.
55. A. Lunghi, F. Totti, R. Sessoli and S. Sanvito, *Nature Communications*, 2017, **8**, 14620.

56. R. Kirmse, J. Stach, W. Dietzsch, G. Steimecke and E. Hoyer, *Inorganic Chemistry*, 1980, **19**, 2679.
57. J.-L. Du, G. R. Eaton and S. S. Eaton, *Applied Magnetic Resonance*, 1994, **6**, 373.
58. J.-L. Du, G. R. Eaton and S. S. Eaton, *Journal of Magnetic Resonance Series A*, 1996, **119**, 240.
59. R. Husted, J.-L. Du, G. R. Eaton and S. S. Eaton, *Magnetic Resonance Chemistry*, 1995, **33**, S66.
60. L. A. Benítez, J. F. Sierra, W. Savero Torres, A. Arrighi, F. Bonell, M. V. Costache and S. O. Valenzuela, *Nature Physics*, 2018, **14**, 303.
61. W. Yan, O. Txoperena, R. Llopis, H. Dery, L. E. Hueso and F. Casanova, *Nature Communications*, 2016, **7**, 13372.
62. J. H. Garcia, M. Vila, A. W. Cummings and S. Roche, *Chemical Society Reviews*, 2018, **47**, 3359.
63. M. Atzori, L. Tesi, E. Morra, M. Chiesa, L. Sorace and R. Sessoli, *Journal of the American Chemical Society*, 2016, **138**, 2154.
64. D. Belo, J. Morgado, E. B. Lopes, I. C. Santos, S. Rabaça, M. T. Duarte, V. Gama, R. T. Henriques and M. Almeida, *Synthetic Metals*, 1999, **102**, 1751.
65. D. G. Branzea, F. Pop, P. Auban-Senzier, R. Clérac, P. Alemany, E. Canadell and N. Avarvari, *138*, 2016, 6838.
66. O. J. Dautel, M. Fourmigué, E. Canadell and P. Auban-Senzier, *Advanced Functional Materials*, 2002, **12**, 693.
67. A. Filatre-Furcate, P. Auban-Senzier, M. Fourmigué, T. Roisnel, V. Dorcet and D. Lorcy, *Dalton Transactions*, 2015, **44**, 15683.
68. A. Filatre-Furcate, T. Roisnel, M. Fourmigué, O. Jeannin, N. Bellec, P. Auban-Senzier and D. Lorcy, *Chemistry- A European Journal*, 2017, **23**, 16004.
69. E. Fujiwara, B. Zhou, A. Kobayashi, H. Kobayashi, Y. Fujishiro, E. Nishibori, M. Sakata, S. Ishibashi and K. Terakura, *European Journal of Inorganic Chemistry*, 2009, 1585.
70. T. Higashino, O. Jeannin, T. Kawamoto, D. Lorcy, T. Mori and M. Fourmigué, *Inorganic Chemistry*, 2015, **54**, 9908.
71. Y. Le Gal, T. Roisnel, P. Auban-Senzier, T. Guizouarn and D. Lorcy, *Inorganic Chemistry*, 2014, **53**, 8755.
72. R. Le Penec, O. Jeannin, P. Auban-Senzier and M. Fourmigué, *New Journal of Chemistry*, 2016, **40**, 7113.
73. J. P. M. Nunes, M. J. Figueira, D. Belo, I. C. Santos, B. Ribeiro, E. B. Lopes, R. T. Henriques, J. Vidal-Gancedo, J. Veciana, C. Rovira and M. Almeida, *Chemistry- A European Journal*, 2007, **13**, 9841.

74. M. Sasa, E. Fujiwara, A. Kobayashi, S. Ishibashi, K. Terakura, Y. Okano, H. Fujiwara and H. Kobayashi, *Journal of Materials Chemistry*, 2005, **15**, 155.
75. W. Suzuki, E. Fujiwara, A. Kobayashi, Y. Fujishiro, E. Nishibori, M. Takata, M. Sakata, H. Fujiwara and H. Kobayashi, *Journal of the American Chemical Society*, 2003, **125**, 1486.
76. N. Tenn, N. Bellec, O. Jeannin, L. Piekara-Sady, P. Auban-Senzier, J. Iñiguez, E. Canadell and D. Lorcy, *Journal of the American Chemical Society*, 2009, **131**, 16961.
77. G. Yzambart, N. Bellec, G. Nasser, O. Jeannin, T. Roisnel, M. Fourmigué, P. Auban-Senzier, J. Iñiguez, E. Canadell and D. Lorcy, *Journal of the American Chemical Society*, 2012, **134**, 17138.
78. B. Zhou, H. Yajima, Y. Idobata, A. Kobayashi, T. Kobayashi, E. Nishibori, H. Sawa and H. Kobayashi, *Chemistry Letters*, 2012, **41**, 154.
79. M. J. Graham, J. M. Zadrozny, M. Shiddiq, J. S. Anderson, M. S. Fataftah, S. Hill and D. E. Freedman, *Journal of the American Chemical Society*, 2014, **136**, 7623.
80. M. Warner, S. Din, I. S. Tupitsyn, G. W. Morley, A. M. Stoneham, J. A. Gardener, Z. Wu, A. J. Fisher, S. Heutz, C. W. M. Kay and G. Aeppli, *Nature*, 2013, **503**, 504.
81. S. R. Hartmann and E. L. Hahn, *Physical Reviews*, 1962, **128**, 2042.
82. D. P. DiVincenzo, *Forsch. Phys. - Reports on Progress in Physics*, 2000, **48**, 771.
83. G. M. Sheldrick, *Acta Crystallographica Section A*, 1990, **46**, 467.
84. G. M. Sheldrick, *Acta Crystallographica Section A*, 2008, **64**, 112.
85. L. J. Farrugia, *Journal of Applied Crystallography*, 1999, **32**, 837.
86. R. C. Clark and J. S. Reid, *Acta Crystallographica Section A*, 1995, **51**, 887.
87. G. R. Hanson, K. E. Gates, C. J. Noble, M. Griffin, A. Mitchell and S. Benson, *Journal of Inorganic Biochemistry.*, 2004, **98**, 903.
88. F. Neese, *WIREs Computational Molecular Science*, 2012, **2**, 73-78.
89. A. D. Becke, *Journal of Chemical Physics*, 1988, **84**, 4524.
90. J. P. Perdew, *Physical Reviews B*, 1986, **33**, 8822.
91. D. A. Pantazis, X.-Y. Chen, C. R. Landis and F. Neese, *Journal of Chemical Theory and Computation*, 2008, **4**, 908.
92. E. van Lenthe, J. G. Snijders and E. J. Baerends, *Journal of Chemical Physics*, 1996, **105**, 6505-6516.
93. E. van Lenthe, A. van der Avoird and P. E. S. Wormer, *Journal of Chemical Physics*, 1998, **108**, 4783-4796.
94. J. H. van Lenthe, S. Faas and J. G. Snijders, *Chemical Physics Letters*, 2000, **328**, 107-112.
95. C. J. van Wüllen, *Journal of Chemical Physics*, 1998, **109**, 392-399.

96. A. Klamt and G. Schüürmann, *Journal of the Chemical Society, Perkin Transactions 2*, 1993, 799.
97. P. Pulay, *Chemical Physics Letters*, 1980, **73**, 393.
98. P. Pulay, *Journal of Computational Chemistry*, 1982, **3**, 556.
99. J. P. Perdew, K. Burke and M. Ernzerhof, *Physical Review Letters*, 1996, **77**, 3865.
100. C. Adamo and V. Barone, *Journal of Chemical Physics*, 1999, **110**, 6158.
101. F. Neese, F. Wennmohs, A. Hansen and U. Becker, *Chemical Physics*, 2009, **356**, 98-109.
102. R. Izsák and F. Neese, *Journal of Chemical Physics*, 2011, **135**, 144105.
103. F. Neese, *Journal of Chemical Physics*, 2001, **115**, 11080.
104. F. Neese, *Journal of Chemical Physics*, 2003, **118**, 3939.
105. *Molekel*, Advanced Interactive 3D-Graphics for Molecular Sciences, Swiss National Supercomputing Center. <https://ugovaretto.github.io/molekel/>.

4.Chapter 4: Rare-earth Group 10 Trimetallics of Dithiooxalate

4.1.Introduction

4.1.1.The Dithiooxalate Ligand

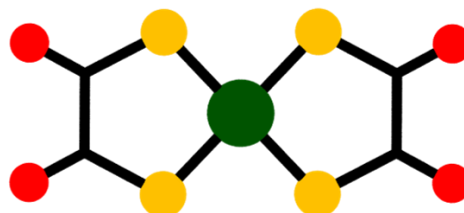


Figure 4.1. Molecular structure of $[\text{Ni}(\text{dto})_2]^-$.

A century of coordination chemistry of the dithiooxalate ligand, $(\text{dto})^{2-}$, has revealed a unique set of properties that sets it apart from other 1,2-dithiolate ligands, i.e. dithiolenes.¹⁻² The salient features are the two binding sites: a dithiolate on one side and an α -diketonate on the other. The utility of the ditopic ligand stems from this asymmetry, where the soft sulfur-donor chelate appeals to mid-to-late transition metal ions whereas Lewis acidic metal ions are drawn to the hard oxygen-donor side of the ligand.² This has led to the assembly of numerous mixed-metal oligomers and coordination polymers by simply combining hard and soft metal ions with the dithiooxalate salt in a one-pot reaction.³⁻¹⁷ The majority of these studies are focussed on the structural topology of the metal ions, and the magnetic properties of the constituent metal ions linked by this ligand.

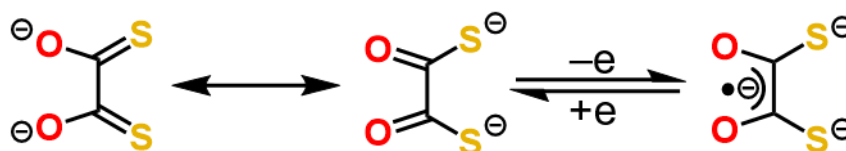


Figure 4.2. Known members of the electron transfer series of the dto ligand and presumed resonance forms.

Electron transfer chemistry – a cornerstone of bis(dithiolene) complexes – is non-existent in monometallic bis(dithiooxalate) species such as archetypal $[\text{Ni}(\text{dto})_2]^{2-}$.² This stems from the resonance stabilisation within the $(\text{dto})^{2-}$ ligand between the dithiolate and diolate limiting forms (Figure 4.2), as evidenced by the short C–S and C–O bonds indicative of multiple bond character.² However reversible one-electron transfer chemistry is operative for the tin halide adducts $[\text{M}\{(\text{dto})\text{SnX}_4\}_2]^{2-}$ ($\text{M} = \text{Ni}, \text{Pd}, \text{Pt}; \text{X} = \text{F}, \text{Cl}, \text{Br}, \text{I}$).⁸⁻⁹ Akin to bis(dithiolene) complexes,¹⁸⁻¹⁹ the redox chemistry is ligand-based, with electrons added to a π^* orbital stabilised by the coordinated Lewis acid generating an O, O' -semiquinonate

radical chelate.²⁰ All attempts at isolating and characterising the reduced Sn adducts were unsuccessful as the halide co-ligands were unable to stabilise a semiquinonate coordinated to the Sn ion.

4.1.1.1. Tin Chemistry of the Dithiooxalate Ligand

Coordination chemistry of the dithiooxalate ligand is dominated by the transition metals with one interloper, tin. Tin was one of the very first metals shown to be sequestered by dithiolenes and can adopt many coordination geometries from the distorted octahedral tris(dithiolene) $[\text{Sn}^{\text{IV}}(\text{dmit})_3]^{2-}$ and $[\text{Sn}^{\text{IV}}(\text{mnt})_3]^{2-}$ to the tetrahedral heteroleptic dialkyl tin dithiolenes $[\text{SnR}_2(\text{dt})]$ which are more akin to organic molecules than transition metal complexes.²¹⁻²³ In fact, dialkyl tin dithiolates occupy a unique role in dithiolene chemistry acting as excellent transmetallating agents; abstracting two halides in exchange for a dithiolene ligand. This is an excellent substitute for some of the lower yielding reactions such as Schrauzer's method as the transmetalation is high yield and clean, requiring only an alcohol to wash away the dialkyl dihalo tin byproduct.²⁴ This methodology was even employed in the synthesis of $[\text{Au}(\text{adt})_2](\text{PPh}_4)$ (see Chapter 2) with the dimethyl tin dianisyldithiolate $[\text{SnMe}_2(\text{adt})]$ (Figure 4.3.).

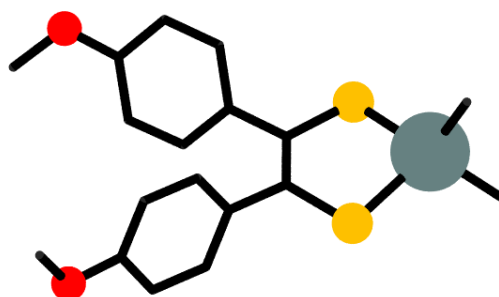


Figure 4.3. Molecular structure of $[\text{SnMe}_2(\text{adt})]$.

Adams utilised this chaperone effect with a dimethyl tin dithiooxalate compound to transfer dithiooxalate to platinum and ruthenium bipyridine or cyclooctadiene complexes.²⁵⁻²⁶ The geometrically inflexible $\text{Pt}^{\text{II}} d^8$ square-planar complexes readily undergo full substitution ejecting the chlorides as a SnMe_2Cl_2 unit as verified by NMR. An interesting case arises for the transmetalation of $[\text{Ru}(\text{Me}_2\text{bipy})(\text{PPh}_3)\text{Cl}_2]$ where upon reaction only one chloride is substituted and a phosphine ligand is lost. In this case the positively charged $[\text{SnMe}_2\text{Cl}]^+$ species is found to coordinate to the diketyl functionality of $(\text{dto})^{2-}$, addition of a polar coordinating solvent such as DMSO allows for elimination of the remaining Ru coordinated chloride. This work highlights the versatility of dialkyl tin protecting groups but also sheds light on the electrochemical phenomena observed 40 years prior in nickel bis(dithiooxalate).

In tandem with tin tetrahalides Coucouvanis employed many other Lewis acids such as $[\text{TiCp}_2]$ and alkyl tin halides, all of which red shift the electronic spectra of $[\text{Ni}(\text{dto})_2]^{2-}$ indicating coordination to the O,O' pocket but do not facilitate electron transfer.²⁷ The absence of electron transfer for the alkyl tin halide adducts is of particular puzzlement as it was assumed the alkyl tin moieties would adopt the same structural motif as their halide counterparts.²⁸ The NMR structure elucidation by Adams shows us a very different structure with a trigonal bipyramidal Sn centre and high susceptibility to solvent effects which cannot be expected to behave in a similar fashion.

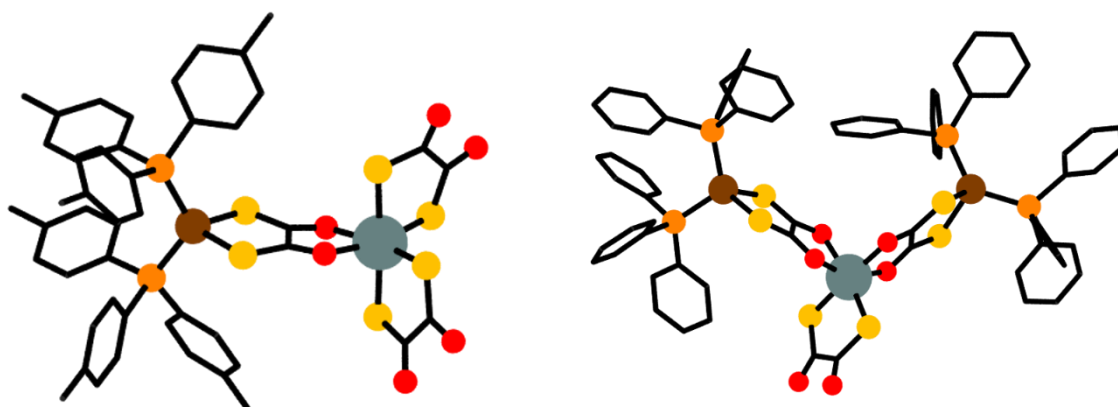


Figure 4.4. Molecular structures of $[\text{Cu}(\text{PTol}_3)_2(\text{dto})_3\text{Sn}]^-$ (left) and $[\{\text{Cu}(\text{PPh}_3)_2\}(\text{dto})_3\text{Sn}]^0$ (right).

Another notable curiosity in Sn dithiooxalate chemistry is the competing oxophilicity and thiophilicity of Sn^{IV} versus transition metals. Coordination to Sn is charge dominated with a preference towards the smaller harder oxygen when available, but in $(\text{dto})^{2-}$ resonance dictates that the oxygen adopts a neutral double bonded structure and yields a SnS_6 core in the tris species $[\text{Sn}(\text{dto})_3]^{2-}$. Coucouvanis et al explored the interactions of this complex with d^{10} $[\text{Cu}^{\text{I}}(\text{PPh}_3)_3]\text{X}$ in the eighth instalment of their “metal complexes as ligands” anthology (Figure 4.4). Upon addition of the copper complex the $(\text{dto})^{2-}$ ligand undergoes a structural rearrangement with the sulfurs coordinating to the thiophilic Cu centre. Concomitant with this is the coordination of the tin centre to the diketyl pocket. Increasing stoichiometric equivalents of copper complex can be added to form bi, tri, and tetrametallic complexes. In each instance the $(\text{dto})^{2-}$ ligand undergoes the described rearrangement.

4.1.2. Rare-earth Metal Coordination Chemistry and Scorpionates

The f-block elements are all very similar in terms of properties on account of the highly centralised and small core nature of the f-orbitals.²⁹ This commonly reduces discussions of them to be principally about size with physical effects attributed to the lanthanide contraction.

The high number of unpaired electrons in the f-orbitals imbues them with excellent magnetic properties for which they are thoroughly investigated.³⁰ The most common oxidation state for all is the +III oxidation state. Being small and highly charged, this renders the lanthanides as hard Lewis acids. This limits the coordination chemistry of the lanthanides to very small donor atoms, typically nitrogen and oxygen.³¹ Their large available coordination number makes them highly susceptible to chelation with multidentate ligands, ranging from 2—9 denticity. Scorpionate ligands are employed frequently in lanthanide chemistry, being pincer shaped ligands; tris(pyrazolyl)borates are potentially the most famous of this class.³²

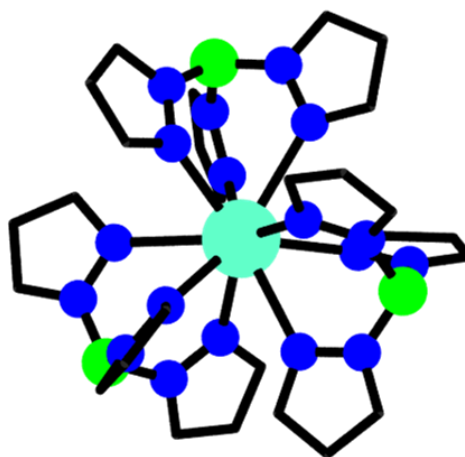


Figure 4.5. Molecular structure of [EuTp₃]

Formed by the reduction of a substituted pyrazole by an alkali metal borohydride in a melt tris(pyrazolyl) borate (Tp) ligands are tridentate and monoanionic. The tetrahedral boron atom is covalently linked to the nitrogen atoms of three pyrazole moieties, the fourth site is occupied by a hydrogen atom. Tp ligands are highly rigid and coordinate facially through the three remaining nitrogen lone pairs. Their negative charge, N-donor functionality, and high denticity make them excellent ligands for lanthanides, the most stable complexes formed are the neutral [LnTp₃] species which are readily synthesised from aqueous solutions of lanthanide salts and KTp and sublime at an impressive 300 C at 10 Torr (Figure 4.5).³² The introduction of other ligating species results in heteroleptic complexes that are often used to form multimetallic species.

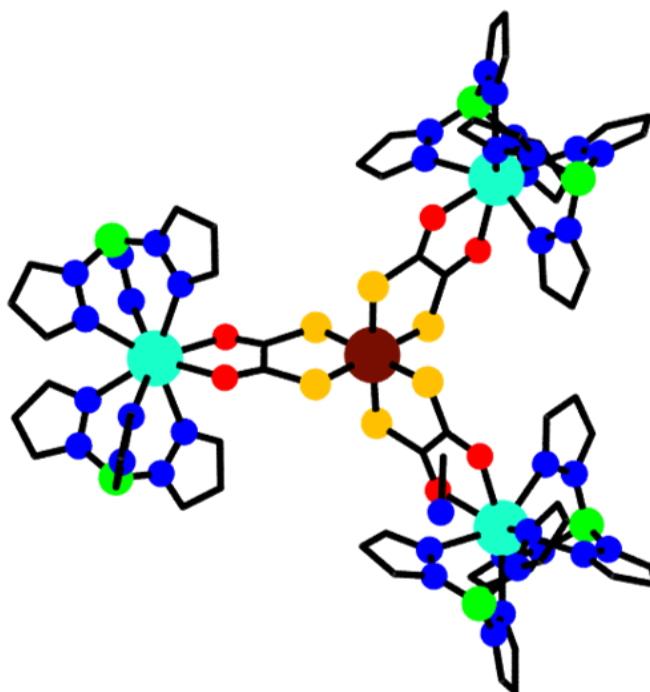


Figure 4.6. Molecular structure of $[\text{Fe}(\text{dto})_3(\text{DyTp}_2)_3]$

4.1.3. Multimetallic Mixed Metal Species

A common ligand used for heteroleptics is a negatively charged bidentate oxygen donor which forms an eight coordinate square antiprismatic arrangement around a rare earth +III ion with two Tp ligands.³³⁻³⁴ Ligands such as oxalates and tetraoxolenes are the favourable choices here owing to their ability to ligate to multiple metal centres.³⁵ The ligand oxalate is known to span lanthanide chromium and cobalt bimetallic complexes.³⁶⁻³⁷ Xu et al exploited Pearson's theory of bases with dithiooxalate to form tetrametallic propeller complexes from one-pot reaction mixtures.³⁸ Adding $\text{FeCl}_3 \cdot 6\text{H}_2\text{O}$, K_2dto , $\text{DyCl}_3 \cdot 6\text{H}_2\text{O}$, and KTp in the appropriate stoichiometric ratio in water forms the complex $[\text{Fe}(\text{dto})_3(\text{DyTp}_2)_3]$ (Figure 4.6) which slowly crystallises out albeit in rather low yield (13%). The complex consists of an octahedral FeS_6 core, low spin $S = 1/2$ from the Fe^{III} ion in a strong ligand field; and three square antiprismatic Dy^{III} ions $S = 5/2$. Each metal centre is a stereocentre and the compound crystallises both enantiomers of iron which is paired with two identical optical configuration Dy and one opposite giving $\Delta/\Delta\Delta\Lambda$ and $\Lambda/\Lambda\Lambda\Delta$. The diamagnetic centre complex $[\text{Co}(\text{dto})_3(\text{DyTp}_2)_3]$ was similarly synthesised from $\text{CoCl}_2 \cdot 6\text{H}_2\text{O}$ to compare the magnetic properties. Both compounds exhibit slow magnetic relaxation. The cobalt analogue has no interaction between the dysprosium centres and can be considered three independent centres which has a magnetic relaxation time of $\tau_0 = 3.6 \times 10^{-8}$ s at low temperature. The iron compound fosters a weak interaction between the Dy^{III} ions which gives rise to a complex energy spectrum of magnetic states with low-lying excited states and a faster relaxation rate at low temperatures.

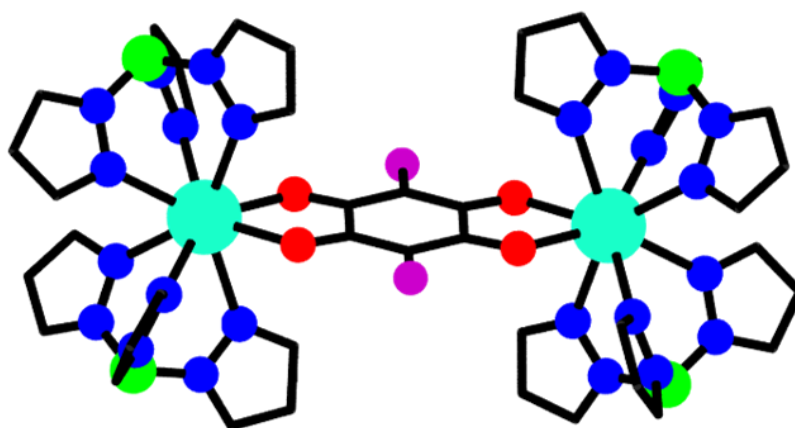


Figure 4.7. Molecular structure of $[(ba)(DyTp_2)_2]$

Boskovic et al similarly used $Dy^{III}Tp_2$ units to create a magnetic complex, in this case with a radical tetraoxolene as the bridging ligand between two Dy^{III} centres (Figure 4.7).³⁹ Fluoranilate (fa)²⁻ and bromanilate (ba)²⁻ are planar six-membered carbon rings with fluorenes or bromine atoms in the para positions and a ketyl and hydroxyl occupying the other sites. Tetraoxolenes are redox active being able to undergo two one-electron reductions and one electron oxidation to form the electron transfer series $(tetrox)^{\cdot-} \rightleftharpoons (tetrox)^{2-} \rightleftharpoons (tetrox)^{3-} \rightleftharpoons (tetrox)^{4-}$. For the complexes $[(ba)(DyTp_2)_2]$ both reductions are found to be reversible and occur at -0.82 and -1.68 V vs $Fc^{+/0}$. The oxidation is irreversible at $+1.19$ V vs $Fc^{+/0}$. Cobaltocene facilitated chemical reduction and isolation of the radically bridged bromanilate species. Unfortunately, while the more electronegative fluoranilate would be expected to give more amenable reduction potentials strong intermolecular forces prevent solvation. The radical $[(ba^{3-})(DyTp_2)_2][CoCp_2]$ exhibits slow magnetic relaxation in zero applied dc magnetic field, in contrast to the diamagnetic parent complex. Exchange coupling between the rare earths and radical reduces the quantum tunnelling magnetisation at zero-field, enhancing its single molecule magnetic properties.

4.1.4.Scope of Chapter

Herein we report the synthesis and characterisation of two heterometallic compounds $[Ni^{II}\{(dto)Y^{III}Tp_2\}_2]$ (**4.1a**) and $[Ni^{II}\{(dto)Gd^{III}Tp_2\}_2]$ (**4.5a**) (Tp = hydrotris(pyrazol-1-yl)borate;), where the α -diketonate site is occupied by Lewis acidic rare earth ions. Both compounds display consecutive one-electron reduction waves in their cyclic voltammograms, but unlike the Sn adducts, the reduced species are isolable, and cobaltocene reduction yields $[CoCp_2][Ni^{II}\{(dto)Y^{III}Tp_2\}_2]$ (**4.1b**) and $[CoCp_2][Ni^{II}\{(dto)Gd^{III}Tp_2\}_2]$ (**4.5b**). The locus of the reduction is confirmed as ligand-based, such that **4.1b** and **4.5b** are the first structurally characterised complexes to possess an elusive $(dto)^{3-}$ ligand. Expanding the scope of utility of this modular system the lanthanide series neodymium through to lutetium (**4.2**—

4.12) was synthesised. The early lanthanides, lanthanum, cerium, and promethium were unisolable under the conditions used. To probe the delocalisation of the open-shell moiety through the central MS_4 core the species $[Pd^{II}\{(dto)Lu^{III}Tp_2\}_2]$ (**4.13**) and $[Pt^{II}\{(dto)Lu^{III}Tp_2\}_2]$ (**4.14**) were synthesised. In situ reduction with cobaltocene of these and their nickel counterpart (**4.12**) allowed for determination that the radical is almost entirely localised on the dioxolane moiety confirmed by the absence of Pd and Pt hyperfine in the EPR spectra.

4.2.Synthesis

Simultaneous stoichiometric addition of aqueous rare earth chloride or nitrate and KTp to a stirred aqueous solution of $K_2[Ni(dto)_2]$ afforded the instant precipitation of the violet heterometallic species in adequate yields (30–70%) that, in most cases, was satisfactory for bulk analysis. Impure sample may be recrystallized from CH_2Cl_2 /hexanes. We attribute the increase in yield when compared to related 3d-4f species to the modular approach of using the preformed bis(dithiooxalate) complex as a synthon.^{5-7, 13} The simultaneous addition of metal and capping ligand to the reaction mixture limits the formation of $[LnTp_2X]$ and $[LnTp_3]$ by-products and circumvents the need for several purification steps in the case of the bis(oxamide) system.⁴⁰⁻⁴¹ Europium and Erbium are outliers producing much lower yields than the remaining lanthanides; while unexplained this is observed in other similar systems. Reaction with any lanthanide greater in size than neodymium under the aqueous conditions was found to not produce any of the desired trimetallic species. While the reaction gives seemingly analytically pure material there are a host of peculiarities that accompany these reactions. Recrystallisation from CH_2Cl_2 /hexanes produces well-formed crystals of the trimetallic but also unveils a host of impurities. Proton NMR of the white impurities unveils broadened shifted peaks suggesting this is some $\{LnTp\}$ species as the spectral augmentation is a result of the magnetic lanthanide and Tp is the only proton containing species. The most likely candidate here is the $[LnTp_3]$ species as this is the most thermodynamically stable, $[LnTp_2X]$ species are known to be highly reactive in air and moisture reacting quickly to form $[LnTp_3]$ species in even the slightest excess of Tp which is in abundance in these reaction mixtures. The bis(Tp) homoleptic $[NiTp_2]$ is also a known impurity in reactions featuring lanthanides larger than Gd. The octahedral Ni^{II} species has a d-d transition giving it a pink hue which was frequently observed in the reaction filtrates. Fortunately, its excellent solubility in hexanes allows for facile removal of it from the reaction mixture. Flash column chromatography is sadly unfeasible for purification of the Ln_2Ni species as the compound is not stable on silica changing hue to a light pink upon loading and is immobile in all common neat eluents and mixtures. There is a possibility that the species exhibits some reversible ligand substitution in solution, however, studies on this are outside the scope of this work as the purity of the materials was sufficient for the required analysis and any impurities would not interfere with subsequent reactions, i.e. reduction. Sublimation or reduction and subsequent oxidation are highlighted as methodologies by which pure bulk material could be isolated. The homoleptic $[LnTp_3]$ species are known to undergo sublimation between 300–330 °C at 10 torr. Reduction by $[CoCp_2]$ yields the monoanionic trimetallics, verified for Y and Gd. This reaction is performed in toluene and results in instant precipitation of pure material. Reoxidation of this pure material by a common oxidant such as I_2 should yield $[CoCp_2]I$ and pure neutral trimetallic species which can be extracted into a non-polar solvent such as toluene.

Simple substitution of the central bis(dithiooxalate) with its group 10 analogues enables facile formations of the varied central metal series in excellent yields (65–70%). The physical properties of the lanthanide substituted series are similar to those found for series with other ligands in that the solubility of the complexes may change depending on the identity of the lanthanide, while virtually nothing else does. This results in Eu, and Tb—Lu displaying much greater solubility than Y, Nd, Sm, and Gd, an unusual effect attributed to ionic radius corroborated by many instances in the literature. The neutral complexes show excellent solubility in all solvents excluding ethers and alkanes.

Table 4.1. Proton NMR Shifts of the Pyrazolyl Ligand Shifted by Rare Earth.

Complex	Ln	¹ H NMR (δ)		
4.1a	Y	7.34	7.09	5.67
4.2	Nd	12.60	7.84	−10.48
4.3	Sm	8.79	6.02	3.68
4.4	Eu	13.77	2.80	0.72
4.5a	Gd	—	—	—
4.6	Tb	33.2	4.32	−40.2
4.7	Dy	22.23	3.59	1.28
4.8	Ho	53.40	25.52	−62.99
4.9	Er	55.52	1.62	−12.12
4.10	Tm	4.83	−52.41	—
4.11	Yb	26.02	4.89	1.32
4.12	Lu	7.32	7.00	5.67

The ¹H NMR spectrum of **4.1a** exhibits three signals assigned to each pyrazolyl proton of the Tp ligands at 7.34, 7.09, and 5.67 ppm, and match those in [Ni(tdo)(LuTp₂)₂] (tdo = trimethylenebis(oxamide)).⁴⁰ The absence of multiple peaks for differing geometrical arrangements of the Tp ligands are attributed to the exchange and rotation of these ligands around the yttrium centre as is commonly encountered in rare earth complexes.⁴² The broad signal at 0.51 ppm is attributed to the B–H proton. Deviations in the chemical shift of the pyrazolyl protons of the Tp ligands for each other rare earth are tabulated in Table 4.1. and found to be in excellent agreement with those found for [Ni(tdo)(LnTp₂)₂]. The ¹³C NMR spectrum exhibited peaks at 104.65, 135.33 and 141.23 ppm for the pyrazolyl rings, and a peak at 200.91 ppm for the carbonyl moiety of the (dto)²⁻ ligand. The IR spectra of **4.1a**—**4.12** are identical and exhibit bands characteristic of the constituent ligands. The bands between 1523–1503 cm⁻¹ are C–O stretching vibrations, and are shifted from ~1600 cm⁻¹

in $[\text{PPh}_4]_2[\text{Ni}(\text{dto})_2]$.⁴³ A similar shift to lower energy is reported for the Sn adduct, $[\text{PPh}_4]_2[\text{Ni}\{(\text{dto})\text{SnCl}_4\}_2]$ (**4.15**).⁹ A second prominent band in **4.15** at 995 cm^{-1} is ascribed to a combination of C–C and C–S vibrations. These vibrations are tentatively assigned at 979 and 976 cm^{-1} in **4.1a** and **4.5a**, respectively, and shifted to lower energy compared with $[\text{PPh}_4]_2[\text{Ni}(\text{dto})_2]$. Bands characteristic of the Tp ligand ($\nu(\text{BH})$ 2457 and 2461 cm^{-1} ; $\nu(\text{CN})$ 1538 and 1535 cm^{-1}) were also observed.

Electrospray ionization mass spectroscopy gave excellent spectra in negative mode (Figure 4.8). Negative ion fragments of the trimetallics were detected between 860 and 920 m/z . The fragments consisted of one lanthanide and two Tp units bound to the bis(dithiooxalate) Ni core. Simulations achieved near perfect match to the experimental spectra. The salient feature here is the isotopic splitting which is entirely dependent on the variable, the lanthanide nuclide. Lanthanides have rich isotopic splitting spectra, the stable isotopes follow a periodicity across the row with odd atomic numbers displaying only one or two stable isotopes, with the minor usually being in a very small proportion ($>3\%$ natural abundance) with the exception of Eu (Table 4.2.). On even numbers there are a consortium of stable isotopes, the greatest number for Sm with 8 stable isotopes. There is always at least one stable isotope of a lanthanide nuclide with non-zero nuclear spin.

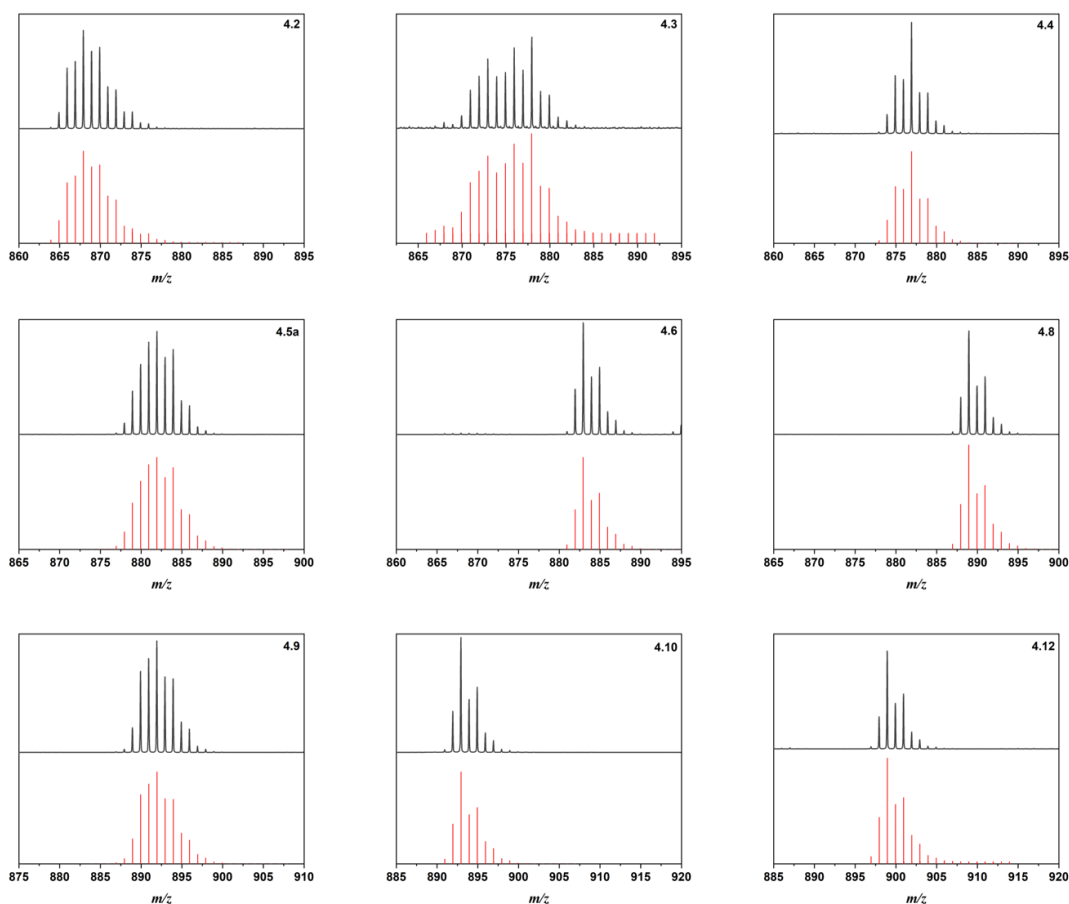


Figure 4.8. Electrospray ionization spectra for selected trimetallics in negative mode.

Table 4.2. Stable Lanthanide Nuclides

Nuclide	Nuclear spin I	Natural abundance
⁸⁹ Y	1/2	100%
¹³⁸ La	5	0.09%
¹³⁹ La	7/2	99.91%
¹³⁶ Ce	0	0.185%
¹³⁸ Ce	0	0.251%
¹⁴⁰ Ce	0	88.45%
¹⁴² Ce	0	11.114%
¹⁴¹ Pr	5/2	100%
¹⁴² Nd	0	27.2%
¹⁴³ Nd	7/2	12.2%
¹⁴⁴ Nd	0	23.8%
¹⁴⁵ Nd	7/2	8.3%
¹⁴⁶ Nd	0	17.2%
¹⁴⁸ Nd	0	5.7%
¹⁵⁰ Nd	0	5.6%
¹⁴⁴ Sm	0	3.07%
¹⁴⁶ Sm	0	trace
¹⁴⁷ Sm	7/2	14.99%
¹⁴⁸ Sm	0	11.24%
¹⁴⁹ Sm	7/2	13.82%
¹⁵⁰ Sm	0	7.38%
¹⁵² Sm	0	26.75%
¹⁵⁴ Sm	0	22.75%
¹⁵¹ Eu	5/2	47.81%
¹⁵³ Eu	5/2	52.19%
¹⁵² Gd	0	0.2%
¹⁵⁴ Gd	0	2.18%
¹⁵⁵ Gd	3/2	14.8%

Nuclide	Nuclear spin I	Natural abundance
¹⁵⁶ Gd	0	20.47%
¹⁵⁷ Gd	$\frac{3}{2}$	15.65%
¹⁵⁸ Gd	0	24.84%
¹⁶⁰ Gd	0	21.86%
¹⁵⁹ Tb	$\frac{3}{2}$	100%
¹⁵⁶ Dy	0	0.056%
¹⁵⁸ Dy	0	0.095%
¹⁶⁰ Dy	0	2.329%
¹⁶¹ Dy	$\frac{5}{2}$	18.889%
¹⁶² Dy	0	25.475%
¹⁶³ Dy	$\frac{5}{2}$	24.896%
¹⁶⁴ Dy	0	28.26%
¹⁶⁵ Ho	$\frac{7}{2}$	100%
¹⁶² Er	0	0.139%
¹⁶⁴ Er	0	1.601%
¹⁶⁶ Er	0	33.503%
¹⁶⁷ Er	$\frac{7}{2}$	22.869%
¹⁶⁸ Er	0	26.978%
¹⁷⁰ Er	0	14.91%
¹⁶⁹ Tm	$\frac{1}{2}$	100%
¹⁶⁸ Yb	0	0.13%
¹⁷⁰ Yb	0	3.04%
¹⁷¹ Yb	$\frac{1}{2}$	14.28%
¹⁷² Yb	0	21.83%
¹⁷³ Yb	$\frac{5}{2}$	16.13%
¹⁷⁴ Yb	0	31.83%
¹⁷⁶ Yb	0	12.76%
¹⁷⁵ Lu	$\frac{7}{2}$	97.41%
¹⁷⁸ Lu	7	2.59%

4.3.X-ray Crystallographic Structure

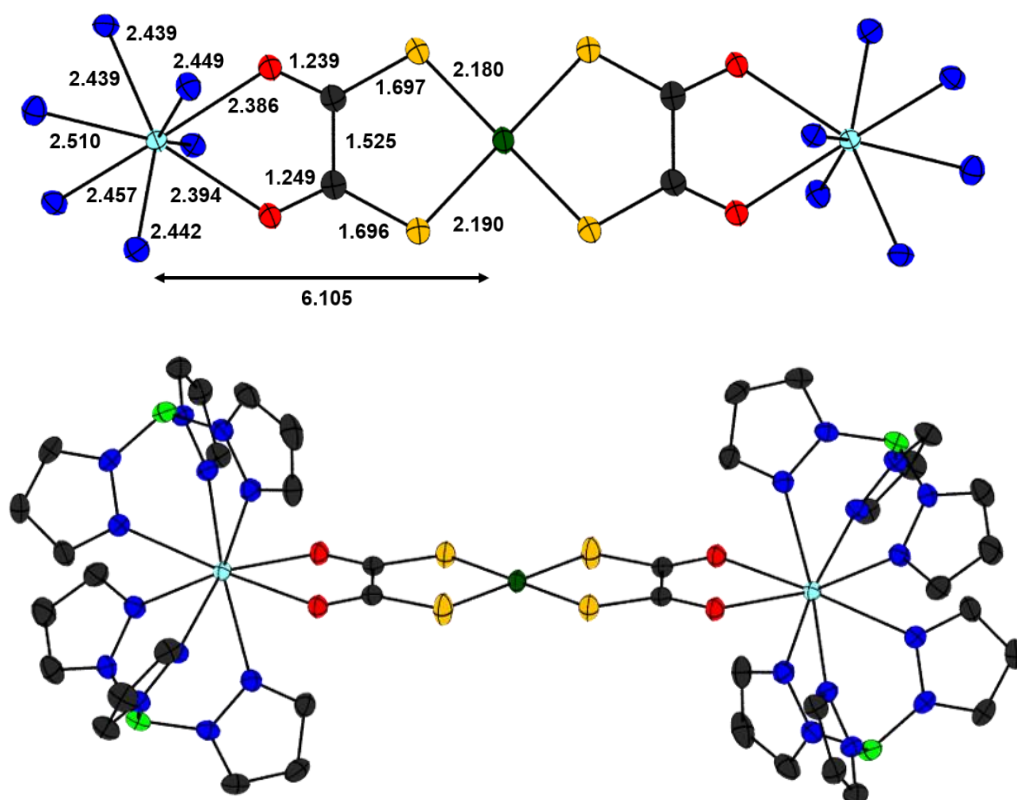


Figure 4.9. Selected bond lengths and distances measured from **4.1a** and below the full molecular structure of the neutral complex in crystals of **4.1a** (Colour palette: Ni, dark green; Y, cyan; N, azure; S, mustard; C, pewter; O, red; B, lime).

Neutral compounds **4.1a**–**4.12** are isostructural with the central nickel atom located on a crystallographic inversion centre (Figure 4.9.). This nickel atom is coordinated to four sulfur atoms of two dto groups, with the Ni–S bond distances and S–Ni–S angles show no significant deviation from each other (Table 4.2.). These metrics are the same as reported for monometallic $[\text{Ni}(\text{dto})_2]^{2-}$,⁴⁴ and **4.15** with capping SnCl_4 units.⁹ Similarly the intraligand S–C, C–C and C–O bond distances are invariant in **4.1a**–**4.12** and **4.15**, though the inclusion of a metal ion in the O,O' pocket results in a lengthening of the C–C and C–O bonds and shortening of the S–C compared to $[\text{Ni}(\text{dto})_2]^{2-}$.⁴⁴ The structural metrics of the $(\text{dto})^{2-}$ underscore its distinctive chemistry in comparison to other 1,2-dithioenes.^{18–19} The S–C bond length of ~ 1.7 Å and the C–C distance of ~ 1.54 Å are representative of a 1,2-dithione group rather than a 1,2-dithiolate, and reveals resonance stabilisation of the negative charge to the conjugated oxygen atoms. This delocalisation of the negative charge to the dioxolene site is amplified with the coordination of a second metal ion with a ~ 0.025 Å reduction in length of the C–O bond compared with the monometallic complex,² as observed in other species with Ln ions in the binding site.^{5–7, 13} In **4.1a**–**4.12** the bridging

$[\text{Ni}(\text{dto})_2]^{2-}$ unit is capped by two eight-coordinate Y, or Nd—Lu ions whose distorted square antiprismatic environment is completed by two facially binding Tp ligands. Both complexes are present as mesomers, where one rare-earth centre has Λ and the other has Δ absolute configuration because centroid in these compounds coincides with the inversion centre.⁴⁵ The Y—O distance of 2.390(2) Å is shorter than the analogous rare earths Ln—O bond at 2.435(2) Å reflecting the slightly larger ionic radius for the latter (Table 4.2.). Both are longer than the Sn—O distance of 2.202(2) Å in **4.15**, a consequence of the higher charge on Sn. The average bond distance for the Tp ligands also display this pattern, and the $M' \cdots M'$ is 12.210 and 12.313 Å in **4.1a** and **4.5a** (Gd representing the midpoint of the lanthanides), respectively.

Table 4.3. Selected Average Bond Distances and Angles^a

	4.1a	4.5a	4.1b	4.5b	4.14
M'	Y	Gd	Y	Gd	Sn
avg. Ni—S	2.1851(9)	2.187(1)	2.168(1)	2.164(1)	2.1803(6)
avg. M' —O	2.390(2)	2.435(2)	2.326(3)	2.370(3)	2.202(2)
avg. S—C	1.696(3)	1.699(4)	1.711(4)	1.714(5)	1.681(3)
avg. C—C	1.525(5)	1.537(5)	1.468(5)	1.466(5)	1.526(3)
avg. C—O	1.244(4)	1.241(4)	1.275(5)	1.271(5)	1.248(3)
avg. M' —N	2.470(3)	2.508(3)	2.497(3)	2.520(4)	
avg. Ni $\cdots M'$	6.105	6.156	6.071	6.099	5.825
$M' \cdots M'$	12.210	12.313	12.114	12.177	11.650
avg. S—Ni—S	92.78(3)	92.72(4)	92.22(4)	92.21(5)	93.07(2)
avg. O— M' —O	66.23(7)	65.30(8)	68.84(7)	68.0(1)	74.41(6)
α^b	0	0	10.3	9.9	0

^a Distances in angstrom; angles in degrees. ^b Dihedral angle between mean NiS_2 planes.

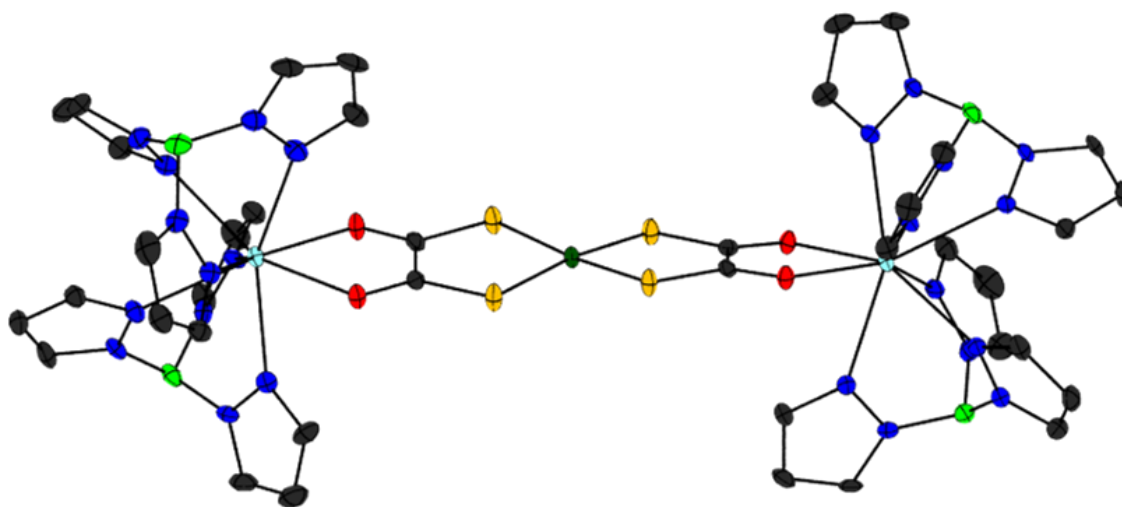


Figure 4.10. Molecular structure of the anion in crystals of **4.1b** (Colour palette: Ni, dark green; Y, cyan; N, azure; S, mustard; C, pewter; O, red; B, lime).

The Y and Gd species were chosen for reduction to investigate the monoanionic species on the grounds that they are the cheapest diamagnetic and paramagnetic rare earths available. The reduced species in **4.1b** and **4.5b** are isostructural and differ from the parent complexes by the absence of a crystallographic inversion centre (Figure 4.10.). This is brought about by a modest tetrahedralisation of the NiS₄ core of 10.3° in **4.1b** and 9.9° in **4.5b** (Table 1). The most interesting change occurs within the dto ligands, this being the first example of structurally characterised (dto)³⁻ ligands in a coordination complex. Reduction of the {Ni(dto)₂} core leads to shortening of the Ni–S and C–C bonds and concomitant lengthening of the S–C and C–O bonds. This is consistent with the additional charge on the dioxolene side of the dto, where the C–O bond distance of 1.275(5) and 1.271(5) Å for **4.1b** and **4.5b**, respectively, are the same length in related semiquinone ligands,⁴⁶⁻⁴⁷ known as a quinoidal distortion.¹⁸⁻¹⁹ The C–C bond is considerably shorter at 1.468(5) and 1.466(5) Å for **4.1b** and **4.5b**, respectively, on account of the increased bond order that in turn reduces the S–C bond order leading to their lengthening by 0.015 Å (Table 1). The increased charge on the dto ligands shortens the Y–O and Gd–O bonds to 2.326(3) and 2.370(3) Å, respectively. These are significantly shorter than in **4.1a** and **4.5a**, and as a consequence the intermetallic separation between these ions is reduced to 12.11 and 12.18 Å in **4.1b** and **4.5b**, respectively.

Table 4.4. Selected Average Bond Distances and Angles^a

M'	Nd	Sm	Eu	Tb	Dy	Ho	Er	Tm	Yb	Lu
avg. Ni–S	2.1975	2.193	2.196(4)	2.188(8)	2.1775	2.190(4)	2.191(7)	2.187(5)	2.1895	2.187
avg. M'–O	2.4965(2)	2.4625(3)	2.454(1)	2.404(7)	2.3980(5)	2.401(8)	2.3915(5)	2.377(1)	2.3675(3)	2.3595(2)
avg. S–C	1.7075(2)	1.6965(4)	1.707 (3)	1.703	1.6915(6)	1.703	1.706(1)	1.6975(5)	1.701(2)	1.6955(3)
avg. C–C	1.540(4)	1.551(5)	1.533	1.514	1.519(6)	1.530	1.532	1.528	1.525(4)	1.525(4)
avg. C–O	1.2495(3)	1.2485(4)	1.249(3)	1.250	1.2355(7)	1.243(6)	1.242(8)	1.242(3)	1.2445(2)	1.2445(3)
avg. M'–N	2.5753(2)	2.5365(3)	2.523(3)	2.475(3)	2.4549(5)	2.473(4)	2.462(4)	2.446(4)	2.442(2)	2.432(2)
avg. Ni···M'	6.239	6.186	6.194	6.125	6.098	6.120	6.113	6.089	6.083	6.070
M'···M'	12.477	12.373	12.388	12.251	12.195	12.239	12.226	12.179	12.165	12.141
avg. S–Ni–S	92.78	92.99	92.66	92.67	92.79	92.82	92.82	92.80	92.87	92.82
avg. O–M'–O	64.15	65.10	64.99	66.17	65.85	66.27	66.54	66.63	66.98	67.13
α^b	0	0	0	0	0	0	0	0	0	0

^aDistances in angstrom; angles in degrees.

4.4. Electronic Structure

4.4.1. Electronic Spectra

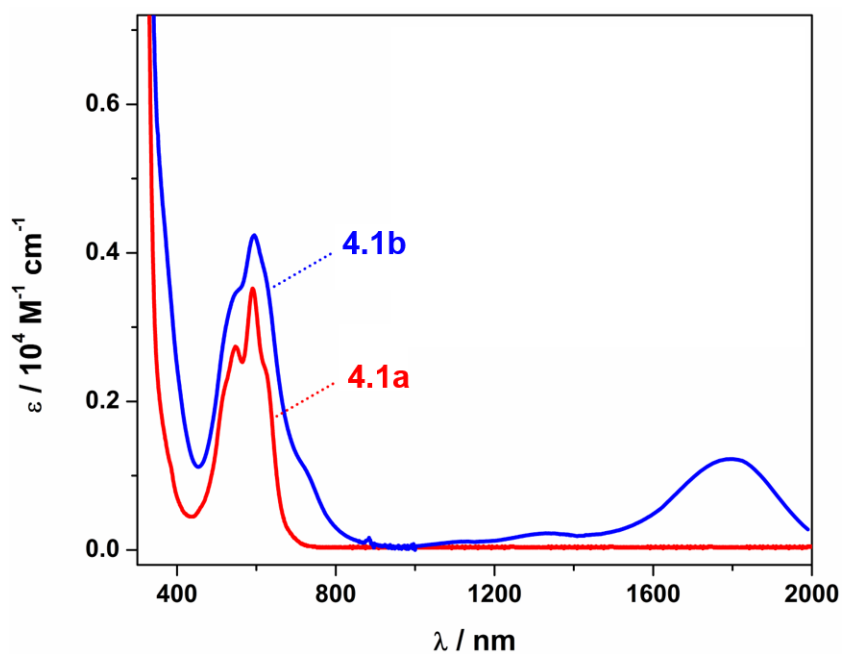


Figure 4.11. Overlay of the electronic spectra of **4.1a** and **4.1b** recorded in CH_2Cl_2 at ambient temperature.

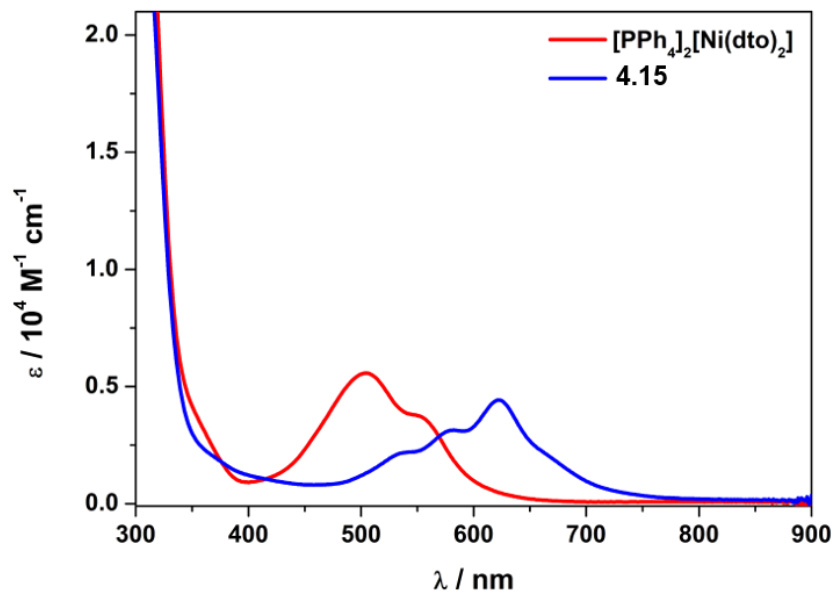


Figure 4.12. Overlay of the electronic spectra of $[\text{PPh}_4]_2[\text{Ni}(\text{dto})_2]$ and $[\text{PPh}_4]_2[\text{Ni}\{(\text{dto})\text{SnCl}_4\}_2]$ recorded in CH_2Cl_2 solution at ambient temperature.

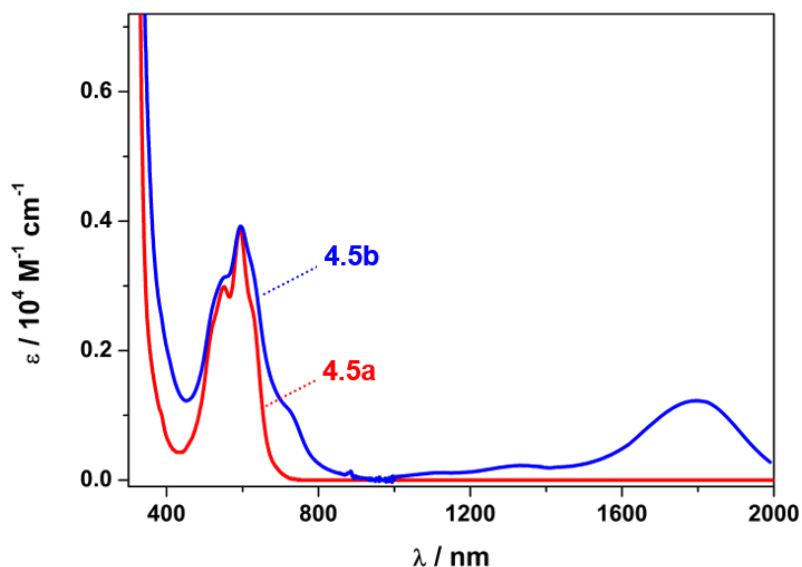


Figure 4.13. Overlay of the electronic spectra of **4.5a** and **4.5b** recorded in CH_2Cl_2 solution at ambient temperature.

Occupation of the α -diketonate pocket of the $(\text{dto})^{2-}$ ligand is accompanied by a colour change from deep burgundy to violet. Latham et al. assigned the peak at 505 nm and shoulder at 564 nm in $[\text{Ni}(\text{dto})_2]^{2-}$ as metal-to-ligand charge transfer (MLCT) excitations into the π^* orbital of the dto ligand.⁴⁸ In heterometallic **4.1a** and **4.5a**, this transition envelope is red-shifted, with two distinct maxima at 592 and 549 nm, and two shoulder features at 620 and 525 nm (Figure 4.11.). A larger red-shift was observed for the Sn adduct **4.15**, with the peaks appearing at 544, 582, 622 and shoulder at 640 nm (Figure 4.12.).⁹ The shift is due to the higher charge on the Sn(IV) ion and increased covalency in contrast to the rare earth ions.

4.4.2. Continuous Wave EPR

The spin ground state of **4.1b** as $S = 1/2$ was confirmed by EPR spectroscopy (Figure 4.14.). The room temperature spectrum revealed a featureless signal at $g = 2.0033$. The shift of the g -value closer to that of the free-electron ($g_e = 2.0023$) confirms that the dioxolene side of the dto ligand is reduced to produce a semiquinone. For dithiolene radicals coordinated to Ni(II), the signal is shifted to higher field on account of the spin-orbit contribution from both metal and sulfur atoms.¹⁸⁻¹⁹ No hyperfine coupling to the ^{89}Y ($I = 1/2$, 100% abundant) nuclei is observed, which stands in contrast to the spectrum recorded on electrochemically-generated $[\text{Ni}\{(\text{dto})\text{SnCl}_4\}_2]^{3-}$ which exhibited coupling to the spin-active Sn isotopes.²⁰ However, ^{89}Y has a significantly smaller nuclear magnetic moment, and the larger spectral linewidth for **4.1b** has obscured any hyperfine structure.⁴⁹⁻⁵⁰ Noticeably the frozen solution spectrum recorded at 130 K is near isotopic with $g = (2.0041, 2.0026, 2.0011)$, and confirms the spin is almost entirely localised to the dioxolene part with negligible Y content.

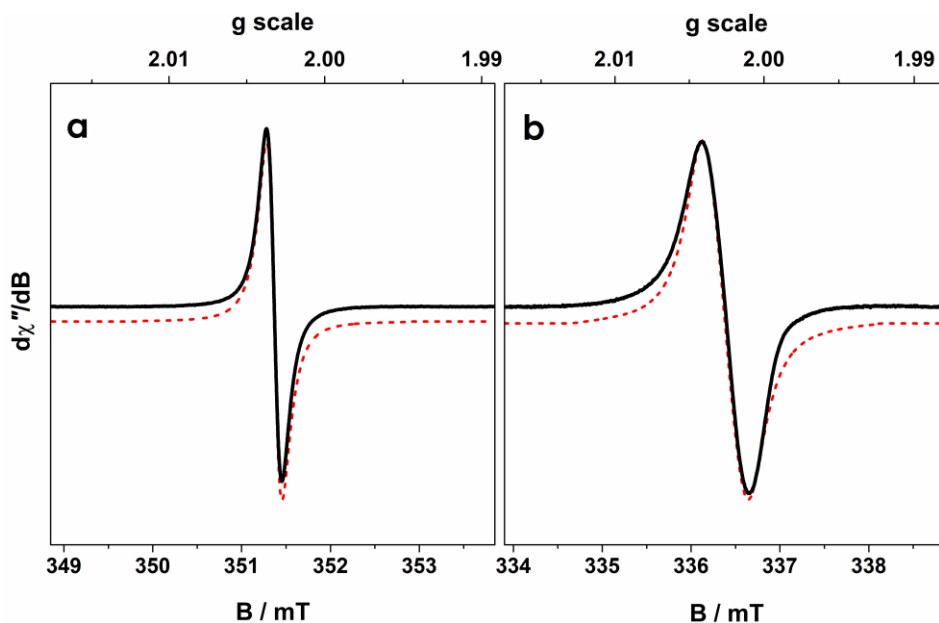


Figure 4.14. X-band EPR spectra of **4.1b** in (a) CH_2Cl_2 solution at 293 K (experimental conditions: frequency, 9.8518 GHz; power, 0.063 mW; modulation, 0.02 mT), and (b) $\text{CH}_2\text{Cl}_2/\text{MeCN}$ at 130 K (experimental conditions: frequency, 9.42841 GHz; power, 0.63 mW; modulation, 0.01 mT). Experimental data are represented by the solid lines and simulations depicted by a dashed trace.

Contribution to the electronic structure of open-shell group 10 bis(dithiolenes) deviates greatly across the group. To further investigate the identity of the radical in the reduced bis(dithioalates) the Pd (**4.13**) and Pt (**4.14**) analogues of the lutetium complexed **4.12** were synthesized. The more expensive Lu was selected for this investigation in place of Y on account of the resultant complex solubility. Attempted formation of the $[\text{Pt}^{\text{II}}\{(\text{dto})\text{Y}^{\text{III}}\text{Tp}_2\}_2]$ species resulted in an intractable powder that was only sparingly soluble in highly polar organic solvents such as DMF and DMSO which, on account of their high polarizability, are incompatible with room temperature EPR spectroscopy. Noting the enhanced solubility of resultant complexes formed with lanthanide ions Lu^{III} was selected as it is the only diamagnetic rare-earth available and has 100% abundant $I = 3/2$ nucleus. In situ reduction of **4.12–4.14** resulted in very similar spectra consisting of a sharp featureless central resonance line (Figure 4.15.). The absence of Pd or Pt hyperfine coupling affirms that the spin is localised to the diketone moiety which has little affect from the core π -system (Figure 4.16–4.17). A purely electrostatic interaction is corroborated by a descending g-value as the group is stepped down. Unfortunately, any hyperfine due to Lu is masked by spectral broadening; if present at all. Doping into a diamagnetic host lattice may reveal some intricacies in the spectra though no such diamagnetic analogue yet exists.

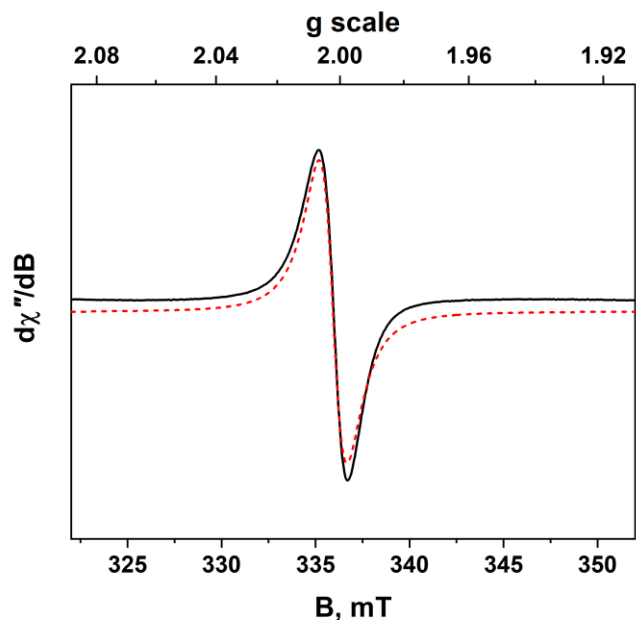


Figure 4.15. X-band EPR spectra of **4.12** in CH_2Cl_2 solution at 293 K (experimental conditions: frequency, 9.4138 GHz; power, 0.063 mW; modulation, 0.4 mT). Experimental data are represented by the solid lines and simulations depicted by a dashed trace.

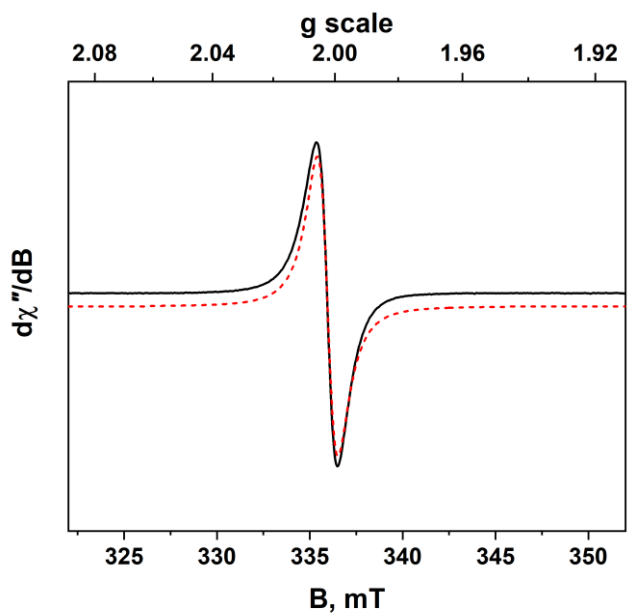


Figure 4.16. X-band EPR spectra of **4.13** in CH_2Cl_2 solution at 293 K (experimental conditions: frequency, 9.4155 GHz; power, 0.063 mW; modulation, 0.1 mT). Experimental data are represented by the solid lines and simulations depicted by a dashed trace.

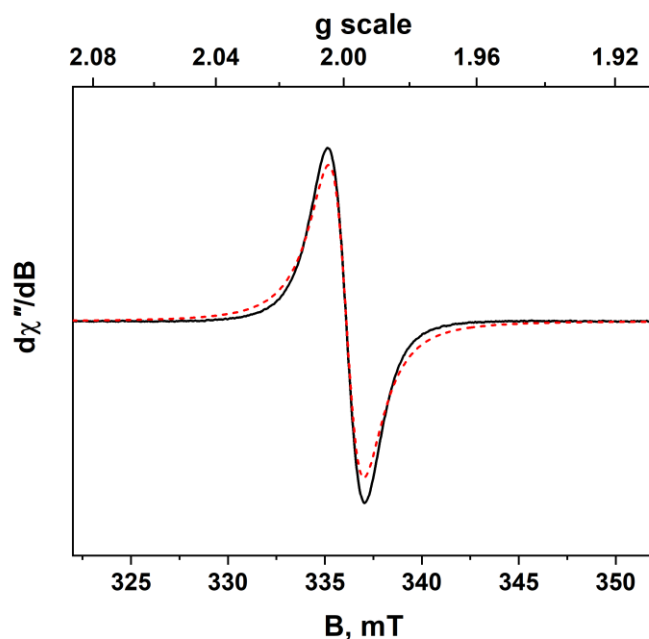


Figure 4.17. X-band EPR spectra of **4.14** in CH_2Cl_2 solution at 293 K (experimental conditions: frequency, 9.4046 GHz; power, 0.63 mW; modulation, 0.1 mT). Experimental data are represented by the solid lines and simulations depicted by a dashed trace.

4.5. Electrochemistry

The redox chemistry of **4.1a** and **4.5a** was assessed by cyclic voltammetry (CV) using the esoteric mixture of 5:1 anisole/ CH_2Cl_2 containing 0.2 M $[\text{N}(\text{tBu})_4]\text{PF}_6$ as supporting electrolyte. Two one-electron processes were evident in both voltammograms with reduction potentials of -1.25 and -1.66 V, versus the ferrocenium/ferrocene ($\text{Fc}^{+/0}$) couple (Figure 4.18.). These processes are classed as quasi-reversible as diagnosed by a large peak-to-peak separation of ~ 0.2 V. The consecutive reduction events match those reported for **5** albeit shifted 0.64 and 0.69 V more negative, respectively.⁸⁻⁹ The reduction of **4.1a** and **4.5a** is more difficult than the Sn analogue on account of less covalent bonding between the transition metals and the dioxolene chelate, as evident in the crystal structure. The reduction process is sequential addition of an electron to each ligand producing the $(\text{dto})^{3-}$ form that is stabilised by the chelation to the Lewis acid metal ion. It is important to note that $[\text{Ni}(\text{dto})_2]^{2-}$ displays no reversible electrochemistry; rather, there is an irreversible event at -2.49 V that is likely nickel-centred, generating Ni(I), which is unstable in this ligand field.²⁰

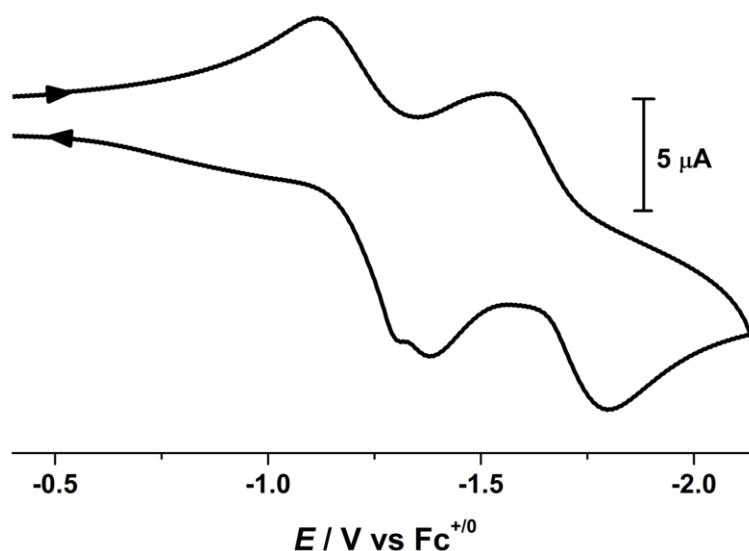


Figure 4.18. Cyclic voltammogram of **4.5a** in 5:1 anisole/ CH_2Cl_2 solution (0.20 M $[\text{N}(\text{tBu})_4]\text{PF}_6$ supporting electrolyte) at 22 °C at a scan rate of 100 mV s^{-1} . Potentials are referenced versus the $\text{Fc}^{+/0}$ couple.

Chemical reduction of **4.1a** and **4.5a** using 1 equiv. of cobaltocene gave **4.1b** and **4.5b**, respectively. This is in stark contrast to **4.15** (and related tin halide adducts) where all attempts to isolate the reduced species were not successful.^{9, 20} This is ascribed to the combined effect of the metal and its co-ligand. Although complexation of the dioxolene moiety facilitates reduction of the dto ligand, there is the additional input from the co-ligand to stabilise the reduced complex toward isolation. This is affirmed by the observation that the LMCT band in the bromo and iodo homologues of **4.15** are both red-shifted but still do not support a reversible redox event.⁹ The bulky Tp ligands accompanying the rare earth ion enables isolation of the reduced complexes. The reduction was accompanied by a distinct colour change from violet to teal with the appearance of a shoulder peak at 710 nm in the electronic spectrum (Figure 4.13.). The salient feature is an intense absorption maximum in the near-infrared (NIR) at 1790 nm ($\epsilon = 1300 \text{ M}^{-1} \text{ cm}^{-1}$) that is synonymous in bis(dithiolene) transition metal complexes and defined as an intervalence charge transfer (IVCT) transition of type $\{\text{Ni}^{\text{II}}(\text{dto}^{3-\cdot})(\text{dto}^{2-})\} \leftrightarrow \{\text{Ni}^{\text{II}}(\text{dto}^{2-})(\text{dto}^{3-\cdot})\}$, which corresponds to a spin-allowed excitation from the highest doubly occupied molecular orbital (HOMO-1) to the singly occupied molecular orbital (SOMO) both of which are ligand-based.¹⁸⁻¹⁹ This IVCT band is not as intense as seen for bis(dithiolene) complexes and indicates the reduction is largely on the dioxolene side of the ligand.

4.6.DFT Calculations

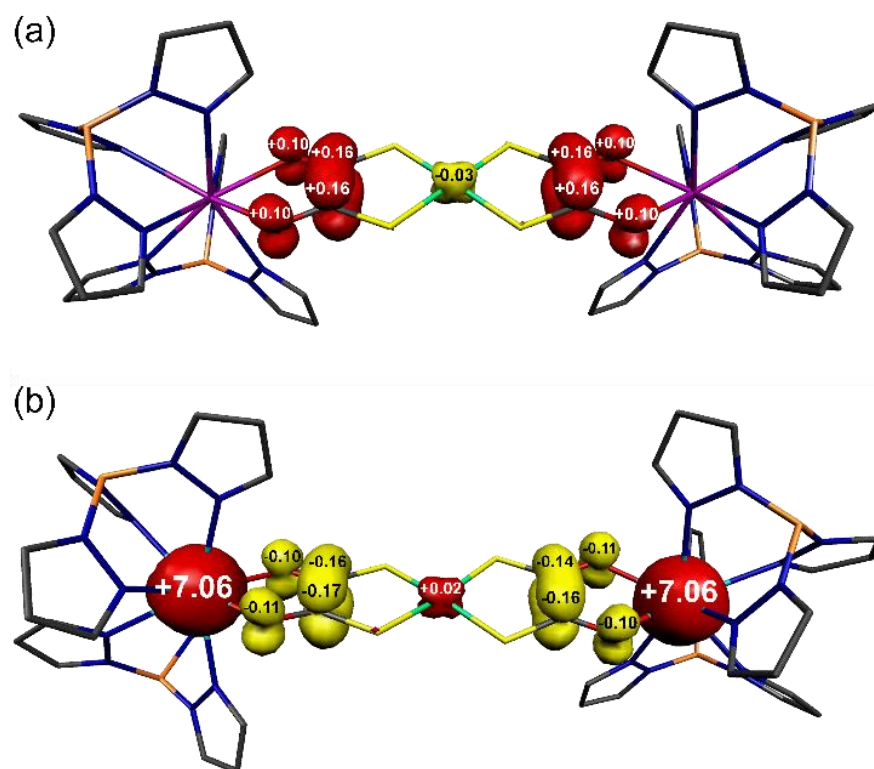


Figure 4.19. Mulliken spin population analysis for (a) **4.5a**, and (b) **4.5b** from spin-unrestricted DFT calculations (red: α -spin; yellow: β -spin).

The electronic structures of one-electron reduced **4.1b** and **4.15** have been examined using spin-unrestricted density functional theoretical (DFT) calculations. The Mulliken spin population of derived from a single-point calculation on the crystallographic coordinates of **4.1b** revealed the unpaired electron is distributed on the dioxolene part of the dto ligand (Figure 4.19.a). The symmetry of the complex distributes +1.04 spins at each end of the bridging $\{\text{Ni}(\text{dto})_2\}$ unit with -0.03 spins on the Ni ion from a minor polarisation of the S–C bonds. Notably there is no spin density on the Y(III) ions in accordance with the absence of hyperfine structure in the EPR spectrum. The identical spin distribution is found in one-electron reduced **4.15** – $[\text{Ni}\{(\text{dto})\text{SnCl}_4\}_2]^{3-}$ (Figure A.1.15.); in the absence of a crystal structure, the electronic structure was calculated on an optimised geometry which exhibited the same intraligand bond distances and angles as seen in **4.1b** and **4.5b** (Figure 4.9.).

The electronic structures of **4.5a** and its one-electron reduced product **4.5b** have been calculated using the broken symmetry (BS) method in order to account for the spin coupling between the terminal Gd(III) $S = 7/2$ ions and $(\text{dto})^-$ radical. It has been shown that DFT can reliably estimate the spin coupling between lanthanide ions and organic radicals. A BS(7,7) calculation for **4.5a** gave isoenergetic $M_S = 0$ state for antiferromagnetically coupled Gd(III) ions, and $M_S = 7$ for ferromagnetically coupled Gd(III) ions. This implies that two paramagnetic centres are uncoupled, as expected for the 12.31 Å separation with negligible

isotropic exchange coupling ($J \approx 0$). Reduction of **4.5a** introduces a third spin centre into the system, and so BS(14,1), BS(8,7) and BS(7,6) calculations that account for all spin coupled permutations were performed on the crystallographic coordinates of **4.5b** (Table 4.3.). The results revealed the BS(14,1) solution as the most stable, which is the parallel alignment of the 7 spins on each Gd(III) ions with the opposed alignment of the single spin on the $(\text{dto})^{3-}$ ligand, i.e. $M_S = 13/2$ (Figure 4.13.b). This solution is marginally more stable than the uncoupled scenario with the Gd(III)-radical exchange interaction estimated at $J = -1.3 \text{ cm}^{-1}$. Although small in magnitude, it does fall in the range for many other Gd(III)-radical systems.⁵¹⁻⁵² This molecule is most closely related to $[\text{Tp}_2\text{Gd}^{\text{III}}(\text{dtbsq})]$ ($\text{dtbsq} = 3,5\text{-di-tert-butylsemiquinonato}$), with $J = -5.7 \text{ cm}^{-1}$.⁴⁶ The smaller exchange estimated for **4.5b** lies in the fact there are two dioxolene units in the complex and the reduced spin concentration on the donor oxygen atoms in $(\text{dto})^{3-}$ compared with benzosemiquinones.⁵³ In spite of this, reduction of the bridging $\{\text{Ni}(\text{dto})_2\}$ unit in **4.5b** enforces a ferromagnetic alignment of the terminal Gd(III) ions, which maximises the total spin ground state of this system, albeit at very low temperatures. However, this spin distribution in the bridging metallodithiooxalate unit can be modified by changing the metal at its core which will not only modulate the covalency but also the geometry and therein the alignment of the magnetic anisotropy of the terminal ions.

4.7. Conclusions

The addition of Lewis acidic rare earth ions to the bis(dithiooxalato)nickel complex ion generated new charge-neutral heterometallic species where the rare earth M(III) ions (M = Y, Nd, Sm, Eu, Gd, Tb, Dy, Ho, Er, Tm, Yb, Lu) occupy the O, O' pocket of both ligands. The salient feature of this system is its high customisability where, in water, rare earths smaller than promethium will form instantaneous precipitates when added to stoichiometric equivalents of a corresponding bis(dithiooxalate) and KTp. Preformation of the central dithiooxalate synthon allows for greater yields than other methods for forming comparable structures.

With stabilising hydrotris(pyrazolyl)borate co-ligands on the rare earth ion, chemical reduction of the bridging bis(dithiooxalato)nickel unit led to the first molecular and electronic structure characterisation of the elusive dithiooxalato radical ligand, (dto)^{3•-} for the Y^{III} and Gd^{III} analogues. This allowed for structural confirmation that the radical was indeed localised on the dioxolane moiety but also shared across both as a class III compound.

Swapping out the central nickel ion with palladium and platinum with supporting lutetium in each instance gave highly soluble species that, once reduced, allowed for further insight to the locality of the radical. A large spectral width obscured any elucidation of hyperfine structure coupling to the Lu $I = 3/2$ nucleus, indicative of a very low contribution to the π -orbital system from the MS₄ core and corroborated by a lowering of the g-value moving down group 10. As such, we envisage these compounds to be of use for forming weakly coupled qubit gates with large spin manifolds.

4.8. Experimental

4.8.1. Synthesis

All air-sensitive manipulations were carried out in an MBraun glovebox or using standard Schlenk techniques. All glassware was dried at 130 °C overnight prior to use. Filter cannulas were prepared using Whatman 25 mm glass microfiber filters and were pre-dried at 130 °C overnight. Dry solvents (CH₂Cl₂, MeCN, toluene) were obtained using an Innovative Technology Inc. Pure Solv 400-5-MD solvent purification system (activated alumina columns). Solvents were sparged with N₂ and stored in ampoules over molecular sieves. The compounds CoCp₂,⁵⁴ K₂[Ni(dto)₂],⁵⁵ [PPh₄]₂[Ni(dto)₂]⁵⁶, K₂[Pd(dto)₂]⁵⁶, and K₂[Pt(dto)₂]⁵⁶ were prepared according to literature procedures. All other reagents were used as received.

[Ni(dto)₂(YTp₂)₂] (4.1a). Solutions of KTp (100 mg; 0.397 mmol) in H₂O (5 mL) and YCl₃ (39 mg; 0.20 mmol) in H₂O (5 mL) were added simultaneously dropwise to a solution of K₂[Ni(dto)₂] (37 mg; 0.10 mmol) in H₂O (10 mL). The violet precipitate that evolved was collected via filtration, washed with H₂O (3 × 5 mL) then Et₂O (3 × 5 mL), and dried in vacuo. Yield: 98 mg (70%).

Anal. Calcd. for C₄₀H₄₀B₄N₂₄NiO₄S₄Y₂: C, 36.15; H, 3.03; N 25.03. Found: C, 36.29; H, 3.12; N, 25.15%. IR (ν / cm⁻¹): ν(B–H) 2464 w, ν(C–N) 1526 m, 1505 m, ν(C=O) 1479 s, 1403 m, 1297 m, 1212 m, 1115 m, 1044 s, 975 m. ¹H NMR (C₆D₆; δ / ppm): 7.34 (t, 12H, pyrazolyl), 7.09 (m, 12H, pyrazolyl), 5.67 (m, 12H, pyrazolyl), 0.51 (m, 4 H, BH). ¹³C NMR (C₆D₆; δ / ppm): 200.91 (s), 141.23 (s), 135.33 (s), 104.65 (s). Absorption spectrum (CH₂Cl₂; λ_{max} / nm (ε / 10⁴ M⁻¹ cm⁻¹)): 525 sh (0.23), 550 (0.28), 590 (0.39), 620 (0.25).

[CoCp₂][Ni(dto)₂(YTp₂)₂] (4.1b). A stirred solution of **4.1a** (60 mg; 0.05 mmol) in toluene (10 mL) was treated dropwise with CoCp₂ (10 mg; 0.05 mmol) in toluene (5 mL) giving the immediate formation of a teal precipitate. The precipitate was collected by filtration, washed with toluene (3 × 5 mL) and dried under vacuum. Yield: 42 mg (30%).

Anal. Calcd. for C₅₀H₅₀B₄CoN₂₄NiO₄S₄Y₂: C, 39.56; H, 3.32; N, 22.14. Found: C, 39.40; H, 3.22; N, 22.24. Absorption spectrum (CH₂Cl₂; λ_{max} / nm (ε / 10⁴ M⁻¹ cm⁻¹)): 556 sh (0.35), 595 (0.42), 622 sh (0.31), 710 sh (0.11), 1110 (0.01), 1320 (0.02), 1790 (0.13).

[Ni(dto)₂(NdTp₂)₂] (4.2). This compound was synthesised in a manner analogous to **4.1a** using NdCl₃·6H₂O (72 mg; 0.20 mmol). Yield: 70 mg (48%).

Anal. Calcd. for C₄₀H₄₀B₄N₂₄NiO₄S₄Nd₂: C, 33.37; H, 2.80; N, 23.35. Found: C, 33.41; H, 2.92; N, 23.46. IR (ν / cm⁻¹): ν(B–H) 2444 w, ν(C–N) 1504 m, ν(C=O) 1402 m, 1292 m, 1212 m, 1115 m, 1044 s, 974 m. Absorption spectrum (CH₂Cl₂; λ_{max} / nm (ε / 10⁴ M⁻¹ cm⁻¹)): 523 sh (0.25), 548 (0.29), 593 (0.35), 623 (0.26).

[Ni(dto)₂(SmTp₂)₂] (4.3). This compound was synthesised in a manner analogous to **4.1a** using Sm(NO₃)₃·6H₂O (90 mg; 0.20 mmol). Yield: 100 mg (70%).

Anal. Calcd. for C₄₀H₄₀B₄N₂₄NiO₄S₄Sm₂: C, 33.09; H, 2.78; N, 23.10. Found: C, 33.14; H, 2.73; N, 23.09. IR (ν / cm⁻¹): ν(B–H) 2474 w, ν(C–N) 1535 m, 1502 m, ν(C=O) 1402 m, 1297 m, 1212 m, 1115 m, 1044 s, 974 m. Absorption spectrum (CH₂Cl₂; λ_{max} / nm (ε / 10⁴ M⁻¹ cm⁻¹)): 525 sh (0.08), 547 (0.12), 595 (0.16), 633 (0.09).

[Ni(dto)₂(EuTp₂)₂] (4.4). This compound was synthesised in a manner analogous to **4.1a** using Eu(NO₃)₃·6H₂O (90 mg; 0.20 mmol). Yield: 34 mg (23%).

Anal. Calcd. for C₄₀H₄₀B₄N₂₄NiO₄S₄Eu₂: C, 33.02; H, 2.77; N, 23.10. Found: C, 33.21; H, 2.86; N, 23.19. IR (ν / cm⁻¹): ν(B–H) 2461 w, ν(C–N) 1522 m, 1503 m, ν(C=O) 1403 m, 1297 m, 1212 m, 1115 m, 1044 s, 976 m. Absorption spectrum (CH₂Cl₂; λ_{max} / nm (ε / 10⁴ M⁻¹ cm⁻¹)): 522 sh (0.18), 553 (0.24), 595 (0.31), 622 (0.22).

[Ni(dto)₂(GdTp₂)₂] (4.5a). This compound was synthesised in a manner analogous to **4.1a** using GdCl₃·6H₂O (74 mg; 0.20 mmol). Yield: 190 mg (65%).

Anal. Calcd. for C₄₀H₄₀B₄N₂₄NiO₄S₄Gd₂: C, 32.78; H, 2.75; N, 22.94. Found: C, 33.02; H, 2.68; N, 23.09. IR (ν / cm⁻¹): ν(B–H) 2464 w, ν(C–N) 1535 m, 1505 m, ν(C=O) 1403 m, 1297 m, 1212 m, 1115 m, 1044 s, 976 m. Absorption spectrum (CH₂Cl₂; λ_{max} / nm (ε / 10⁴ M⁻¹ cm⁻¹)): 525 sh (0.22), 546 (0.28), 589 (0.39), 620 (0.24).

[CoCp₂][Ni(dto)₂(GdTp₂)₂] (4.5b). This compound was synthesised following the procedure for **4.1a** using **4.5a** (30 mg; 0.02 mmol) and CoCp₂ (4 mg; 0.02 mmol). Yield: 13 mg (40%).

Anal. Calcd. for C₅₀H₅₀B₄CoN₂₄NiO₄S₄Gd₂: C, 36.29; H, 3.05; N, 20.32. Found: C, 36.36; H, 2.97; N, 20.17. Absorption spectrum (CH₂Cl₂; λ_{max} / nm (ε / 10⁴ M⁻¹ cm⁻¹)): 556 sh (0.31), 595 (0.39), 622 sh (0.31), 710 sh (0.11), 1110 (0.01), 1320 (0.02), 1790 (0.13).

[Ni(dto)₂(TbTp₂)₂] (4.6). This compound was synthesised in a manner analogous to **4.1a** using TbCl₃·6H₂O (75 mg; 0.20 mmol). Yield: 92 mg (63%).

Anal. Calcd. for C₄₀H₄₀B₄N₂₄NiO₄S₄Tb₂: C, 32.71; H, 2.75; N, 22.88. Found: C, 32.81; H, 2.77; N, 22.67. IR (ν / cm⁻¹): ν(B–H) 2466 w, ν(C–N) 1533 m, 1502 m, ν(C=O) 1403 m, 1297 m, 1212 m, 1115 m, 1044 s, 976 m. Absorption spectrum (CH₂Cl₂; λ_{max} / nm (ε / 10⁴ M⁻¹ cm⁻¹)): 521 sh (0.21), 547 (0.25), 592 (0.32), 624 (0.22).

[Ni(dto)₂(DyTp₂)₂] (4.7). This compound was synthesised in a manner analogous to **4.1a** using DyCl₃·6H₂O (75 mg; 0.20 mmol). Yield: 99 mg (67%).

Anal. Calcd. for C₄₀H₄₀B₄N₂₄NiO₄S₄Dy₂: C, 32.55; H, 2.73; N, 22.77. Found: C, 32.35; H, 2.65; N, 22.79. IR (ν / cm⁻¹): ν(B–H) 2474 w, ν(C–N) 1533 m, 1502 m, ν(C=O) 1403 m, 1297

m, 1212 m, 1115 m, 1044 s, 977 m. Absorption spectrum (CH_2Cl_2 ; $\lambda_{\text{max}} / \text{nm}$ ($\epsilon / 10^4 \text{ M}^{-1} \text{ cm}^{-1}$)): 524 sh (0.21), 544 (0.30), 582 (0.41), 618 (0.26).

[Ni(dto)₂(HoTp₂)₂] (4.8). This compound was synthesised in a manner analogous to **4.1a** using $\text{Ho}(\text{NO}_3)_3 \cdot 5\text{H}_2\text{O}$ (88 mg; 0.20 mmol). Yield: 75 mg (50%).

Anal. Calcd. for $\text{C}_{40}\text{H}_{40}\text{B}_4\text{N}_{24}\text{NiO}_4\text{S}_4\text{Ho}_2$: C, 32.44; H, 2.72; N, 22.70. Found: C, 32.64; H, 2.79; N, 22.76. IR (ν / cm^{-1}): $\nu(\text{B-H})$ 2474 w, $\nu(\text{C-N})$ 1533 m, 1505 m, $\nu(\text{C=O})$ 1403 m, 1297 m, 1212 m, 1115 m, 1044 s, 977 m. Absorption spectrum (CH_2Cl_2 ; $\lambda_{\text{max}} / \text{nm}$ ($\epsilon / 10^4 \text{ M}^{-1} \text{ cm}^{-1}$)): 523 sh (0.27), 547 (0.32), 592 (0.40), 624 (0.28).

[Ni(dto)₂(ErTp₂)₂] (4.9). This compound was synthesised in a manner analogous to **4.1a** using $\text{Er}(\text{NO}_3)_3 \cdot 5\text{H}_2\text{O}$ (89 mg; 0.20 mmol). Yield: 45 mg (30%).

Anal. Calcd. for $\text{C}_{40}\text{H}_{40}\text{B}_4\text{N}_{24}\text{NiO}_4\text{S}_4\text{Er}_2$: C, 32.34; H, 2.71; N, 22.63. Found: C, 32.12; H, 2.72; N, 22.41. IR (ν / cm^{-1}): $\nu(\text{B-H})$ 2468 w, $\nu(\text{C-N})$ 1537 m, 1503 m, $\nu(\text{C=O})$ 1403 m, 1297 m, 1212 m, 1115 m, 1044 s, 978 m. Absorption spectrum (CH_2Cl_2 ; $\lambda_{\text{max}} / \text{nm}$ ($\epsilon / 10^4 \text{ M}^{-1} \text{ cm}^{-1}$)): 520 sh (0.30), 547 (0.37), 594 (0.46), 623 (0.32).

[Ni(dto)₂(TmTp₂)₂] (4.10). This compound was synthesised in a manner analogous to **4.1a** using $\text{Tm}(\text{NO}_3)_3 \cdot 5\text{H}_2\text{O}$ (89 mg; 0.20 mmol). Yield: 101 mg (68%).

Anal. Calcd. for $\text{C}_{40}\text{H}_{40}\text{B}_4\text{N}_{24}\text{NiO}_4\text{S}_4\text{Tm}_2$: C, 32.27; H, 2.71; N, 22.58. Found: C, 32.26; H, 2.70; N, 22.63. IR (ν / cm^{-1}): $\nu(\text{B-H})$ 2469 w, $\nu(\text{C-N})$ 1537 m, 1502 m, $\nu(\text{C=O})$ 1403 m, 1297 m, 1212 m, 1115 m, 1044 s, 978 m. Absorption spectrum (CH_2Cl_2 ; $\lambda_{\text{max}} / \text{nm}$ ($\epsilon / 10^4 \text{ M}^{-1} \text{ cm}^{-1}$)): 520 sh (0.52), 547 (0.64), 592 (0.79), 621 (0.56).

[Ni(dto)₂(YbTp₂)₂] (4.11). This compound was synthesised in a manner analogous to **4.1a** using $\text{YbCl}_3 \cdot 6\text{H}_2\text{O}$ (77 mg; 0.20 mmol). Yield: 120 mg (81%).

Anal. Calcd. for $\text{C}_{40}\text{H}_{40}\text{B}_4\text{N}_{24}\text{NiO}_4\text{S}_4\text{Yb}_2$: C, 32.09; H, 2.69; N, 22.45. Found: C, 32.26; H, 2.76; N, 22.59. IR (ν / cm^{-1}): $\nu(\text{B-H})$ 2472 w, $\nu(\text{C-N})$ 1533 m, 1505 m, $\nu(\text{C=O})$ 1403 m, 1297 m, 1212 m, 1115 m, 1044 s, 977 m. Absorption spectrum (CH_2Cl_2 ; $\lambda_{\text{max}} / \text{nm}$ ($\epsilon / 10^4 \text{ M}^{-1} \text{ cm}^{-1}$)): 518 sh (0.31), 545 (0.39), 592 (0.47), 623 (0.33).

[Ni(dto)₂(LuTp₂)₂] (4.12). This compound was synthesised in a manner analogous to **4.1a** using $\text{Lu}(\text{NO}_3)_3 \cdot 6\text{H}_2\text{O}$ (94 mg; 0.20 mmol). Yield: 76 mg (67%).

Anal. Calcd. for $\text{C}_{40}\text{H}_{40}\text{B}_4\text{N}_{24}\text{NiO}_4\text{S}_4\text{Lu}_2$: C, 32.01; H, 2.69; N, 22.40. Found: C, 32.09; H, 2.72; N, 22.32. IR (ν / cm^{-1}): $\nu(\text{B-H})$ 2476 w, $\nu(\text{C-N})$ 1533 m, 1502 m, $\nu(\text{C=O})$ 1403 m, 1297 m, 1212 m, 1115 m, 1044 s, 978 m. Absorption spectrum (CH_2Cl_2 ; $\lambda_{\text{max}} / \text{nm}$ ($\epsilon / 10^4 \text{ M}^{-1} \text{ cm}^{-1}$)): 523 sh (0.21), 548 (0.28), 592 (0.38), 615 (0.24).

[Pd(dto)₂(LuTp₂)₂] (4.13). This compound was synthesised in a manner analogous to **4.12** using $\text{K}_2[\text{Pd}(\text{dto})_2]$ (42 mg; 0.10 mmol) to give a mustard product. Yield: 111 mg (72%).

Anal. Calcd. for $C_{40}H_{40}B_4N_{24}PdO_4S_4Lu_2$: C, 31.02; H, 2.60; N, 21.71. Found: C, 31.09; H, 2.62; N, 21.65. IR (ν / cm^{-1}): $\nu(\text{B-H})$ 2478 w, $\nu(\text{C-N})$ 1532 m, 1506 m, $\nu(\text{C=O})$ 1404 m, 1292 m, 1220 m, 1113 m, 1048 s, 969 m. Absorption spectrum (CH_2Cl_2 ; $\lambda_{\text{max}} / \text{nm}$ ($\epsilon / 10^4 \text{ M}^{-1} \text{ cm}^{-1}$)): 365 (0.88), 391 sh (1.09), 407 (1.30), 435 (0.86), 472 sh (0.14), 491 sh (0.09).

[Pt(dto)₂(LuTp₂)₂] (4.14). This compound was synthesised in a manner analogous to **4.12** using $\text{K}_2[\text{Pt}(\text{dto})_2]$ (51 mg; 0.10 mmol) to give a crimson product. Yield: 118 mg (72%).

Anal. Calcd. for $C_{40}H_{40}B_4N_{24}PtO_4S_4Lu_2$: C, 29.34; H, 2.46; N, 20.53. Found: C, 29.01; H, 2.51; N, 20.42. IR (ν / cm^{-1}): $\nu(\text{B-H})$ 2482 w, $\nu(\text{C-N})$ 1532 m, 1508 m, $\nu(\text{C=O})$ 1405 m, 1287 m, 1216 m, 1119 m, 1056 s, 972 m. Absorption spectrum (CH_2Cl_2 ; $\lambda_{\text{max}} / \text{nm}$ ($\epsilon / 10^4 \text{ M}^{-1} \text{ cm}^{-1}$)): 360 (0.30), 408 (0.31), 418 (0.32), 450 sh (0.28), 475 (0.46), 502 (0.52), 572 sh (0.07).

[PPh₄]₂[Ni(dto)₂(SnCl₄)₂] (4.15). In a 50 mL Schlenk flask was dissolved $[\text{PPh}_4]_2[\text{Ni}(\text{dto})_2]$ (98 mg; 0.10 mmol) in CH_2Cl_2 (8 mL) and treated dropwise with 1.0 M SnCl_4 in CH_2Cl_2 (0.20 mL; 0.20 mmol) to give a deep blue solution. Stirring was continued for 10 min, and then the mixture was layered with hexanes (16 mL). Upon standing overnight, a microcrystalline indigo solid was collected by filtration and dried under vacuum. Yield: 82 mg (54%).

Anal. Calcd. for $C_{52}H_{40}Cl_8NiO_4P_2S_4Sn_2$: C, 41.67; H, 2.69. Found: C, 41.79; H, 2.61. IR (ν / cm^{-1}): 2361 w, 1629 w, 1581 w, $\nu(\text{C=O})$ 1485 s, 1435 s, 1106 s, 991 m. $^1\text{H NMR}$ (CD_2Cl_2 ; δ / ppm): 7.92 (m, 4H, PPh_4^+), 7.76 (m, 8H, PPh_4^+), 7.62 (m, 8H, PPh_4^+). $^{13}\text{C NMR}$ (CD_2Cl_2 ; δ / ppm): 209.73 (s), 136.20 (s), 134.88 (s), 131.11 (s), 117.93 (d, $J_{\text{CP}} = 86.60 \text{ Hz}$). Absorption spectrum (CH_2Cl_2 ; $\lambda_{\text{max}} / \text{nm}$ ($\epsilon / 10^4 \text{ M}^{-1} \text{ cm}^{-1}$)): 535 (0.22), 579 (0.31), 622 (0.44).

4.8.2. Physical Characterisation and Theoretical

X-ray Crystallographic Data Collection and Structure Refinement. Diffraction quality crystals of **4.1a** – **4.12**, and **4.1b** and **4.5b** were obtained by slow diffusion of diethyl ether into concentrated dichloromethane and acetonitrile solutions, respectively, of the complex. Crystals of **4.15** were grown from diffusion of hexane into a dichloromethane solution of the complex at -25 °C. The crystals were coated with paratone oil and mounted on the end of a nylon loop attached to the end of the goniometer. Data were collected using either a Bruker D8 Venture or a Bruker SMART APEX CCD diffractometer equipped with a Kryoflex attachment supplying a nitrogen stream at 150 K. Structure solution and refinement were carried out with SHELXS-97⁵⁷ and SHELXL-97⁵⁸ either using the Olex2⁵⁹ or WinGX⁶⁰ software packages. Data collection and reduction were performed using the APEX3 or APEX2 programs. Corrections for incident and diffracted beam absorption effects were applied using empirical absorption corrections.⁶¹ All non-hydrogen atoms were refined with anisotropic thermal parameters. Solvent molecule sites were found and included in the refinement of structure were generally refined with anisotropic thermal parameters. The positions of hydrogen atoms were calculated based on stereochemical considerations and kept fixed isotropic during refinement. Final unit cell data and refinement statistics are collected in Table 4.5.

Table 4.5. Crystallographic Data for compounds in Chapter 4.

compound formula	4.1a ·2CH ₂ Cl ₂ C ₄₂ H ₄₄ B ₄ Cl ₄ N ₂₄ NiO ₄ S ₄ Y 2	4.5a ·2CH ₂ Cl ₂ C ₄₂ H ₄₄ B ₄ Cl ₄ Gd ₂ N ₂₄ NiO ₄ S 4	4.1b ·CH ₃ CN C ₅₂ H ₅₃ B ₄ CoN ₂₅ NiO ₄ S ₄ Y ₂	4.5b ·CH ₃ CN C ₅₂ H ₅₃ B ₄ CoGd ₂ N ₂₅ NiO ₄ S 4	4.15 C ₅₂ H ₄₀ Cl ₈ NiO ₄ P ₂ S ₄ Sn 2
fw	1498.82	1635.50	1559.13	1695.81	1498.71
T, K	150(2)	150(2)	150(2)	150(2)	150(2)
λ, Å	0.71073	0.71073	0.71073	0.71073	0.71073
2θ range, deg	4.66–50.58	4.62–52.44	4.41–50.52	4.40–56.54	4.40–56.58
crystal system	triclinic	triclinic	monoclinic	monoclinic	monoclinic
space group	<i>P</i> $\bar{1}$	<i>P</i> $\bar{1}$	<i>P</i> 2 ₁ / <i>c</i>	<i>P</i> 2 ₁ / <i>c</i>	<i>P</i> 2 ₁ / <i>n</i>
a, Å	7.7805(7)	7.754(2)	21.452(3)	21.551(1)	7.5323(4)
b, Å	11.4660(9)	11.475(2)	18.321(3)	18.3268(9)	21.605 (1)
c, Å	17.794(1)	17.902(4)	18.014(3)	18.074(1)	17.984(1)
α, deg	79.227(3)	79.546(3)	90	90	90
β, deg	86.607(3)	86.774(3)	113.699(2)	113.674(2)	90.339(2)
γ, deg	72.168(3)	72.601(3)	90	90	90
V, Å ³	1484.5(2)	1494.7(5)	6483(2)	6537.7(7)	2926.6(3)
Z	1	1	4	4	2
ρ, g cm ⁻³	1.677	1.817	1.597	1.723	1.701
μ, mm ⁻¹	2.637	2.887	2.504	2.728	1.771
crystal size, mm	0.20 × 0.07 × 0.02	0.10 × 0.08 × 0.02	0.18 × 0.12 × 0.10	0.22 × 0.19 × 0.02	0.42 × 0.06 × 0.02
colour, habit	purple plate	blue plate	blue block	green plate	blue lath
reflections collected	19317	16210	108563	67695	36852
independent data	5418	5327	13599	16204	7242
parameters / restraints	390 / 0	385 / 0	839 / 0	839 / 0	331 / 0
GoF ^a	1.070	1.022	1.030	1.049	1.063
R1 ^{b,c} / wR2 ^{d,e}	0.0383 / 0.0934	0.0314 / 0.0426	0.0444 / 0.0868	0.0383 / 0.0902	0.0290 / 0.0646
R1 ^{b,e} / wR2 ^{d,e}	0.0466 / 0.0969	0.0592 / 0.0633	0.0960 / 0.1094	0.0642 / 0.1069	0.0420 / 0.0738
largest diff. peak, e	0.938	1.453	0.724	1.492	0.667
largest diff. hole, e	-0.509	-0.850	-0.496	-1.398	-0.393

^a GoF = $\{\sum[w(F_o^2 - F_c^2)^2]/(n - p)\}^{1/2}$, where n = number of reflections and p is the total number of parameters refined. ^b R1 = $\sum||F_o| - |F_c||/\sum|F_o|$. ^c R indices for data cut off at $I > 2\sigma(I)$. ^d wR2 = $\{\sum[w(F_o^2 - F_c^2)^2]/\sum[w(F_o^2)^2]\}^{1/2}$, where $w = 1/[\sigma^2(F_o^2) + (aP)^2 + bP]$, $P = (F_o^2 + 2F_c^2)/3$. ^e R indices for all data.

Table 4.5.cont. Crystallographic Data for compounds in Chapter 4

compound	4.2.2 CH ₂ Cl ₂	4.3.2 CH ₂ Cl ₂	4.4.2 CH ₂ Cl ₂	4.6.2 CH ₂ Cl ₂	4.7.2 CH ₂ Cl ₂
formula	C ₄₂ H ₄₄ B ₄ Cl ₄ Nd ₂ N ₂₄ NiO ₄ S ₄	C ₄₂ H ₄₄ B ₄ Cl ₄ Sm ₂ N ₂₄ NiO ₄ S ₄	C ₄₂ H ₄₄ B ₄ Cl ₄ Eu ₂ N ₂₄ NiO ₄ S ₄	C ₄₂ H ₄₄ B ₄ Cl ₄ Tb ₂ N ₂₄ NiO ₄ S ₄	C ₄₂ H ₄₄ B ₄ Cl ₄ Dy ₂ N ₂₄ NiO ₄ S ₄
fw	1609.46	1621.70	1624.92	1638.84	
T, K	150(2)	150(2)	150(2)	150(2)	150(2)
λ, Å	0.71073	0.71073	0.71073	0.71073	0.71073
2θ range, deg	4.67–53.83	4.60–54.67	4.72–43.72	4.64–49.17	4.668–43.426
crystal system	triclinic	triclinic	triclinic	triclinic	triclinic
space group	<i>P</i> $\bar{1}$				
a, Å	7.777(4)	7.773(5)	7.773(9)	7.770(3)	7.740(3)
b, Å	11.529(6)	11.513(7)	11.520(13)	11.471(4)	11.415(5)
c, Å	18.050(9)	17.984(10)	17.99(2)	17.857(7)	17.758(8)
α, deg	80.749(5)	80.023(6)	79.815(15)	79.243(5)	79.276(7)
β, deg	86.317(5)	86.666(6)	86.900(15)	86.646(5)	86.702(7)
γ, deg	73.476(6)	72.712(5)	72.909(16)	72.100(4)	72.242(7)
V, Å ³	1531.07	1513.41	1515(3)	1488.0(10)	1468.1(11)
Z	1	1	1	1	1
ρ, g cm ⁻³	1.746	1.779	1.781	1.829	1.862
μ, mm ⁻¹	2.348	2.600	2.729	3.048	3.225
crystal size, mm	0.15 × 0.10 × 0.07	0.16 × 0.10 × 0.06	0.15 × 0.09 × 0.05	0.15 × 0.10 × 0.08	0.18 × 0.15 × 0.09
colour, habit	purple block				
reflections collected	20745	16797	15580	19065	19134
independent data	6672	6826	5983	6166	6048
parameters / restraints	385 / 0	385 / 0	385 / 0	385 / 0	385 / 0
GoF ^a	1.153	1.155	1.011	1.039	1.018
R1 ^{b,c} / wR2 ^{d,c}	0.0160 / 0.0405	0.0213 / 0.0706	0.0467 / 0.0836	0.0411 / 0.0854	0.0434 / 0.0748
R1 ^{b,e} / wR2 ^{d,e}	0.0174 / 0.0485	0.0231 / 0.0728	0.0714 / 0.0928	0.0578 / 0.0917	0.0664 / 0.0883
largest diff. peak, e	0.44	0.60	1.27	1.39	1.36
largest diff. hole, e	-0.58	-0.91	-1.24	-1.58	-1.26

Table 4.5.cont. Crystallographic Data for compounds in Chapter 4

compound	4.8.2CH₂Cl₂	4.9.2CH₂Cl₂	4.10.2CH₂Cl₂	4.11.2CH₂Cl₂	4.12.2CH₂Cl₂
formula	C ₄₂ H ₄₄ B ₄ Cl ₄ Ho ₂ N ₂₄ NiO ₄ S ₄	C ₄₂ H ₄₄ B ₄ Cl ₄ Er ₂ N ₂₄ NiO ₄ S ₄	C ₄₂ H ₄₄ B ₄ Cl ₄ Tm ₂ N ₂₄ NiO ₄ S ₄	C ₄₂ H ₄₄ B ₄ Cl ₄ Yb ₂ N ₂₄ NiO ₄ S ₄	C ₄₂ H ₄₄ B ₄ Cl ₄ Lu ₂ N ₂₄ NiO ₄ S ₄
fw	1650.86	1655.52	1658.86	1667.08	1670.94
T, K	150(2)	150(2)	150(2)	150(2)	150(2)
λ, Å	0.71073	0.71073	0.71073	0.71073	0.71073
2θ range, deg	4.65–53.16	3.79–53.29	4.67–49.49	4.68–52.91	4.68–52.90
crystal system	triclinic	triclinic	triclinic	triclinic	Triclinic
space group	<i>P</i> $\bar{1}$				
a, Å	7.792(4)	7.795(2)	7.780(2)	7.809(2)	7.807(4)
b, Å	11.488(6)	11.487(3)	11.459(3)	11.466(3)	11.456(5)
c, Å	17.823(9)	17.812(5)	17.774(5)	17.740(5)	17.721(8)
α, deg	79.367(6)	79.129(3)	78.989(4)	79.002(3)	78.968(5)
β, deg	86.780(6)	86.640(4)	86.506(4)	86.494(3)	86.410(6)
γ, deg	72.368(6)	72.148(3)	71.685(4)	71.875(3)	71.934(5)
V, Å ³	1494.4(13)	1490.8(8)	1476.5(8)	1481.86	1478.92
Z	1	1	1	1	1
ρ, g cm ⁻³	1.834	1.844	1.866	1.868	1.876
μ, mm ⁻¹	3.316	3.485	3.681	3.829	4.013
crystal size, mm	0.17 × 0.15 × 0.08	0.17 × 0.10 × 0.08	0.18 × 0.17 × 0.12	0.20 × 0.15 × 0.08	0.17 × 0.10 × 0.08
colour, habit	purple block				
reflections collected	22753	17858	19014	19287	15898
independent data	6245	6252	6006	6120	6074
parameters / restraints	385 / 0	385 / 0	385 / 0	385 / 0	385 / 0
GoF ^a	1.035	1.024	1.017	1.024	1.032
R1 ^{b,c} / wR2 ^{d,c}	0.0256 / 0.0574	0.0278 / 0.0593	0.0323 / 0.0644	0.0176 / 0.0420	0.0178 / 0.0409
R1 ^{b,e} / wR2 ^{d,e}	0.0310 / 0.0599	0.0353 / 0.0622	0.0434 / 0.0681	0.0193 / 0.0428	0.0199 / 0.0419
largest diff. peak, e	1.34	1.33	1.19	1.34	0.60
largest diff. hole, e	-1.39	-1.20	-0.90	-0.99	-0.71

Other Physical Methods. Electronic absorption spectra were collected using a Shimadzu UV-3600 UV/vis/NIR spectrophotometer. IR spectra were collected using either a Shimadzu IRAffinity-1S or a Shimadzu FTIR 8400S spectrophotometer. ^1H and ^{13}C NMR data were recorded on an AVIII 400 MHz instrument and were referenced internally to the residual solvent. X-band EPR spectra were collected on a Bruker ELEXSYS E500 spectrometer and simulations were performed using Bruker's Xsophe software package.⁶² Cyclic voltammetry measurements were performed with a Metrohm Autolab P128 potentiostat. The electrode configuration consisted of a 2 mm glassy carbon working electrode, a platinum auxiliary electrode and a reference electrode consisting of Ag/AgNO₃ (0.01 M in MeCN) incorporated into a salt bridge containing supporting electrolyte (to minimize Ag⁺ leakage). The measurements were collected using a 1 mM solution of **4.1a** and **4.5a** dissolved in 5:1 anisole/dichloromethane containing 0.2 M [N(ⁿBu)₄]PF₆ as electrolyte. All reduction potentials are referenced versus the ferrocenium/ferrocene (Fc⁺⁰) couple. Microanalyses were performed at London Metropolitan University.

Calculations. The program package ORCA was used for all calculations.⁶³ The geometry of [Ni{(dto)SnCl₄]₂]³⁻ was fully optimised using the BP86 functional,⁶⁴⁻⁶⁵ employing the D3 dispersion correction⁶⁶ in and acetonitrile solvent with the conductor like screening model (COSMO).⁶⁷⁻⁶⁹ The scalar relativistically recontracted def2-TZVP basis set was used for all atoms.⁷⁰⁻⁷¹ Auxiliary basis sets used to expand the electron density in the calculations were chosen to match the orbital basis. Electronic structures were calculated on crystallographic or optimised coordinates using the PBE0 hybrid functional.⁷²⁻⁷⁴ The RIJCOSX algorithm was used to speed the calculation of Hartree–Fock exchange.⁷²⁻⁷⁶ Increased integration accuracy (SPECIALGRIDINTACC 7) was used for metal atoms and sulfur. Calculations included the zeroth-order regular approximation (ZORA) for relativistic effects⁷⁷⁻⁷⁹ as implemented by van Wüllen.⁸⁰ The self-consistent field calculations were tightly converged ($1 \times 10^{-8} E_h$ in energy, $1 \times 10^{-7} E_h$ in the charge density, and 1×10^{-7} in the maximum element of the DIIS⁸¹⁻⁸² error vector). The geometry was converged with the following convergence criteria: change in energy $<10^{-5} E_h$, average force $<5 \times 10^{-4} E_h \text{ Bohr}^{-1}$, and the maximum force $10^{-4} E_h \text{ Bohr}^{-1}$. We used the broken symmetry (BS) approach to describe our computational results for **4.5a** and **4.5b**.⁸³⁻⁸⁷ We adopt the following notation: the given system was divided into two fragments. The notation BS(*m*,*n*) refers then to a broken symmetry state with *m* unpaired α -spin electrons essentially on fragment 1 and *n* unpaired β -spin electrons localised on fragment 2. In most cases, fragments 1 and 2 correspond to the metal and the ligands, respectively. In this notation the standard high-spin, open-shell solution is written as BS(*m* + *n*,0). The BS(*m*,*n*) notation refers to the initial guess to the wave function. The variational process does, however, have the freedom to converge to a solution of the form BS(*m* – *n*,0) in which effectively the *n* β -spin electrons pair up with *n* < *m* α -spin electrons on the partner fragment. Such a solution is then a standard

$M_S \cong (m - n)/2$ spin-unrestricted Kohn-Sham solution. The exchange coupling constants J were calculated using Eq. 1,⁸⁸⁻⁸⁹, assuming the spin-Hamiltonian Eq. 2 is valid.

$$J = \frac{E_{HS} - E_{BS}}{\langle \hat{S}^2 \rangle_{HS} - \langle \hat{S}^2 \rangle_{BS}} \quad (1)$$

$$\hat{H} = -2J\hat{S}_A \cdot \hat{S}_B \quad (2)$$

Spin density plot were obtained using Molekel.⁹⁰

4.11.References

1. Jones, H. O.; Tasker, H. S., *Journal of the Chemical Society, Transactions*. **1909**, 95, 1904-1909.
2. Dietzsch, W.; Strauch, P.; Hoyer, E., *Coordination Chemistry Reviews* **1992**, 121, 43-130.
3. Boyd, P. D. W.; Hope, J.; Raston, C. L.; White, A. H., *Australian Journal of Chemistry* **1990**, 43 (3), 601-607.
4. Bradley, J. M.; Carling, S. G.; Visser, D.; Day, P.; Hautot, D.; Long, G. J., *Inorganic Chemistry* **2003**, 42, 986.
5. Siebold, M.; Eidner, S.; Kelling, A.; Kumke, M. U.; Schilde, U.; Strauch, P., *Zeitschrift fur Anorganische und Allgemeine Chemie* **2006**, 632, 1963-1965.
6. Siebold, M.; Kelling, A.; Schilde, U.; Strauch, P., *Zeitschrift fur Naturforschung B* **2005**, 60, 1149.
7. Siebold, M.; Korabik, M.; Schilde, U.; Mrozinski, J.; Strauch, P., *Chemical Papers* **2008**, 62, 487.
8. Coucouvanis, D., *Journal of the American Chemical Society* **1970**, 92, 707-709.
9. Coucouvanis, D.; Baenziger, N. C.; Johnson, S. M., *Journal of the American Chemical Society* **1973**, 95, 3875-3886.
10. Coucouvanis, D.; Piltingsrud, D., *Journal of the American Chemical Society* **1973**, 95, 5556-5563.
11. Leitheiser, M.; Coucouvanis, D., *Inorganic Chemistry* **1977**, 16, 1611.
12. Hollander, F. J.; Coucouvanis, D., *Inorganic Chemistry* **1973**, 13, 2381.
13. Xu, G.-F.; Gamez, P.; Tang, J.; Clérac, R.; Guo, Y.-N.; Guo, Y., *Inorganic Chemistry* **2012**, 51, 5693-5698.
14. Frasse, C.; Trombe, J. C.; Gleizes, A.; Galy, J., *Comptes Rendus de l'Academie Sciences, Series II* **1985**, 200, 403.
15. Gleizes, A.; Maury, F.; Cassoux, P.; Galy, J., *Zeitschrift fur Kristallographie* **1981**, 155, 293.
16. Trombe, J. C.; Gleizes, A.; Galy, J., *Comptes Rendus de l'Academie Sciences, Ser. II* **1982**, 294, 1369.
17. Gleizes, A.; Verdaguer, M., *Journal of the American Chemical Society* **1984**, 106, 3727.
18. Ray, K.; Petrenko, T.; Wieghardt, K.; Neese, F., *Dalton Transactions* **2007**, 1552.
19. Sproules, S.; Wieghardt, K., *Coordination Chemistry Reviews* **2011**, 255, 837.
20. Bowmaker, G. A.; Boyd, P. D. W.; Campbell, G. K., *Inorganic Chemistry* **1982**, 21 (9), 3565-3568.

21. Yamada, J.-i.; Tanaka, S.; Segawa, J.; Hamasaki, M.; Hagiya, K.; Anzai, H.; Nishikawa, H.; Ikemoto, I.; Kikuchi, K., *The Journal of Organic Chemistry* **1998**, *63* (12), 3952-3960.
22. Allen, C. W.; Brown, D. B., *Inorganic Chemistry* **1974**, *13* (8), 2020-2023.
23. da Cruz, A. G. B.; Wardell, J. L.; Rocco, A. M., *Journal of Materials Science* **2008**, *43* (17), 5823-5836.
24. Chandrasekaran, P.; Greene, A. F.; Lillich, K.; Capone, S.; Mague, J. T.; DeBeer, S.; Donahue, J. P., *Inorganic Chemistry* **2014**, *53* (17), 9192-9205.
25. Adams, C. J., *Journal of the Chemical Society, Dalton Transactions* **2002**, (7), 1545-1550.
26. Adams, C. J.; Fey, N.; Weinstein, J. A., *Inorganic Chemistry* **2006**, *45* (16), 6105-6107.
27. Coucouvanis, D., *Journal of the American Chemical Society* **1970**, *92* (3), 707-709.
28. Leitheiser, M.; Coucouvanis, D., *Inorganic Chemistry* **1977**, *16* (7), 1611-1614.
29. Cotruvo, J. A., *ACS Central Science* **2019**, *5* (9), 1496-1506.
30. Woodruff, D. N.; Winpenny, R. E. P.; Layfield, R. A., *Chemical Reviews* **2013**, *113* (7), 5110-5148.
31. Kagan, H. B., *Chemical Reviews* **2002**, *102* (6), 1805-1806.
32. Apostolidis, C.; Rebizant, J.; Kanellakopoulos, B.; von Ammon, R.; Dornberger, E.; Müller, J.; Powietzka, B.; Nuber, B., *Polyhedron* **1997**, *16* (7), 1057-1068.
33. Moss, M. A. J.; Jones, C. J., *Polyhedron* **1989**, *8* (4), 555-558.
34. Mikhalyova, E. A.; Zeller, M.; Jasinski, J. P.; Butcher, R. J.; Carrella, L. M.; Sedykh, A. E.; Gavrilenko, K. S.; Smola, S. S.; Frasso, M.; Cazorla, S. C.; Perera, K.; Shi, A.; Ranjbar, H. G.; Smith, C.; Deac, A.; Liu, Y.; McGee, S. M.; Dotsenko, V. P.; Kumke, M. U.; Müller-Buschbaum, K.; Rentschler, E.; Addison, A. W.; Pavlishchuk, V. V., *Dalton Transactions* **2020**, *49* (23), 7774-7789.
35. Dunstan, M. A.; Rousset, E.; Boulon, M.-E.; Gable, R. W.; Sorace, L.; Boskovic, C., *Dalton Transactions* **2017**, *46* (40), 13756-13767.
36. Sanada, T.; Suzuki, T.; Yoshida, T.; Kaizaki, S., *Inorganic Chemistry* **1998**, *37* (18), 4712-4717.
37. Subhan, M. A.; Sanada, T.; Suzuki, T.; Kaizaki, S., *Inorganica Chimica Acta* **2003**, *353*, 263-268.
38. Xu, G.-F.; Gamez, P.; Tang, J.; Clérac, R.; Guo, Y.-N.; Guo, Y., *Inorganic Chemistry* **2012**, *51* (10), 5693-5698.
39. Reed, W. R.; Dunstan, M. A.; Gable, R. W.; Phonsri, W.; Murray, K. S.; Mole, R. A.; Boskovic, C., *Dalton Transactions* **2019**, *48* (41), 15635-15645.
40. Sanada, T.; Suzuki, T.; Kaizaki, S., *Journal of the Chemical Society, Dalton Transactions* **1998**, 959.

41. Sanada, T.; Suzuki, T.; Yoshida, T.; Kaizaki, S., *Inorganic Chemistry* **1998**, *37*, 4712.
42. Long, D. P.; Chandrasekaran, A.; Day, R. O.; Bianconi, P. A., *Inorganic Chemistry* **2000**, *39*, 4476.
43. Junnosuke, F.; Kazuo, N., *Bulletin of the Chemical Society, Japan* **1964**, *37*, 528.
44. Román, P.; Luque, A.; Gutiérrez-Zorilla, J. M.; Beitia, J. I., *Zeitschrift für Kristallographie* **1992**, *198*, 213.
45. Connelly, N. G., Royal Society of Chemistry (Great Britain) and International Union of Pure and Applied Chemistry. In *Nomenclature of inorganic chemistry. IUPAC recommendations 2005*, Royal Society of Chemistry: 2005.
46. Caneschi, A.; Dei, A.; Gatteschi, D.; Sorace, L.; Vostrikova, K., *Angewandte Chemie International Edition* **2000**, *39*, 246.
47. Caneschi, A.; Dei, A.; Gatteschi, D.; Poussereau, S.; Sorace, L., *Dalton Transactions* **2004**, 1048.
48. Latham, A. R.; Hascall, V. C.; Gray, H. B., *Inorganic Chemistry* **1965**, *4*, 788.
49. Eaton, D. R., *Inorganic Chemistry* **1964**, *3*, 1268.
50. Prabhananda, B. S.; Felix, C. C.; Kalyanaraman, B.; Sealy, R. C., *Journal of Magnetic Resonance*. **1988**, *76*, 264.
51. Gupta, T.; Rajeshkumar, T.; Rajaraman, G., *Physical Chemistry Chemical Physics* **2014**, *16*, 14568.
52. Rajeshkumar, T.; Rajaraman, G., *Chemical Communications* **2012**, *48*, 7856.
53. Kapre, R. R.; Bothe, E.; Weyhermüller, T.; DeBeer George, S.; Muresan, N.; Wieghardt, K., *Inorganic Chemistry* **2007**, *46*, 7827.
54. Pauson Peter, L., *Encyclopedia of Reagents for Organic Synthesis* **2001**.
55. Jones, H. O.; Tasker, H. S., *Journal of the Chemical Society, Transactions* **1909**, *95* (0), 1904-1909.
56. Román, P.; Beitia, J. I.; Luque, A.; Guzmán-Miralles, C., *Polyhedron* **1995**, *14* (8), 1091-1096.
57. Sheldrick, G. M., *Acta Crystallographica Section A* **2008**, *64*, 112.
58. Sheldrick, G. M., *Acta Crystallographica* **2015**, *C71*, 3.
59. Dolomanov, O. V.; Bourhis, L. J.; Gildea, R. J.; Howard, J. A. K.; Puschmann, H., *Journal of Applied Crystallography*. **2009**, *42*, 339.
60. Farrugia, L. J., *Journal of Applied Crystallography* **1999**, *32*, 837.
61. Clark, R. C.; Reid, J. S., *Acta Crystallographica Section A* **1995**, *51*, 887.
62. Hanson, G. R.; Gates, K. E.; Noble, C. J.; Griffin, M.; Mitchell, A.; Benson, S., *Journal of Inorganic Biochemistry* **2004**, *98*, 903.
63. Neese, F., *WIREs Computational Molecular Science* **2012**, *2*, 73-78.
64. Becke, A. D., *Journal of Chemical Physics* **1988**, *84*, 4524-4529.
65. Perdew, J. P., *Physical Reviews B* **1986**, *33*, 8822-8824.

66. Grimme, S.; Antony, J.; Ehrlich, S.; Krieg, H., *Journal of Chemical Physics* **2010**, *132*, 154104.
67. Klamt, A.; Schüürmann, G., *Journal of the Chemical Society, Perkin Transactions 2* **1993**, 799-805.
68. Klamt, A.; Jonas, V., *Journal of Chemical Physics* **1996**, *105*, 9972-9981.
69. Klamt, A., *Journal of Chemical Physics* **1995**, *99*, 2224-2235.
70. Pantazis, D. A.; Neese, F., *Journal of Chemical Theory and Computation* **2009**, *5*, 2229-2238.
71. Weigend, F.; Ahlrichs, R., *Physical Chemistry Chemical Physics* **2005**, *7*, 3297-3305.
72. Adamo, C.; Barone, V., *Journal of Chemical Physics* **1999**, *110*, 6158.
73. Perdew, J. P.; Burke, K.; Ernzerhof, M., *Physical Review Letters* **1996**, *77*, 3865.
74. Perdew, J. P.; Burke, K.; Ernzerhof, M., *Physical Review Letters* **1997**, *78*, 1396.
75. Izsák, R.; Neese, F., *Journal of Chemical Physics* **2011**, *135*, 144105.
76. Neese, F.; Wennmohs, F.; Hansen, A.; Becker, U., *Chemical Physics* **2009**, *356*, 98-109.
77. van Lenthe, E.; Snijders, J. G.; Baerends, E. J., *Journal of Chemical Physics*. **1996**, *105*, 6505-6516.
78. van Lenthe, E.; van der Avoird, A.; Wormer, P. E. S., *Journal of Chemical Physics* **1998**, *108*, 4783-4796.
79. van Lenthe, J. H.; Faas, S.; Snijders, J. G., *Chemical Physics Letters* **2000**, *328*, 107-112.
80. van Wüllen, C. J., *Journal of Chemical Physics* **1998**, *109*, 392-399.
81. Pulay, P., *Chemical Physics Letters* **1980**, *73*, 393-398.
82. Pulay, P., *Journal of Computational Chemistry* **1982**, *3*, 556-560.
83. Noodleman, L., *Journal of Chemical Physics* **1981**, *74*, 5737-5743.
84. Noodleman, L.; Case, D. A.; Aizman, A., *Journal of the American Chemical Society* **1988**, *110*, 1001-1005.
85. Noodleman, L.; Davidson, E. R., *Chemical Physics* **1986**, *109*, 131-143.
86. Noodleman, L.; Norman, J. G.; Osborne, J. H.; Aizman, A.; Case, D. A., *Journal of the American Chemical Society* **1985**, *107*, 3418-3426.
87. Noodleman, L.; Peng, C. Y.; Case, D. A.; Monesca, J. M., *Coordination Chemistry Reviews* **1995**, *144*, 199-244.
88. Soda, T.; Kitagawa, Y.; Onishi, T.; Takano, Y.; Shigetou, Y.; Nagao, H.; Yoshioka, Y.; Yamaguchi, K., *Chemical Physics Letters* **2000**, *319*, 223-230.
89. Yamaguchi, K.; Takahara, Y.; Fueno, T., In *Applied Quantum Chemistry*, Smith, V. H., Ed. Reidel: Dordrecht, The Netherlands, 1986; p p. 155.

90. *Molekel*, Advanced Interactive 3D-Graphics for Molecular Sciences, Swiss National Supercomputing Center. <https://ugovaretto.github.io/molekel/>.

5. Conclusions and Futurework

Overall, the work presented within this thesis constitutes the first investigations of radical ligands as electron spin qubits. The relaxation times in these complexes involving dithiolene ligands, in which the radical character is distributed across multiple atoms, are unsurprisingly influenced by the electronic structure of the complex to large degrees. The excellent coherence times afforded by these radical ligands in the presence of significant amounts of decohering nuclear spins completely mitigates the need to eliminate nuclear spins for operable qubits, and the modular nature of the coordination complexes investigated facilitate the possibility of facile multiqubit architectures.

Chapter 2 provides the foray into radical ligand qubits as homoleptic and heteroleptic dithiolene species. The heteroleptic phosphine species in this chapter is the key to multiqubit systems. The monometallic species possess the longest phase memory time in spite of the coordinating ^{31}P atoms and greater number of protons, it illustrates the potential of high customisability, with the extensive number of phosphines available it is predicted many other two or more qubit systems will be produced here. The first step would be to introduce some form of *g*-engineering to the system possibly by aligning the radicals orthogonal to each other with, say, a tetrahedral Cu^{I} d^{10} between two bridging phosphines. Another option would be the replacement of one dithiolene in the bimetallic **2.4** with an alternate dithiolene ligand. Both options would allow for disambiguation of one spin in relation to the other and result in single qubit addressability in a two-qubit system to facilitate algorithms.

Chapter 3 introduces the quadrupolar effect to electron spin qubits at a magnitude that has a measurable effect. Thankfully, the excellent coherence times inherent to this complex allow for long values to be recorded at varying quadrupolar field positions, even at a reduction in T_1 by 12% at the lowest contribution from the EFG. The coupling to an electric field via a quadrupole may be the key to producing electrically accessible spin qubits. Investigations of this are underway. The ability for the complex **3.1b** to form a semiconducting molecular alloy also provides an alternative means of electrical addressability via charge transport.

Chapter 4 expands the synthetic versatility of bis(dithiooxalate) systems introducing lanthanides to the complexes and allowing for one-electron reduction of the dto ligand itself. With a magnetic lanthanide, these tripartite spin systems can be used to perform algorithms after full magnetic characterisation. The high customisability of these systems is highlighted as most lanthanide ions are compatible with this system and the radical *g*-value can be attenuated by central metal identity. Coherence time measurements are the next logical step.

A. Appendix

A.1. Calculations

Table A.1.1. Geometry Optimized Coordinates for $[\text{Ni}(\text{adt})_2]^{1-}$

Ni	-0.00029825743218	-0.00003020622874	0.00020983146906
S	-1.98847849560950	-0.74664757447997	0.36008686322961
S	0.51124280411028	-1.82106437117618	-1.02937928165127
S	1.98923951503879	0.74467840489050	-0.35575411423935
S	-0.51340754331312	1.82325988482596	1.02501550081562
C	-2.04601520617188	-2.34779122132835	-0.34633465179148
C	-0.92490089574182	-2.82484885471497	-0.99768717572959
C	2.04627226194205	2.34671983488618	0.34864986208579
C	0.92357453427453	2.82597981887388	0.99558564419946
O	-6.92363300131926	-5.10915968964770	0.59025082485497
O	-0.43321255190888	-7.66722924425314	-3.93575926865271
C	-0.83839052417237	-4.097111101989070	-1.74921540519866
C	0.29869355519659	-4.92918449928982	-1.64960158463574
H	1.10856220736251	-4.64451711410756	-0.97581599862651
C	0.40539942895270	-6.10653688351866	-2.38231478488170
H	1.28697895446555	-6.74348030816725	-2.28989796718715
C	-0.62787133996282	-6.49318791654795	-3.25287257506160
C	-1.76418272594054	-5.67928716547397	-3.37660062809297
H	-2.57531623602556	-5.94455196739351	-4.05330067631088
C	-1.85571347561224	-4.49918666885172	-2.63306240396115
H	-2.73700699215406	-3.86889071663632	-2.75597314155047
C	-1.46837568308878	-8.09100491165358	-4.83418691919698
H	-1.11644189655521	-9.03316565383924	-5.26759306456755
H	-1.62759494229940	-7.35255766544797	-5.63552772797427
H	-2.41517096912247	-8.26264511944455	-4.29894728025893
C	-3.30090004190568	-3.10041981700179	-0.11951973195689
C	-3.28752753498875	-4.40892131514793	0.39382992942027
H	-2.33195934996031	-4.88572221898825	0.61560233722279
C	-4.46797558610501	-5.11425779329955	0.64453434196566
H	-4.41048012303446	-6.12233159890461	1.05141647996189
C	-4.55960351759103	-2.50934362637434	-0.36230745093740
H	-4.60272414432376	-1.49343543934022	-0.75790706359404
C	-5.74336983086918	-3.19859295144248	-0.12160615928833
H	-6.71091511131378	-2.73562285146561	-0.32310498181494
C	-5.70662736020664	-4.50960206009609	0.38289655675979
C	-6.92354515019206	-6.44988120558585	1.10113337130586
H	-7.97766406947984	-6.73586529672863	1.18307870667318
H	-6.45038923484756	-6.49748209778251	2.09420454165648
H	-6.40689716279201	-7.13816563573162	0.41364415714622
O	6.93144364180946	5.09953060069762	-0.57368861574645
O	0.42544900434970	7.67635002848869	3.91937081241461
C	0.83550621337586	4.10011564839349	1.74375269045409
C	-0.30073762225302	4.93262464381801	1.63823601056665
H	-1.10857466348135	4.64663117968030	0.96257743272742
C	-0.40909445151912	6.11201182362736	2.36741061757902
H	-1.28991384013622	6.74931383042922	2.27034750136841
C	0.62157057048958	6.50033492862429	3.24030957010255
C	1.75694838522016	5.68604621384028	3.36994028715894
H	2.56603345357797	5.95258939281743	4.04858904734039
C	1.85021036311168	4.50393211713167	2.62981116850631
H	2.73075322356713	3.87345937649390	2.75715838533279

C	1.45811600132839	8.10209688249572	4.81973200670031
H	1.10514703243550	9.04538551812633	5.24981591595426
H	1.61491523096581	7.36561012062384	5.62334899198054
H	2.40645595789532	8.27219320968272	4.28674052809228
C	3.30300947445694	3.09730365295773	0.12519677923819
C	3.29355950603033	4.40456811574003	-0.39133098038970
H	2.33959544002137	4.88210855367427	-0.61836457274981
C	4.47603639275741	5.10772890382177	-0.63866502214707
H	4.42160285530267	6.11489048366171	-1.04822121662966
C	4.55985892995304	2.50515358006201	0.37486158896188
H	4.59990154100647	1.49015966254573	0.77310953765511
C	5.74556800080864	3.19227332652975	0.13765307011594
H	6.71161497937321	2.72856015996095	0.34454532341176
C	5.71273716409094	4.50209020193072	-0.37019642394273
C	6.93538338420741	6.43924638253918	-1.08717597681197
H	7.99025245903876	6.72344658232895	-1.16563310418435
H	6.46611169062949	6.48571960272020	-2.08213759598867
H	6.41716537428365	7.12961001306090	-0.40296266867715

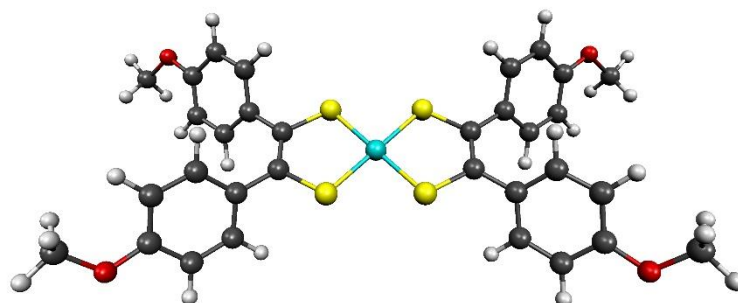


Figure A.1.1. Geometry-optimized structure of $[\text{Ni}(\text{adt})_2]^{1-}$

Table A.1.2. Geometry Optimized Coordinates for $[\text{Pd}(\text{adt})_2]^{1-}$

Pd	0.56397426376863	4.71956681712097	0.68585414780852
S	-0.26236121898536	5.25719061627819	-1.38896401988043
S	-0.59930765700378	2.74482955401775	0.51627614993446
S	1.43199959790231	4.16200704407379	2.74065476391617
S	1.69175945268564	6.71279239344739	0.87316976311115
O	-3.16649114528073	4.22073327000115	-7.21548676460580
O	-5.00757357260908	-1.50211875466403	-1.93979932443916
O	5.28570742896870	4.58524753659836	8.04082310529316
O	5.12101421011305	11.48447420980631	3.87109674498637
C	-1.24521618641594	3.89259184371556	-1.87509215898249
C	-1.41509717634259	2.80857131487739	-1.03166526031725
C	2.42766714505970	5.52083310281567	3.21663610983731
C	2.51844937900947	6.64542672975510	2.41489784376474
C	-1.78864792256153	3.98572441223845	-3.25153441234396
C	-2.41770909240419	5.15732298832323	-3.70711255649432
H	-2.54515558542361	5.99439753214345	-3.01854474663473
C	-2.89648581552667	5.27818096930205	-5.01543100070587
H	-3.38762505040321	6.20165945688282	-5.31870111487931
C	-2.74148846959673	4.21060222250136	-5.91109479712740
C	-2.10566818502221	3.03334183276031	-5.47924878450842
H	-1.97411086928607	2.21286028421617	-6.18704882340848
C	-1.64095843526342	2.92712003404252	-4.17380292785284
H	-1.13816510092927	2.01159168610642	-3.86086894841490

C	-3.81083880243785	5.41062254147741	-7.69347570722102
H	-4.73181177699192	5.61978980567601	-7.12754984534021
H	-4.06204808993676	5.21098549624683	-8.74056832427153
H	-3.13670497276618	6.27959660030203	-7.63373905615349
C	-2.32244639220608	1.66672990560492	-1.29823537248086
C	-1.91272166345567	0.34251565375516	-1.06592760347350
H	-0.89417740694156	0.15446066132207	-0.72281674974127
C	-2.77058870660550	-0.74265642290615	-1.26999287670478
H	-2.40545999768915	-1.75219178816771	-1.08479409814825
C	-4.08244727666739	-0.51589796252698	-1.70987858743789
C	-4.51649324112618	0.80159068125544	-1.93710245869733
H	-5.54330957792815	0.97091648791850	-2.26544487262001
C	-3.64988982463567	1.86854349442353	-1.73453008606521
H	-4.00885025142838	2.88437759768565	-1.90371442208339
C	-4.60609533692190	-2.85770062082794	-1.69632151395135
H	-3.76285730812938	-3.14625377314331	-2.34297068027291
H	-5.48005677843085	-3.47307715138412	-1.93645849448932
H	-4.32808610466275	-3.00695597553343	-0.64127916967438
C	3.19021663145145	5.31639333711941	4.47151168223237
C	4.57091375781055	5.57018335908862	4.53903125156308
H	5.08847284307977	5.94593988294605	3.65560705205716
C	5.30657092543872	5.34168814773633	5.70504260019778
H	6.37642323453539	5.54658912580943	5.70782054990929
C	4.66188717440629	4.84379133904204	6.84699646651242
C	3.28340155616119	4.57533602139054	6.79934556456501
H	2.78815590597931	4.18834673114404	7.69172312605666
C	2.56670290473945	4.80415027953829	5.62993370745949
H	1.49667392657008	4.59121530607550	5.60811123495672
C	6.69610708441536	4.83512514150471	8.11898281106456
H	7.25156212816341	4.20939976581765	7.40337782491825
H	6.98765030348313	4.57052481794485	9.14106320393205
H	6.92400422921272	5.89680204066451	7.93355270819818
C	3.23388302060561	7.89005479371161	2.78506939872861
C	4.07039540271954	8.54788835619495	1.86719451036299
H	4.22449326917974	8.10968860432070	0.87963192286925
C	4.72086742316653	9.74380338187808	2.18619856465586
H	5.36751355088193	10.21283890801144	1.44566058953692
C	4.53466163050207	10.31758538952500	3.45177639943522
C	3.69090799430504	9.68326719687979	4.38038387738369
H	3.53744053537511	10.14501518325580	5.35734055805601
C	3.05534067290035	8.49320602665641	4.04900229051221
H	2.39396998323675	8.02247644882819	4.77740963310673
C	5.97448553212480	12.16822119482955	2.94255925979492
H	6.83174011021481	11.54056488779799	2.65244160214877
H	6.33361559151454	13.05830341903750	3.46983485109481
H	5.41981119233460	12.47238258571278	2.04122768946112

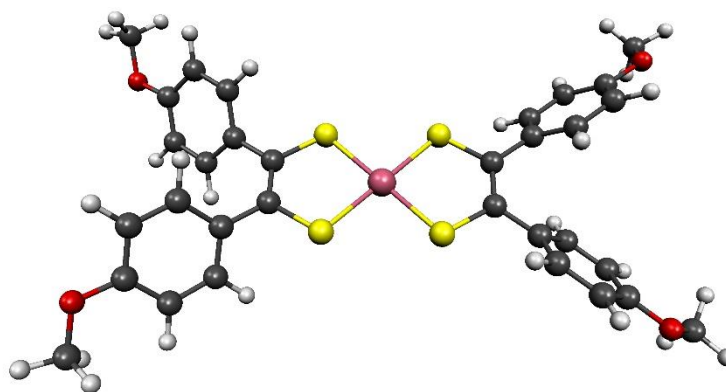


Figure A.1.2. Geometry-optimized structure of $[\text{Pd}(\text{adt})_2]^{1-}$

Table A.1.3. Geometry Optimized Coordinates for $[\text{Pt}(\text{adt})_2]^{1-}$

Pt	1.94107342218879	6.90043087076864	9.10656513302129
S	2.82568265320148	4.80133893623246	8.82630148870193
S	2.81685660275389	7.42350416933659	7.05337704055156
S	1.02480492645378	6.37110665789657	11.14266089679651
S	1.08416440047413	9.00931681600538	9.39240990131470
O	6.47494444447489	0.07105060580874	6.01082392918297
O	5.70606376617657	6.54543072265202	1.23548002007565
O	-2.67403511834867	7.05551982443765	16.52605098021474
O	-1.79926746704550	14.01818105530960	12.58395794877750
C	3.62373728649749	4.82661319660471	7.26620006327675
C	3.60810413239998	5.96766459566922	6.48769024930757
C	0.21516515309872	7.82388296123279	11.69075346081720
C	0.25545324340230	8.97996473388477	10.93508035771527
C	4.33943468544226	3.57510635318098	6.92005821156290
C	3.72428091270594	2.32068576911309	7.07091837254540
H	2.69045150998545	2.27343350001577	7.41666814447516
C	4.39587850220260	1.12863459445133	6.77948937622721
H	3.87494978260033	0.18019985756240	6.90374844249495
C	5.72271983569628	1.17376400916231	6.32855320396768
C	6.36145906973708	2.41770607691692	6.18341024624017
H	7.39910979902258	2.44321118692951	5.84700385403490
C	5.67945685328290	3.59286691876105	6.47563904678652
H	6.19627077340660	4.54754247026104	6.37112627580436
C	5.86134091220442	-1.21674055818430	6.16438139423107
H	5.56664644327510	-1.39541560052213	7.21018578047761
H	6.62386822759834	-1.94530682241341	5.86814635762643
H	4.98026628594430	-1.31874232712259	5.51160959147020
C	4.16770750114997	6.07307671955879	5.11810212715301
C	3.86033037845427	5.12940775911872	4.12359913152935
H	3.21049663446586	4.28769827563575	4.36687907835519
C	4.35217138225531	5.24570944938961	2.81995677063568
H	4.07884619331898	4.49502361540215	2.07954453977126
C	5.17396461715522	6.33125849909765	2.48149514370561
C	5.48928591153200	7.28952722087256	3.45970909750569
H	6.13070051721520	8.13058986435014	3.19014824513240
C	4.98934188769920	7.16063157304953	4.75107494826482
H	5.24517698011956	7.91155845428769	5.50067325235108
C	5.41404052342720	5.58058529053647	0.21470500761645
H	5.79289238712346	4.58376139414734	0.48881993373191

H	5.92925701432830	5.93542352790331	-0.68419944688486
H	4.33174149483635	5.52159690456909	0.01991565227075
C	-0.55009657311144	7.66263865832062	12.95052662895292
C	0.02925743312613	7.05759117519309	14.08635260139120
H	1.07132804800144	6.73675433946556	14.04680135057624
C	-0.69620590092178	6.87152945183754	15.25840376660480
H	-0.23497402045276	6.41065990339663	16.13376691226186
C	-2.03838934361436	7.28040187211286	15.33101212216926
C	-2.63967500086721	7.87281444956500	14.21090090239651
H	-3.68254218607718	8.18572155793851	14.23168167424686
C	-1.89611350229983	8.05558005220819	13.04193760065406
H	-2.38012685528780	8.50655159612676	12.17479094125965
C	-4.04657031581655	7.45859881186071	16.63148271544202
H	-4.15705751361966	8.54322827387583	16.47249551865487
H	-4.35262082922910	7.20397119449259	17.65193365799940
H	-4.67781364795413	6.91511334897039	15.91151224133194
C	-0.31275175690434	10.28454641680340	11.35222186800332
C	-0.05091030915332	10.82557203103185	12.62923190396668
H	0.56905690133397	10.26566153527105	13.33028023630421
C	-0.55419771980710	12.06381335357227	13.00913082007726
H	-0.33823751099025	12.47451730065007	13.99683015745673
C	-1.34266040522322	12.81155060913944	12.11717881749756
C	-1.60734793439487	12.30108058549650	10.83868074852149
H	-2.21348952735103	12.85723504899661	10.12469091784953
C	-1.09092002518680	11.05424823233192	10.47117543695121
H	-1.30860874937826	10.66584719486536	9.47490109226404
C	-2.60131461116717	14.81138610857647	11.69736747441540
H	-2.03623030417571	15.09636254354079	10.79606609802226
H	-2.86696449188001	15.71091510511651	12.26277970123457
H	-3.51799080951058	14.27683412737361	11.40288784465753

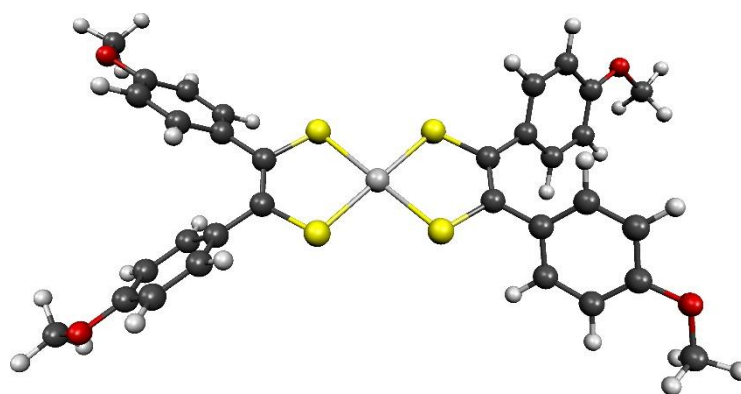


Figure A.1.3. Geometry-optimized structure of $[\text{Pt}(\text{adt})_2]^{1-}$

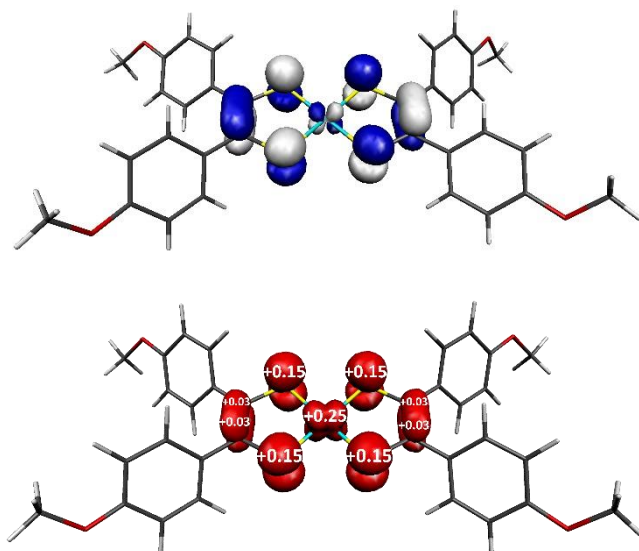


Figure A.1.4. Depiction of the singly-occupied molecular orbital (left) and Mulliken spin population analysis (right) of $[\text{Ni}(\text{adt})_2]^{1-}$

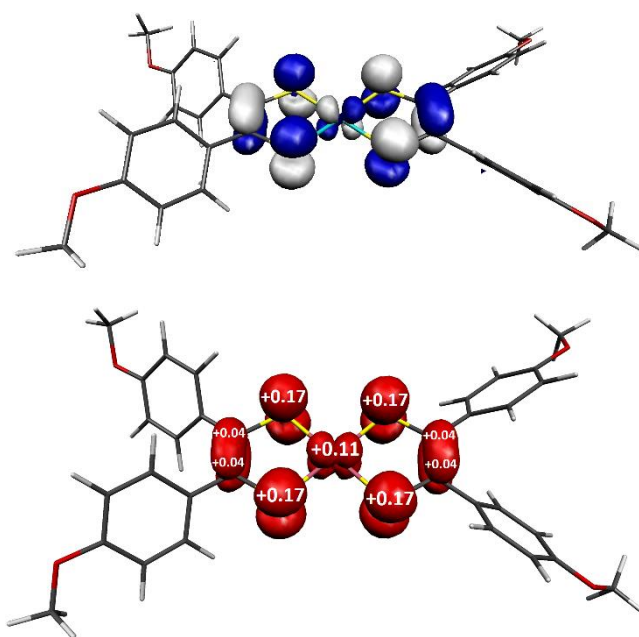


Figure A.1.5. Depiction of the singly-occupied molecular orbital (left) and Mulliken spin population analysis (right) of $[\text{Pd}(\text{adt})_2]^{1-}$

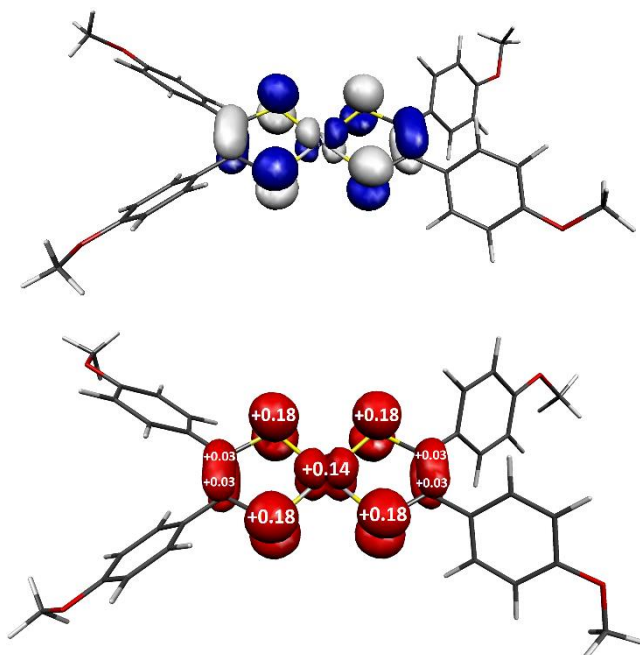


Figure A.1.6. Depiction of the singly-occupied molecular orbital (left) and Mulliken spin population analysis (right) of $[\text{Pt}(\text{adt})_2]^{1-}$

Table A.1.4. Geometry Optimized Coordinates for $[\mathbf{2.4}]^{2+}$

Ni	1.37771486412472	11.35356661673846	11.34033163562849
S	2.49908942284741	9.87330129838096	12.49248677317713
S	2.49103600858026	12.96182373311985	12.31412989074694
P	-0.11741336483122	9.89164994855657	10.72839592954049
P	0.61602296298384	12.73184605999638	9.81790485516629
O	6.02263026711480	7.67551194430161	17.59138699581222
O	7.43193095851857	15.71689816666264	15.64951272002040
C	3.54059161073799	10.78066747566682	13.56278915554207
C	3.61912319229321	12.19222638250413	13.39449555283057
C	-0.89461161107968	10.47679470582520	9.14996995936740
C	-0.60886345885707	11.80742581534385	8.76208040926016
C	-1.73312335704160	9.67123519771707	8.35394528679556
H	-1.94488344043324	8.63529292557763	8.66015073602809
C	4.22442104933534	10.01841263234510	14.61369151126291
C	4.66036519166104	8.68007840219840	14.38258443734232
H	4.53807685088905	8.24103139838325	13.38075692328322
C	5.26254977764816	7.93152758663224	15.38675010883872
H	5.62277303815920	6.90943372738403	15.20191232042742
C	5.43424454809973	8.48041958993471	16.68633064876931
C	4.98634970023109	9.79938928259069	16.94565485382587
H	5.08062340373456	10.24120344728382	17.94703904353819
C	4.40052138700332	10.54936776008768	15.92242409551948
H	4.03321401779268	11.55940013325577	16.15066896882273
C	6.23684655164184	8.14490022776741	18.92321566624585
H	6.89925256037528	9.03701019014388	18.93617795648400
H	6.72884967845218	7.31627788854491	19.46355264255831
H	5.27653057092795	8.39022097557742	19.42509215105997
C	4.61971880585250	13.06493876914024	14.02276344809701
C	4.28787300119512	14.39695815313973	14.40884718313765

H	3.24989165865201	14.74390365080423	14.29491548717732
C	5.24031953131755	15.25001104065570	14.95460512468525
H	4.97961702409901	16.26732879472758	15.27983533990399
C	6.58376644614823	14.81644017571465	15.11627452586835
C	6.94039959165216	13.50407972261582	14.71806529233485
H	7.97623794602992	13.14926474227390	14.80687662371880
C	5.96939653114613	12.64835138120448	14.18950546190714
H	6.27031196419790	11.64368846923957	13.86117727143920
C	8.79962406996999	15.36337537926257	15.85764582818639
H	8.89372358563368	14.50266594562724	16.55438520583489
H	9.27989592685996	16.25116039547123	16.30667880428570
H	9.30545770859604	15.11964869003447	14.89892254195384
C	-1.48130392230457	9.85745941478535	11.96506697983402
C	-1.14528247713301	9.50484418974959	13.29423178785909
H	-0.10420435654492	9.24942476654643	13.55021208713066
C	-2.13634685600468	9.48113512421274	14.28615900225035
H	-1.86788309753102	9.19692236875163	15.31492712466105
C	-3.46270043414588	9.82708130703500	13.97125918817501
H	-4.23599782826024	9.81615300765369	14.75456244824371
C	-3.79739925781590	10.19082982040140	12.65677138454830
H	-4.83350099836933	10.46410334785838	12.40516503480749
C	-2.81369915309482	10.20611032893815	11.65299371821671
H	-3.09457835937305	10.48568137323563	10.62698017622038
C	0.33806346659623	8.14167582745530	10.41050564974289
C	-0.47086027636182	7.06220096870931	10.82850959694008
H	-1.40180879357003	7.25067062670329	11.38493723239843
C	-0.07873025576244	5.74293822513672	10.54449776888796
H	-0.70918229675114	4.90416707011984	10.87624182541614
C	1.11729377726899	5.49487163054277	9.84965136745224
H	1.42413878070874	4.45989656691899	9.63476533958125
C	1.92894526383852	6.56760980939157	9.43938827854890
H	2.87264793341073	6.37355272055492	8.90742518943205
C	1.54656955038965	7.88748470712993	9.72214028375262
H	2.19434960916870	8.72532376694165	9.41967492790054
C	-0.24733616569438	14.25158114173660	10.37019334313583
C	-1.63872908806306	14.23473008684955	10.61785673637740
H	-2.23374069978748	13.33671958835957	10.39170577658417
C	-2.27181664009100	15.36581521724228	11.15654701288024
H	-3.35630599441894	15.34605456411878	11.34310995860531
C	-1.52436356217408	16.51694191773995	11.46034682560801
H	-2.02256459292942	17.40245798424193	11.88380203389868
C	-0.13882311043684	16.53442429265568	11.22653605603676
H	0.45064257502120	17.43252284286884	11.46644240172463
C	0.50323877569043	15.40726216534394	10.68897959285203
H	1.58966174302076	15.43047704082238	10.51535206837862
C	1.92405926441917	13.27479068520719	8.63999499937599
C	3.13861198360928	12.55457084738350	8.61682265132091
H	3.29359002876580	11.72451830496410	9.32496396561009
C	4.15492111356159	12.91532114494602	7.71723197104664
H	5.10238238171691	12.35521236384016	7.71062524569121
C	3.97019923997965	14.00062614427015	6.84372768796641
H	4.77318590481344	14.29113970754125	6.14890618694102
C	2.76671573391263	14.72816981957528	6.87055632622164
H	2.62742054041164	15.58969429695270	6.19972543863471
C	1.74433231704599	14.37085573703568	7.76508965527817
H	0.81806954679584	14.96455624766906	7.79734843831115
P	-2.79658789053248	12.11160173312833	5.21236548316313
P	-3.53057348934827	9.27144809206997	6.12331511016625
C	-2.02002399323144	11.52655299767055	6.79114592722257

C	-2.30563702569360	10.19586113984954	7.17892942052372
C	-1.18142246766120	12.33207496450988	7.58712174647121
H	-0.96983036538559	13.36810085532433	7.28107808522354
C	-1.43142003811122	12.14751917031445	3.97712310110148
C	-1.76635167709584	12.50096438103104	2.64789634414959
H	-2.80733554365836	12.75590184109066	2.39105851539135
C	-0.77435041894170	12.52603346119518	1.65694317850424
H	-1.04199278360692	12.81086246557245	0.62812923644724
C	0.55197060963987	12.18093993719288	1.97292768034277
H	1.32603896450276	12.19302773987997	1.19040266313364
C	0.88567420503061	11.81671881440742	3.28752984501650
H	1.92174324902298	11.54413714465164	3.54000661607700
C	-0.09903436885651	11.79984931949228	4.29029953098964
H	0.18116014071750	11.52022569009924	5.31648272439615
C	-3.25390449747648	13.86108860975746	5.53055759259230
C	-2.44577282841405	14.94147579531371	5.11340336673307
H	-1.51428295333734	14.75411786268107	4.55752570653154
C	-2.83928055789918	16.26026121328463	5.39773094812218
H	-2.20942115179651	17.09974549719343	5.06665755945536
C	-4.03579542267508	16.50693793828466	6.09221962476093
H	-4.34367664279693	17.54154269675468	6.30741907488297
C	-4.84655866504686	15.43327728293793	6.50182106528196
H	-5.79061209729733	15.62622874161537	7.03356085930179
C	-4.46287026400107	14.11387866824074	6.21862344386202
H	-5.10989121904371	13.27531555471150	6.52070502509754
C	-2.66762360670986	7.75155279685045	5.57081936147586
C	-1.27627308678950	7.76829262973644	5.32298905767490
H	-0.68098644950528	8.66597531437849	5.54975966324181
C	-0.64342827148751	6.63734109791491	4.78372719966936
H	0.44108697807354	6.65692514876007	4.59731268796426
C	-1.39126677495181	5.48682428863859	4.47856338375488
H	-0.89329070990934	4.60146733335838	4.05451497191039
C	-2.77695059257360	5.46984794678489	4.71153946706290
H	-3.36671918685797	4.57222543983523	4.47059811923925
C	-3.41865435885212	6.59664285337701	5.25030978185987
H	-4.50534297531177	6.57417561525838	5.42232163677293
C	-4.83876802089361	8.72911327262837	7.30120760518427
C	-6.05279057098572	9.45020881882914	7.32483316255496
H	-6.20724838951481	10.28067274236390	6.61707763065510
C	-7.06921587059855	9.08983260608500	8.22445515147908
H	-8.01628930143483	9.65059287684205	8.23144070058288
C	-6.88512948446875	8.00405459688929	9.09750086825249
H	-7.68823363278771	7.71381249913689	9.79230265295004
C	-5.68218392490894	7.27562667020241	9.07018707202398
H	-5.54345933606496	6.41369037645395	9.74061433543472
C	-4.65972231293842	7.63250264835910	8.17558204054400
H	-3.73391458407683	7.03812554798596	8.14285726521491
Ni	-4.29112273461371	10.64940443669872	4.59920402575785
S	-5.41032744568681	12.12929043290422	3.44467383078156
S	-5.40550982686471	9.04101244925921	3.62658314094477
O	-8.92721436237433	14.32493975883294	-1.65968381778846
O	-10.34434367718014	6.28618012662390	0.28815046474011
C	-6.45187016600885	11.22177742292477	2.37457304754212
C	-6.53186888936908	9.81047483785105	2.54433539400287
C	-7.13413672085671	11.98355378515568	1.32230356212516
C	-7.56954260895071	13.32234083702771	1.55172063054903
H	-7.44823173637429	13.76223569625354	2.55330559477860
C	-8.17010996519501	14.07034675624808	0.54616614562830
H	-8.52998103850610	15.09280895239428	0.72966794013911

C	-8.34051134365603	13.52044302857123	-0.75315035627293
C	-7.89304445690561	12.20100533130575	-1.01078652988361
H	-7.98637686777948	11.75835895924877	-2.01189585507440
C	-7.30894491325880	11.45156742412467	0.01382426487882
H	-6.94182281528259	10.44115952547807	-0.21309081390212
C	-9.14004584877026	13.85443214095380	-2.99133383452775
H	-9.80332901736275	12.96297196003652	-3.00429315315962
H	-9.63042964871647	14.68299847306621	-3.53322428228210
H	-8.17928693199527	13.60752127393404	-3.49157358833582
C	-7.53240990529286	8.93789600243353	1.91580573076269
C	-7.20083070950737	7.60546459758163	1.53088658615354
H	-6.16311295338671	7.25813988026843	1.64599075733858
C	-8.15316588677162	6.75247873236716	0.98484162938353
H	-7.89264458141503	5.73482284650955	0.66052062594309
C	-9.49623782686447	7.18659603531151	0.82155479489362
C	-9.85258261272682	8.49947099859012	1.21834097689758
H	-10.88815210923341	8.85471929604296	1.12825575680441
C	-8.88170611039890	9.35504746650058	1.74736837707254
H	-9.18238645154511	10.36019145002756	2.07443574510147
C	-11.71161495589584	6.64030953379625	0.07828858886184
H	-11.80448336406080	7.50038167192076	-0.61940746059619
H	-12.19196507516414	5.75236696451678	-0.37035290712458
H	-12.21826227127439	6.88529025374714	1.03625956651794

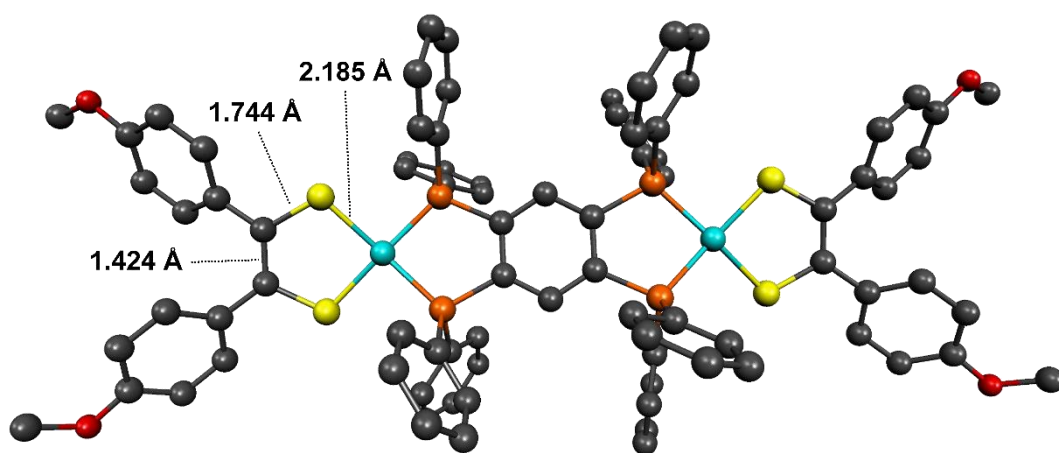


Figure A.1.7. Geometry-optimized structure of $[2.4]^{2+}$

Table A.1.5. Geometry Optimized Coordinates for $[2.5]^{1+}$

Ni	10.84973298332259	9.96050024642930	3.55496329378698
S	9.46390668495712	11.18922634036232	2.39294438712532
S	9.95260410252496	10.68737419806108	5.41184585155346
P	12.15973868315295	9.64317853782454	1.83882159203120
P	11.85152257158329	8.31028861201714	4.58016854003435
O	5.26868780857288	16.21659791051481	1.46460556403688
O	5.24151303200552	13.28903337556705	9.19070186150623

C	8.49478270651472	12.05110145679508	3.55548955508272
C	8.64576786021872	11.73392636834269	4.93574671810861
C	14.98543102040669	6.58804661100078	1.59338991774436
H	15.70094281510736	6.18259580120090	0.86177720232501
C	14.16491450902189	7.66995399702506	1.23881269671092
H	14.23841507585312	8.11150131058598	0.23334218896559
C	13.24765944247506	8.18943453069427	2.17577897042096
C	13.14024981269727	7.60529400527806	3.45772626707370
C	13.97784092216792	6.52767036926663	3.81282430668941
H	13.90754201281827	6.07567674225462	4.81408007552111
C	14.89719473995281	6.02300415311769	2.87991587208301
H	15.54555996210579	5.17678528621959	3.15424923168274
C	7.61453849042544	13.10165937200650	3.02178147679050
C	6.97968719410044	12.94799422692866	1.76129041478691
H	7.10405071812859	12.00221108951223	1.21217257750486
C	6.18224543402253	13.95567212749084	1.20913790768597
H	5.69475191794009	13.78279510989221	0.24053319371294
C	6.01056498516903	15.17717270932683	1.90536275669322
C	6.65349271191164	15.35682063797596	3.15679254081528
H	6.52965291247972	16.31983388778397	3.67336446651070
C	7.43112043623335	14.34107839646698	3.70340570017651
H	7.93919217425583	14.51450383624215	4.66212225497470
C	4.60210965685541	16.11825923928449	0.20813988871847
H	5.32283723106917	15.97552673815025	-0.62565048958005
H	4.07036356080537	17.07649759886188	0.06736439668191
H	3.86376181448173	15.28708215972178	0.20215844513262
C	7.74337790523669	12.18143212861005	6.00761131777150
C	6.33947082662617	12.26438404204253	5.80700235511447
H	5.91742558184720	12.00833774956000	4.82498596942889
C	5.46967825442504	12.62104627741491	6.84285065908428
H	4.38907549383055	12.65196056865311	6.64586732389300
C	5.98673112190263	12.92235643706148	8.12601618899170
C	7.38666031021126	12.84023739259447	8.34567166236644
H	7.77211947209097	13.08542586551632	9.34593116118329
C	8.23994797598267	12.46667228714563	7.31263263012212
H	9.32331398172980	12.40955857325563	7.49764033778698
C	3.82757789459162	13.40150005752977	9.04938055340582
H	3.55397382879262	14.16722421091017	8.29148892932618
H	3.44384322187430	13.71391408363131	10.03722470028403
H	3.36717222992410	12.42895270416653	8.77011525425572
C	11.44354327124092	9.34235016983502	0.17535335525202
C	10.23286559058449	8.61696574440803	0.10489359971203
H	9.72358075912122	8.31061677510946	1.03219772304284
C	9.67461901889433	8.30217691628395	-1.14356796122323
H	8.72948446821082	7.74071838641092	-1.19354621192992
C	10.31507187061994	8.71366658558590	-2.32539531283001
H	9.87444391126320	8.46901065855223	-3.30375562953571
C	11.51429876366080	9.44383665569213	-2.25913976298811
H	12.01300787410015	9.77217654180454	-3.18355306583392
C	12.08077097710667	9.76151246356556	-1.01345951181211
H	13.01531143501078	10.34122368340900	-0.96846346904977
C	13.29789145860254	11.07953843883111	1.67496360152516
C	12.78629498197391	12.29890914561918	1.17005411034444
H	11.73698162249131	12.36580466244565	0.84319476831355
C	13.61439255315907	13.42839565473346	1.09133308954785
H	13.21151140413866	14.37034807024827	0.68914733050532
C	14.94983695751750	13.36081721292367	1.52820914855857
H	15.59547116637483	14.25020491910003	1.46581925469176
C	15.45665316049494	12.15738535191664	2.04603663150324

H	16.49966068380203	12.09939479082175	2.39223553943112
C	14.63627765595442	11.01876444779119	2.12262749825506
H	15.04547430881787	10.08108469281682	2.52676080799827
C	10.66128392928032	6.93964797521996	4.87495201894736
C	10.58224096129594	5.83395090839825	3.99890545657067
H	11.28022586023372	5.74106840339763	3.15286495750125
C	9.61348151528290	4.83780816013650	4.20759354606855
H	9.56481013164112	3.97516403430195	3.52517039431700
C	8.71506843439300	4.93871919848311	5.28277975662107
H	7.95974208391102	4.15443863560120	5.44606851003047
C	8.78086022459558	6.04516460909236	6.14885452936879
H	8.07636467248488	6.13204710252011	6.99042322638441
C	9.74181232662699	7.04688513314596	5.94506082412874
H	9.77327226855955	7.91871268268243	6.61663436774249
C	12.70575258241269	8.62487825216012	6.17494015952703
C	12.84508582732185	7.63446231687895	7.17278721834130
H	12.37974139881212	6.64507497785350	7.04474949343458
C	13.57042325626884	7.91798651877019	8.34188761811766
H	13.67666070232485	7.14455116357112	9.11831510215909
C	14.15438833725481	9.18387572727575	8.52321001058893
H	14.71807780247393	9.40188251588992	9.44316038328233
C	14.01062916246897	10.17377769071573	7.53546430529371
H	14.45865663028728	11.16861068127802	7.67934148569870
C	13.28532051836306	9.89953192312367	6.36534037330046
H	13.15517239816321	10.67927806130485	5.59798406299547

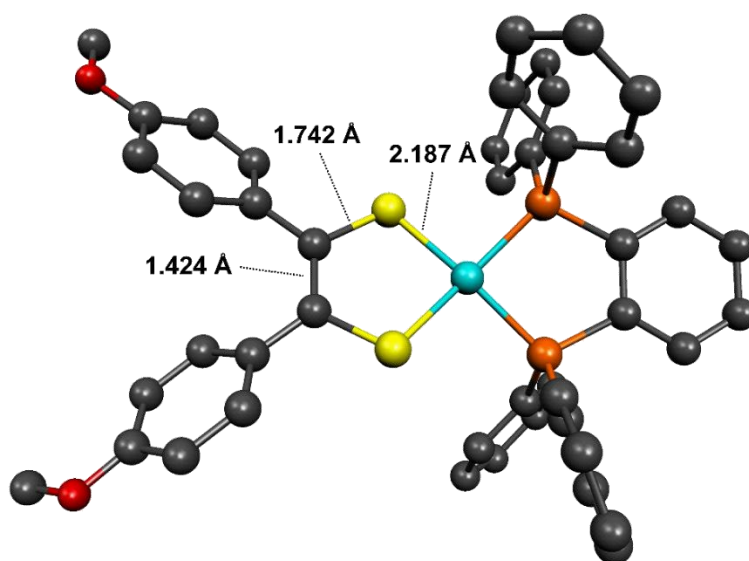


Figure A.1.8. Geometry-optimized structure of $[2.5]^{1+}$

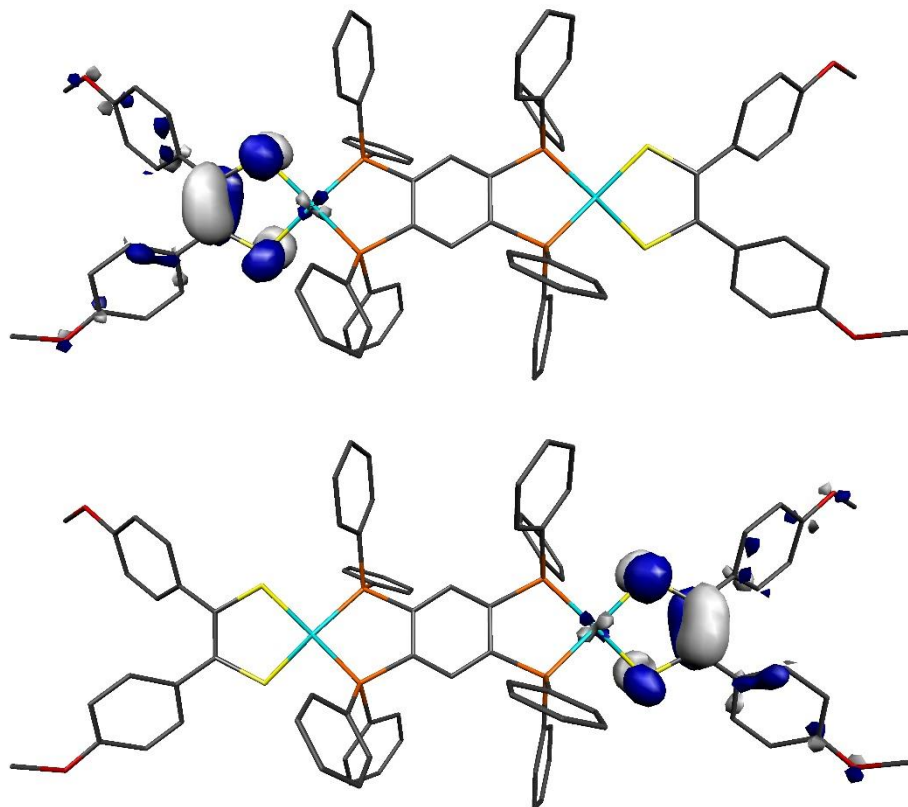


Figure A.1.9. Depiction of the magnetic orbitals of $[2.4]^{2+}$

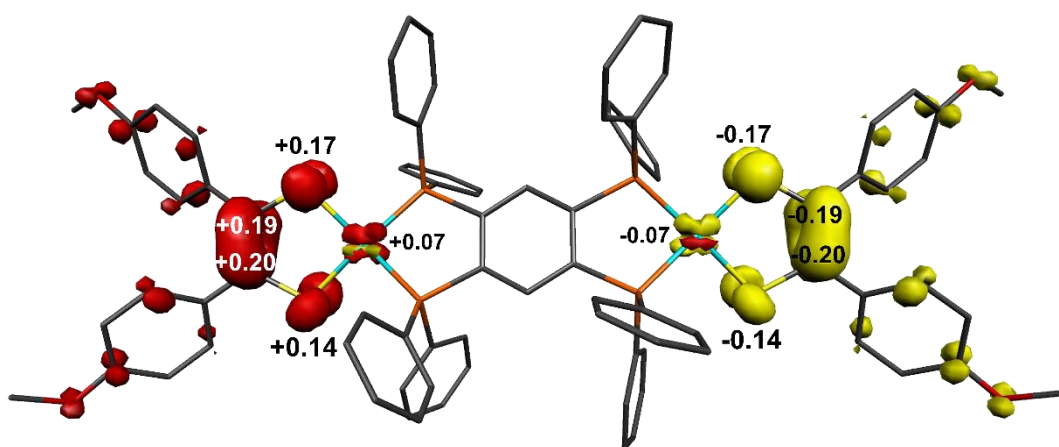


Figure A.1.10. Mulliken spin distribution for $[2.5]^{2+}$

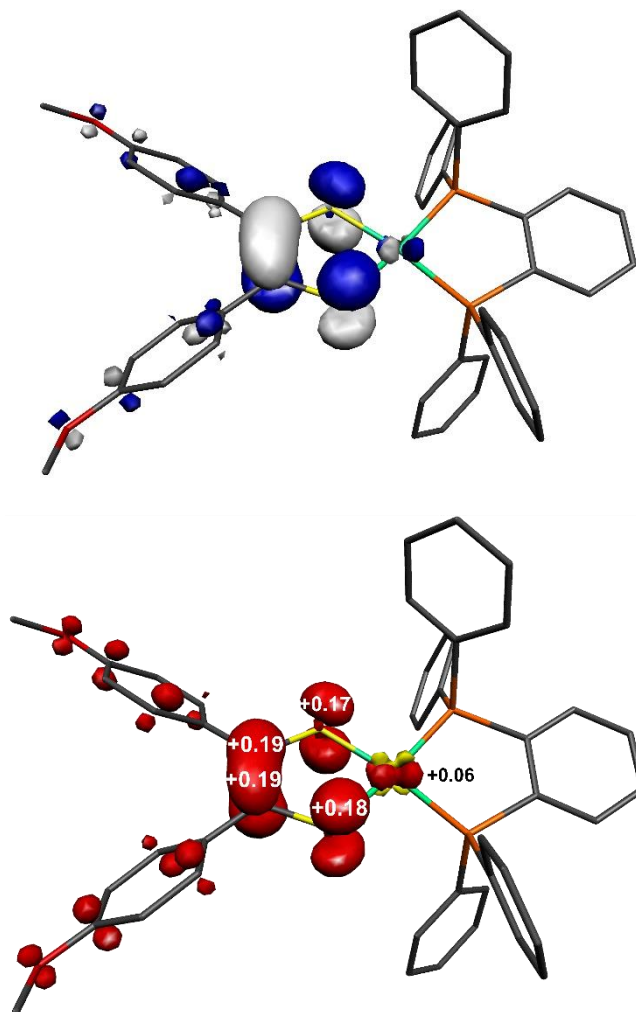


Figure A.1.11. Depiction of the singly-occupied molecular orbital (left) and Mulliken spin population analysis (right) of [2.5]¹⁺

Table A.1.6. Geometry Optimized Coordinates for [Au(adt)₂]¹⁻

Au	1.96230628143174	6.90668020231104	9.11925912678939
S	2.80961994197524	4.73467133369890	8.81916046856897
S	2.90093814119653	7.46076887384144	7.03884328659729
S	1.08214596161679	6.38094858380935	11.23398618806152
S	1.04875749162892	9.05634171196861	9.37573434240507
O	6.42480913000891	0.02281887460201	5.98251015789347
O	5.79003002034103	6.53863728777067	1.25882153409500
O	-2.62172778305325	7.10584481428868	16.57922469643197
O	-1.87699598127055	14.02299191530276	12.54388646385502
C	3.63672666356426	4.81370275507454	7.24876757809949
C	3.65329121302678	5.94868966374995	6.49415482026685
C	0.23623896946782	7.86322652817795	11.72287780216986
C	0.24654238848881	8.99225796755220	10.95857578368775
C	4.33596428089161	3.55229656269780	6.90370992942186
C	3.69207877990072	2.30767764833393	7.01415745203739
H	2.64830354750774	2.27405157186524	7.33062282504546
C	4.34770671201865	1.10771931820271	6.71785927326769
H	3.80555627274459	0.16767431809476	6.81115405855798
C	5.68620058742089	1.13453604963550	6.30137141259437
C	6.35338703598308	2.36769026207593	6.19747879940502
H	7.39967227560710	2.37820483636589	5.88780612478795
C	5.68861122478782	3.55042871482610	6.49891666634504
H	6.22584113445848	4.49698431213613	6.42929424083658
C	5.78140291766010	-1.25462867082015	6.09406517121407
H	5.45472780935763	-1.44717188079765	7.12782089513578
H	6.53670300733910	-1.99311491739990	5.80414171840377
H	4.91631982438012	-1.32576859294039	5.41606880729882
C	4.21967754651239	6.06096618120504	5.12746737091767
C	3.86445111896564	5.15807974168810	4.11140678713079
H	3.17150596502019	4.34663376442813	4.33849428227355
C	4.36802802028445	5.27487441829067	2.81223941216694
H	4.05995056280742	4.55521655450767	2.05502121456540
C	5.24499317278827	6.32443304305024	2.49932877511856
C	5.60631702964308	7.24420945500048	3.49850003700770
H	6.29055869952175	8.05694103594064	3.24767454409172
C	5.09742298974551	7.11283537269731	4.78627744637938
H	5.39058489513822	7.83283276659660	5.55245567166871
C	5.44331477502156	5.61864277824516	0.21410710034101
H	5.76915943646652	4.59586481189802	0.45945153229734
H	5.97376720232328	5.96944733741992	-0.67742016276189
H	4.35862981647810	5.62310324033071	0.02296064191807
C	-0.52212148477581	7.69817719748636	12.98671145424498
C	0.07997625539257	7.14572834743199	14.13787182188657
H	1.13391072251799	6.86478190009044	14.10703719935259
C	-0.63839698246360	6.96239517730261	15.31487173938349
H	-0.16071084732528	6.54162142460540	16.20151430551441
C	-1.99487250022010	7.32284407820898	15.37799096990246
C	-2.61835223249577	7.86203990090076	14.24307495985733
H	-3.67203701234048	8.13717550066132	14.25760051831534
C	-1.88320349719478	8.03766642240442	13.06770735440234
H	-2.38268295731277	8.44492018243625	12.18773516444392
C	-4.00950219740208	7.45630154977373	16.67382699229269
H	-4.16260797119323	8.531444460237974	16.48843184719814
H	-4.30694073032304	7.21468976692222	17.69995076953808
H	-4.61725237474185	6.87094441502766	15.96664423352042
C	-0.33634571093276	10.29647821910879	11.35658106535664
C	-0.06052378606827	10.86923635584578	12.61683071956341
H	0.58421507588808	10.33456988284355	13.31529613086873
C	-0.58503008001732	12.10244486596845	12.98378462647859
H	-0.36139967266469	12.53591548051826	13.96003362244383
C	-1.40340965189933	12.81734073386701	12.09163140317644
C	-1.67759125982366	12.27856756132221	10.82690520833624

H	-2.30510651990233	12.81050861650009	10.11287272526958
C	-1.14376524536884	11.03479968843097	10.47412062845994
H	-1.37166141112721	10.62391916282348	9.48915273044537
C	-2.70293739977026	14.78670416488542	11.65341200279077
H	-2.15429671926780	15.06299800183196	10.73938573777526
H	-2.97533705961950	15.69259907274076	12.20520548653527
H	-3.61486882874491	14.23247118195872	11.38131930625873

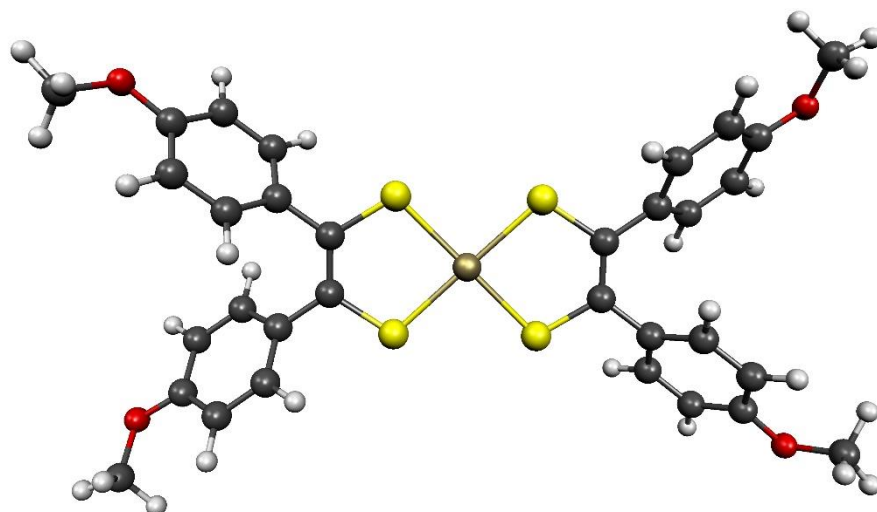


Figure A.1.12. Geometry optimized structure of $[\text{Au}(\text{adt})_2]^{1-}$

Table A.1.7 Geometry Optimized Coordinates for $[\text{Au}(\text{adt})_2]^0$

Au	1.93713316707976	6.89705687473567	9.10773435821241
S	2.81589645830381	4.75163650463472	8.81921906830205
S	2.84426962340421	7.44489118441999	7.02865963969128
S	1.02990299364328	6.35938120813379	11.19148597972429
S	1.04832718081823	9.03952522837965	9.37961471097849
O	6.45929395114957	0.08336239538893	6.02210786539775
O	5.71027076739101	6.54737722140889	1.26099143832105
O	-2.65364792904097	7.06098277518437	16.51927322891990
O	-1.79240720891744	14.00484930259426	12.56042805998715
C	3.61503191270193	4.82307395331260	7.26617779286605
C	3.60802527311951	5.96874393580900	6.49134163340266
C	0.21668603478611	7.82178311828736	11.69352713442752
C	0.24769043802603	8.97602629414517	10.93111809432008
C	4.32785834599251	3.57545568616660	6.91807901864157
C	3.70172872042996	2.32323263770724	7.05349594059224
H	2.65985199152067	2.27664871900785	7.37404579793798
C	4.37317796782217	1.13355502587265	6.76351450381532
H	3.84746237098576	0.18582056787614	6.86812132003677
C	5.70880777846157	1.17935569482398	6.33446470645058
C	6.35560729339900	2.42358584371369	6.20617706954454
H	7.39822029498107	2.44600676249628	5.88659339788315
C	5.67515161147602	3.59782884129569	6.49273423312832
H	6.19618607672273	4.55150696685434	6.40479579326153
C	5.84632052264239	-1.21037165335126	6.15619262232020
H	5.53939529758638	-1.39612408101240	7.19645005763733
H	6.61641823406041	-1.93186388162207	5.86424667353019
H	4.97628107783719	-1.30650080433091	5.48900474905229

C	4.17212563861515	6.07331227610051	5.12804093430384
C	3.85796089804534	5.12996846763068	4.13344200558988
H	3.20175204069470	4.29287582077393	4.37396259661765
C	4.34903890615525	5.24995718433414	2.83302018162909
H	4.07216687487890	4.50465873924672	2.08904270765945
C	5.17807489778980	6.33429225623683	2.49898615198702
C	5.50041260998661	7.28904830090245	3.48048681765824
H	6.14979741843123	8.12421588350603	3.21357883323387
C	4.99942595293849	7.16077237777564	4.76917220481634
H	5.26645998976676	7.90388843121483	5.52245427591749
C	5.41622809247865	5.59014098198828	0.22926272270116
H	5.79189960078928	4.59149725015355	0.49819142589355
H	5.93581632174786	5.95211620851901	-0.66362109938027
H	4.33445990073715	5.54000773549123	0.03305893561848
C	-0.54228852880584	7.66582303831192	12.95275934552787
C	0.04546785694105	7.06529762827379	14.08809833481386
H	1.09133690550971	6.75700465626866	14.05265461510544
C	-0.67771737217071	6.88099304577312	15.25916300553952
H	-0.21399575221015	6.42924683740823	16.13734719399746
C	-2.02366465273852	7.28318748439857	15.32933290264510
C	-2.63066736779843	7.87029188705891	14.20669650114792
H	-3.67520326027574	8.17631665459944	14.22840787271630
C	-1.89100970161520	8.05561297079404	13.03917273101530
H	-2.37779491723298	8.49882170144343	12.17002051903382
C	-4.03113249536627	7.45640310389457	16.63255835072885
H	-4.14596451450051	8.53998267490578	16.47463286445433
H	-4.32738437056486	7.19925187996097	17.65468503683947
H	-4.66009330957020	6.90717053906600	15.91608628974124
C	-0.32139734024845	10.27608874477957	11.34572723667556
C	-0.04569569008409	10.82165291240960	12.61919892043184
H	0.58304038863354	10.26795908581368	13.31681381730283
C	-0.54394734194331	12.06114160679367	12.99148263170436
H	-0.31897109288978	12.48101913891627	13.97280583294548
C	-1.34219671091109	12.80239211869922	12.09909455917081
C	-1.62153828254909	12.28275415237384	10.82580547097852
H	-2.23857281856990	12.83227128461887	10.11660954924328
C	-1.10822441434281	11.03633826232750	10.46181758253155
H	-1.34311492665305	10.63730505881374	9.47385879646584
C	-2.59975053543720	14.80289366784942	11.67792725590617
H	-2.03896149995395	15.08118425112267	10.77277266830762
H	-2.85305147189720	15.70388794067407	12.24566257306134
H	-3.52139917219296	14.27165343684446	11.39586895933974

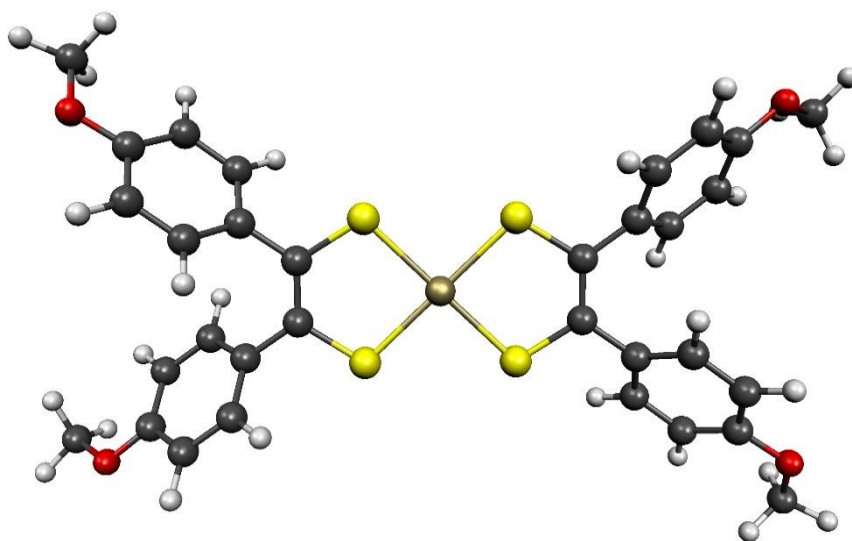


Figure A.1.13. Geometry optimized structure of **3.1b**

Table A.1.8. Geometry Optimised Coordinates of $[\text{Ni}\{(\text{dto})\text{SnCl}_4\}_2]^{3-}$

Ni	7.24220486735497	-0.00125928183015	-0.00038838104396
Sn	3.27227626859123	4.24559530888593	-0.31580885399695
Sn	11.21608648669772	-4.24430310132482	0.31625284495994
S	5.88687966851599	0.90083272922594	1.44052100787507
S	6.54544292094644	1.29129304937509	-1.60455178179268
S	8.59796483303221	-0.90287274156502	-1.44116735751390
S	7.93888608617029	-1.29391068592622	1.60373543354103
C	9.43872166513971	-2.09351491754809	-0.54620116191454
C	9.13315574790041	-2.27416893025212	0.87059537647200
C	5.04706766603047	2.09236844660285	0.54585531505234
C	5.35227513798697	2.27261936828200	-0.87108327682069
O	10.34312461087323	-2.84436792276738	-1.08950156370346
O	9.77878080225017	-3.17748258317036	1.53753267952272
O	4.14396613775119	2.84447430108600	1.08955212621328
O	4.70726746554199	3.17650663582398	-1.53782971914616
Cl	5.09644882835872	5.77957665306195	0.26491936510856
Cl	2.58914496421611	5.60830544286013	-2.19594825656832
Cl	1.82753206066509	5.16186456844314	1.39651190636042
Cl	1.65759970508673	2.48687935014829	-0.87757127057371
Cl	9.39455773020883	-5.78090924713054	-0.26594396571801
Cl	11.90010500390006	-5.60637481127512	2.19648273201604
Cl	12.66333039431271	-5.15796978486666	-1.39536652582686
Cl	12.82768094846876	-2.48318184613882	0.87940332749786

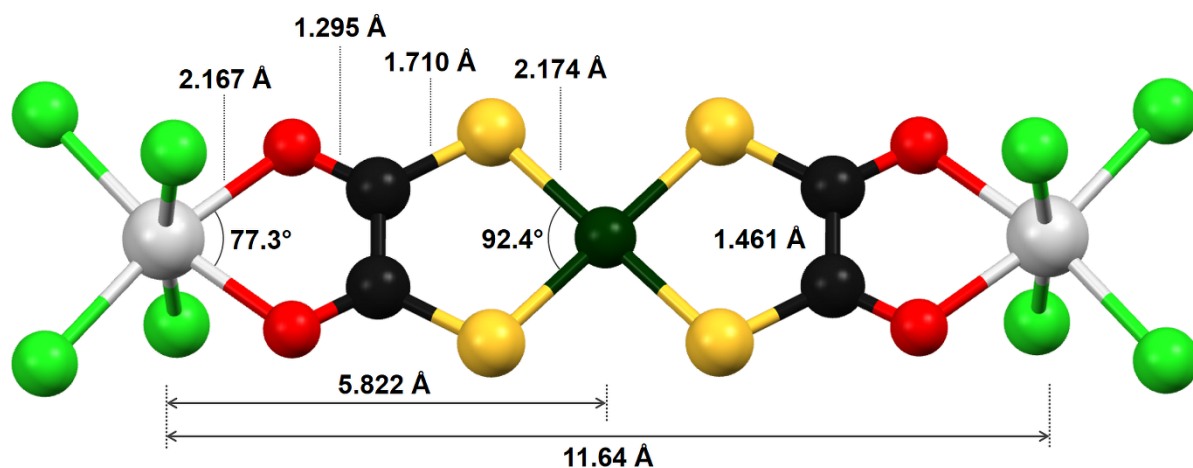


Figure A.1.14. Salient metrics for the optimised structure of $[\text{Ni}\{(\text{dto})\text{SnCl}_4\}_2]^{3-}$

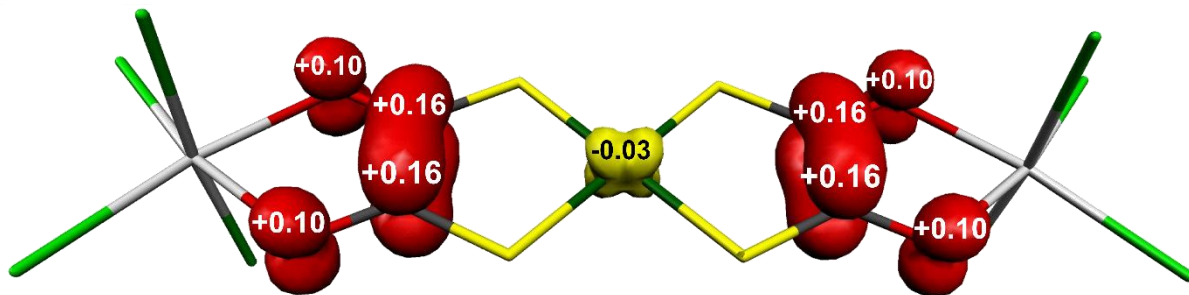


Figure A.1.15. Mulliken spin population analysis for [Ni{(dto)SnCl₄}₂]³⁻ (red: α-spin; yellow: β-spin)

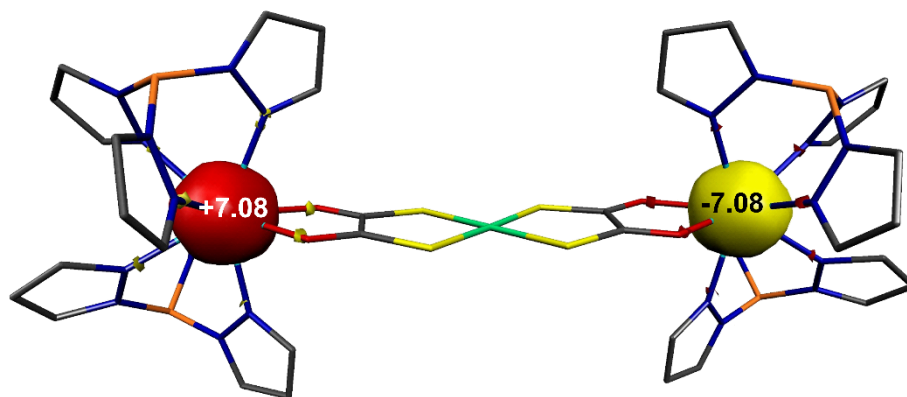


Figure A.1.16 Mulliken spin population analysis for **4.5a** (red: α -spin; yellow: β -spin)

Table A.1.9 Total Energies and Exchange Couplings from BS Calculations

	M_S	Spin Arrangement	Total Energy / E_h	$J_{\text{calcd}} / \text{cm}^{-1}$
4.5a	7	↑↑↑↑↑↑↑↑ ↑↑↑↑↑↑↑↑	-29435.25132341	+0.02
	0	↑↑↑↑↑↑↑↑ ↓↓↓↓↓↓↓↓	-29435.25131849	
BS(14,1)	$15/2$	↑↑↑↑↑↑↑↑ ↑ ↑↑↑↑↑↑↑↑	-29434.71500317	-1.23
	$13/2$	↑↑↑↑↑↑↑↑ ↓ ↑↑↑↑↑↑↑↑	-29434.71508175	
4.5b	$15/2$	↑↑↑↑↑↑↑↑ ↑↑↑↑↑↑↑↑	-29434.71500480	+477.71
	$1/2$	↑↑↑↑↑↑↑↑ ↓↓↓↓↓↓↓↓	-29434.59307375	
BS(7,6)	$13/2$	↑↑↑↑↑↑↑↓ ↑↑↑↑↑↑↑↑	-29434.71508126	+629.34
	$1/2$	↓↓↓↓↓↓↓↓↓ ↑↑↑↑↑↑↑↑	-29434.59459394	

A.1. Relaxation data

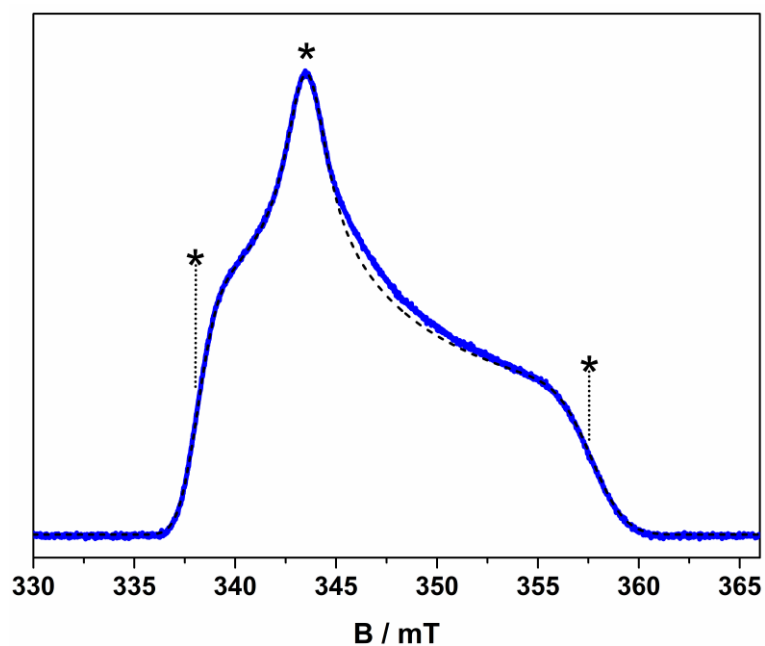


Figure A.2.1. ESE detected EPR spectrum (blue line) and simulation (dashed line) of a 1 mM solution of **3.1b** in 4:1 $\text{CCl}_4/\text{Cl}_3\text{CCN}$ recorded at 10 K. Asterisks indicates field positions for relaxation measurements.

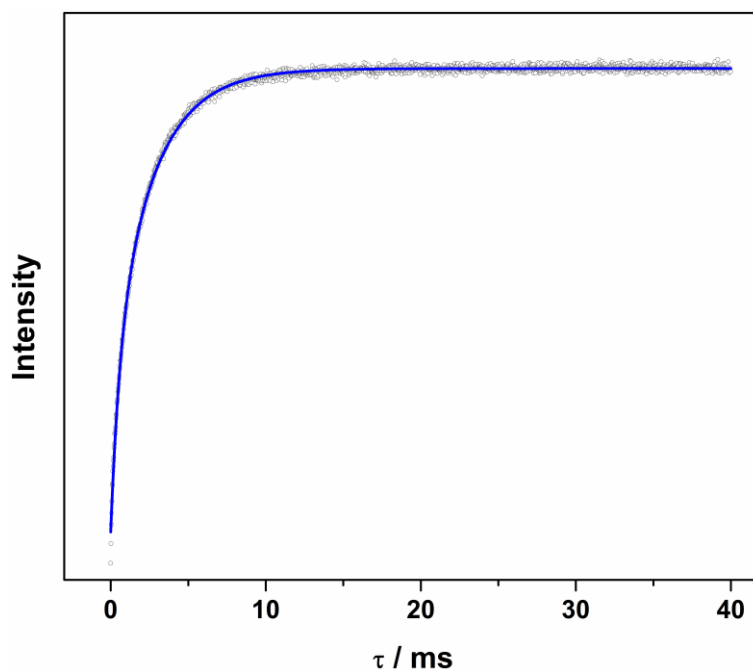


Figure A.2.2 Inversion recovery data (open circles) and biexponential fit (blue line) of a 1 mM solution of **3.1b** in 4:1 $\text{CCl}_4/\text{Cl}_3\text{CCN}$ recorded at 10 K and 343.5 mT.

Table A.2.1 Fit parameters for inversion recovery data of **3.1b** in 4:1 CCl₄/Cl₃CCN at 343.5 mT

T	A _f	T _{1,f} / μs	A _s	T _{1,s} / μs
5	0.385(3)	7000(100)	0.414(2)	58300(400)
10	0.72(1)	560(10)	1.41(1)	2630(20)
20	2.54(6)	44.7(9)	5.51(6)	139.9(8)
40			6.23(2)	9.65(3)
60			6.0(4)	3.1(7)
80			27.2(1)	1.61(1)

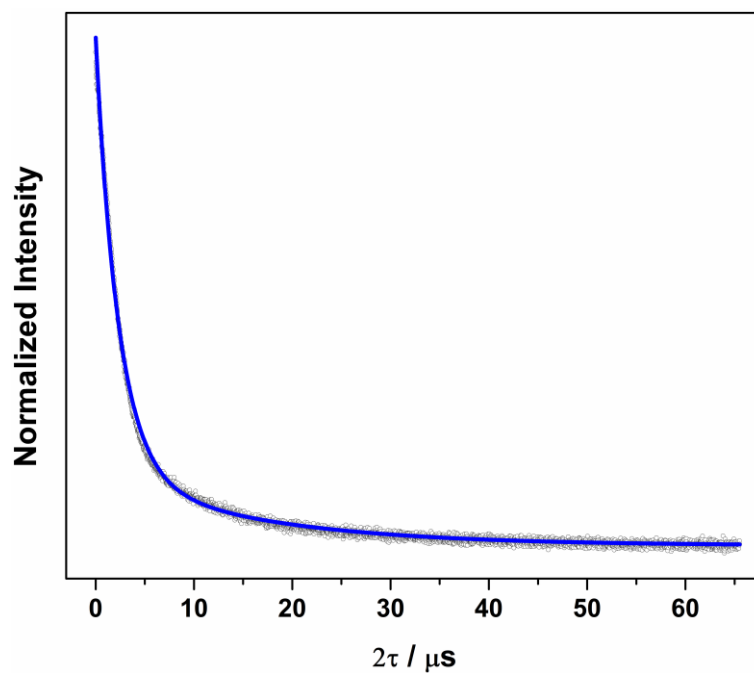


Figure A.2.3. Hahn-echo decay curve (open circles) and biexponential fit (blue line) of a 1 mM solution of **3.1b** in 4:1 CCl₄/Cl₃CCN recorded at 10 K and 343.5 mT.

Table A.2.2. Biexponential fit parameters for Hahn-echo decay curves of **3.1b** in 4:1 CCl₄/Cl₃CCN at 343.5 mT

T	A_f	T_{M,f} / μs	A_s	T_{M,s} / μs
5	29.72(5)	0.194(1)	3.75(3)	11.5(1)
10	55.7(1)	2.36(1)	12.0(1)	15.7(2)
20	80.3(3)	2.20(1)	15.7(3)	13.7(1)
40	101(2)	1.70(2)	13(2)	8.0(6)
60	145.6(2)	1.13(1)	30.2(1)	2.52(2)
80	220(10)	0.29(3)	48(8)	2.6(5)

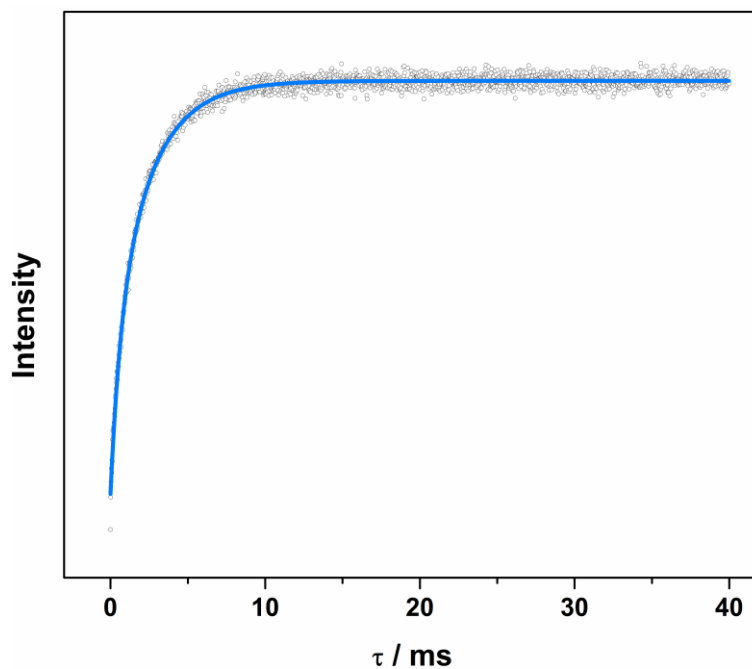


Figure A.2.4. Inversion recovery data (open circles) and biexponential fit (blue line) of a 1 mM solution of **3.1b** in 4:1 CCl₄/Cl₃CCN recorded at 10 K and 338.1 mT.

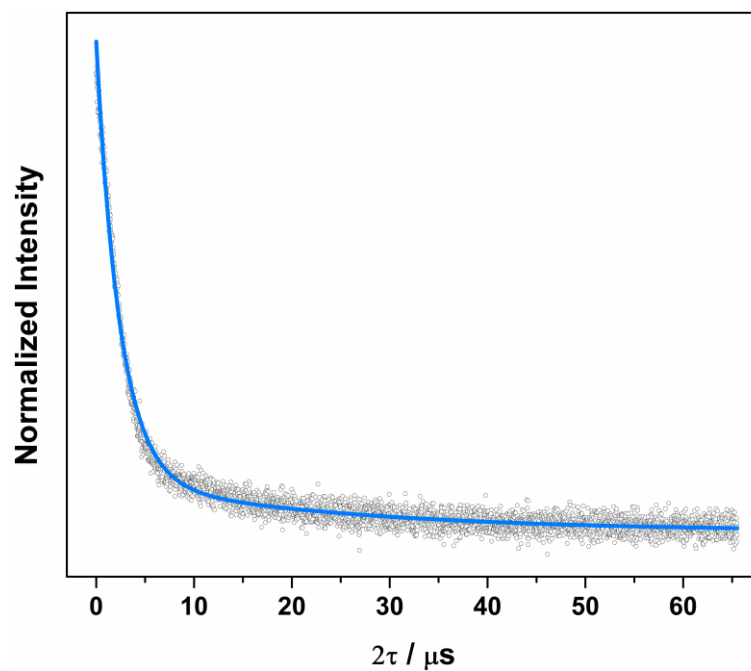


Figure A.2.5. Hahn-echo decay curve (open circles) and biexponential fit (blue line) of a 1 mM solution of **3.1b** in 4:1 CCl₄/Cl₃CCN recorded at 10 K and 338.1 mT.

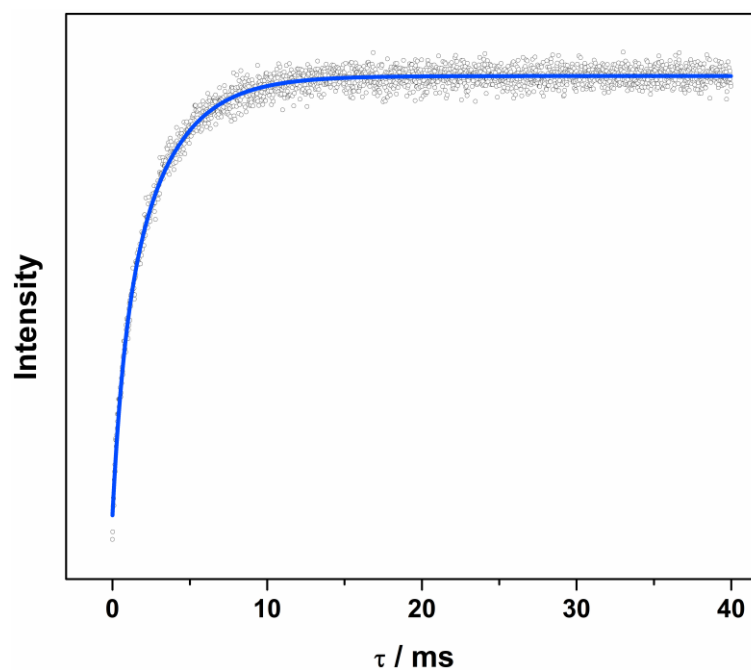


Figure A.2.6. Inversion recovery data (open circles) and biexponential fit (blue line) of a 1 mM solution of **3.1b** in 4:1 CCl₄/Cl₃CCN recorded at 10 K and 357.5 mT.

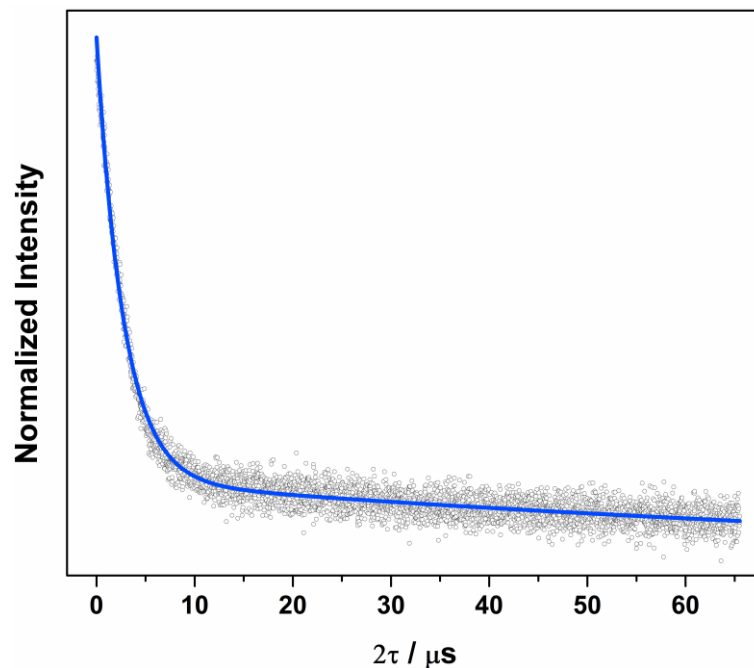


Figure A.2.7. Hahn-echo decay curve (open circles) and biexponential fit (blue line) of a 1 mM solution of **3.1b** in 4:1 CCl₄/Cl₃CCN recorded at 10 K and 357.5 mT.

Table A.2.3. Biexponential fit parameters for inversion recovery data of **3.1b** in 4:1 CCl₄/Cl₃CCN at 10 K

B / mT	A_f	T_{1,f} / ms	A_s	T_{1,s} / ms
338.1	0.97(5)	0.62(4)	1.95(5)	2.43(4)
343.5	0.72(1)	0.56(1)	1.41(1)	2.63(2)
357.5	1.50(8)	0.70(5)	3.08(9)	2.95(6)

Table A.2.4. Biexponential fit parameters for Hahn-echo decay curves of **3.1b** in 4:1 CCl₄/Cl₃CCN at 10 K

B / mT	A_f	T_{M,f} / μs	A_s	T_{M,s} / μs
338.1	94.0(4)	2.3(1)	18.8(2)	15.8(1)
343.5	55.7(1)	2.36(1)	12.0(1)	15.7(2)
357.5	120.7(5)	2.50(2)	17.6(4)	17.6(1)

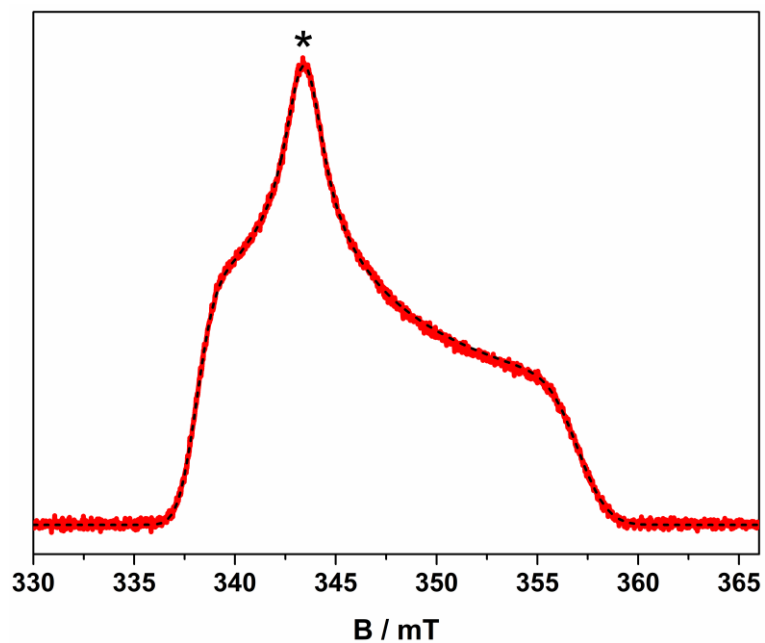


Figure A.2.8. ESE detected EPR spectrum (red line) and simulation (dashed line) of a 1 mM solution of **3.1b** in 4:1 $\text{CDCl}_3/\text{Cl}_3\text{CCN}$ recorded at 10 K. Asterisk indicates field position for relaxation measurements.

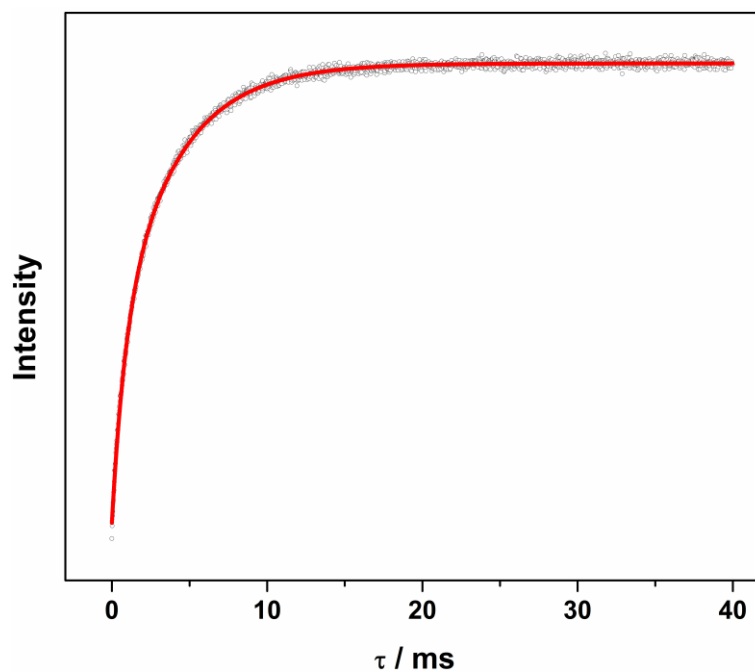


Figure A.2.9. Inversion recovery data (open circles) and biexponential fit (red line) of a 1 mM solution of **3.1b** in 4:1 $\text{CDCl}_3/\text{Cl}_3\text{CCN}$ recorded at 10 K and 343.5 mT.

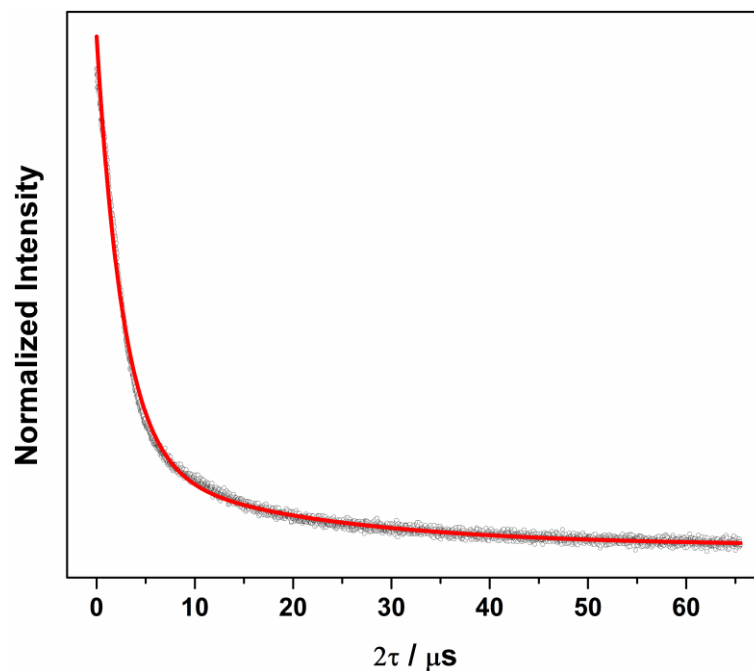


Figure A.2.10. Hahn-echo decay curve (open circles) and biexponential fit (red line) of a 1 mM solution of **3.1b** in 4:1 $\text{CCl}_4/\text{Cl}_3\text{CCN}$ recorded at 10 K and 343.5 mT.

Table A.2.5. Biexponential fit parameters for inversion recovery data of **3.1b** in 4:1 $\text{CDCl}_3/\text{Cl}_3\text{CCN}$ at 343.5 mT

T	A_f	$T_{1,f} / \text{ms}$	A_s	$T_{1,s} / \text{ms}$
5	0.491(4)	17.2(2)	0.727(4)	85.8(5)
10	0.475(6)	0.83(2)	0.820(7)	3.81(2)
20	1.20(2)	0.044(1)	2.71(2)	0.183(1)

Table A.2.6. Biexponential fit parameters for Hahn-echo decay curves of **3.1b** in 4:1 $\text{CDCl}_3/\text{Cl}_3\text{CCN}$ at 343.5 mT

T	A_f	$T_{M,f} / \mu\text{s}$	A_s	$T_{M,s} / \mu\text{s}$
5	41.1(2)	2.58(2)	6.7(1)	17.0(5)
10	46.0(1)	2.65(1)	6.7(1)	19.3(5)
20	102.9(4)	2.55(2)	14.6(4)	13.8(4)

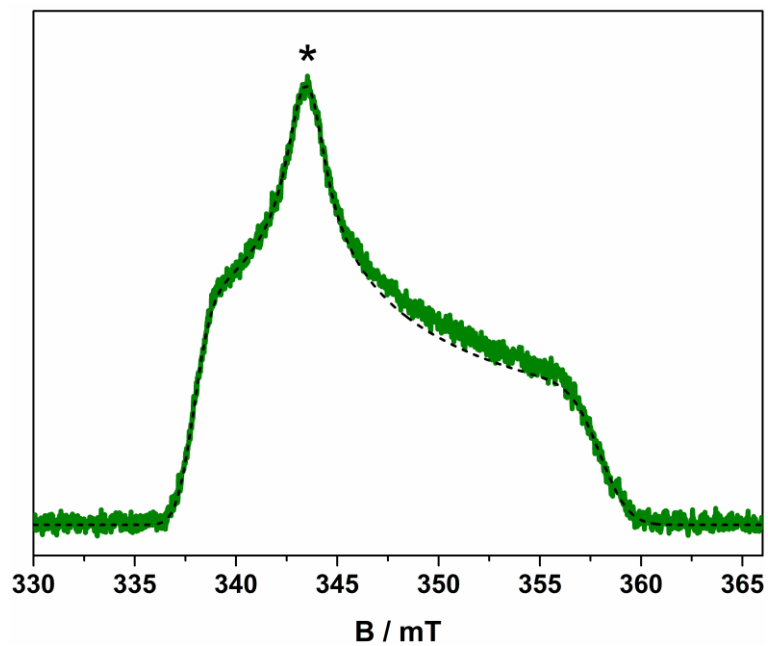


Figure A.2.11. ESE detected EPR spectrum (green line) and simulation (dashed line) of a 1 mM solution of **3.1b** in 4:1 CS₂/CCl₄ recorded at 10 K. Asterisk indicates field position for relaxation measurements.

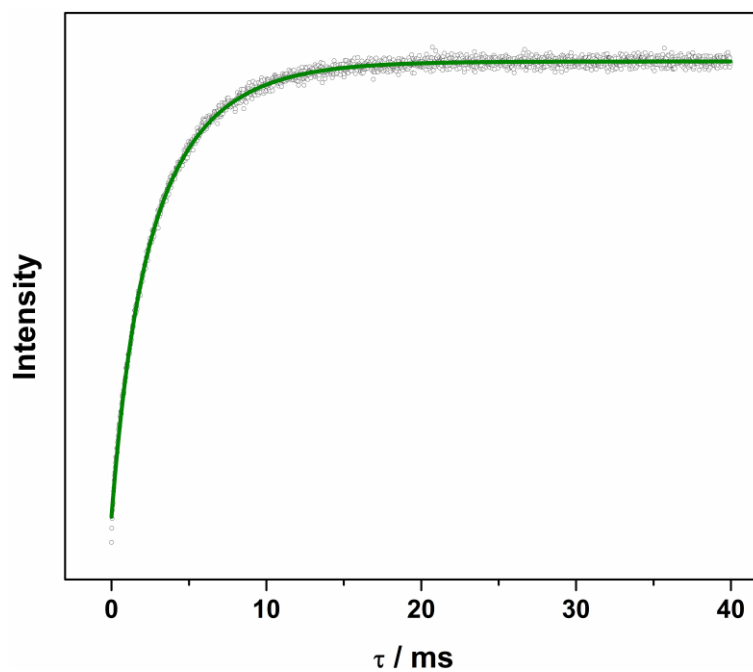


Figure A.2.12. Inversion recovery data (open circles) and biexponential fit (green line) of a 1 mM solution of **3.1b** in 4:1 CS₂/CCl₄ recorded at 10 K and 343.5 mT.

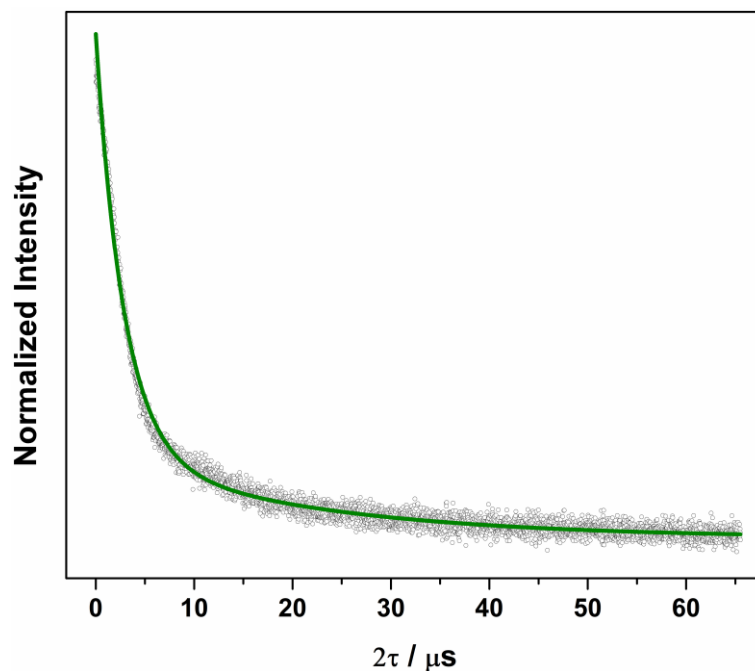


Figure A.2.13. Hahn-echo decay curve (open circles) and biexponential fit (green line) of a 1 mM solution of **3.1b** in 4:1 CS₂/CCl₄ recorded at 10 K and 343.5 mT.

Table A.2.7. Biexponential fit parameters for inversion recovery data of **3.1b** in 4:1 CS₂/CCl₄ at 343.5 mT

T	A_f	T_{1,f} / ms	A_s	T_{1,s} / ms
5	0.346(8)	15.1(6)	0.766(7)	92.0(8)
10	3.8(2)	1.31(5)	7.5(2)	3.89(5)
20	4(1)	0.11(1)	4(1)	0.19(2)

Table A.2.8. Biexponential fit parameters for Hahn-echo decay curves of **3.1b** in 4:1 CS₂/CCl₄ at 343.5 mT

T	A_f	T_{M,f} / μs	A_s	T_{M,s} / μs
5	138(1)	2.84(4)	23(1)	16.9(8)
10	143.7(7)	2.79(2)	22.8(6)	21.0(7)
20	115(1)	2.69(4)	18(1)	17.1(4)

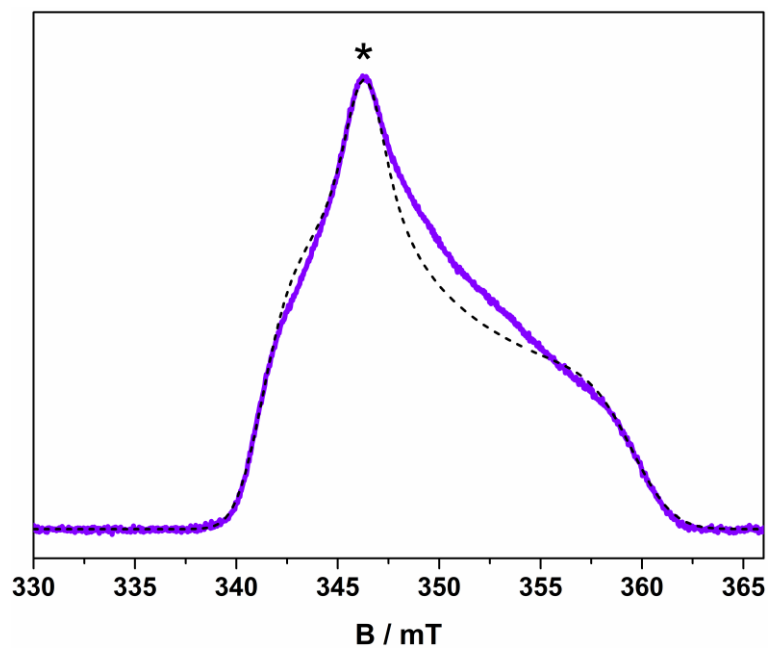


Figure A.2.14. ESE detected EPR spectrum (violet line) and simulation (dashed line) of a 1 mM solution of **3.1b** in 4:1 $\text{Cl}_3\text{CCN}/\text{CCl}_4$ recorded at 10 K. Asterisk indicates field position for relaxation measurements.

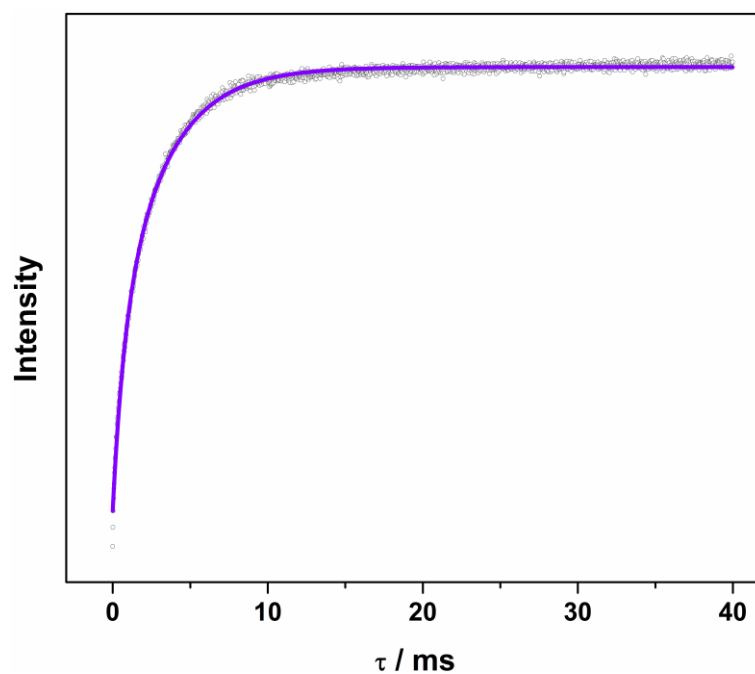


Figure A.2.15. Inversion recovery data (open circles) and biexponential fit (violet line) of a 1 mM solution of **3.1b** in 4:1 $\text{Cl}_3\text{CCN}/\text{CCl}_4$ recorded at 10 K and 346.2 mT.

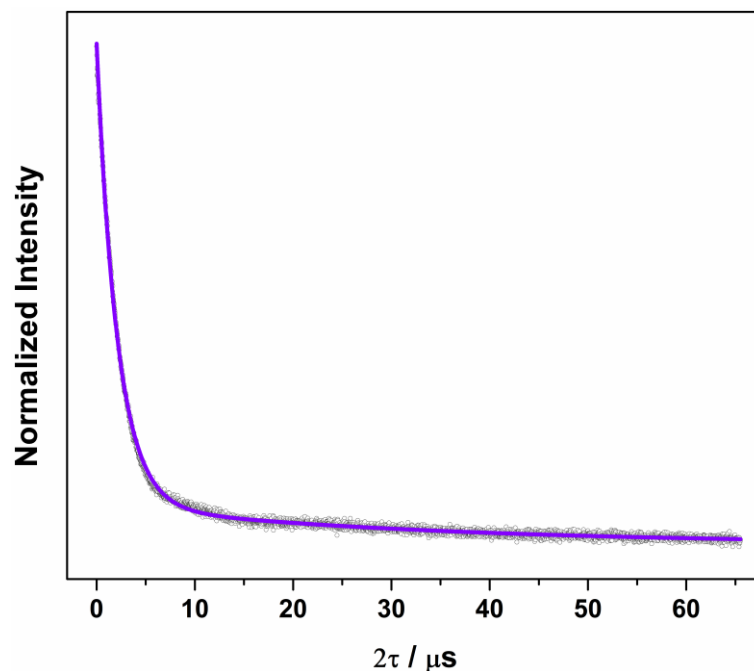


Figure A.2.16. Hahn-echo decay curve (open circles) and biexponential fit (violet line) of a 1 mM solution of **3.1b** in 4:1 Cl₃CCN/CCl₄ recorded at 10 K and 346.2 mT.

Table A.2.9. Biexponential fit parameters for inversion recovery data of **3.1b** in 4:1 Cl₃CCN/CCl₄ at 346.2 mT

T	A_f	T_{1,f} / ms	A_s	T_{1,s} / ms
5	0.497(3)	7.97(9)	0.441(3)	56.1(3)
10	0.362(7)	0.7(2)	0.709(8)	3.09(2)
20	0.56(1)	0.023(1)	2.78(1)	0.122(1)

Table A.2.10. Biexponential fit parameters for Hahn-echo decay curves of **3.1b** in 4:1 Cl₃CCN/CCl₄ at 346.2 mT

T	A_f	T_{M,f} / μs	A_s	T_{M,s} / μs
5	35.6(1)	1.85(1)	2.59(6)	14.0(4)
10	40.1(1)	1.95(5)	2.95(3)	15.2(6)
20	64.4(1)	1.8(1)	6.23(8)	14.4(4)

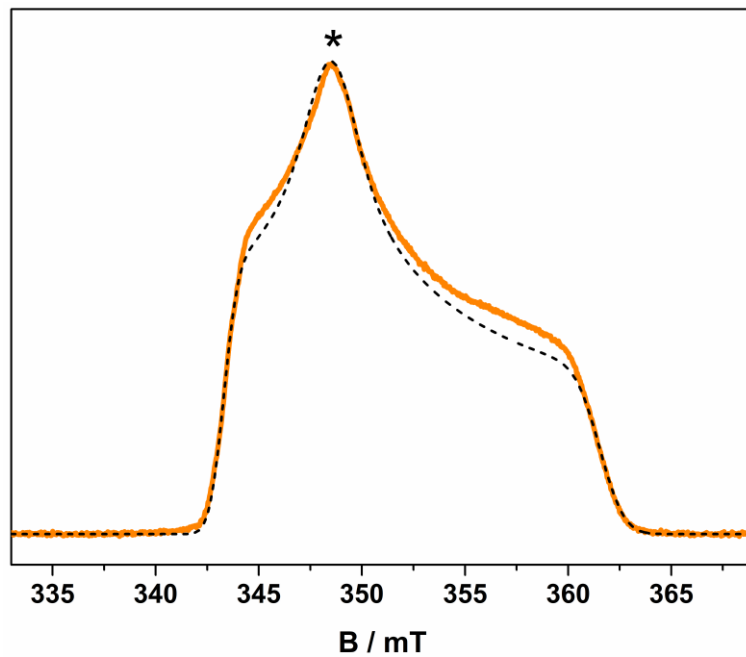


Figure A.2.17. ESE detected EPR spectrum (orange line) and simulation (dashed line) of a polycrystalline sample of **3.1b** diluted 2% in $[\text{Ni}(\text{adt})_2]$ recorded at 10 K. Asterisk indicates field position for relaxation measurements.

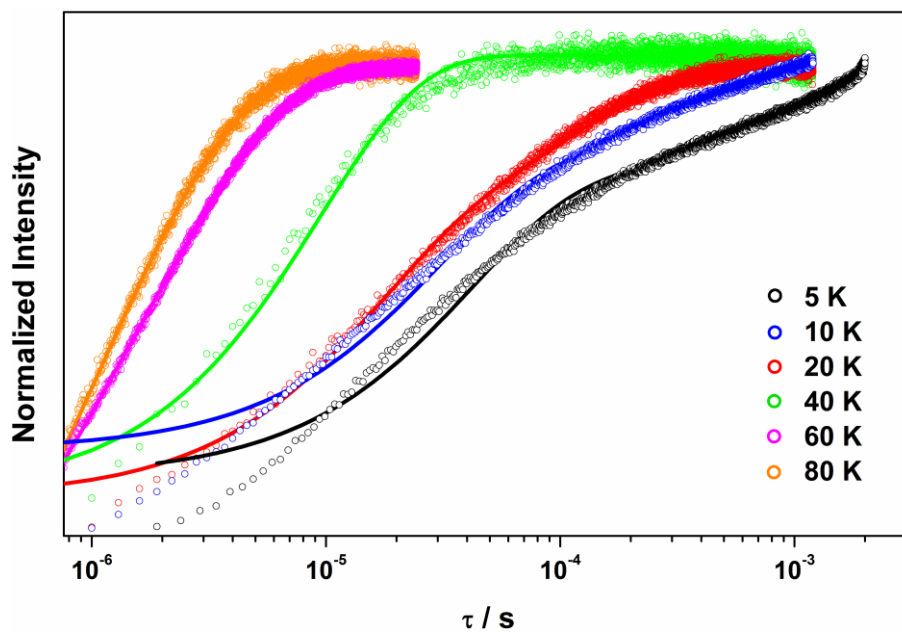


Figure A.2.18. Inversion recovery data (open circles) and biexponential fit (solid line) of a polycrystalline sample of **3.1b** diluted 2% in $[\text{Ni}(\text{adt})_2]$ at 348.5 mT.

Table A.2.11. Biexponential fit parameters for inversion recovery data of **3.1b** diluted 2% in $[\text{Ni}(\text{adt})_2]$ at 348.5 mT

T	A_f	$T_{1,f} / \mu\text{s}$	A_s	$T_{1,s} / \mu\text{s}$
5	3.14(1)	41.5(3)	1.56(1)	1030(10)
10	3.33(1)	30.2(2)	1.75(1)	336(3)
20	2.81(2)	18.5(3)	1.91(2)	123(1)
40	4.9(4)	5.0(5)	3.1(5)	16(1)
60	31.6(6)	1.05(3)	49.0(7)	3.08(2)
80	17.9(7)	0.72(4)	27(1)	2.04(2)

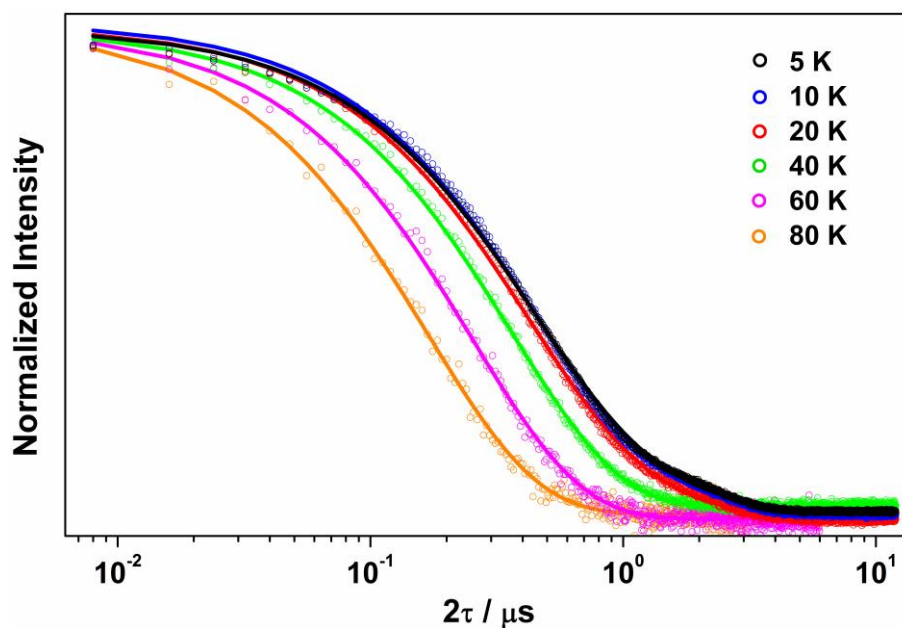


Figure A.2.19. Hahn-echo decay curve (open circles) and biexponential fit (solid line) of a polycrystalline sample of **3.1b** diluted 2% in $[\text{Ni}(\text{adt})_2]$ at 348.5 mT.

Table A.2.12. Fit parameters for Hahn-echo decay curves of **3.1b** diluted 2% in [Ni(adt)₂] at 348.5 mT

T	A_f	$T_{M,f} / \mu\text{s}$	A_s	$T_{M,s} / \mu\text{s}$
5	134.0(9)	0.406(3)	25.6(9)	1.36(3)
10	88.6(7)	0.409(3)	14.3(7)	1.44(4)
20	92.9(9)	0.389(4)	13.4(9)	1.33(5)
40			40.7(9)	0.36(1)
60			71(2)	0.25(1)
80			667(5)	0.17(1)

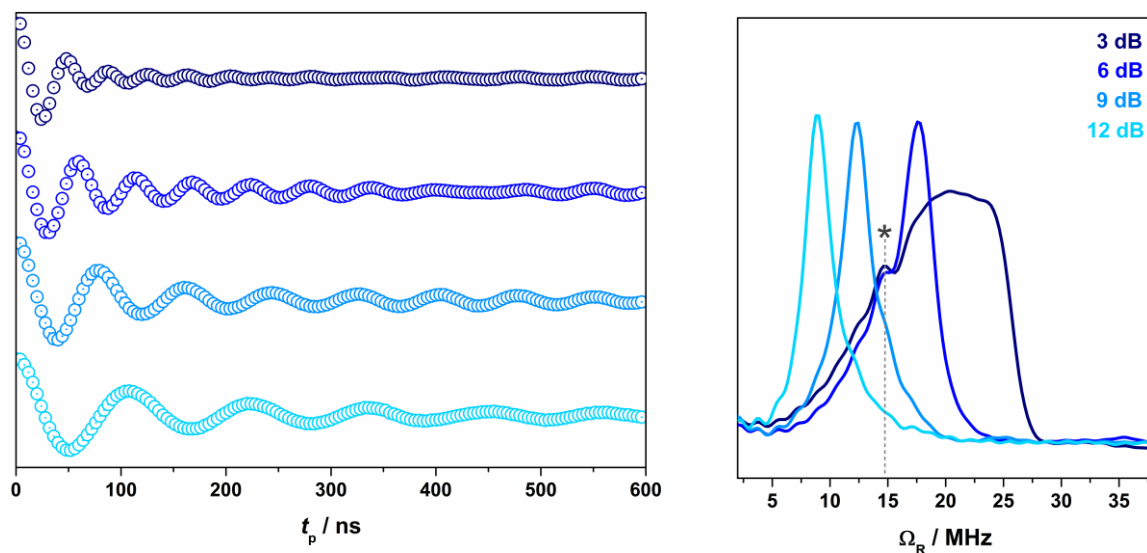


Figure A.2.20. Rabi oscillations (left) and corresponding frequencies from the Fourier transfer of the data (right) for **3.1b** in 4:1 CCl₄/Cl₃CCN at 10 K and 343.5 mT from variable power nutation measurements. The asterisk in the Fourier transform data indicate the peak matching the Larmor frequency of ¹H (14.6 MHz) within error.

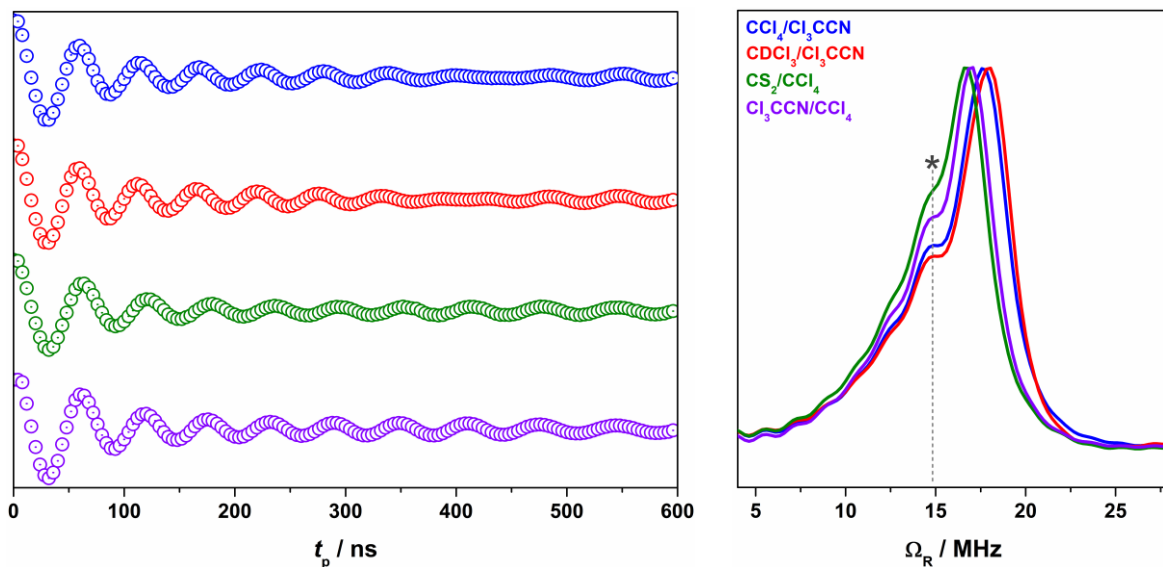


Figure A.2.21. Nutation data (left) and Fourier transforms of the data (right) for **3.1b** in 4:1 CCl₄/Cl₃CCN (blue), 4:1 CDCl₃/Cl₃CCN (red), 4:1 CS₂/CCl₄ (green), and 4:1 Cl₃CCN/CCl₄ (violet) at 10 K and 343.5 mT. The asterisk in the Fourier transform data indicate the peak matching the Larmor frequency of ¹H (14.6 MHz) within error.

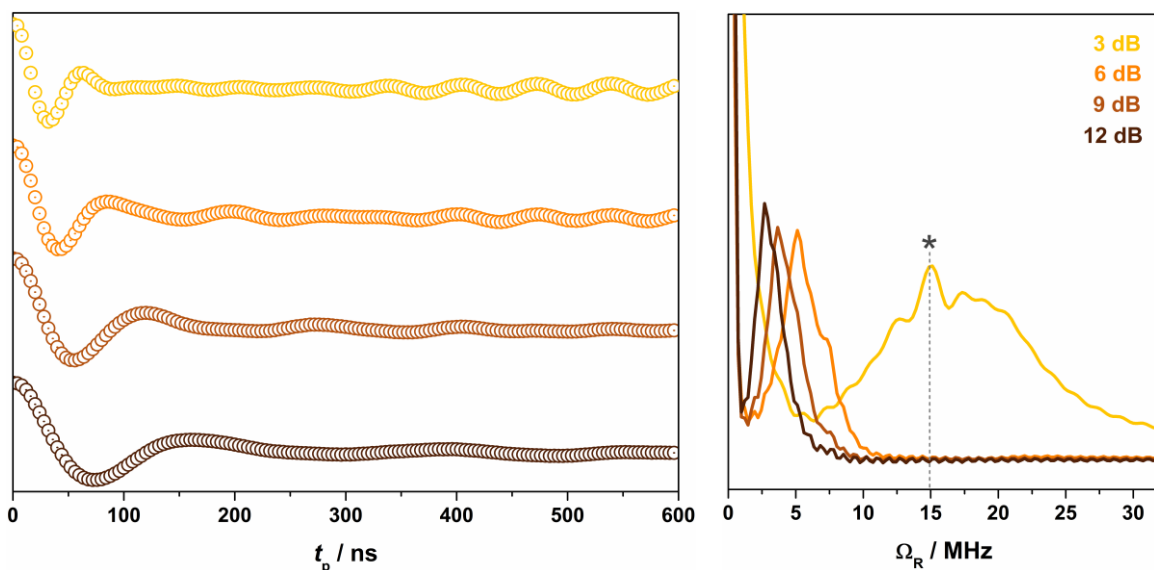


Figure A.2.22. Rabi oscillations (left) and corresponding frequencies from the Fourier transfer of the data (right) for **3.1b** in diluted 2% in [Ni(adt)₂] at 10 K and 348.5 mT from variable power nutation measurements. The Rabi frequency at 3 dB microwave power is obscured in the Fourier transform from coupling to the Larmor frequency of ¹H (14.6 MHz) within error.

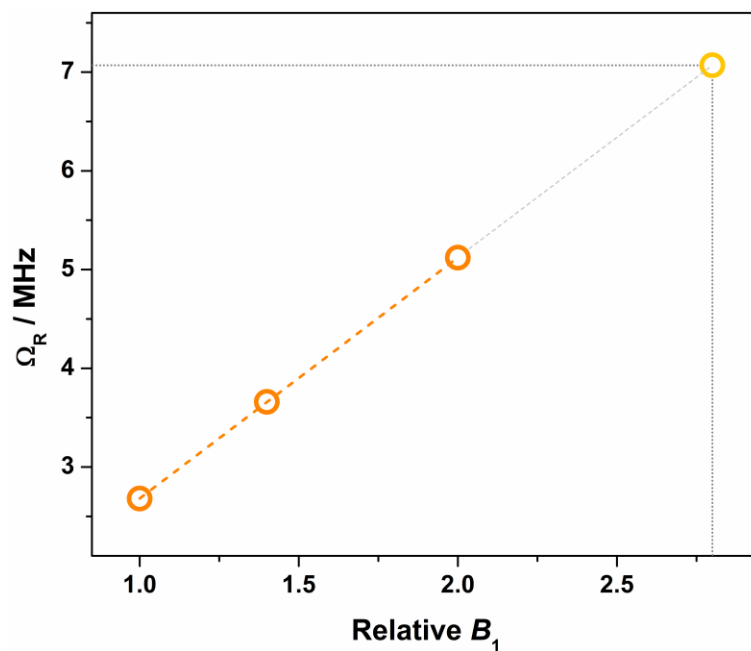


Figure A.2.23. Linear dependence of the oscillation frequency (Ω_R) with respect to the B_1 field for polycrystalline **3.1b** diluted 2% in $[\text{Ni}(\text{adt})_2]$. Pumpkin-colored open circles indicate oscillation frequency and the corresponding dashed line the line of best fit. The gray extrapolation line is used to estimate the Rabi frequency for relative $B_1 = 2.82$ (microwave power = 3 dB) of 7.07 MHz as indicated by sight lines.